This is to certify that the
dissertation entitled

PREPARATION, CHARACTERIZATION AND APPLICATION OF
BORON-DOPED DIAMOND POWDERS: APPLICATION AS AN
ELECTROCATALYST SUPPORT AND A STATIONARY PHASE
FOR HPLC

presented by

Vernon Matthew Swope

has been accepted towards fulfillment
of the requirements for the

Doctoral degree in Chemistry

Greg M. Swain
Major Professor's Signature

December 17, 2010
Date

MSU is an Affirmative Action/Equal Opportunity Employer

PREPA
DOPED D

PREPARATION, CHARACTERIZATION AND APPLICATION OF BORON-DOPED DIAMOND POWDERS: APPLICATION AS AN ELECTROCATALYST SUPPORT AND A STATIONARY PHASE FOR HPLC

By

Vernon Matthew Swope

A DISSERTATION

Submitted to
Michigan State University
in partial fulfillment of the requirements
for the degree of

DOCTOR OF PHILOSOPHY

Chemistry

2010

PREPAR
DOPED D

In this

boron-doped m

coated powder

diamond powd

membrane fuel

B-UNCD

CH_4 concentrat

morphology, mi

Ultrananocrysta

concentration w

in the gas pha

significant micr

B_2H_6 in the gas

B-UNCD

and carbon blac

electron micros

formed on the p

non-diamond sp

ABSTRACT

PREPARATION, CHARACTERIZATION AND APPLICATION OF BORON-DOPED DIAMOND POWDERS: APPLICATION AS AN ELECTROCATALYST SUPPORT AND A STATIONARY PHASE FOR HPLC

By

Vernon Matthew Swope

In this dissertation the growth, physical and electrochemical properties of boron-doped microcrystalline (BMD) and ultrananocrystalline (B-UNCD) diamond coated powders was studied. Targeted uses of these electrically conducting diamond powders are as an electrocatalyst support for the polymer electrolyte membrane fuel cell and as a stationary phase for HPLC.

B-UNCD thin films on Si were prepared with varying B_2H_6 (0-50 ppm) and CH_4 concentration (0.5 to 3% v/v) to investigate the dependence of the B-UNCD morphology, microstructure and phase purity on the source gas composition. Ultrananocrystalline diamond was only formed at the 1% CH_4 level. Boron concentration within the films was linearly dependent on the boron concentration in the gas phase as determined by nuclear reaction analysis. There were no significant microstructural changes among the films grown between 0-50 ppm B_2H_6 in the gas phase.

B-UNCD formation on diamond powders (500, 100, and 3-6 nm diam.) and carbon black powders (glassy carbon and Ketjen black) was evaluated using electron microscopy, Raman spectroscopy, EELS, and XRD. The B-UNCD formed on the powder is the predominant microstructural phase deposited, with non-diamond sp^2 carbon phases interspersed.

Electroc
made with B
aqueous acid
slide with Na
performed in
Ag/AgCl. The
temperature a
packed into a
performed on
powders: grap
boron-doped d
while the ca
degradation.

The perf
phase in elect
and its stabil
compared. The
values (*i.e.* -1.2
play a key rol
stationary pha
comparison to t

Electrochemical and *in situ* Raman spectroscopic measurements were made with BMD powders before, during and after potentiostatic polarization in aqueous acid. Electrodes were prepared by casting a powder slurry on a glass slide with Nafion serving as the binder. The potentiostatic polarization was performed in either 0.1 M $HClO_4$ or 0.1 M H_2SO_4 at 1.0, 1.2 and 1.4 V vs. Ag/AgCl. The polarizations were conducted at two temperatures: room temperature and 80 °C. Similar studies were conducted using B-UNCD powders packed into a pipette electrode with no binder. Comparison studies were also performed on Vulcan XC-72 and several microstructurally-varied sp^2 carbon powders; graphite, glassy carbon and acetylene black. It was found that the boron-doped diamond powders are dimensionally stable and corrosion resistant, while the carbon black powders underwent more severe microstructural degradation.

The performance of boron-doped diamond powder (BDDP) as a stationary phase in electrochemically modulated liquid chromatography was investigated and its stability as a packing relative to porous graphitic carbon (PGC) was compared. The results show that BDDP is stable over a wide range of E_{appl} values (*i.e.* -1.2 to +1.2 V vs. Ag/AgCl). The data also reveal that electrostatics play a key role in the adsorption of the aromatic sulfonates on the BDDP stationary phase, and that these analytes are more weakly retained in comparison to the PGC support.

In memory of my father
Jerry D. Swope, 1939-2007
Who I sadly lost while on my journey at MSU

The decis
necessary to en
future in taking th
of my decision.
reversed. It is w
completion of thi
daughter Annika

I was fortu
Greg Swain acce
and encouragem
Advanced Micros
valuable advice f

I will miss
project members
too comfortable.
appreciate havin
the only other Am
HPLC system for
may serve us bet

My friends
completing my

ACKNOWLEDGEMENTS

The decision to come to Michigan State was not made lightly. It was necessary to end my previous career and inherit all the uncertainties for the future in taking that step. Unselfishly, my wife Amy was undaunted in her support of my decision. I am not sure I could be so generous if the situation were reversed. It is with her help and patience during the last 5 years that made completion of this degree possible. I am truly blessed to have her and my daughter Annika in my life.

I was fortunate that through an inexplicable lax of good sense, my advisor Greg Swain accepted me into the group. I am thankful for his guidance, support, and encouragement over the last few years. Dr. Xudong Fan with the Center for Advanced Microscopy and Michael Becker with Fraunhofer USA also provided valuable advice for my research.

I will miss my group mates, both past and present, especially the fuel cell project members: Isao, Liang, Doo Young, Ayten and Xingyi. Lest she becomes too comfortable, I must find someone to pester Xingyi in my absence. I appreciate having Matt Fhaner as my sounding board, as for some time he was the only other American student in the group. Dr. Hong Zhao and I fought with an HPLC system for several months before coming to the scientific conclusion that it may serve us better as a boat anchor on a fishing trip.

My friends and family have been there for everything I needed while completing my degree. Many thanks to my mother and siblings for their

encouragement
the initial shoc
enough words t
provided by bot
to thank my lat
faith in my abili
Paul Malewski a
assistance.

Financial
(DE-FG03-95ER

encouragement and help. Even my father-in-law seems to have recovered from the initial shock of hearing that I quit my job to return to school! There aren't enough words to express my sincere gratitude and appreciation for the support provided by both my immediate and extended family members. I would also like to thank my late father, who passed away during this endeavor, for his unfailing faith in my abilities and his pride in my achievements. Special thanks to Chief Paul Malewski and Mark Carmen, both of whom stayed in touch and offered assistance.

Financial support from the Department of Energy, Office of Basic Science (DE-FG03-95ER146577) and Fraunhofer USA is gratefully acknowledged.

TABLE OF CONTENTS

CHAPTER 3 –Physical, Electrical and Electrochemical Characterization of Boron-Doped Ultrananocrystalline Diamond thin-Films Deposited from $CH_4/H_2/Ar/B_2H_6$ Source Gas Mixtures

CHAPTER 4 – Microscopic Interpretation of Bare, Boron-doped Diamond Coated, and Pt-decorated Carbon Powders

CHAPTER 5 – Microstructural Stability of Boron-Doped-Diamond-Coated Diamond Powders During Potentionstatic Polarization in Aqueous Acid as Probed Using Electrochemical Methods and In-situ Raman Spectroscopy: Comparison with sp^2 Carbon Powders

CHAPTER 6 – The Physiochemical and Electrochemical Properties of Diamond Powders Coated with Boron-Doped Ultrananocrystalline Diamond (B-UNCD)

CHAPTER 7 –Electrochemically Modulated Liquid Chromatography Using a Boron-Doped Diamond Powder Stationary Phase

List of Tables

List of Figures

Figure 3.8

Figure 3.9

Figure 3.10

Figure 3.11

Figure 3.12

Figure 3.13

Figure 3.14

Figure 4.1

Figure 4.2

Figure 4.3

Figure 4.4

Figure 4.5

Figure 4.6

Figure 4.16

Figure 4.17

Figure 4.18

Figure 4.19

Figure 5.1

Figure 5.2

Figure 5.3

Figure 5.4

Figure 5.5

Figure 5.6

Figure 5.7

Figure 5.8

Figure 5.9

Figure 6.1

Figure 6.2

Figure 6.3

Figure 6.4

Figure 6.5

Figure 6.6

Figure 6.7

Figure 6.8

Figure 7.1

Figure 7.2

Figure 7.3

Figure 7.4

Figure 7.5

Figure 7.6

1.1 Introductio

Carbon is

carbon allotropes

important commo

and production c

black (sp^2 bonde

produced yearly

paints and make

commercial app

diamond now s

carbon's availab

applications suc

carbon electrode

and relatively ine

A limitatio

acids under ano

sp^2-bonded carb

$C + 2H$

Chapter 1

Introduction

1.1 Introduction

Carbon is the fourth most abundant element on the planet. The main carbon allotropes, diamond, graphite and carbon black powders, have been important commodities to mankind since at least the Neolithic period. Our use and production of carbon continues, with over 8.1×10^5 metric tons of carbon black (sp^2 bonded) powder and more than 100 tons of synthetic diamond now produced yearly.[1] Carbon black powders are used as coloring agents for tires, paints and makeup. Diamond grit is an important cutting abrasive with broad commercial applications in saw blades, grinders, and polishers. Synthetic diamond now surpasses natural diamond in industrial applications.[1] Due to carbon's availability and non-toxicity, it is also used in many electrochemical applications such as batteries, fuel cells, and chemical sensors. Advantages of carbon electrodes compared to metals include low cost, wider potential window, and relatively inert electrochemistry.

A limitation to traditional carbon black electrodes is degradation in aqua acids under anodic potentials. In acidic media, potential-dependent corrosion of sp^2-bonded carbon materials occurs according to Equation 1.1.[2]

$$C + 2H_2O \rightarrow CO_2 + 4H^+ + 4e^- \qquad E^\circ = 0.118 \text{ V vs. SHE} \qquad (1.1)$$

Kinoshita and Bett found that electrochemical corrosion of carbon black occurs through a two-step process: surface oxide formation followed by carbon gasification to CO_2.[3] Another study by Antonucci et al. reported a direct correlation between the charge passed and the O/C atomic ratio (2 to 14%) when polarized at an applied potential of 1 V vs. SHE.[4] Potential-dependent carbon degradation is an important problem in two electrochemical applications: the electrocatalyst support in polymer electrolyte membrane fuel cells (PEMFC), and the stationary phase in electrochemically modulated liquid chromatography (EMLC).

Hydrogen has received much attention in recent years as a clean, plentiful source of energy to power automobiles that may serve as an alternative to commonly used fossil fuels.[5] The principal hydrogen energy conversion device used today is the (PEMFC). Unlike gasoline engines which convert chemical energy into heat, the PEMFC converts the chemical energy of hydrogen directly into electrical energy. The theoretical conversion efficiency exceeds 80% for a fuel cell directly converting hydrogen to electric power, whereas the conversion efficiency of combustion engines is typically below 50%.[6] The key component of the PEMFC is the membrane electrode assembly (MEA).[7-9] The MEA consists of two electrodes that contain an electrocatalyst dispersed on a high surface area support, connected through an external circuit and separated by a solid polymer electrolyte membrane. Both the anode and cathode of MEAs currently used in PEMFCs consist of electrocatalytic metal particles supported on high surface area carbon powders.

One factor limiting the performance of PEM fuel cells at present is degradation of the electrocatalyst layer, in particular, corrosion of the carbon support. During extended operation with start-stop cycling and fuel starvation, the cathode can experience high potentials. It has been observed that the cathode potential may reach 1.5 V vs. RHE in fractions of a second during the fuel cell start-up .[10, 11] At this stage, the carbon support undergoes severe electrochemical corrosion according to eq. 1.1. Electrochemical corrosion of the support causes catalyst particle agglomeration, increases the ohmic resistance through the powder network, and increases the gas diffusion resistance due to collapse of the porous structure.

Electrochemically-modulated liquid chromatography (EMLC) is a separation technique that manipulates retention through changes in the potential applied (E_{appl}) to a conductive particle, which acts both as the stationary phase and working electrode in a chromatographic column designed to function as a three-electrode electrochemical cell.[8-22] The main advantage of the EMLC method is that an extra variable, the applied potential, is available to increase the efficiency of separations at the column. Carbonaceous packings (*e.g.*, porous graphitic carbon (PGC)) have been used in various types of liquid chromatography separations.[1,8]

There are several types of conductive packings that can be employed for EMLC, including uncoated glassy carbon (GC),[12] PGC,[9-22] and graphitic particles coated with a conductive polymer like polyvinylferrocene or polypyrolle.[23-25] For use in EMLC, the stationary phase material must meet the operational requirements in place for both liquid chromatography and electrochemistry, which encompasses a high surface area, compositional and structural stability, and a high electrical conductivity. To date, the greatest degree of success in EMLC is with PGC as the stationary phase. However, the possible oxidation of PGC at large anodic values of E_{appl} can prove problematic with respect to compositional stability and, therefore retention reproducibility.[26,27]

Clearly, materials with improved stability and durability are needed for PEMFC operation, and as the stationary phase in EMLC. Electrically-conducting diamond is a promising candidate to replace carbon black in the PEMFC and EMLC applications. The goal of the research presented herein is to develop a high surface area (100 m^2/g), microstructurally stable material with improved corrosion resistance at high potentials (1.2 - 1.6 V vs. SHE) for use as the electrocatalyst support in a PEMFC and as the stationary phase in EMLC. Emphasis was placed on preparing conductive diamond coated powders with differing morphologies and surface areas to suit a variety of applications, and assess the synthetic diamond coating. In addition to the proposed use for conductive diamond powders in the PEMFC and EMLC column, it is foreseeable this material may be adopted for other applications where potentiostatic conditions in a harsh chemical environment exist.

1.2 sp^2 Carbons

Graphite is a crystalline sp^2-bonded carbon with a hexagonal lattice structure consisting of layers of carbon atoms arranged in fused hexagonal rings with an interlayer spacing of 3.354 Å. Graphite is defined by the coherence lengths of the crystallites along *a*-axis (L_a) parallel and *c*-axis (L_c) perpendicular to the layer planes as shown in Figure 1.1A. Graphite has the most well-ordered sp^2-bonded carbon microstructure, characterized by an *ABAB* stacking of the graphene sheets.

Carbon blacks are amorphous carbons consisting of randomly oriented small graphitic crystallites with values for L_a and L_c in the range of 15 to 25 Å, respectively. Carbon black is produced by the thermal decomposition of hydrocarbons in oxygen poor conditions at *ca.* 1300° C.[12-14] By controlling the manufacturing conditions, carbon blacks can be produced with particle sizes varying from less than 50 Å to greater than 3000 Å, leading to a surface areas ranging from 10 to 1000 m^2/g.[12] Carbon blacks are turbostratic in nature, composed of a bidimensional organization of stacked graphitic planes that are arbitrarily rotated with respect to one another, as shown in Figure 1.1B.[15] High-

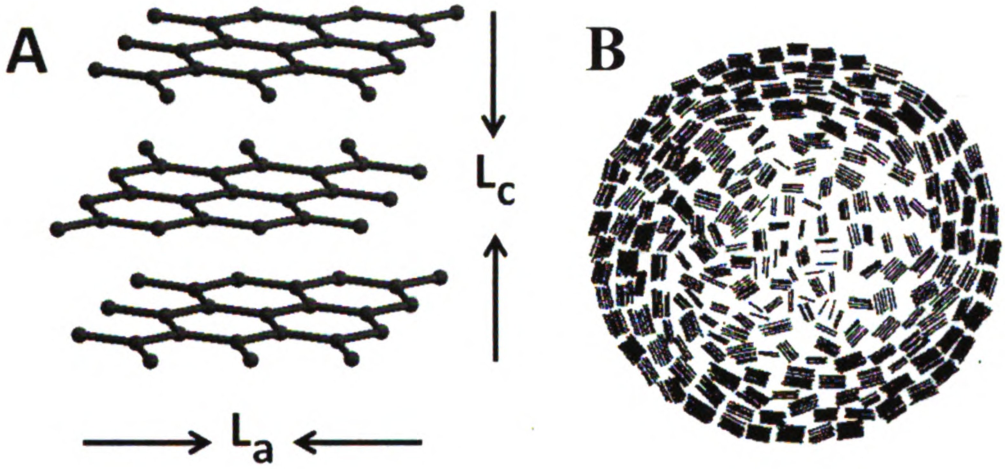

Figure 1.1. Microstructures of (A) graphite, and (B) carbon black. Adapted from reference [12].

resolution transmission electron microscopy measurements have shown that carbon blacks are composed of small spherical particles that join together to form agglomerates.[16] The agglomerates coalesce as a result of Van der Waals forces to form larger aggregates.[16]

1.3 Diamond

Diamond is a carbon allotrope and the hardest naturally occurring bulk solid. The hardness arises from the strong tetrahedral coordinated covalent bonds each carbon atom forms with its neighbor. Diamond has a face centered cubic lattice structure where the C-C bond length is 1.54Å and the lattice constant is 3.56Å (Figure 1.2). Most natural diamonds are formed when carbon solids are compressed at high-pressure, high-temperature conditions existing at depths of 140 to 190 kilometers (87 to 120 mi) in the Earth's mantle. In its natural or undoped form, diamond is an excellent electrical insulator with a bandgap of 5.5 eV.[17] Natural diamond is classified as type I and type II. Type I is yellowish due to nitrogen impurities, while type II is optically clear.

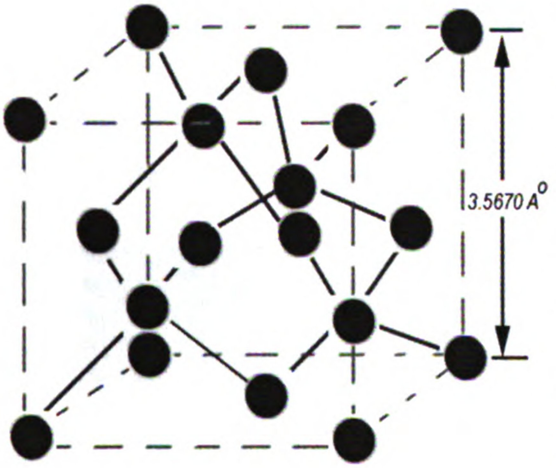

Figure 1.2. A face-centered cubic diamond crystal cell.

The two most common methods for producing synthetic diamond are the high-pressure, high-temperature (HPHT) method and chemical vapor deposition (CVD). The HPHT method mimics natural diamond formation. The process involves placing graphite between large mechanical presses to produce pressures of ~ 5 GPa at 1500 °C to convert graphite to diamond.[18, 19] Most CVD methods utilize a carbon-containing reactant source gas such as methane, and an energy source to promote reactant dissociation, onto a substrate (*e.g.*, Si, W, Mo).[18, 20-23] Energy sources used to promote reactant dissociation include microwave, DC discharge, and hot-filament. Diamond growth in CVD occurs at relatively low pressure (10 to 500 Torr) and moderate high temperature (700-800°C). Higher quality CVD diamond is produced with low carbon concentrations of 0.5 – 1.0% in the source gas.[18, 24-27] Table 1.1 lists several important properties of both natural and CVD diamond.

Table 1.1. Physical properties for natural (type IIa) and synthetic CVD diamond

Property	Type II	CVD	Ref.
Density (g/cm^3)	3.52	3.52	28
Hardness (Gpa)	57-104	50-100	29, 30
Thermal Conductivity (W/cm/K) at 298 K	20-23	10-21	29
Optical transmissivity	225 nm to far IR	225 to far IR	31
Electrical Resistivity (Ω•cm)	10^{16}	10^{-2} - 10^{16}	32
Band gap (eV)	5.45	5.5	33
Electron mobility	1600	3800	34

Microwave plasma-assisted chemical vapor deposition (PACVD) is a common deposition method used for all diamond growth presented in this dissertation. In PACVD, microwave energy is coupled into a deposition chamber, causing the source gas components to dissociate into reactive species. Both microcrystalline (grain size ~1-3 μm) and ultrananocrystalline (grain size ~5-50 nm) diamond thin films can be grown via PACVD by selection of the appropriate source gas composition, pressure, and microwave power. These parameters control the relative nucleation rate and subsequent diamond crystallite size. A brief introduction to the growth mechanisms for microcrystalline and ultrananocrystalline thin films is provided in following sections.

The nomenclature referring to synthetic diamond growth includes homoepitaxial, microcrystalline, nanocrystalline, and ultrananocrystalline.[20] Homoepitaxial diamond refers to continued diamond growth onto a single crystal with the new diamond layers having the same crystallographic orientation as the original.[17, 35] Since approx. 2001, microcrystalline diamond refers to polycrystalline diamond grown in hydrogen-rich plasmas. Since grain size increases with growth time using a hydrogen-rich plasma, the actual grain size of microcrystalline diamond could be as small as 100 nm with short time. Though often having grains < 1 μm in diameter, these films are still referred to as "microcrystalline", since continued growth would eventually achieve that moniker. Nanocrystalline diamond is now used to refer to diamond films with grains of *ca.* 50-200 nm in diameter formed as a result of short growth time or hydrogen-poor conditions.[20] Ultrananocrystalline diamond (previously nanocrystalline) now refers to polycrystalline diamond with grains 3-50 nm in diameter grown in argon-rich plasmas.[36-38]

1.3.1 Microcrystalline Diamond

High quality microcrystalline diamond is grown in hydrogen-rich environments with a CH_4/H_2 composition of ≤1%.[17, 26] Figure 1.3 is a scanning electron micrograph of microcrystalline diamond grains grown by CVD. The primary growth species in hydrogen-rich plasmas is $CH_3^\bullet$ with atomic hydrogen playing several key roles: (i) generation of the $CH_3^\bullet$ reactants in the gas phase via hydrogen abstraction from methane, (ii) generation of a $CH_3^\bullet$ adsorption or attachment sites on the growth surface by hydrogen atom abstraction from a surface-bound hydrogen-terminated carbon atom (*i.e.*, generation of an active site) and (iii) gasification (*e.g.*, CH_4 and C_2H_2) of nondiamond sp^2 carbon impurity that forms during the growth.[37, 39, 40] Hydrogen etching of sp^2 reduces the growth rate but leads to more phase-pure diamond with a low fraction of grain boundary as compared to ultrananocrystalline diamond.

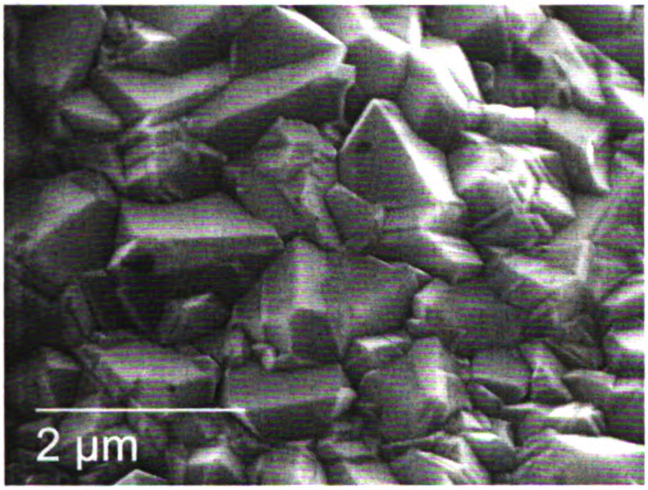

Figure 1.3. Electron micrograph of CVD grown microcrystalline diamond.

1.3.2 Ultrananocrystalline Diamond

Ultrananocrystalline diamond (UNCD) is grown from Ar-rich source gas mixtures where $[H]/[CH_4] \leq 5$. In methane–hydrogen plasmas, noble gas addition has a profound effect on the chemical characterization of the plasma, including additional ionization and dissociation of source gases.[41]

A small amount of H_2 must be present in the source gas in order to maintain a stable plasma at relatively high microwave power and suppress graphite formation.[42, 43] Early studies showed that UNCD could be grown in completely hydrogen-free gas chemistry; however; now it is generally agreed that for UNCD deposition to occur hydrogen must be present in small amounts.[20, 38] Atomic hydrogen is thought to play a number of roles including abstraction reactions, termination of dangling carbon bonds, and gasification of nondiamond sp^2 carbon at the growth surface.[44, 45] Reducing the concentration of hydrogen while continually increasing the hydrocarbon content of the plasma causes the growth of UNCD.[38, 46-48] UNCD consists of nanometer sized diamond grains (2-20 nm) and *ca.* 0.5 nm-wide grain boundaries.[49-51] The grains are pure crystalline diamond and randomly oriented, and the grain boundaries are of a complex mixture of sp^2 and sp^3 bonded carbon. Adding B_2H_6 to the source gas results in boron-doping as with microcrystalline diamond. The effect of the $CH_4/Ar/H_2$ source gas mixture on the morphology and microstructure of diamond films has become clearer over the last decade. For example, Zhou et al. studied diamond films as a function of the Ar level in CH_4/H_2 microwave plasmas.[52] In another example, Jiao et al. studied the nucleation and growth of UNCD films grown from CH_4/Ar source gas mixtures with and without added H_2.[38] Lin et al. mapped how the $CH_4/Ar/H_2$ source gas CH_4 level was held constant at 1% while the Ar/H_2 ratio was changed in hot filament CVD and its influences the diamond film microstructure and morphology.[53] UNCD was formed at Ar levels above 96% and CH_4/H_2 levels between 2 and 6%. The compositional map they developed is comparable to that reported by Gruen and coworkers for microwave CVD, which suggests that the gas phase chemistry that accompanies UNCD growth is similar for the two growth methods.[52]

Previously, the primary diamond growth species in UNCD was thought to be the carbon dimer, C_2, derived from collisionally-induced fragmentation of the source gas, CH_4, via reactions 1.2 and 1.3 in atmospheres containing low levels of hydrogen.[36, 47, 52]

$$2CH_4 \rightarrow C_2H_2 + 3H_2 \qquad (1.2)$$

$$C_2H_2 \rightarrow C_2 + H_2 \qquad (1.3)$$

In particular, it was thought that C_2 could directly insert into the growing diamond lattice, with little or no energy barrier. P.W. May et al. have suggested a slightly modified UNCD growth mechanism.[46] They propose that UNCD formation is a modification of previously determined C_1H_x growth pathways for hydrogen-rich plasmas. Their studies determined that as $[H_2]$ in the plasma decreases ultrananocrystalline growth becomes the predominant morphology when $[CH_3] / ([C] + [CH]) < 50$.

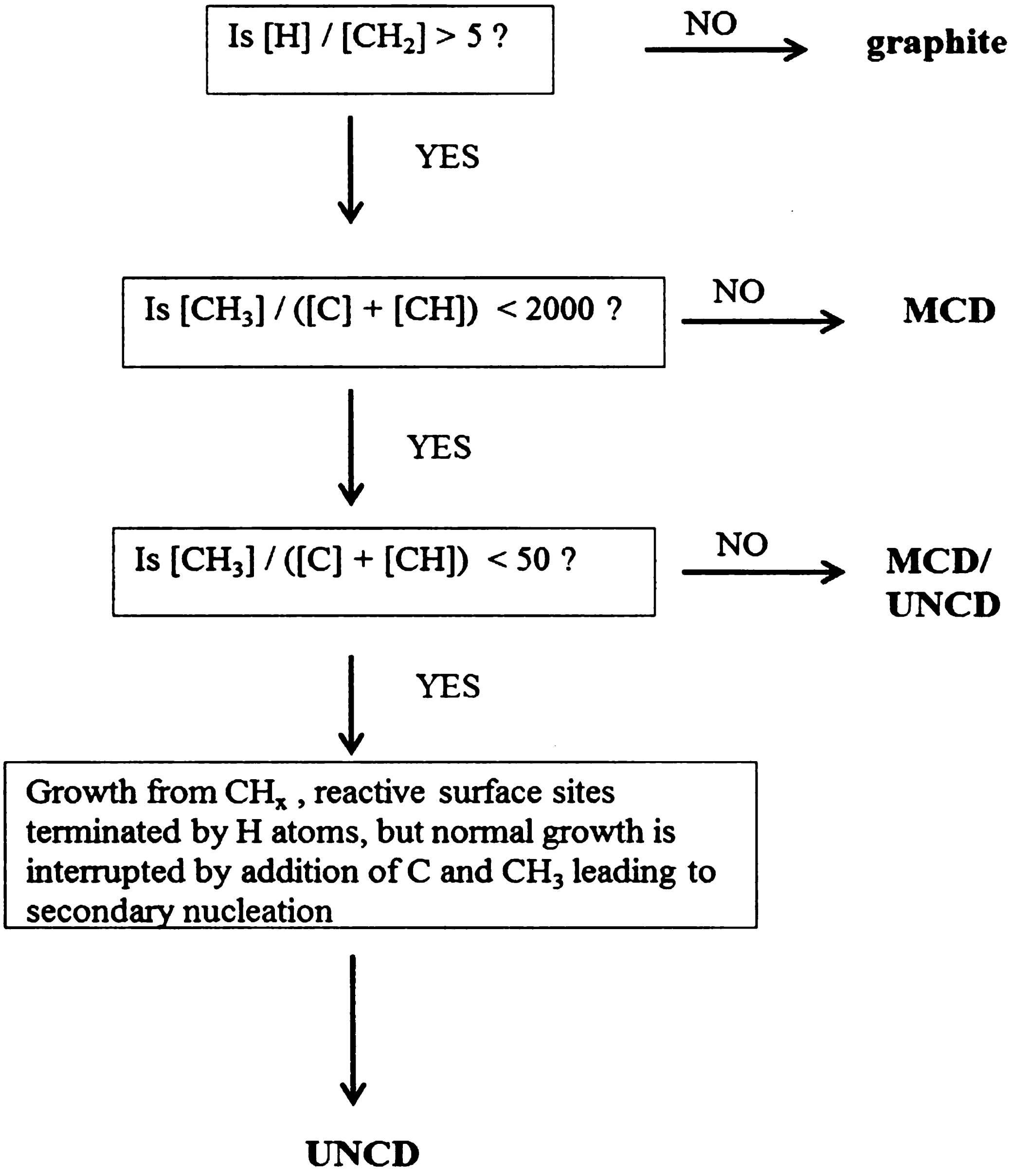

Figure 1.4. CVD source gas conditions and their impact on carbon deposition and diamond types. Adopted from P.W. May et al., Journal of Applied Physics, 100, 024301/1, (2006).

This model for diamond growth is described in Figure 1.4. Diamond growth can be considered to be a stepwise addition of carbon atoms to the existing diamond lattice catalyzed by the presence of excess atomic H. The atomic H formed in the plasma abstracts a surface H to form H_2, leaving behind a dangling bond. A gas phase CH_x radical can collide and react with the dangling bond. Hydrogen abstraction and methyl addition may then occur at the adjacent surface site. A further H abstraction process on one of the chemisorbed groups creates a radical, which attacks the other nearby carbon group to form the ring structure and lock the two carbons into the diamond lattice It was suggested that as the ratio of [H]:[CHx] close to the substrate decreases below about 2, the crystallite size (<d>) drops below 10 nm. However, this ratio should be balanced accordingly to minimize formation of amorphous carbon. The required [H]:[CHx]

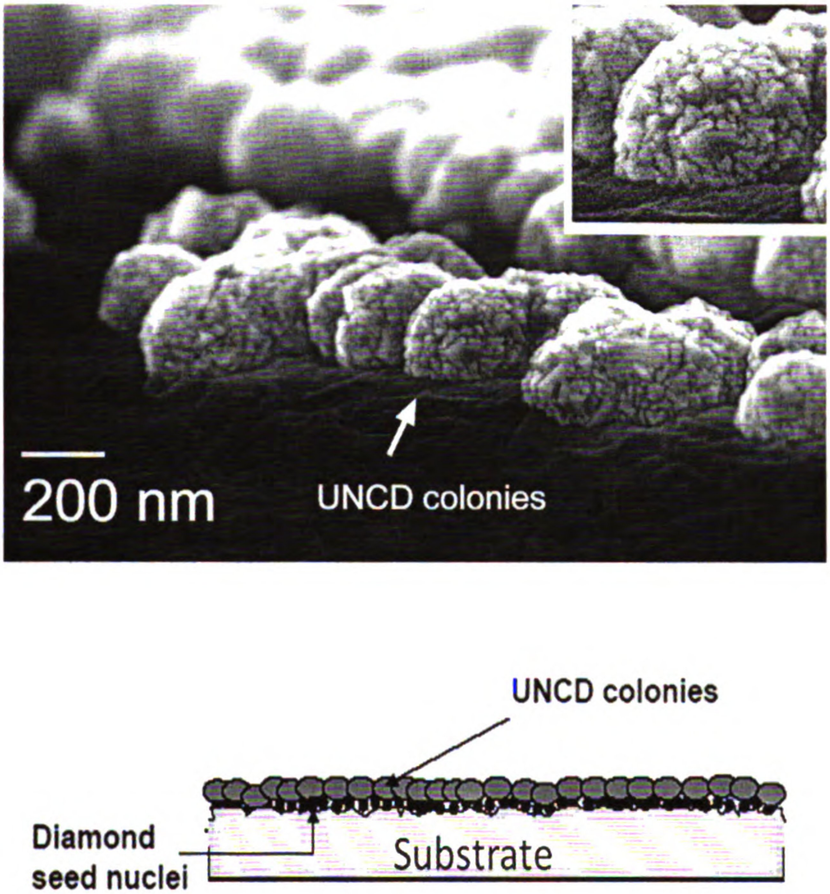

Figure 1.5. Growth process of UNCD. Illustration of UNCD colony formation on a substrate surface (bottom), adopted from Butler and Sumant, *CVD*, 14, 2008 . SEM of UNCD colonies during early stages of growth on a tungsten wire (top) grown in the Swain lab. The arrow indicates a UNCD colony enlarged in the inset.

ratio is obtained due to the unique conditions prevailing in higher pressure Ar-rich gas mixtures. In an Ar-rich plasma the collisions between CH_x and inert Ar are elastic. The reactive CH_x species can survive long enough to strike the surface whereupon they contribute to diamond growth. The combination of growth by CH_3 and growth from a significant fraction of other CH_x species leads the surface to continually renucleate (or more accurately, restructure) during growth, resulting in very small grain sizes.[54, 55] A growth schematic and electron micrograph of UNCD in the early stages of growth are shown in Figure 1.5.

1.4 Boron-Doped Diamond

Diamond is a wide bandgap material and is normally an electrical insulator. However, when doped with impurities, such as boron, electrical conductivity is introduced in a controlled manner. Boron is a p-type dopant in diamond and is normally introduced in the gas phase during chemical vapor deposition where it is incorporated into the crystal structure during growth.[17, 18, 40, 56] At B-doping levels below *ca.* 10^{19} B/cm^3, boron-doped diamond (BDD) behaves more like a semiconductor and when doped at higher levels behaves more like a semimetal.

Research on planar BDD films since the early 1990's has shown that BDD possesses outstanding physiochemical, electronic and electrochemical properties.[56-62] One particular property of relevance for electrocatalysis is the superb microstructural stability and corrosion resistance of the material during electrochemical polarization.[56-70] Much of what is known about structure-function relationships at diamond electrodes has come from studies using thin-film electrodes[26, 56, 57, 60-62, 71-74]. The mechanism for boron insertion of surface bound BH and B species into a growing diamond lattice is thought to occur by a similar mechanism as carbon addition.[40] Cheesman et al. summarized several boron insertion pathways.[40] A schematic representation of BH into the diamond crystal proposed by Cheesman is shown in figure 1.6. As with carbon addition, boron addition to the diamond crystal starts with hydrogen abstraction and formation of a radical site. BH addition occurs at the radical site, followed by ring opening BH insertion and hydrogen termination. This direct mechanism of boron insertion is the most thermodynamically favorable, having a low energy barrier (E_a = 32.5 kJ/mol) and is exothermic (ΔE = -89.5 kJ/mol). Direct incorporation of boron up to 10^{22} B/cm^3 into the lattice during growth introduces electrical conductivities of 100-1000 S/cm without compromising diamond's other unique properties, such

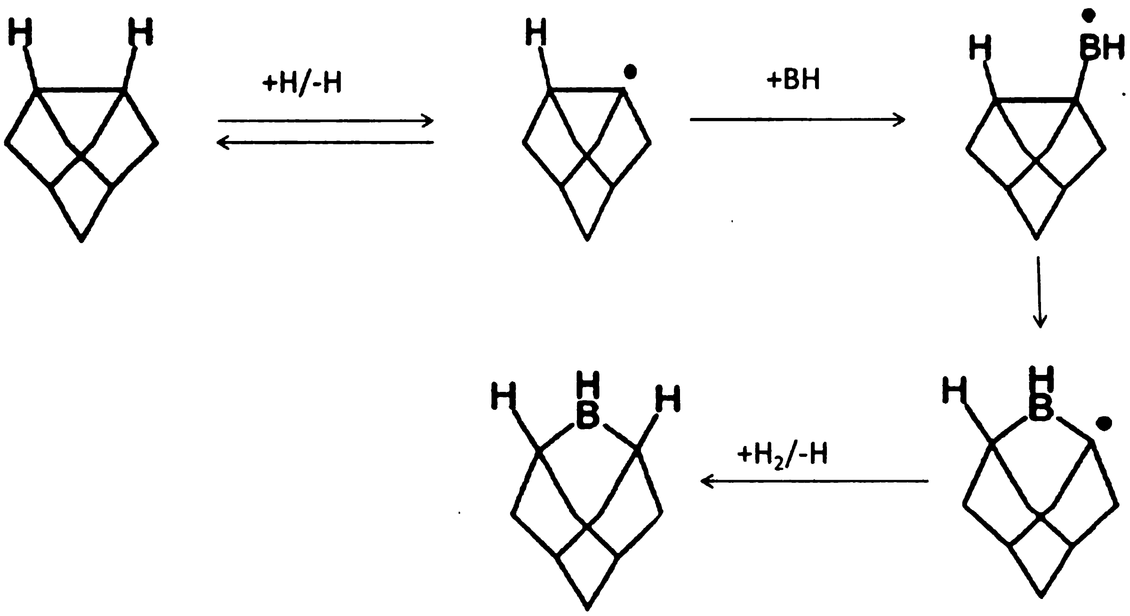

Firgure 1.6. Boron incorporation into a diamond lattice. Adopted from Cheesman et al., Physical Chemistry Chemical Physics 7:1121 (2005).

as microstructural stability, making it sufficiently conducting for many electrochemical applications.[17, 56, 57, 59, 67, 70, 75-78] At high concentrations of boron in the gas phase (> 12,000 ppm B/C), diamond growth is suppressed and microcrystalline graphite begins to form.[78, 79]

1.5 BDD Powder

Unfortunately, these planar electrode geometries have low specific surface area and do not lend themselves to use in electrochemical energy storage and conversion, or applications requiring porosity. Previous work provides good insight into BDD characteristics as they apply to planar films. A key question this work sought to answer is whether BDD can be deposited on small powder particles (*i.e.* higher surface area) but still maintain microstructural stability and similar electrochemical characteristics as planar BDD films? To answer this question several sizes of insulating diamond powders ranging in size from 10 µm – 3 nm were coated with BDD diamond and evaluated.

There are currently three methods to produce synthetic diamond powders; (i) the high-temperature high-pressure (HPHT) method, (ii) the detonation method, and (iii) ball-milling or mechanically crushing diamond films into powder. In the HPHT, diamond particulates are separated from larger gem quality diamond and screened by size. HPHT-produced diamond is high quality with little sp^2 content. In the detonation method, diamond nanocrystals typically 5 nm in diam. can be formed by detonating carbon-containing explosives inside a metal chamber.[80, 81] To date, no one has successfully doped diamond in either the

HPHT or detonation method. BDD powders can be obtained by the ball milling method. Ball milling works on the same principal as rock tumbling. Free standing diamond thin films are placed inside a revolving container with stainless steel balls as the milling media. The benefit of the ball milling method is that the product is highly conducting phase-pure BDD powder when BDD is the starting material. Major drawbacks to ball milling are tediousness, low production volume, and relatively low surface area (*i.e.* >1 μm diam.) due to difficulties in breaking hard diamond into smaller particles.

Both HPHT and detonation diamond powders with high specific surface areas (> 100 m^2/g) are commercially available and can be obtained with nominal diameters from 10 μm down to 1 nm. However, as mentioned, none possesses inherent electrical conductivity. Any conductivity that does exist can be attributed to non-diamond sp^2 carbon impurity at the powder surface. Because of this, the electrical conductivity becomes highly dependent on any factor that will disturb this surface impurity such as by electrochemical, chemical, or thermal oxidation. For example, oxidative treatments, either gas phase or electrochemical, can remove this impurity phase and eliminate any electrical conductivity. The Swain group was the first to report on the overcoating of insulating diamond powder with a layer of boron-doped diamond.[82, 83] In this core-shell approach, a boron-doped microcrystalline diamond layer was deposited on 8-12μm diam. diamond powder particles using microwave CVD and a hydrogen-rich source gas mixture (Figure 1.7). In this approach, the electrical conductivity is controlled by the doped-diamond layer (carrier concentration and mobility) and not by some

Figure 1.7. S
diamond powd
serves as the s

adventitious n
specific surfac
original work
electrical cond
m^2/g and 1 S
received atten
material for fu
capacitors.[86]
prepared by cr
application, e
nanodiamond

Other w

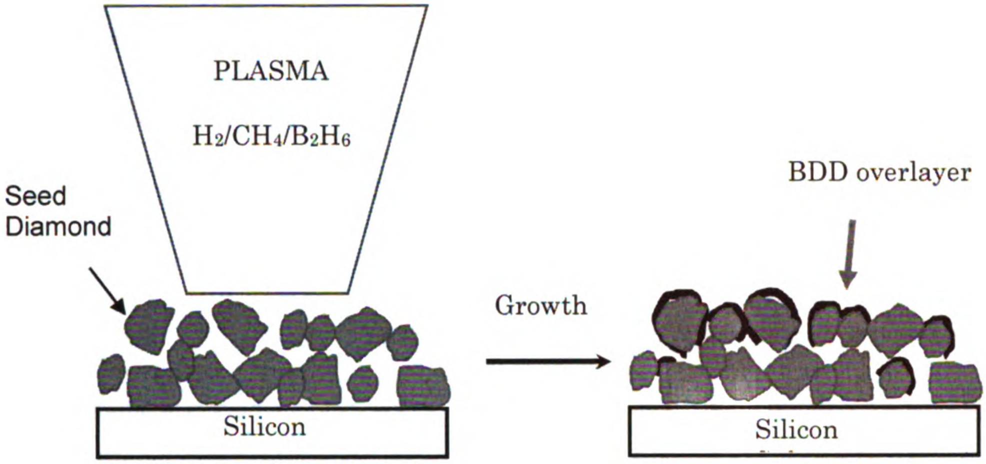

Figure 1.7. Schematic of boron-doped diamond overlayer on commercial diamond powders via plasma-assisted chemical vapor deposition. A silicon wafer serves as the substrate.

adventitious non-diamond sp^2 carbon impurity. The ultimate targets are a specific surface area ≥100 m^2/g and electrical conductivity ≥10 S/cm. In that original work using 8-12 μm diam. powder, the specific surface area and electrical conductivity of the doped diamond powder were below these targets: 2 m^2/g and 1 S/cm.[82] Electrically-conductive diamond powder has also recently received attention by other researchers as a possible electrocatalyst support material for fuel cells[84, 85] and as an electrode for electrochemical double layer capacitors.[86] For the first application, boron-doped diamond powder was prepared by crushing a free-standing boron-doped diamond film. For the second application, electrical conductivity was introduced by surrounding detonation nanodiamond powder particles with a graphite shell.

Other work from our group has demonstrated that metal catalyst-diamond composite elec

good dimensio

morphology o

composition. T

plasmas as

Microcrystalline

fraction of g

ultrananocrysta

than 500 nm ir

sites, leading t

Figure 1.8. S

exacerbated by

jagged edges

growth on pow

with an argon-r

and ability of t

composite electrodes can be formed that exhibit good electrocatalytic activity and good dimensional stability.[69, 87-89] As described in the previous section, the morphology of the BDD coating may be controlled by the source gas composition. The significance between hydrogen-rich and hydrogen-poor plasmas as they apply to diamond powders is the renucleation rate. Microcrystalline conditions produce an excellent quality coating with a lower fraction of grain boundary but with a slower renucleation rate than ultrananocrystalline growth conditions. The effect is that on smaller particles, less than 500 nm in diameter, there are more crystal defects with fewer nucleation sites, leading to high hydrogen etching but low diamond growth rates. This is exacerbated by the non-uniform shape of diamond powders and their many jagged edges (Figure 1.8). Therefore, a hydrogen-rich plasma was used for growth on powders ≥ 1 μm. For powders <1 μm, UNCD deposition conditions with an argon-rich source gas mixture was used due to a higher nucleation rate and ability of the smaller ultrananocrystalline grains to encapsulate nanometer

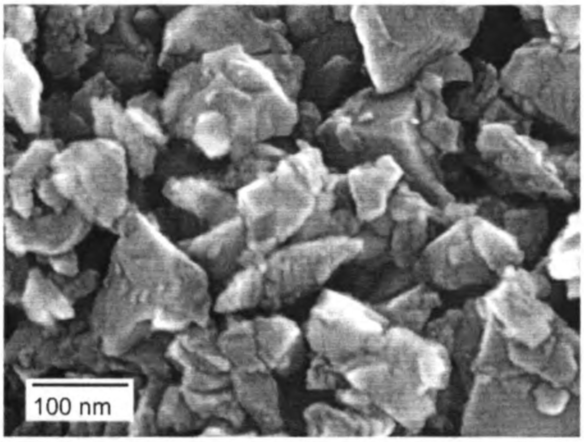

Figure 1.8. SEM of 100 nm diameter HPHT diamond powder before growth

sized particles with a BDD layer more efficiently. Ultrananocrystalline conditions are also more favorable when coating sp^2 particles with BDD, as a hydrogen-rich plasma would etch the sp^2 before substantial BDD growth could occur.

1.6 Specific Goals

This project is a continuation of previous research by the Swain group into the physiochemical properties of boron-doped diamond and especially its potential as an electrocatalyst support. In our previous work, planar BDD films and BDD coated powders (diam. > 1 μm) were investigated as possible electrocatalyst supports.[82, 89] Based on results from our previous work, the research hypothesis put forth is: *BDD coated powders with progressively higher surface areas will also be microstructurally stable and possess excellent electrochemical properties, such as favorable electron transfer kinetics and corrosion resistance in harsh chemical environments.*

The specific goals to meet in testing the hypothesis are:

1) Develop and optimize plasma-assisted chemical vapor deposition growth conditions for BDD coating powders with nominal diameters of < 1 μm, and specific surface areas *ca.* 100 m^2/g after coating.
    - Determine how changes to the CH_4 or B_2H_6 concentration in the source gas during growth impact B-UNCD formation.
2) Evaluate the elemental composition, microstructure, morphology, crystallinity, and electrical conductivity of the BDD coating. Primary evaluation methods include:

3) Investiga

BDD co

aqua ac

Concurr

decorating the

membrane ele

1.7 Outline

This dissertat

Chapter 1 -

resistant BDD

the project.

Chapter 2 - d

- Raman spectroscopy
- Electron microscopy including EELS and EDS
- XRD
- Conductivity tests using *i-V* curves

3) Investigate the electrochemical properties and dimensional stability of the BDD coated powders, especially while undergoing anodic polarization in aqua acids. Electrochemical tests include:
   - In-situ Raman spectroscopy to observe possible microstructural changes during anodic polarization
   - Electrochemical testing in a pipette electrode to evaluate the electrochemical properties of the bare BDD coated powder
   - Use of the powders as the stationary phase in EMLC

Concurrent to this work, other researchers in our group are focusing on decorating these BDD powders with Pt, assembling the powders into the membrane electrode assembly, and testing the powders in a hydrogen fuel cell.

1.7 Outline of the Dissertation

This dissertation is divided into 8 chapters:

Chapter 1 - provides background information regarding the need for corrosion-resistant BDD powders, motivations for the research, and the specific aims for the project.

Chapter 2 - describes the experimental methods used.

Chapter 3 - des

in the source

determine opti

the effect of va

gas concentra

films were gro

carbon and hy

Chapter 4 - pr

pre/post BDD

microscopy. Th

Raman spectr

investigates th

diamond pow

Chapter 5 – r

powders du

electrochemi

Chapter 6 –

coated dian

assessed u

binder. The

redox coup

Chapter 3 - describes the effect of varying the methane and boron concentrations in the source gas during B-UNCD growth. The purpose of this work was to determine optimal growth conditions for B-UNCD. In the first set of films grown the effect of varying the CH_4 level during growth at 0.5, 1, 2, and 3% of the total gas concentration was studied. To evaluate the effect of boron a second set of films were grown in varied B_2H_6 concentrations of 0, 1, 10, and 50 ppm while carbon and hydrogen concentrations were held constant.

Chapter 4 - provides an in-depth microscopic investigation of carbon powders pre/post BDD coating. Their morphology was determined with electron microscopy. The powder microstructure was determined with electron diffraction, Raman spectroscopy and electron energy loss spectroscopy. This chapter also investigates the morphology and dispersion of platinum catalyst particles onto diamond powder.

Chapter 5 – reports on the microstructural stability of sp^2 and sp^3-bonded carbon powders during potentiostatic polarization in aqueous acid probed using electrochemical methods and in-situ Raman spectroscopy.

Chapter 6 – this chapter discusses the electrochemical response of B-UNCD coated diamond powders. The electrochemical behavior of the powders was assessed using a pipette electrode that housed the packed powder with no binder. Their electrochemical properties were evaluated using several different redox couples and the dimensional stability was tested under anodic polarization at 1.4 V vs

Chapter 7

column fo

Chapter 8

at 1.4 V vs (Ag/AgCl) @ 1 h in 0.5 M H_2SO_4 at 80°C.

Chapter 7 – introduces preliminary work using a BDD powder packed HPLC column for EMLC separations as compared to a porous graphite packed column.

Chapter 8 – conclusions and future directions.

1.8 Refe

[1] A.
W

[2] A

[3] K

[4] P
C
o

[5] S
I
(2003)

[6]

[7]

[8]

[9]

[10]

[11]

[12

1.8 References

[1] A. Yarnell, in C&EN News, Vol. 82, American Chemical Society, Washington, 2004, p. 26.

[2] A. J. Appleby, *Corrosion (Houston, TX, United States)* **43**:398 (1987).

[3] K. Kinoshita and J. Bett, *Carbon* **11**:237 (1973).

[4] P. L. Antonucci, E. Passalacqua, L. Pino, and N. Giordano, in 2nd Int. Conf. on Engineering Materials, Vol. 1, Proceedings of the 2nd Int. Conf. on Engineering Materials, Bologna-Modena, Italy, 1988, p. 527.

[5] S. Report of the Basic Energy Sciences Workshop on Hydrogen Production, and Use, *Argonne National Laboratory: Argonne, IL* (2003).

[6] W. Vielstich, A. Lamm, and H. A. Gasteiger, Handbook of fuel cells : fundamentals, technology, and applications, Wiley, Chichester, England ; New York, 2003.

[7] H. A. Gasteiger, J. E. Panels, and S. G. Yan, *Journal of Power Sources* **127** (2004).

[8] S. Lister and G. McLean, *Journal of Power Sources* **130** (2004).

[9] V. Mehta and J. S. Cooper, *Journal of Power Sources* **114**:32 (2003).

[10] C. A. Reiser, L. Bregoli, T. W. Patterson, J. S. Yi, J. D. Yang, M. L. Perry, and T. D. Jarvi, *Electrochemical and Solid-State Letters* **8**:A273 (2005).

[11] S. Sathirajan, B. Merzougui, and P. T. Yu, 2008.

[12] K. Kinoshita, Carbon : Electrochemical and Physicochemical Properties, Wiley, New York, 1988.

[13] J.

[14] K.

[15] J.
E

[16] T
4

[17] K
H

[18]

[19]

[20]

[21]

[22]

[23]

[24]

[25

[2

[13] J. Lahaye, G. Prado, and J. B. Donnet, *Carbon* **12**:27 (1974).

[14] K. I. Makarov and V. K. Pechik, *Carbon* **7**:279 (1969).

[15] J.-B. Donnet and A. Voet, Carbon Black: Physics, Chemistry, and Elastomer Reinforcement, Marcel Dekker, New York, 1976.

[16] T. Ungar, J. Gubicza, G. Ribarik, C. Pantea, and T. W. Zerda, *Carbon* **40**:929 (2002).

[17] K. Kobashi, Diamond Films, Chemical Vapor Deposition for Oriented and Heteroepitaxial Growth, Elsevier Science, 2005.

[18] J. Asmussen and D. K. Reinhard, eds., Diamond Films Handbook, Marcel Dekker, New York, 2002.

[19] W. Brock Alexander, P. H. Holloway, L. Heatherly, and R. E. Clausing, *Surface and Coatings Technology* **54-55**:387 (1992).

[20] J. E. Butler and A. V. Sumant, *Chemical Vapor Deposition* **14**:145 (2008).

[21] M. Frenklach, *Abstracts of Papers of the American Chemical Society* **200**:114 (1990).

[22] S.-T. Lee, Z. Lin, and X. Jiang, *Mat. Sci. Eng.* **25**:123 (1999).

[23] W. A. Yarbrough and R. Messier, *Science (Washington, D. C., 1883-)* **247**:688 (1990).

[24] J. C. Angus, A. Argoitia, R. Gat, L. Zhidan, M. Sunkara, L. Wang, and Y. Wang, *Philos. Topics* **342**:195 (1994).

[25] M. Frenklach and K. E. Speak, *Journal of Materials Research* **3**:133 (1988).

[26] J. A. Bennett, J. Wang, Y. Show, and G. M. Swain, *Journal of the Electrochemical Society* **151**:E306 (2004).

[27] Y.
18

[28] J.
P

[29] A

[30] D

[31] S
(

[32]

[33]

[34]

[35]

[36]

[37]

[38]

[39]

[40]

[27] Y. Show, V. M. Swope, and G. M. Swain, *Diamond and Related Materials* **18**:1426 (2009).

[28] J. E. Field, The Properties of Natural and Synthetic Diamond, Academic Press, New York, 1992.

[29] A. Sawabe and T. Inuzuka, *Thin Solid Films* **137**:89 (1986).

[30] D. K. Ferry, *Physical Review B* **12** (1975).

[31] S. E. Coe and R. S. Sussmann, *Diamond & Related Materials* **9**:1726 (2000).

[32] M. I. Landstrass and K. V. Ravi, *Applied Physics Letters* **55**:975 (1989).

[33] C. Y. Fong and B. M. Klein, eds., Diamond: Electronic Properties and applications, Kluwer Academic Publishers, Norwell, Ma, 1995.

[34] J. Isberg, J. Hammersberg, E. Johnansson, T. Wikstrom, D. J. Twitchen, A. J. Whitehead, S. E. Coe, and G. A. Scarsbook, *Science* **297**:1670 (2002).

[35] M. Donato, G. Faggio, G. Messina, R. Potenza, S. Santangelo, M. Scoccia, C. Tuve, and G. Veronarinati, *Diamond and Related Materials* **15**:517 (2006).

[36] D. M. Gruen, *MRS Bulletin* **23**:32 (1998).

[37] D. M. Gruen, *Annual Review of Materials Science* **29**:211 (1999).

[38] S. Jiao, A. Sumant, M. A. Kirk, D. M. Gruen, A. R. Krauss, and O. Auciello, *Journal of Applied Physics* **90**:118 (2001).

[39] J. E. Butler and R. L. Woodin, *Phil. Trans. R. Soc. Lond. A* **342**:209 (1993).

[40] A. Cheesman, J. N. Harvey, and M. N. R. Ashfold, *Physical Chemistry Chemical Physics* **7**:1121 (2005).

[41] W
Ap

[42] D.
Jo

[43] A
D
(1

[44] M

[45] W

[46] F
1

[47] C

[48]

[49]

[50]

[51]

[52]

[53]

[41] W. Zhu, A. Inspektor, A. Badzian, T. Mckenna, and R. Messier, *Journal of Applied Physics* **68** (1990).

[42] D. Zhou, D. M. Gruen, L. C. Qin, T. G. McCauley, and A. R. Krauss, *Journal of Applied Physics* **84**:1981 (1998).

[43] A. N. Goyette, J. E. lawler, L. W. Anderson, D. M. Gruen, T. G. McCauley, D. Zhou, and A. R. Krauss, *Journal of Physics D: Applied Physics* **31** (1998).

[44] M. Frenklach, *Journal of Applied Physics* **65**:5142 (1989).

[45] W. L. Hsu, *Journal of Vacuum Science & Technology A* **6**: (1988).

[46] P. W. May and Y. A. Mankelevich, *Journal of Applied Physics* **100**:024301/1 (2006).

[47] O. A. Williams, M. Daenen, J. D'Haen, K. Haenen, J. Maes, V. V. Moshchalkov, M. Nesladek, and D. M. Gruen, *Diamond and Related Materials* **15**:654 (2006).

[48] J. Birrell, J. E. Gerbi, O. Auciello, J. M. Gibson, J. Johnson, and J. A. Carlisle, *Diamond and Related Materials* **14**:86 (2005).

[49] R. Arenal, O. Stephan, P. Bruno, and D. M. Gruen, *Applied Physics Letters* **94** (2009).

[50] J. Birrell, J. A. Carlisle, O. Auciello, D. M. Gruen, and J. M. Gibson, *Applied Physics Letters* **81**:2235 (2002).

[51] J. Birrell, J. E. Gerbi, O. Auciello, J. M. Gibson, D. M. Gruen, and J. A. Carlisle, *Journal of Applied Physics* **93**:5606 (2003).

[52] D. Zhou, T. G. McCauley, L. C. Qin, A. R. Krauss, and D. M. Gruen, *Journal of Applied Physics* **83**:540 (1998).

[53] T. Lin, G. Y. Yu, A. T. S. Wee, Z. X. Shen, and K. P. Loh, *Applied Physics Letters* **77**:2692 (2000).

[54] F
F

[55] F
(

[56] C
e

[57] S
I

[58]

[59]

[60]

[61]

[62]

[63]

[64]

[65]

[66]

[54] P. W. May, M. N. R. Ashfold, and Y. A. Mankelevich, *Journal of Applied Physics* **101**:053115/1 (2007).

[55] P. W. May and Y. A. Mankelevich, *Journal of Applied Physics* **100**:024301 (2006).

[56] G. M. Swain, in Electroanal. Chem., Vol. 22 (A. J. Bard and I. Rubinstein, eds.), Marcel Dekker, 2003, p. 181.

[57] S. Alehashem, F. Chambers, J. W. Strojek, G. M. Swain, and R. Ramesham, *Analytical Chemistry* **67**:2812 (1995).

[58] Y. Show, M. A. Witek, P. Sonthalia, and G. M. Swain, *Chemistry of Materials* **15**:879 (2003).

[59] M. C. Granger, M. Witek, J. Xu, J. Wang, M. Hupert, A. Hanks, M. D. Koppang, J. E. Butler, G. Lucazeau, M. Mermoux, J. W. Strojek, and G. M. Swain, *Analytical Chemistry* **72**:3793 (2000).

[60] J. Xu, Q. Chen, and G. M. Swain, *Analytical Chemistry* **70**:3146 (1998).

[61] H. B. Martin, A. Argoitia, U. Landau, A. B. Anderson, and J. C. Angus, *Journal of the Electrochemical Society* **143**:L133 (1996).

[62] B. V. Sarada, T. N. Rao, D. A. Tryk, and A. Fujishima, *Journal of the Electrochemical Society* **146**:1469 (1999).

[63] J. Chmiola, G. Yushin, Y. Gogotsi, C. Portet, P. Simon, and P. L. Taberna, *Science (Washington, DC, U. S.)* **313**:1760 (2006).

[64] T. P. Weber, P. T. Jackson, and P. W. Carr, *Analytical Chemistry* **67**:3042 (1995).

[65] P. T. Jackson, T. Y. Kim, and P. W. Carr, *Anal Chem* **69**:5011 (1997).

[66] E.-Y. Ting and M. D. Porter, *Analytical Chemistry* **69**:675 (1997).

[67] G. M. Swain, *Journal of the Electrochemical Society* **141**:3382 (1994).

[68] R. Declements and G. M. Swain, *Journal of the Electrochemical Society* **144**:856 (1997).

[69] J. Wang, G. M. Swain, T. Tachibana, and K. Kobashi, *Journal of New Materials for Electrochemical Systems* **3**:75 (2000).

[70] Q. Chen, M. C. Granger, T. E. Lister, and G. M. Swain, *Journal of the Electrochemical Society* **144**:3806 (1997).

[71] Y. Show, M.-I. A. Witek, P. Sonthalia, and G. M. Swain, *Chemistry of Materials* **15**:879 (2003).

[72] I. Yagi, H. Notsu, T. Kondo, D. A. Tryk, and A. Fujishima, *Journal of Electroanalytical Chemistry* **473**:173 (1999).

[73] S. Wang and G. M. Swain, *J. Phys. Chem. C* **111**:3986 (2007).

[74] N. R. Wilson, S. L. Clewes, M. E. Newton, P. R. Unwin, and J. V. MacPherson, *Journal of Physical Chemistry B* **110**:5639 (2006).

[75] A. E. Fischer, Y. Show, and G. M. Swain, *Analytical Chemistry* **76**:2553 (2004).

[76] S. Wang, V. M. Swope, J. E. Bulter, T. Feygelson, and G. M. Swain, *Diamond and Related Materials* **18**:669 (2009).

[77] K. Miyata, K. Kumagai, K. Nishimura, and K. Kobashi, *Journal of Materials Research* **8**:2845 (1993).

[78] M. Bernard, A. Deneuville, and P. Muret, *Diamond & Related Materials* **13**:282 (2004).

[79] F. Pruvost, E. Bustarret, and A. Deneuville, *Diamond and Related Materials* **9**:295 (2000).

[80] V. Y. Dolmatov, *Russian Chemical Reviews* **70**:607 (2001).

[81] N. V. Novikov, G. P. Bogatyreva, and M. N. Voloshin, *Physics of the Solid State (Translation of Fizika Tverdogo Tela (Sankt-Peterburg))* **46**:600 (2004).

[82] A. E. Fischer and G. M. Swain, *Journal of the Electrochemical Society* **152**:B369 (2005).

[83] V. M. Swope, I. Sasaki, A. Ay, and G. M. Swain, *ECS Trans.* **3**:27 (2007).

[84] N. Spataru, X. Zhang, T. Spataru, D. A. Tryk, and A. Fujishima, *Journal of the Electrochemical Society* **155**:B264 (2008).

[85] N. Spataru, X. Zhang, T. Spataru, D. A. Tryk, and A. Fujishima, *Journal of the Electrochemical Society* **155**:D73 (2007).

[86] J. B. Zang, Y. H. Wang, H. Huang, and W. Tang, *Electrochimica Acta* **52**:4398 (2007).

[87] J. Wang, G. M. Swain, T. Tachibana, and K. Kobashi, *Electrochemical and Solid State Letters* **3**:286 (2000).

[88] J. Wang and G. M. Swain, *Electrochemical and Solid-State Letters* **5**:E4 (2002).

[89] J. A. Bennett, Y. Show, S. Wang, and G. M. Swain, *Journal of the Electrochemical Society* **152**:E184 (2005).

Chapter 2

Experimental Methods

2.1 Boron-doped Diamond Growth

Conductive diamond was grown on all substrates by microwave plasma-assisted chemical vapor deposition (CVD, 1.5 kW, ASTeX Inc., Lowell, MA). A block diagram of a typical reactor system is in shown in Figure 2.1. The source gases (*e.g.*, Ar, H_2, CH_4, and B_2H_6) enter the chamber at controlled rates regulated by mass flow controllers. Microwave energy is focused into a quartz bell jar (10 cm diam. x 17 cm height), which ignites a plasma. The plasma forms in close proximity to the substrate and contains the reactive species necessary

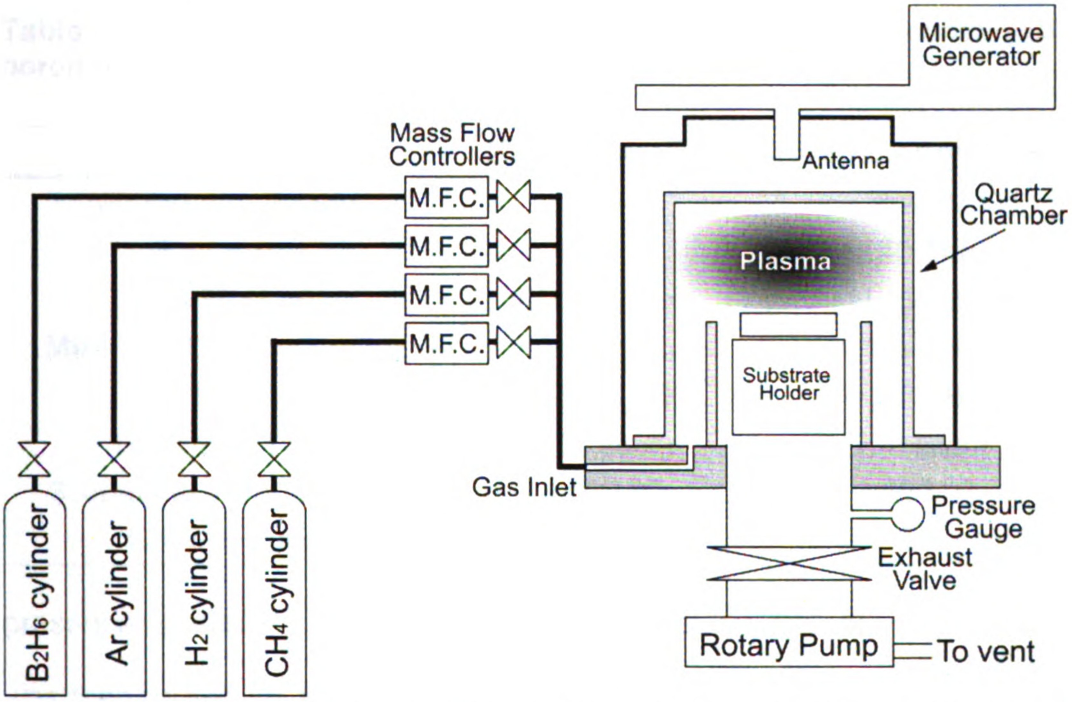

Figure 2.1. Microwave plasma-assisted CVD reactor used to grow microcrystalline and ultrananocrystalline boron-doped diamond thin-film electrodes.[1]

for growth. The chamber pressure is maintained by a throttle exhaust valve and rotary pump that is operated continuously during film growth.

The specific deposition conditions used for diamond growth of each diamond type on Si are listed in Table 2.1. All source gases were ultrahigh purity (99.999%). At the end of the deposition period, the CH_4 and B_2H_6 gas flows were stopped and the films remained exposed to a H_2 (microcrystalline) or an Ar/H_2 (ultrananocrystalline) plasma for an additional 10 min. The plasma power and pressure were slowly reduced over a 15 min period to cool the samples in the presence of atomic hydrogen to a temperature below 400 °C. The plasma power was then turned off and the films were cooled to room temperature under a flow of H_2 (microcrystalline) or Ar/H_2 (ultrananocrystalline).

Table 2.1. Growth conditions for microcrystalline and ultrananocrystalline boron-doped diamond thin film deposited on Si.

	Microcrystalline	Ultrananocrystalline
Microwave Power	1000 W	800 W
Pressure	45 Torr	140 Torr
Gas Mixture	$CH_4/H_2/B_2H_6$	$Ar/H_2/CH_4/B_2H_6$
Methane Concentration	0.5% CH_4	1% CH_4
Dopant	10 ppm B_2H_6	10 ppm B_2H_6
Total Gas Flow	200 sccm	100 sccm
Substrate Temperature	~800 °C	~800 °C
Growth Time	10 h	2 h

2.1.1 Boron-doped Diamond Thin Film Deposition

Ultrananocrystalline diamond thin films were grown on *p-type* Si (111) (0.05 cm thick x 1 cm^2 in area,~10^{-3} Ω-cm, Virginia Semiconductor Inc., Fredricksburg, VA). The substrates were pretreated by mechanically scratching with 3-6 or 100 nm diameter powder on a felt polishing pad for 5 min. The scratched substrates were then sonicated in a slurry of 3-6 nm diamond powder in isopropanol (1g/100 mL) for 30 min. The substrates were then washed sequentially by sonication in ultrapure water, isopropyl alcohol (IPA), acetone, IPA, and ultrapure water to remove polishing debris from the surface. Embedded diamond powder, as well as defects introduced by the scratching, serve as the initial diamond nucleation sites.

2.1.2 Boron-doped Diamond Overcoating of Diamond Powder

The boron-doped ultrananocrystalline diamond overlayer was grown on insulating diamond powders (8-12 μm, Diamond Innovations; MD500 nm and M 100 nm, Tomei Diamond Co., Cedar Park, TX; 3-6nm diam. *Nanostructured and Amorphous Materials*, Houston, TX,). The core-shell method to overcoat electrically insulating diamond powder with a conductive layer of boron-doped diamond is illustrated in Figure 2.2. The diamond powders were prepared for deposition by sequential cleaning in warm (60°C) aqua regia (30 min) and warm 30% hydrogen peroxide (30 min) to remove nondiamond sp^2-bonded carbon and metallic impurities. The clean powder was then copiously rinsed with ultrapure water, isopropyl alcohol (IPA), and acetone by ultrasonication. Each liquid was carefully decanted and afterward the powder was dried at 80 °C overnight in air. The diamond deposition was performed by thinly spreading approximately 30 mg of the powder over a silicon wafer that was placed in the reactor. The deposition conditions for the conductive diamond layer are the same as those in Table 2.1.

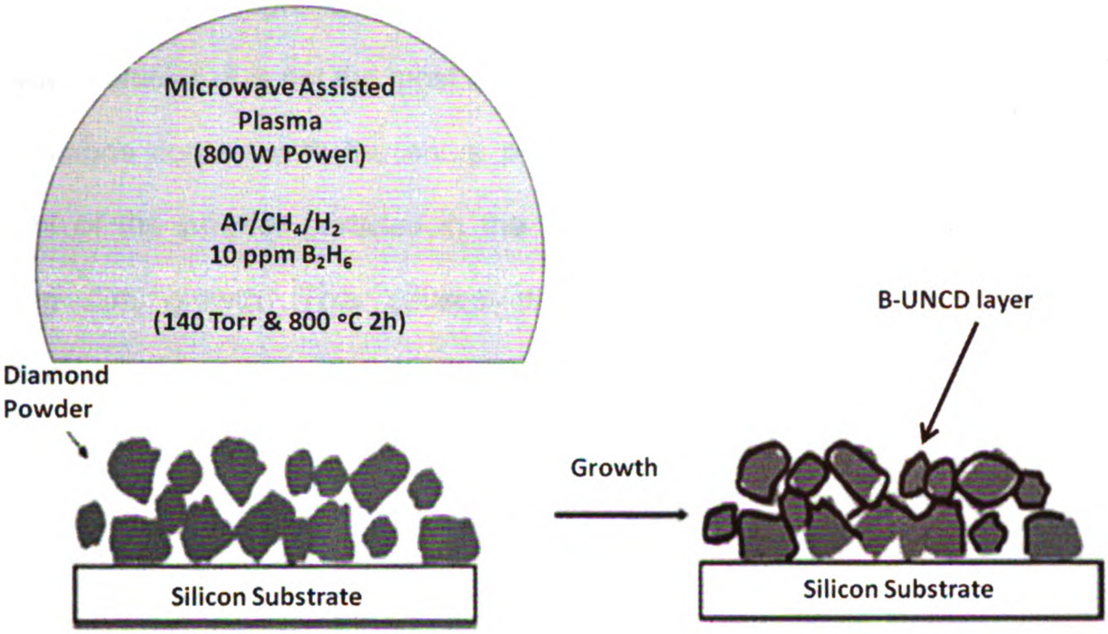

Figure 2.2. **Illustration of the core-shell concept for coating diamond powders with a layer of boron-doped ultrananocrystalline diamond.**

8-12 μm powders were coated using microcrystalline diamond deposition conditions using a 4 h deposition time. B-UNCD conditions were used for all other powders. These powder samples were coated twice using a 1.5 h time for each deposition (3 h total). After the first growth, the sample was mixed and re-spread over the silicon wafer in order to enhance the diamond coverage over the powder surface. Post-growth, the powders were cleaned chemically, as described above, with an additional hydrofluoric and nitric acid exposure to remove any silicon impurity.[4] After this step, the diamond surface is mainly oxygen terminated. Depending upon the desired surface termination, the powders were sometimes returned to the reactor after the acid washing step and exposed to a hydrogen plasma for 30 min. This re-hydrogenated the surface.

While this approach led to both full and partial coating of the substrate powder particles, it is not the most ideal because of the difficulty ensuring uniform plasma/gas contact with the entire particle surface. Additionally, the variable height of the powder particles in the plasma leads to temperature variations during film growth. This causes differences in overlayer thickness and microstructural quality. Particles that experienced higher temperatures had more nondiamond carbon impurity content.

2.1.3 Boron-doped Diamond Overcoating of Carbon Black Powder

Glassy carbon powder (Sigradur G, HTW GmBH, Germany, 4 μm diam. and 2m^2/g.) was used as-received without any cleaning or seeding. An overlayer of B-UNCD was grown using the following conditions: (i) a source gas ratio of 1% CH_4, 7% H_2 and 92% Ar. 10 ppm of B_2H_6, (0.01% in hydrogen), (ii) a microwave power of 800 W, and (iii) a system pressure of 140 Torr. The sample was coated twice, and the growth period for each was 2 h. After each growth, the same post-growth annealing and cool-down procedure in atomic hydrogen was applied, as explained above. These powders were used as-grown without any chemical treatment after coating. Ketjen black powder was coated similarly to the glassy carbon powder except 3 growth periods (1.5 h ea.) were used.

2.2 Material Characterization

Several analytical methods were employed to characterize the diamond film properties, including (X-ray diffraction (crystallinity), Raman spectroscopy (microstructure), SEM (morphology), *I-V* curves (electrical properties). These same methods were also employed to assess the chemical and physical changes of the sp^2- and sp^3-bonded carbon powders before and after accelerated degradation testing.

2.2.1 X-Ray Diffraction Spectroscopy (XRD)

The crystallinity of diamond was studied by XRD. Spectra were obtained by scanning 2θ from 20 to 100 on a RikaguRotaflex RTP300 RC instrument. X-rays were produced at 1.540 Å from a Cu anode.

2.2.2 Raman Spectroscopy

Raman spectra were recorded in a backscattered collection geometry using a 100 mW argon ion laser (MellesGriot CW) at 514.5 nm, an Olympus BH-2 microscope assembly, and a Spex 1250 spectrograph with a 600 grooves/mm holographic grating. The detector was a Symphony 2000 x 800 charge-coupled device (Horiba Jobin-Yvon) with a pixel size of 15 μm. All spectra were recorded at room temperature using an incident power density of approximately 1.4 kW/cm^2 (10 mW at the sample and 30 μmdiam spot size) and a 45 s integration time. The spectrograph was calibrated using the first-order phonon peak for cubic diamond (a high-pressure, high temperature-grown single-crystal sample) at 1332.6 cm^{-1}.

2.2.3 Scanning Electron Microscopy (SEM)

Sample morphology was probed by SEM using a JEOL-6300F, 6400V, and 7500F- FE microscopes (JEOL Ltd., Tokyo, Japan). Thin films were attached to the aluminum SEM stub with epoxy. Electrical contact with the stub was made by painting a small section of the film and the aluminum stub with carbon paste. Powders were mounted by drop casting onto double sided carbon tape applied to the aluminum stub. For the JEOL 6400V and JEOL 6300F the powders were gold sputter coated (EMSCOPE SC50, Ashford, Kent, Great Britain) or osmium coated by chemical vapor deposition (NEOC-AN, Meiwa ShojiCo. LTD, Japan). No gold or osmium coating was used for images acquired with the JEOL 7500F.

2.2.4 Transmission Electron Microscopy (TEM)

TEM images were collected using a Jeol 2200FS FE-TEM at 200 kV, which was also equipped with a scanning transmission electron microscopy mode. Electron energy loss spectra (EELS) were captured with a Gatan 1024 x 1024 multi-scan camera. Powder samples were sonicated in isopropanol and then drop cast onto 300 mesh copper grid with a lacey formvar/carbon coating (Ted Pella #01883-F). EELS line scans were collected in the STEM mode with a spot size of 0.7 nm. To limit background signal from the carbon support, spectra were collected from particles residing in the voids of the support where the electron beam passes through the sample only.

Thin films were prepared for TEM analysis by first ultrasonically sectioning a 3 mm disc from the film. The disc was then mounted with epoxy diamond-side onto a slotted gold TEM grid. This left the Si substrate exposed to chemical etching by HF and HNO_3 acid. The remaining diamond film was thinned by Ar ion beam milling until perforated in the middle. The mounted sample is illustrated in Figure 2.3.

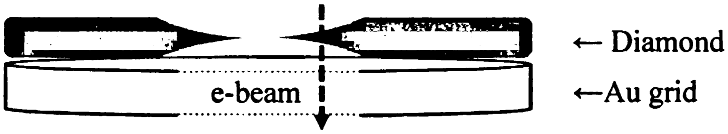

Figure 2.3. Schematic of a thinned diamond film mounted on a slotted Au grid.

2.2.5 Electrical Resistance

A home-made cell was used to measure the electrical resistance of the dry, packed powder before and after overcoating with conducting diamond. The measurement assembly is similar to that shown in Figure 2.4. Electrical resistance measurements were made by placing a fixed quantity (*ca.* 30 mg) between two metal plates and measuring the contact-to-contact resistance with an ohmmeter. The top metal plate was attached to a copper rod (0.114 cm^2), which fits inside a glass tube used to contain the powder sample between the two plates. A 240 g weight was placed on the top metal piece to ensure a constant force was applied during the measurement. The powder resistance was also calculated from *i-V* curves, measured as a function of the applied dc voltage

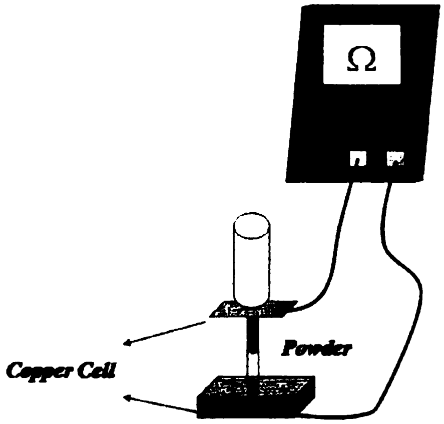

Figure 2.4.: Schematic diagram of the apparatus used to measure *i-V* curves for the powder samples.

(+6, +10, and +20 mV). All resistance measurements were made without the use of a binder. All powder resistances prior to doped diamond growth were > 40 MΩ.

2.2.6 Specific surface area measurements

The powder surface area was determined by the BET method. Nitrogen adsorption isotherms were recorded at −196°C using a MicromeriticsTristar 3000 sorptometer. Approximately 100-300 mg powder sample was out gassed at 90°C and 10^{-6} Torr for a minimum of 12 h prior to analysis. The sample, in vacuum, was exposed to different amounts of N_2 gas and the chamber pressure was measured. The greater the coverage of adsorbed gas, the lower the system pressure is. An adsorption isotherm was generated by plotting $1/v\ [(P_0/P) - 1]$ vs. P/P_0 (BET plot) where P and P_0 are the equilibrium and the saturation pressures of nitrogen at the isotherm temperature, and v is the volume of gas adsorbed. Surface areas were calculated from the linear part of the BET plot according to International Union of Pure and Applied Chemistry (IUPAC) recommendations.

2.3 Electrochemical Characterization

Electrochemical measurements are important to record as they provide insight on the physicochemical properties of conductive diamond powder. The working potential window, the background current and various voltammetric features are all diagnostics of the surface microstructure and chemistry, electronic properties, and electric double-layer structure.

Cyclic voltammetry was used to 1) probe the electrochemical properties of the B-UNCD powder and glassy carbon powders, 2) evaluate the microstructural stability of B-UNCD-diamond and B-UNCD-glassy carbon powders, and 3) study the electrochemical properties of Pt nanoparticles deposited on the B-UNCD-diamond powders.

All of the electrochemical measurements were performed using a

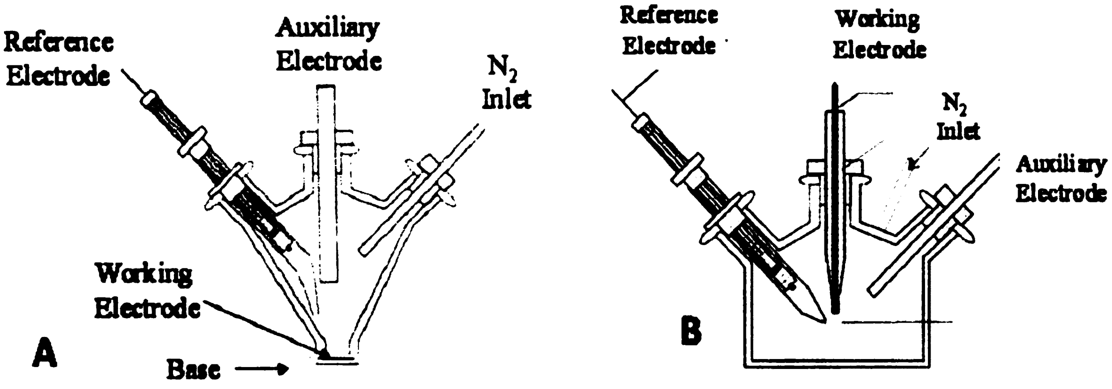

Figure 2.5. Schematic of glass cells used for electrochemical characterization. (A) Single compartment, three-electrode electrochemical cell for film electrodes, and (B) a single compartment three-electrode electrochemical cell for pipette electrodes.

CHI650a computerized potentiostat (CH Instruments Inc., Austin, TX) with a graphite rod counter electrode and an Ag/AgCl reference electrode (4 M KCl, $E^{\circ\prime}$ = -65 mV vs. SCE). All measurements were made at room temperature (25 ± 1 °C), unless otherwise noted, and all solutions were deoxygenated with N_2 for at least 20 min prior to a measurement and blanketed with the gas during the measurement. Details of the electrode preparation procedures and the electrochemical cells used for each electrode morphology are provided below.

2.3.1 Film Electrodes

The diamond thin film on Si (*ca.* 0.2 cm^2 area) or glassy carbon electrode was sealed against the bottom of a single-compartment electrochemical cell with a Viton® o-ring, as shown in Figure 2.5.[3] The backside of the Si substrate was scratched, cleaned, and coated with graphite in order to ensure good ohmic contact with a metal current collector plate. All electrodes were used after a 20 min soak in distilled isopropyl alcohol.[5]

2.3.2 Carbon Powder Electrodes

Electrode fabrication methods for powder electrodes commonly employ me method of anchoring the particles to maintain surface area and electrical ntact during the experiment. For example, composite electrodes can be pared using a polymer binder or other chemical, like paraffin oil.[6] Polymeric lers tend to reduce the particle–particle contact, thereby increasing the ctrode resistance. Furthermore, the mixing, pressing, and heating steps ded for the electrode preparation are laborious and time consuming. The pipette electrode architecture used in this work enables electrochemical characterization of the doped diamond powders without the need for a binder. Electrochemical characterization was performed with electrodes prepared by packing the powder with a plastic pipette tip (#104 BioDot, Scientific Inc., Burton, MI).[7] The procedure involved first melting the narrow end of the tube closed. Then, 5–10 mg of either boron-doped diamond or GC powder (Sigradur G, HTW GmBH, Germany) was packed into the tube with a 1 mm diam. copper metal rod. This metal rod also served as the current collector (see Fig. 2.6). The powders were packed to a height of 6–7 mm with the Cu wire contacting the top of the powder. The Cu wire was pressed into the powder layer to form good ohmic contact. The closed end of the tip was then carefully cut to expose the powder with a geometric area of ~0.002 cm^2. All currents reported herein are normalized to this geometric area.

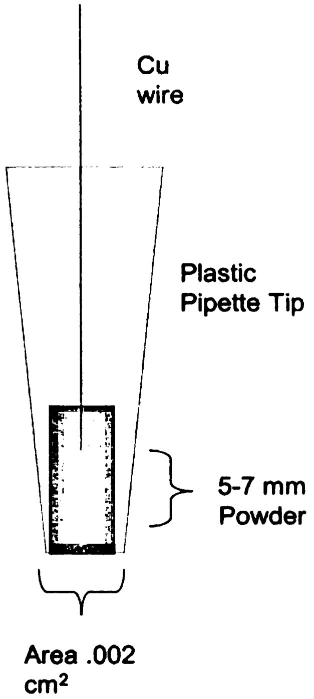

Figure 2.6. Diagram of the pipette electrode used for testing the electrochemical properties of the conducting powders.

2.3.2 Polarization Studies

B-UNCD-diamond powder and platinized diamond powders were subjected to applied potentials from 1.0 to 1.6 V vs. Ag/AgCl at 25 and 80 °C in 0.5 M H_2SO_4 for 1 h periods. The measurements were performed in the continuous amperometric mode with the current being recorded as a function of time. The single compartment glass electrochemical cell was heated by water circulation. The solution temperature was measured before and after the polarization and remained constant (± 5 °C). The recorded current-time profiles were integrated to determine the charge passed at a given potential. For a faradaic process, the charge passed is related to the number of moles electrolyzed according to Equation 2.1:

$$Q = nFN \qquad [2.1]$$

where Q is the integrated charge (Coulombs), *n* is the number of electrons involved per reaction, *F* is the Faraday constant, and *N* is the number of moles electrolyzed.

2.3.4 Reagents

All chemicals were analytical-grade quality or better, and were used without additional purification. Solutions (1 mM) of potassium ferrocyanide (Aldrich), potassium hexachloroiridate (Aldrich), hexaammineruthenium (III) chloride (Aldrich),anthraquinone-2,6-disulfonate,disodium salt (AQDS), and ferric sulfate (Matheson Coleman and Bell) were freshly prepared. The supporting electrolytes were 1 M KCl (Fisher Scientific), 0.5 M H_2SO_4 (99.999%, Aldrich), and 0.1 M $HClO_4$ (99.999%, Aldrich). All redox analyte solutions were prepared daily using ultrapure water (>18 MΩ-cm) from an E-pure water purification system (Barnstead) in glassware that was cleaned by a three-step process: ethanol/KOH bath, alconox/ultrapure water solution, and an ultrapure water rinse.

2.4 Chapter Specific Methods

2.4.1 Optical emission spectroscopy (Chapter 3)

Optical emission spectroscopy was used to monitor the C_2 dimer present in the plasma (λ_{emis} = 516 nm). A fused silica optical fiber was employed to collect light emitted from the plasma and to direct it to the entrance slit of a spectrograph. The spectrograph consisted of a monochromator (Oriel, 77200, Stratford, CT) with focal length of 250 mm, a holographic reflection grating of 1200 lines/mm, and a photomultiplier tube (Oriel, 70680, Stratford, CT).

2.4.2 Pt deposition on diamond powders (Chapter 4)

The diamond powder was impregnated with Pt by wet chemical deposition. In this method, an appropriate quantity of the Pt(II) acetylacetonate salt (Aldrich) was dissolved in 25 mL of ethanol and acetic acid (Aldrich) 3:2 v/v (Eq. 2.2 – 2.4). After that, an appropriate amount of the diamond powder was added to yield a theoretical catalyst loading of 20% w/w. The mixture was homogenized by ultrasound mixing for 30 min (Fisher Scientific FS30 Sonicator).

Reduction of Pt(II) to metal Pt by Ethanol:

$$CH_3CH_2OH + H_2O \rightarrow CH_3COOH + 4H^+ + 4e^- \qquad [2.2]$$

$$Pt^{2+} + 2e^- \rightarrow Pt \qquad [2.3]$$

the net reaction is

$$2Pt^{2+} + CH_3CH_2OH + H_2O \rightarrow 2Pt + CH_3COOH + 4H^+ \qquad [2.4]$$

The solvent was then slowly evaporated while stirring. The powder was then submitted to a thermal treatment at 400 °C for 30 min in order to stabilize the platinum.

X-ray Photoelectron Spectroscopy (XPS) of the platinized diamond samples were recorded using a Physical Electronics PHI 5400 spectrometer with a magnesium X-ray source. A take-off angle of 45° was used for all measurements at a base pressure less than 5 x 10^{-9} Torr. The electronic interaction between the Pt and diamond was studied by measuring the binding energy shift of the Pt 4f level.

2.4.3 Powder film electrode preparation and in-situ Raman spectroscopy (Chapter 5)

Powder Film Electrode Preparation. The powder electrodes were formed as a film on glass substrates (1 x 2 cm^2). The glass was cleaned prior to use with soapy water (Alconox, Inc.). After rinsing and drying, the glass substrates were cleaned in warm aqua regia for 30 min, and then rinsed with ultrapure water and distilled IPA. Graphite (Super Graphite Co.) and glassy carbon (Sigradur G, HTW GmBH) powders were used as received. The two carbon blacks, acetylene black (C-55, Chevron) and Vulcan XC-72R (ElectroChem, Inc.), were heated to 300 °C in air prior to use in order to remove residual solvent. A certain volume of a colloidal Nafion solution (5 wt%, ElectroChem, Inc.) was then mixed ultrasonically with 2 mL of IPA for 30 s. Carbon powder (10 to 40 mg) was then added to the solution followed by additional ultrasonic agitation for several minutes. A film electrode was then formed by drop casting 150 mL of the powder/polymer

solution onto a clean glass slide. Some films were formed using multiple drop-castings in order to cover the entire substrate. The films were dried in air at room temperature for *ca.* 1 h after each solution casting, and then overnight after the last casting. After this period, the films were dried in air for 2 h at 90 °C. The amount of Nafion binder used to form the electrode as well as the powder coverage is given in Table 1. A challenge with preparing these powder film electrodes is the avoidance of cracks during the curing process, which leads to excessive ohmic resistance.

Table 2.2. Physical properties of the sp^2 and sp^3 carbon powders and the powder films with a Nafion binder.

		[S/cm]§	BET surface area [m^2/g]*	d_{002} [Å]**	Nafion [wt %]	Film coverage [mg/cm^2]
sp^2 carbon	Graphite	6	3.0	3.37	10	3.75
	Glassy carbon	2	2.3	3.44	10	1.5
	Acetylene black	2	68	3.49	15	0.75
	Vulcan XC-72	1	220	3.62	20	0.375
sp^3 carbon	8-12 mm Boron doped diamond	2	0.63	N/A	5	64

§ 30 mg of powder was placed in a glass tube (0.114 cm^2) with a 240 g weight.
* N_2 adsorption at -196 °C.
** obtained from powder XRD.

Electrochemistry. All potentiostatic and potentiodynamic polarizations were recorded at room temperature (*ca.* 25 °C) or 80 °C using an analog potentiostat/galvanostat (Model 273, Princeton Applied Research, Princeton, NJ). An Ag/AgCl reference electrode (4 M KCl with saturated AgCl) and a large area graphite rod counter electrode were employed to complete the electrochemical cell. All potentials are reported herein versus this reference. For the

electrochemical measurements, half of the carbon powder electrode was immersed into the solution, which was either 0.1 M $HClO_4$ at room temperature or 0.1 M H_2SO_4 at 80 °C. Electrical connection to the carbon film was made by contacting copper foil with the non-wetted portion of the powder. Contact was maintained using an alligator clip. The type of clip and the tension were such that there was minimal damage to the powder film. For the high temperature polarizations, the entire cell was placed in an oven at 80 °C. The openings of the electrochemical cell were sealed with parafilm to minimize evaporative loss of water, thus the solution volume changed little during the polarization.

Before the initial polarization at 1.0 V, background potentiodynamic *i-E* curves (cyclic voltammetric) were recorded for the carbon film after equilibration in the aqueous acid at the open circuit potential (OCP). A stable OCP was usually reached within 1 h. After recording a background potentiodynamic *i-E* curve (0.2 to 1.0 V at 50 mV/s), potentiostatic polarizations were conducted at 1.0, 1.2, and then 1.4 V vs. Ag/AgCl for 60 min each at room temperature and for 30 min each at 80 °C. After each polarization, a background potentiodyanmic *i-E* curve was again recorded in the same electrolyte. The initial curves were unchanging with cycle number; evidence of full wetting of the thin powder electrode.

In-situ Raman Spectroscopy. A homemade cell for the in-situ Raman measurements was used (Fig. 2.7). All spectra were collected with an incident power density of 1.4 kW/cm^2 (without the glass cap, see Fig. 2.7), except for Vulcan XC-72R for which the laser intensity was reduced by 75% to minimize damage to the material. Electrical contact was made by attaching a Cu wire to the film surface with a conducting epoxy (CW2400, ITW Chemtronics) cured at 60 °C for 30 min. An objective lens having a working distance of 0.75 cm (ULWD MSPlan 80, Olympus) was immersed in the electrolyte solution with a home-made glass cap applied for protection. The carbon film was gently pressed against a Viton O-ring positioned at the bottom of a Teflon cell. The o-ring was used to define the area of the powder electrode exposed to the solution. Pt counter and Ag/AgCl reference electrodes were also mounted in this cell to complete the circuit.

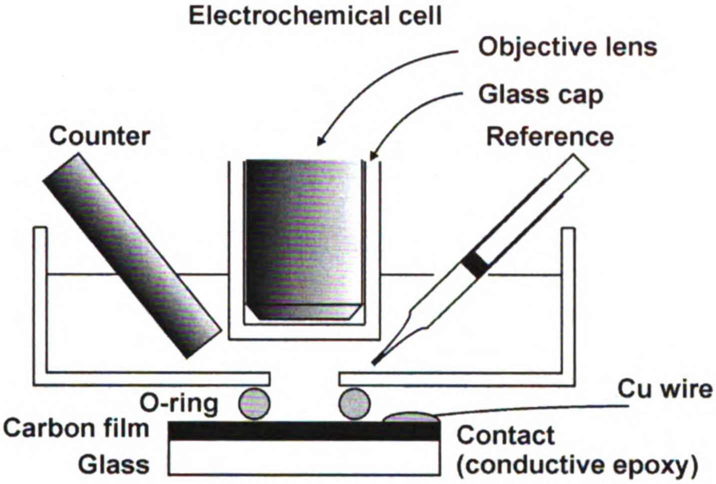

Figure 2.7. Diagram of the cell used for the in-situ Raman spectroelectrochemical measurements.

2.4.3 Electrochemically Modulated Liquid Chromatography (Chapter 7)

Chromatographic Column Construction. The EMLC column (Fig. 2.8) consists of a Nafion cationic-exchange membrane in a tubular form (Perma Pure) that is placed inside a porous stainless steel cylinder. The Nafion membrane serves as a container for the stationary phase. The stainless steel cylinder prevents the deformation of the Nafion tubing under the high pressure of chromatographic flow and acts as the auxiliary electrode in a three-electrode electrochemical cell. BDD powders (specific surface area *ca.* 1 m^2/g and conductivity ca. 2 S/cm) were dispersed in a dibromomethane/acetonitrile (1:1, v/v) slurry and then packed in an EMLC column at 6000 psi using acetonitrile for *ca.* 30 min. The same column and packing procedures were used to prepare a PGC (5 μm particles) column. The surface area of the BDDP and PGC stationary phase is *ca.* 1 m^2 and 15 m^2, respectively. These values were calculated based on BET adsorption measurements (*ca.* 1 m^2/g for BDDP and *ca.* 100 m^2/g for PGC), and the amount of material loaded into the column (*ca.* 1 g for BDDP and *ca.* 0.15 g for PGC).

Instrumentation: Chromatographic experiments were performed using Agilent 1200 Series system equipped with solvent cabinet, autosampler, quaternary pumping system, and diode array detector. This unit was interfaced to a Pentium IV 600 MHZ computer equipped with Chemstation software for control of injection sequences, data acquisition, and flow rate parameters. The potential of the working electrode/chromatographic packing was controlled using an AMEL Instruments Model 2055 high power potentiostat (Milan, Italy).

Mode of Operation: After packing, both EMLC columns were equilibrated with degassed mobile phase (0.10 M $LiClO_4$) at a flow rate of 0.4 mL/min until a stable detector response was obtained (*ca.* 30 min). After each change in E_{appl} the system was allowed to achieve a stable baseline, which typically required

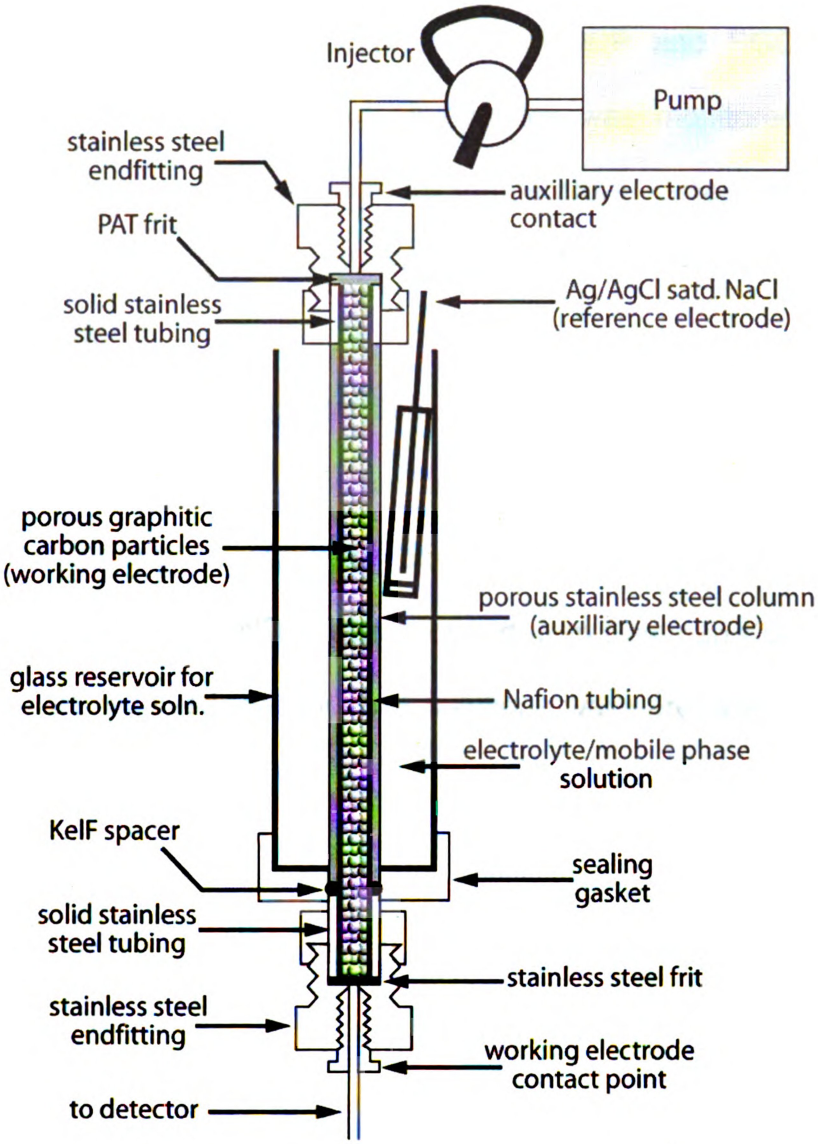

Figure 2.8. Schematic of the EMLC column.

ca. 10 min with a BDDP column and *ca.* 30 min for a PGC-packed column. Injection volumes were set at 5 µl, and injections of the analyte mixtures were repeated four times at each value of E_{appl}. Individual injections of each analyte were performed in triplicate for peak identification and for retention time determination when elution bands overlapped. An injection of water was performed to determine the dead volume of the column for calculation of k'. The dead volume was 0.28 and 0.41 mL for BDDP and PGC-packed column, respectively. The absorbance of all analytes was monitored at 210 nm. All experiments were performed at room temperature. Details of the experiments that examined the day-to-day stability of the BDDP as a packing material are given in Chapter 7.

Chemicals and Reagents: Sodium 4-toluenesulfonate (TS), disodium 1,3-benzenedisulfonate (BDS), sodium benzenesulfonate (BS), dibromomethane, lithium perchlorate, acetonitrile purchased from Aldrich. Disodium 1,5-naphthalenedisulfonate (NDS) was acquired from Eastman Kodak. All chemicals were used as received. All aqueous solutions were prepared with HPLC grade water.

2.5 References

[1] G. M. Swain, in Electroanal. Chem., Vol. 22 (A. J. Bard and I. Rubinstein, eds.), Marcel Dekker, 2003, p. 181.

[2] Y. Show, M. A. Witek, P. Sonthalia, and G. M. Swain, *Chemistry of Materials* **15**:879 (2003).

[3] M. C. Granger, M. Witek, J. Xu, J. Wang, M. Hupert, A. Hanks, M. D. Koppang, J. E. Butler, G. Lucazeau, M. Mermoux, J. W. Strojek, and G. M. Swain, *Analytical Chemistry* **72**:3793 (2000).

[4] B. Schwartz and H. Robbins, *Journal of the Electrochemical Society* **123**:1903 (1976).

[5] D. A. Skoog, J. F. Holler, and T. A. Nieman, Principles of Instrumental Analysis 5th Edition, Harcourt Brace College Publishers, Philadelphia, 1998.

[6] M. Rice, Z. Galus, and R. N. Adams, *Journal of Electroanalytical Chemistry and Interfacial Electrochemistry* **143** (1983).

[7] R.-I. Stefan and S. G. Bairu, *Analytical Chemistry* **75**:5394 (2003).

Chapter 3

Physical, Electrical and Electrochemical Characterization of Boron-Doped Ultrananocrystalline Diamond Thin-Films Deposited from $CH_4/H_2/Ar/B_2H_6$ Source Gas Mixtures

Abstract

Thin-film ultrananocrystalline diamond was deposited on a Si substrate by microwave-assisted chemical vapor deposition (CVD) using different $CH_4/Ar/H_2/B_2H_6$(Ar-rich) source gas mixtures. The dependence of the film morphology, microstructure and phase purity on both the B_2H_6 (0-50 ppm) and CH_4 concentration (0.5 to 3% v/v,) in the source gas was investigated. The H_2 concentration was maintained constant at 5% while the Ar level ranged from 92 to 94.5%.

The boron concentration in the films varied from *ca.* 10^{18} - 10^{20} cm^{-3}, as determined by boron nuclear reaction analysis (BNRA). Raman spectroscopy and NEXAFS examination indicated the film microstructure is unaffected by boron doping until the source gas concentration reaches 50 ppm. At this gas phase concentration, there is an increase in signal for sp^2-bonded carbon and a reduction in the absolute second band gap for diamond. The grain boundary width, as determined by high resolution TEM, for moderately doped films was 0.2 – 0.5 nm, which is similar to undoped UNCD.[1-7]

At the lowest CH_4 concentration (0.5%), faceted microcrystalline diamond was predominant with a grain size of 0.5 μm or greater. Phase-pure and relatively smooth ultrananocrystalline diamond thin film, with a nominal grain size of *ca.* 15 nm, was formed at a CH_4 concentration of 1%. A diamond-like carbon film was produced with a mixture of sp^2-bonded carbon and UNCD. The film grown with 3% CH_4 actually possessed a microstructure similar to that of glassy carbon. The C_2 dimer level in the source gas was monitored using the Swan band optical emission intensity at 516 nm. The emission intensity and the film growth rate both scaled proportionally with the CH_4 concentration in the source gas, consistent with the dimer being an important growth precursor. Noteworthy is the fact that in this Ar-rich plasma, C_2 is a growth precursor for multiple carbon microstructures including microcrystalline and ultrananocrystalline diamond, amorphous or diamond-like carbon, and microcrystalline graphite. In summary, the morphology, microstructure and phase purity of the carbon films formed varied significantly over a narrow range of CH_4 concentrations in the Ar-rich H_2/Ar source gas. Ultrananocrystalline diamond was only formed at the 1% CH_4 level.

3.1 Introduction

Ultrananocrystalline diamond (UNCD) films are normally grown by microwave-assisted CVD in hydrogen-poor, argon-rich source gas mixtures.[1, 8] This technique involves using a 1% CH_4/Ar plasma that leads to the generation of C_2 molecular precursors, which in turn results in the growth of phase-pure diamond films with a 5-15 nm grain sizes and 0.3-0.4 nm wide grain boundaries.

UNCD films exhibit a number of interesting material properties for applications such as field emission devices, conformal wear-resistant coatings, and electrochemical electrodes. UNCD can be made electrically conductive by doping, commonly with boron or nitrogen. The purpose of this work was to study the microstructure and morphology of B-UNCD films with variable diborane gas phase concentrations from 0 – 50 ppm and methane concentrations from 0.5-3%. The films were grown on Si substrates, which allowed for easier characterization of the physicochemical properties and comparison to previous work. For clarity, [B] in the gas phase during growth is expressed in ppm, while the [B] in a film is expressed as [B] cm^{-3}.

Boron doping produces p-type (B-UNCD) films while nitrogen doping, or incorporation, produces n-type (N-UNCD) films. The changes in morphology and microstructure due to boron doping in diamond prepared by chemical vapor deposition in a hydrogen-rich plasma has been reported.[9, 10] However, the effect of boron doping in ultrananocrystalline (B-UNCD) diamond grown in argon-rich plasmas is not as well studied. Previously, we reported that films grown under both conditions have similar electrochemical behavior even though several differences in their Raman spectra are observed.[11] Gruen et al. has reported on the properties of N-UNCD.[2, 5]

The gas phase diborane concentration range of 0-50 ppm was chosen because doping at these levels produces films with low electrical resistance (*ca.* $0.01\,\Omega\cdot cm$ for 10-ppm) suitable for many electrical and electrochemical applications. Additionally, we sought to compare B-UNCD with previous work on

B-doped microcrystalline diamond films produced using hydrogen-rich plasmas. In that work, significant microstructural changes were observed when gas phase boron concentrations ≥ 50 ppm are used.[9, 10]

In order to better understand the relationship between the reactive carbon level and the film morphology and microstructure, the structure of thin carbon films deposited from $CH_4/H_2/Ar$ (Ar-rich) source gas mixtures with varying levels of CH_4 from 0.5 to3% was investigated. Compositional mapping has been reported for ultrananocrystalline diamond films deposited using both microwave-plasma and hot filament CVD.[6, 12-15] In all but one of these studies, the CH_4 level was fixed and the H_2 and/or Ar levels were varied. For example, Zhou et al. studied the growth of diamond films as a function of the Ar level inCH_4/H_2 microwave plasma.[6] In another report, Jiao et al. studied the nucleation and growth of ultrananocrystalline diamond films grown from CH_4/Ar source gas mixtures with and without added H_2.[13] Lin et al. mapped how the $CH_4/Ar/H_2$ source gas composition in hot-filament CVD influences the diamond film microstructure and morphology.[12] Ultrananocrystalline diamond was formed at Ar levels above 96% and CH_4/H_2 levels between 2 and 6%. More recently, Azevedo et al. reported on the morphology and microstructure of nanocrystalline diamond films deposited with variable CH_4 levels (0.5 to 3.5%) using hot-filament CVD, while keeping the Ar concentration constant at 90%.[15] The balance of the source gas was H_2, which ranged from 6.5 to 9.5%. They found that diamond was formed at CH_4 levels at or below 2%. Above 2%, there was a gradual transition from diamond to graphite. In general, for microwave CVD, variation of source gases containing 1% CH_4 and no Ar (H_2 rich) to source gases containing 1% CH_4 and no H_2 (Ar-rich) produces a fundamental change in the plasma chemistry, growth mechanism, growth rate and film structure. In this work, the CH_4 level was varied from 0.5 to 3%, while the H_2 level was held constant at 5%. The balance of the source gas was Ar, which ranged from 92 to 94.5%. The films used in the electrochemical measurements were deposited using similar conditions but with 2 ppm of B_2H_6 added for boron doping. Variations in the CH_4 level over this narrow compositional range produce a progressive transition in film structure from microcrystalline diamond at 0.5%, UNCD at 1%, diamond like carbon at 2%, and nanocrystalline graphite at 3%. The film morphology, crystallinity, microstructure and electrochemical properties were strongly affected by the changes in CH_4 concentration in these Ar-rich mixtures.

Previously, the primary diamond growth species in UNCD was thought to be the carbon dimer, C_2, derived from collisionally-induced fragmentation of the source gas, CH_4, via reactions 1.2 and 1.3 in atmospheres containing low levels of hydrogen.[6, 16, 17]

$$2CH_4 \rightarrow C_2H_2 + 3H_2 \qquad (1.2)$$

$$C_2H_2 \rightarrow C_2 + H_2 \qquad (1.3)$$

In particular, it was proposed that C_2 could directly insert into the growing diamond lattice, with little or no energy barrier. P.W. May et al. have suggested a slightly modified UNCD growth mechanism.[18] They proposed that UNCD is simply an extension of previously proposed C_1H_x growth pathways for microcrystalline diamond but under proper conditions leads to ultrananocrystalline growth. This model considers diamond growth to be a stepwise addition of carbon atoms to the existing diamond lattice catalyzed by the presence of excess atomic H. The atomic H formed in the plasma abstracts a surface H to form H_2, leaving behind a dangling bond. A gas phase CH_x radical can collide and react with the dangling bond. Hydrogen abstraction and methyl addition may then occur at the adjacent surface site. A further H abstraction process on one of the chemisorbed groups creates a radical, which attacks the other nearby carbon group to form the ring structure and lock the two carbons into the diamond lattice.

It is suggested that as the ratio of [H]:[CHx] close to the substrate decreases below about 2, the crystallite size (<d>) is predicted to drop below 10 nm. However, this ratio should be balanced accordingly to minimize formation of amorphous carbon. The required [H]:[CHx] ratio is obtained due to the unique conditions prevailing in higher pressure Ar-rich gas mixtures. In an Ar-rich plasma the collisions between CHx and inert Ar are elastic. The reactive CHx species can survive long enough to strike the surface, whereupon they contribute to diamond growth. The combination of growth by CH_3 and growth from a significant fraction of other CHx species, leads the surface to continually renucleate (or more accurately, restructure) during growth, resulting in very small grain sizes.[19, 20]

The C_2 dimer level still provides qualitative information for carbon concentration and CH_4 dissociation. The C_2 dimer level present in the plasma

was qualitatively assessed from the Swan band optical emission at 516 nm.[6] It was found that both the growth rate and the dimer emission intensity increased with the CH_4 concentration in the source gas.

Characterization data from scanning electron microscopy (SEM), transmission electron microscopy (TEM), X-ray diffraction, Raman spectroscopy, and electrochemical measurements are reported.

3.2 Effect of Boron Concentration

3.2.1 Boron Nuclear Reaction Analysis and Resistivity of Films Grown with Varying Diborane Concentration

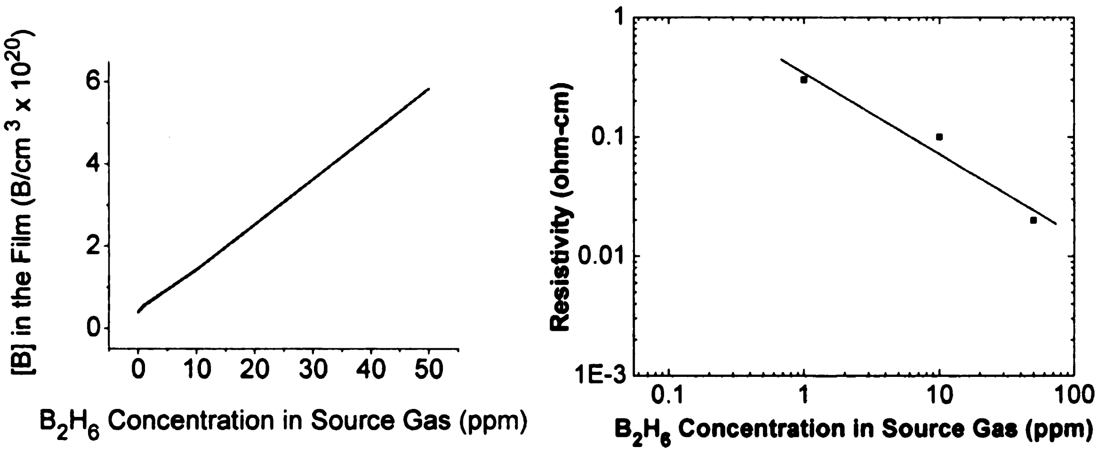

Figure 3.1. Boron concentration and electrical resistivity of B-UNCD films as a function of the diborane concentration in the gas phase during growth. The boron concentration was determined by boron nuclear reaction analysis and the resistivity was determined by four-point probe measurements.

Figure 3.1 shows a plot of the boron-doping level as a function of the gas phase diborane concentration. The boron-doping level was measured by boron nuclear reaction analysis (NRA) at the Center for Surface Analysis and

Microscopy at Case Western Reserve University. NRA uses energetic, low mass ions, such as protons or neutrons, to induce nuclear reactions on light elements. The particles emitted by these nuclear reactions can be used to measure the light element content and profiles in thin films. The plot reveals a linear trend of increasing doping level with increasing diborane concentration in the source gas. Also in Figure 3.1 is a plot of the film resistivity as a function of the gas phase diborane concentration. A reasonably linear trend is seen (least squares correlation coefficient of 0.9543) in the plot with the resistivity decreasing as the diborane concentration in the source gas increases.

3.2.2 Electron Microscopy of Films with Varying Diborane Concentration

After growth, the films were examined by optical and scanning electron microscopy. All films were continuous without any cracks or voids visible on the surface. Figure 3.2 is an SEM image of a 10 ppm doped film. The film consists of nodular features ranging from 9-60 nm in diameter with a mean of 20 ±9 nm. These nodular features are actually clusters of individual diamond grains with an average diameter of about 10-15 nm as was later determined by TEM. A columnar growth structure was not found in the cross-section SEM image; the significance being that grain size is independent of growth time and film thickness.[21, 22]

Grain boundaries are an important indicator of diamond polycrystalline film quality, as larger grain boundaries serve as formation sites for non-diamond carbon. High quality UNCD films are thought to have only 5% sp^2 bonding, which

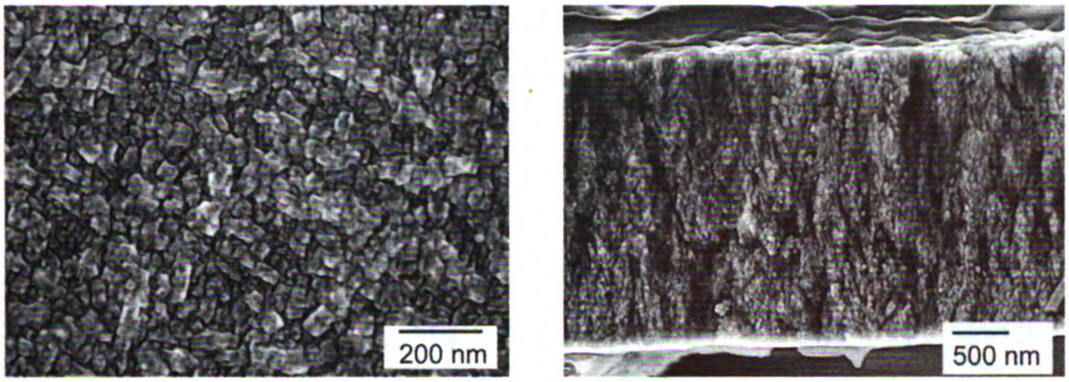

Figure 3.2. SEM images of a 10-ppm B-UNCD film. Top-view (left) and cross-section (right).

resides in the grain boundary volume.[5, 21] The large number of defects and grain boundaries likely contribute to surface electronic states that may become electrochemically influential. The HRTEM images in Figure 3.3 show a grain boundary of a 10 ppm B-UNCD film. The grain boundary width is 0.3-0.5 nm, similar to that for an undoped UNCD film.[2, 23, 24] Since boron incorporates into the diamond lattice, not just at the grain boundary as with N-UNCD, moderate B-doping does not appear to significantly influence the grain size or grain boundary width. Selected area aperture (SAA) EELS and electron diffraction patterns taken from the image area confirmed the image consists of diamond, and established there were no significant microstructural changes to this area of the film during sample preparation. The selected area electron diffraction pattern (SAED) in Figure 3.4 shows an intense spotted-ring pattern, which can be indexed to (111), (220), (311), and (400) planes of cubic diamond.[21] Electron energy loss spectra (EELS) acquired for the 10 ppm B-UNCD film supports the SAED result as there was little contribution from sp^2 bonded carbon (Figure 3.4).[2, 7, 25-27] For phase-pure diamond approaching 100% sp^3 bonding, there is no π-bonded carbon and

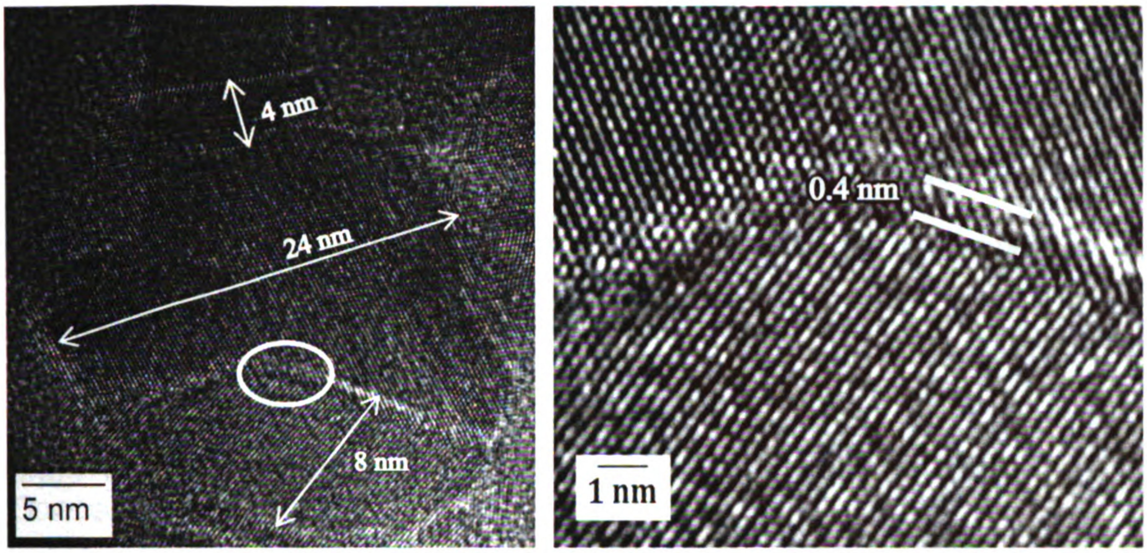

Figure 3.3. Representative HRTEM images of a 10 ppm B-UNCD with grain sizes of *ca.* 20 nm diameter (left) and a grain boundary (right). The grain boundaries are 0.3-0.5 nm across.

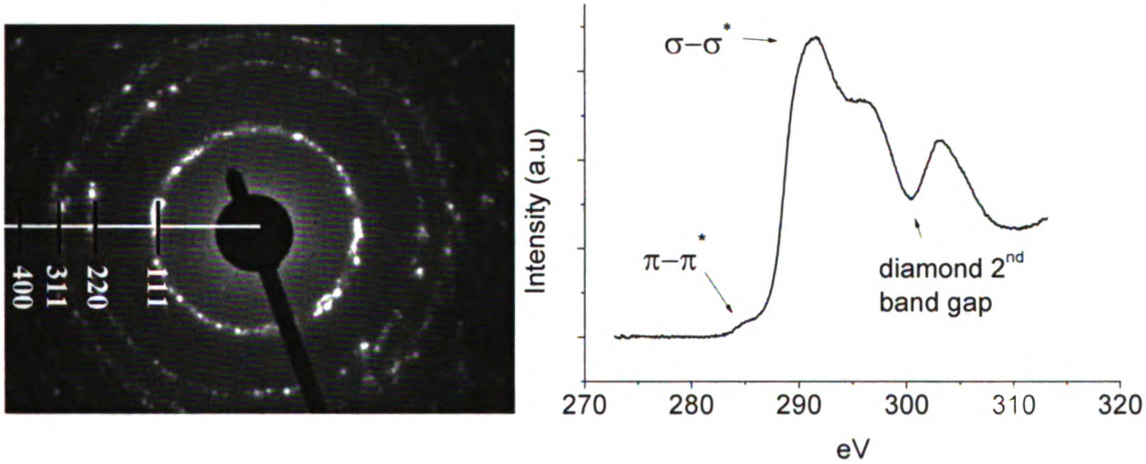

Figure 3.4. SAED ring pattern of a 10 ppm B-UNCD film (left) acquired from the same area of the film as the HRTEM image in Figure 3.3, and EELS data (right) from the same area.

accordingly no peak is observed at 285 eV. The EELS data for the 10 ppm B-UNCD film in Figure 3.4 does have a small rise at 285 eV for C(1s)→π^* transitions from the sp^2 bonded carbon in the grain boundaries. The magnitude of the peak corresponds to an sp^2 content of ≤5% based on comparison between the peaks at 285 and 290 eV, consistent with EELS studies of UNCD by Birrell et al.[5, 25, 28, 29] The peak at 290 eV is due to C(1s) → σ^* transitions from the C-C bonds in diamond. The dip at *ca.* 300 eV is due to the second absolute band gap of diamond.[30, 31] The second absolute band gap of diamond is observed at 12.6 eV, whereas the first bandgap is at 5.5 eV.[32, 33]

3.2.3 Raman Spectroscopy and XRD of Films with Varying Diborane Concentration

Raman spectroscopy is a useful characterization tool for evaluating the diamond film quality because the line positions and widths are strongly affected by changes in the film microstructure. As compared to microcrystalline diamond films with a grain size of 1 μm, it can be roughly estimated that the grain boundary density in ultrananocrystalline diamond with a grain size of 10 nm is 10^6 times higher. The visible Raman spectrum for UNCD is dominated by the sp-bonded carbon residing in the grain boundaries, which can possess several microstructures ranging from pure sp^2 carbon to amorphous sp^3 carbon, or combinations of the two.[22] Due to resonance effects, the Raman scattering cross section (visible light) for sp^2 bonded carbon is much greater (50x) than that for sp^3 bonded carbon, and scattering from the former can dominate the Raman spectrum.[34] Figure 3.5 shows a series of visible Raman spectra for films grown with different B_2H_6 concentrations. All the films exhibit peaks near 1150, 1333, 1470, and 1550 cm^{-1}. The 1150 and 1470 cm^{-1} bands correspond to C–H stretching and bending modes coupled with C=C chains in trans-polyacetylene (t-

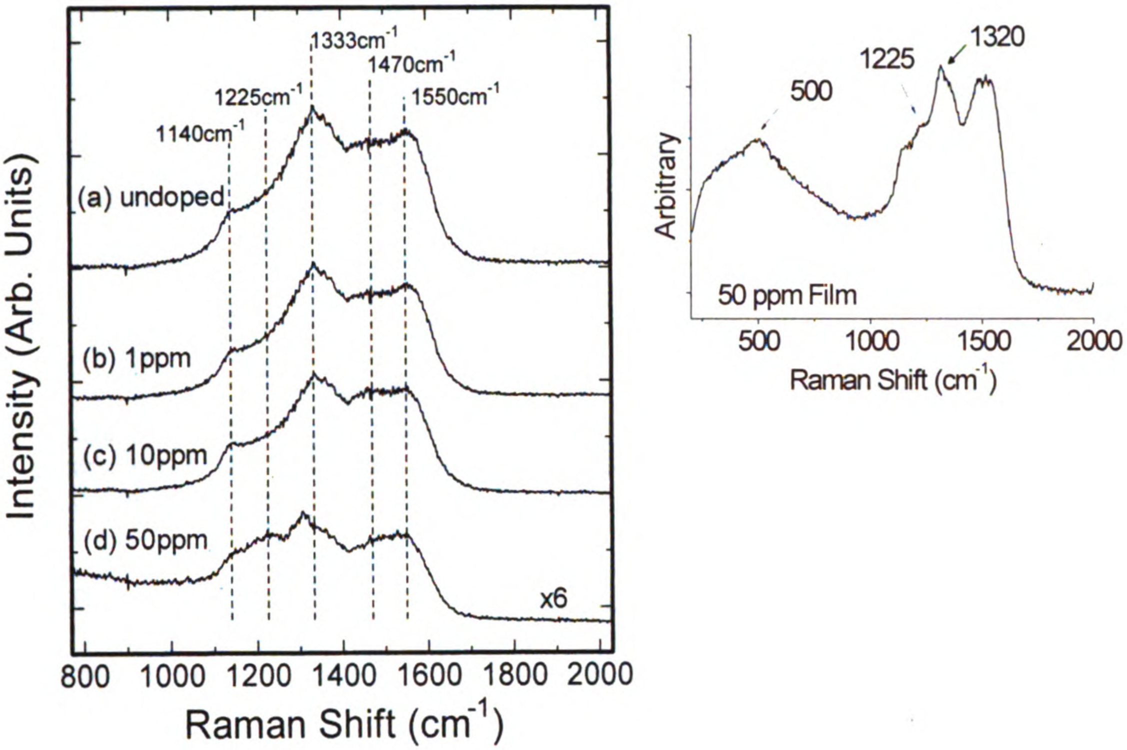

Figure 3.5. Raman spectra for 0-50 ppm boron doped UNCD films (left) and a spectrum for a 50 ppm B-UNCD film over a wider spectral range (right). The 50 ppm film has additional peaks at 500 and 1225 cm^{-1}, and the diamond peak has shifted from 1333 to ca. 1320 cm^{-1}.

PA or poly-CHx). The grain boundary bonding is believed to resemble t-PA segments, which resides in the grain boundaries.[21, 35, 36] The 1333 cm^{-1} peak is due to the T_{2g} vibrational mode for cubic diamond (so-called first-order phonon mode). [24-27] The 1550 cm^{-1} peak likely arises from olefinic C–C vibrations of a mixed sp^2–sp^3 microstructure. There is not a contribution for the in-plane stretching mode (E_{2g}^2 of "G" peak) of graphite near 1580 cm^{-1} in any of the films. This is in agreement with the XRD data for the films. XRD spectra for the 10 and 50 ppm films are shown in Figure 3.6. The spectra exhibit peaks for the (111), (220), and (311) planes of cubic diamond.

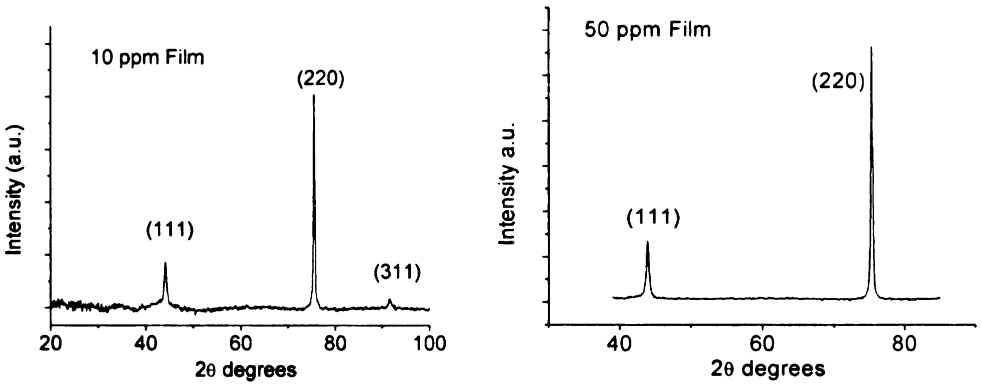

Figure 3.6. XRD spectra for 10 (left) and 50 ppm (right) B-UNCD films. Only peaks for cubic diamond are present. No peak at 27° for graphite was observed in the spectrum for any of the films.

For the 50 ppm film, there are additional Raman peaks at 500 and 1225 cm^{-1}, and the first-order phonon peak for diamond is downshifted from 1333 cm^{-1} to *ca.* 1320 cm^{-1}. The origin of the broad bands at *ca.* 500 and 1220 cm^{-1} observed for the 50 ppm film has been the subject of some debate. Originally, the band at 1220 cm^{-1} was proposed to arise from boron atoms by Ager III et al.[37] Others have attributed this band to scattering by local regions of microstructural disorder brought about by the incorporation of high levels of substitutional boron.[10, 38] However, a similar band along with one around 500 cm^{-1} have been observed for undoped diamond films, as reported by Buckley and co-workers.[39] Therefore, these bands may not be directly related to boron incorporation in the film. Gonon et al. have suggested that these bands are related to maxima in the phonon density of states of diamond and arise from scattering by phonons outside the center of the Brillouin zone.[40] This is based on the theoretical phonon density of states (PDOS) for diamond,[41] which has a maximum around 1200 cm^{-1} and matches quite closely the band observed in the spectrum. May et al. gave another explanation for these bands. They noted that the positions of these two bands agreed with the two maxima in the PDOS and supposed that they are associated with a relaxation of the wave vector selection rules.[19] More recently, Vlasov et al. studied the vibrational modes of heavily boron-doped diamond using isotopic substitution of boron and carbon. They found none of the bands in the Raman spectra shifted upon B^{10} substitution, whereas shifts to lower frequency were observed for all bands upon C^{13} substitution, as compared to a sample with natural isotope abundances.[42] Their results support the assignment of these bands to perturbed diamond lattice phonons (*i.e.,* microstructurally disordered carbon) and not to any boron-related vibrational mode.

With regard to the peak at *ca.* 500 cm^{-1}, previous reports have directly correlated the peak intensity with the boron in the film, as determined by secondary ion mass spectrometry.[10, 43] Bernard et al. found that the wavenumber (*W*) in cm^{-1} of the Lorentzian component of the peak at *ca.* 500 cm^{-1} is related to [B] cm^{-3} by:

$$[B]\,cm^{-3} = 8.44x10^{30}\exp^{-0.048W(cm^{-1})} \qquad [3.1]$$

The Lorentzian component for the peak in the 50 ppm film is at 488 cm^{-1}, giving a Boron concentration of $6x10^{20}$ cm^{-3} (3,200 ppm). This matches the boron concentration in the film determined by nuclear reaction analysis, which was also $6x10^{20}$ cm^{-3}. Further work would be needed to validate equation 3.1 for use with B-UNCD due to the increased defects in the film and controversy surrounding the peaks origin. The results are nonetheless interesting, and seem to support the boron concentration 500 cm^{-1} peak intensity relationship reported by Bernard et al. for microcrystalline films.

There are three possibilities for the down-shift of the first-order phonon mode in the 50 ppm film from 1333 to 1320 cm^{-1}; a decrease in crystal size reducing phonon lifetimes according to the phonon confinement model, tensile stress, or a change of symmetry from cubic to hexagonal (Lonsdaleite) diamond.[34, 44-48] Tensile stress in diamond films normally occurs from a lattice mismatch between the substrate and diamond film. The silicon substrates used throughout this study were of the same orientation and production batch, so changes in diamond growth due to substrate differences are not expected. We therefore consider the shift due to either a change of symmetry to 6d (hexagonal) diamond at the grain boundaries or phonon confinement.

Hexagonal diamond is found naturally, can be prepared by shock loading of graphite or natural diamond, and by CVD.[34, 44, 49, 50] Raman scattering from hexagonal diamond with space group *P63/mmc* exhibits a broad peak in the range 1315–1326 cm^{-1}. In particular, stacking faults and twins can give rise to crystal regions with local hexagonal symmetry near grain boundaries. M.C. Rossi investigated the microstructure of CVD polycrystalline diamond by scanning laterally across neighboring crystals using micro-Raman spectroscopy and found a change from cubic to hexagonal symmetry close to the grain boundary.[49] Shock loading of highly crystalline graphite produces hexagonal diamond with a single phonon peak at *ca.* 1317 cm^{-1}.[34, 51] More frequently, hexagonal diamond is observed in Raman spectra of CVD films as a shoulder at *ca.* 1320 cm^{-1} of a more intense peak for cubic diamond at *ca.* 1332 cm^{-1}.[22, 38, 49] In the present case, any spectral contribution from hexagonal diamond is expected to co-exist

with that of cubic diamond, as the XRD spectrum for the 50 ppm film verifies the bulk microstructure as face-centered cubic diamond. Figure 3.6 shows typical XRD spectra for a 10 and 50 ppm B-UNCD film. The spectra exhibit peaks for the (111), (220), and (311) planes of cubic diamond. There were no additional peaks observed for (100), (101), (102), or (103) planes as expected for hexagonal diamond.[51, 52] Considering the lack of peaks for hexagonal diamond in the XRD data and only a single peak for diamond in the Raman spectrum, the downshift from 1333 to 1320 cm^{-1} being due to hexagonal diamond in the 50 ppm film is precluded.

The phonon confinement model predicts the Raman line shape to asymmetrically broaden and shift to lower frequencies as grain size decreases ≤10 nm.[46, 47, 53, 54] For both the 10 and 50 ppm doped film the grain size determined by TEM was *ca.* 10 - 20 nm, slightly above the predicted threshold to cause a downshift. However, the first order phonon for diamond is often downshifted to 1326 – 1328 cm^{-1} for diamond powders as large as 100 nm. Lattice defects in diamond also lead to a reduction in phonon lifetime and shift to lower frequencies. There seems to be some variability in the literature with regards to the exact grain size that produces significant downshifting of the diamond peak. [46, 47, 53, 55] The previous work reports peak positions at both 1326 and 1332 cm^{-1} for ultrananocrystalline films. [46, 47, 53, 55] Of more interest here, why does the 50 ppm film exhibit the downshift when the other films do not when there is no apparent change in nominal grain diameter? The most reasonable explanation is boron-induced changes to the lattice. For example, F. Brunet et al.

reported on high-resolution X-ray diffraction studies on the lattice constants of boron-doped homoepitaxial and polycrystalline diamond films containing from 0 to $8x10^{20}$ [B] cm^{-3}. Their results show that boron incorporation induces a large expansion of the diamond lattice when [B] > 10^{20} cm^{-3}.[56, 57] Ando et al. demonstrated significant changes to the Raman spectrum of boron-doped diamond films as [B] increased.[43] The downshift of the diamond line to 1320 cm^{-1} in the 50 ppm film is lower than that for other ultrananocrystalline films reported in the literature. It appears then, that at 50 ppm there are boron-induced changes to the diamond lattice leading to a downshift of the diamond peak from 1332 to 1320 cm^{-1}. This is consistent with the phonon confinement model, but the exact nature of the change to the lattice is not yet clear.

3.2.4 NEXAFS of Films with Varying Diborane Concentration

Like Raman spectroscopy, the C1s NEXAFS spectra for various carbon materials (e.g., diamond, HOPG, amorphous carbon) are quite distinct from one another. NEXAFS is highly useful for ascertaining the quality of carbons and probes the local atomic order of a material. Figure 3.7 shows a series of NEXAFS spectra for the top-side and back-side of UNCD films deposited with different diborane levels in the source gas. The top-side corresponds to the growth surface and the back-side corresponds to the side of the film in contact with the Si substrate. The back-side was exposed by chemically etching away the Si substrate. Looking at the top-side series, one can see that the spectral features are largely unchanged with the diborane level in the source gas. All

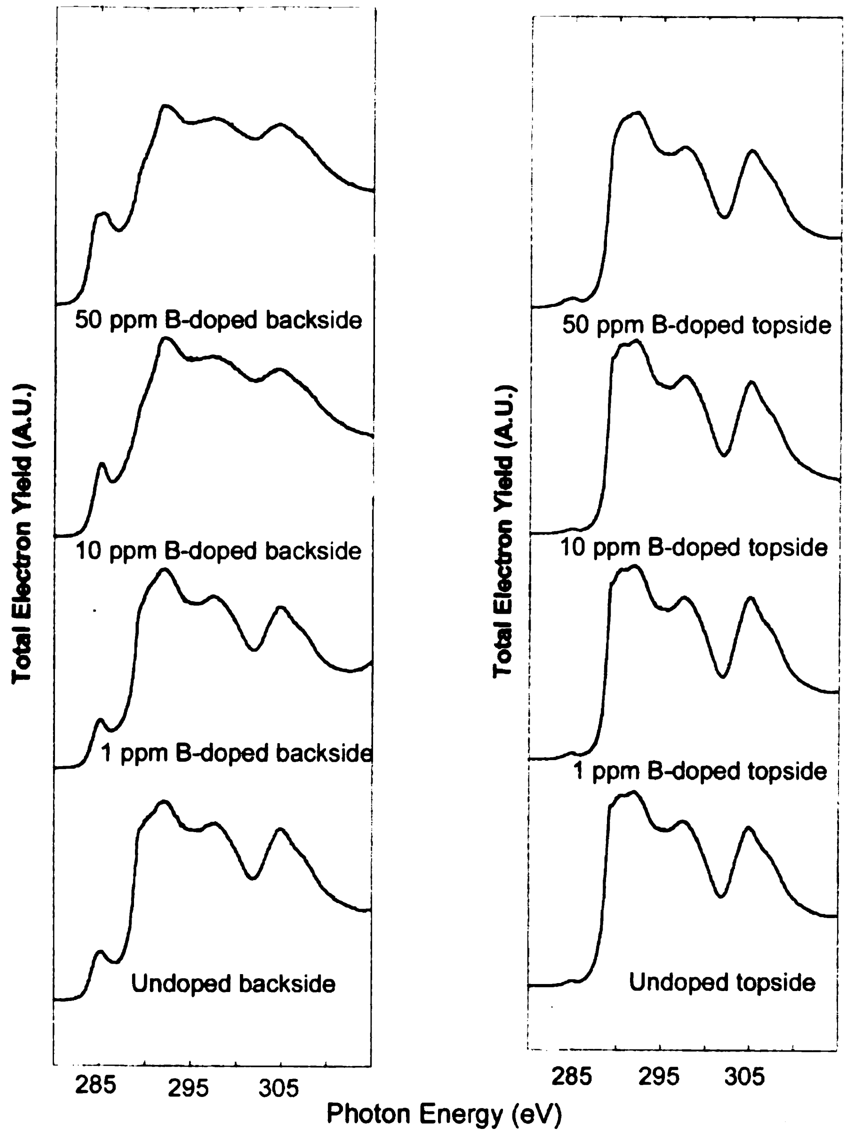

Figure 3.7. NEXAFS spectra for the top-side and back-side of UNCD films deposited with different diborane levels in the source gas.

spectra show a sharp absorption edge at 289.5 eV and the presence of a second bandgap feature at ~302 eV. For the undoped film, the σ* feature that peaks at ~290 eV is detectable but not so for the films grown with higher diborane levels, particularly the 50 ppm film. This sharp absorption edge and the presence of the σ* peak are characteristic of sp^3 bonded carbon. Importantly, all four films contain only a weak π* peak at 285eV, which does not grow much in intensity with the diborane concentration. These results suggest the films consist

largely of sp^3 bonded diamond with minimal sp^2 carbon impurity regardless of the diborane level in the source gas. Interestingly, the spectra for the back-side are quite different. As the diborane level in the source gas is increased, the σ^* and second bandgap feature at 302 eV decrease while the π^* signal increases in intensity. Clearly, the backside contains less diamond character as the diborane level is increased. This suggests that the diborane level is affecting the film growth. The nature of the boron-containing species in the gas phase in contact with the growth surface is not clear. It is known that boron compounds in the gas phase induce secondary nucleation.[43] In the plasma, diborane dissociates into BH_3 and BH radical species according to the following reaction:

$$B_2H_6 \rightarrow 2BH_3\bullet \rightarrow 2BH\bullet + 2H_2. \qquad [3.2]$$

It can be expected that the radicals present will modify the $CH_x\bullet$ and $H\bullet$ species in the plasma. Furthermore, it has been reported that H-C-B compounds can form at very high diborane levels.[43] The NEXAFS is considered congruently with the Raman spectra. Clearly, the data reveal that more sp^2-bonded carbon forms at the substrate surface with higher diborane levels. The sp^2 carbon exists in a diamond-like carbon (DLC) microstructure as there is no indication of any ordered graphitic carbon in the Raman spectra near 1580 cm^{-1}. Also the NEXAFS σ-σ^* transition for both graphite and disordered sp^2 is up-shifted from 290 to approx. 294eV as compared to both diamond and DLC.[27] Here the back-side NEXAFS spectra for both the 10 and 50 ppm films show a gradual slope from 285 to 290 eV indicating a mixed sp^3-sp^2 bonding; however, the peak for the σ-σ^* transition remains at 290 eV, consistent with a DLC microstructure.

3.2.5 Discussion of Varying Diborane Concentration During Growth

The mechanism of electrical conduction in B-UNCD films has not been thoroughly investigated. Boron is incorporated as a p-type dopant into the diamond crystal structure in both single and microcrystalline films. An important question for B-UNCD is whether boron resides in the grains, grain boundaries, or both? As discussed above, the electrical conduction through UNCD, either undoped or with incorporated nitrogen, appears to be mainly through the grain boundaries.[58] The grain boundaries possess a high density of π-states and good connectivity so that a high degree of electrical conduction exists. If the π-state density and the connectivity are disturbed, the film conductivity decreases considerably. Through-grain electron transport would make the UNCD films less prone to conductivity changes caused by alterations in the grain boundary microstructure. Our group previously conducted electrochemical studies of both undoped and B-UNCD films that demonstrated strong evidence for boron residing in the lattice rather than the grain boundary.[59] The electrochemical response for $Fe(CN)_6^{3-/4-}$ and $Ru(NH3)_6^{3+/2+}$ for both films was evaluated before and after H_2O_2 washing/hydrogen-plasma treatment. Peroxide washing followed by re-hydrogenation in a hydrogen-rich plasma helps to remove sp^2 carbon and disrupt remaining π-networks at the surface by H-termination. After treatment, there was an increase in ΔE_p for both redox couples for undoped UNCD, while there were relatively minor changes in ΔE_p for B-UNCD. Those results suggest that the electronic properties of the boron-doped films are dominated by the acceptor concentration in the diamond lattice, rather than by the physicochemical properties of the grain boundaries.[59]

As non-diamond carbon is known to reside in the grain boundary, changes to the grain boundaries induced by increased boron should be accompanied by an increase in grain boundary width, and greater intensity for non-diamond carbon in the Raman and NEXAFS spectra. Electron microscopy of the films (Figures 3.2-3.3) shows that there are no abnormalities at the surface of the film or an increase in grain boundary width. Significant increases in non-diamond carbon or changes to the diamond crystal structure normally produce visible morphological differences, such as those in Figure 3.8c-d. None of these features are present for the 0-50 ppm B-UNCD films.

The Raman, XRD, and NEXAFS spectra are similar, except for the 50 ppm film. The NEXAFS spectrum for the back-side of the 50 ppm film indicates an increase for π-bonded carbon near the C-Si interface. However, there is a reduction of π-bonded carbon in the 50 ppm film with increased growth time as the NEXAFS, Raman, and XRD spectra for the top side are that of good quality UNCD with minimal non-diamond (π-bonded) carbon content.

It appears that for UNCD films grown with diborane source gas concentrations up to 50 ppm, there are no significant changes in the morphology or microstructure for any of the films. At 50 ppm, there is an increase in π-bonded carbon, either C=C or B_xC_x moieties, at the start of diamond growth followed by heavily doped B-UNCD at the surface. Boron appears to incorporate into the UNCD lattice structure similarly to microcrystalline films. Evidence for boron residing in the grains is the fact that neither the grain size or grain boundary width was altered with increased boron doping, while at the same time the boron concentration in the film linearly followed the diborane concentration during growth.

3.3 Effect of CH_4 Concentration

Another important goal of this work was to determine the optimum source gas composition, with regard to the CH_4 concentration, for depositing ultrananocrystalline diamond. We sought to learn how a varying CH_4 concentration affected the formation of ultrananocrystalline diamond when the H_2 level was kept constant. Similar studies have been reported for a fixed CH_4 concentration and a varying H_2 level.[8]

3.3.1 Microscopy of Films with Varying CH_4 Levels

Figure 3.8 presents SEM micrographs of thin films deposited with CH_4 concentrations ranging from 0.5 to 3%. The sample deposited with 0.5% CH_4 is a multi-faceted, polycrystalline film with an average crystallite size of 0.5 µm or less (Figure 3.8a). The crystallites are randomly-oriented and the level of secondary nucleation on the surface is low, based on the absence of multiple smaller growths on the larger crystallite facets or in the grain boundaries. This image is characteristic of microcrystalline diamond. The crystallite size and surface roughness increased with the growth time (*i.e.,* film thickness). For example, the root-mean-square surface roughness (R_{rms}) of a film deposited for 2-h, as determined from an AFM image over a 5 x 5 μm^2 area, was *ca.* 50 nm, while the R_{rms} for a film deposited for 4-h was 100 nm. The nominal crystallite size also increased from 0.5 to 1 μm with growth time (2- or 4-h). Cross-section SEM images of films deposited with 0.5% CH_4 revealed a columnar growth structure.

A completely different morphology is seen in Figure 3.8b for the film deposited with 1% CH_4 as the crystallite size is much smaller and the film consists of nodular features 50-100 nm in diameter. Moreover, a columnar growth structure was not found in the cross-section SEM images. Previously reported TEM images showed that these nodular features are clusters of individual diamond grains with an average diameter of about 15 nm.[60] The R_{rms} of the film was as low as 35 nm across a 5 x 5 μm^2 area and was independent of the growth time (*i.e.*, film thickness). Figure 3.8c shows a micrograph of a film deposited with 2% CH_4. This film possesses a "cauliflower" morphology. There was no evidence of any columnar growth in cross-section SEM images. Some of the features appear similar in size to those of the film deposited with 1% CH_4; however, the R_{rms} surface roughness is larger with a value of 94 nm over a 5 x 5 μm^2 area. Figure 3.6d shows an image of a film deposited with 3% CH_4. This film possesses quite a different morphology from the other three. It consists of clusters of platelet-like features. The clusters are a few micrometers in diameter and each platelet feature is less than 0.5 μm in length and randomly-oriented. Clearly, the SEM

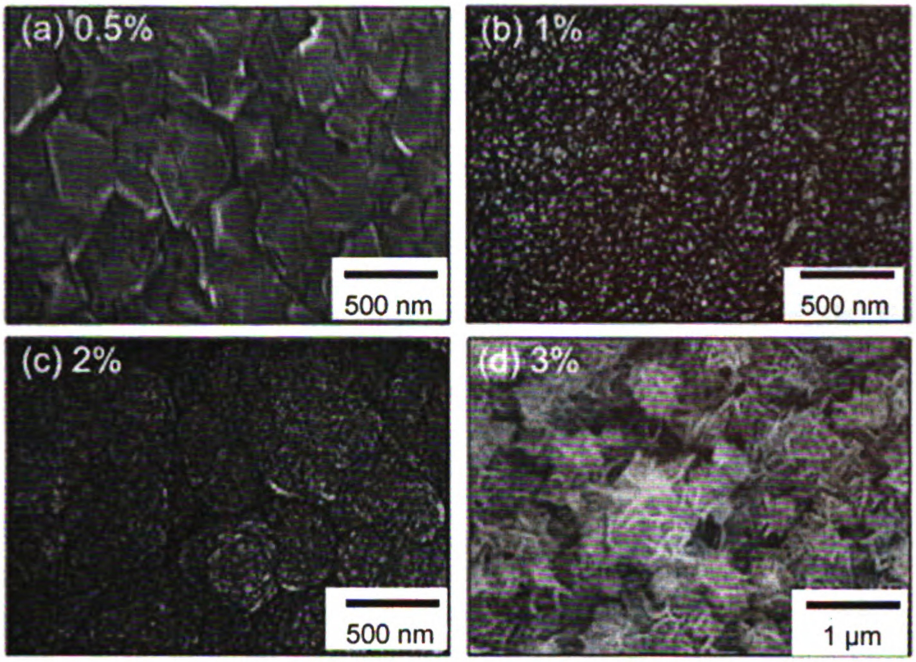

Figure 3.8. SEM images of carbon films deposited with various CH_4 concentrations in the Ar/H_2 source gas mixture: (a) 0.5, (b) 1, (c) 2 and (d) 3%. The balance of the source gas was 5% H_2 and 92–94.5% Ar. The growth time was 2 h for the 0.5, 1 and 2% films, and 0.25 h for the 3%.

images reveal the film morphology can be significantly varied by small adjustments of the CH_4 concentration in the source gas.

3.3.2 XRD of Films with Varying CH_4 Levels

Figure 3.9a and (b) show X-ray diffraction patterns for the films grown with 0.5 and 1% CH4. Each spectrum has relatively sharp and narrow diffraction peaks with 2θ values of 44.0°, 75.5°, and 91.5°. These peaks can be indexed to the (111), (220), and (311) planes of the cubic diamond, respectively.[13, 61] Even though there is a transition from a microcrystalline to a nanocrystalline morphology, as evidenced by the SEM images, both films are composed primarily of cubic diamond with no bulk graphitic phases detected. For example, there is no graphite (002) line intensity detected at 2θ of 26°.[62, 63] The relative peak intensities are about the same for both diamond films but the absolute peak intensities for the 1% film are higher because of a greater film thickness (5 vs. 2 μm). The line widths for the 1% film are also broader because of a reduction in the nominal grain size from the micrometer to the nanometer scale. Fig.3.9c and (d) show X-ray diffraction patterns for the films grown with 2 and 3% CH_4 respectively. Compared to the diffraction pattern for the 1% film, the diamond line intensities are attenuated and the line widths are significantly broadened, as shown in Figure 3.9c. New peaks emerge at 2θ values of 26.7, 42.3, 54.1, and 77.6° that are characteristic of glassy carbon.[64] The lattice spacing calculated from the 2θ position of each new peak, are 3.41, 2.13, 1.69, and 1.23 Å.[64] The broad and asymmetric graphite peaks predominate for the 3%film as the diamond peaks nearly disappear. The 002 line width at *ca.* 26° becomes more intense and narrow compared to the peak for the 2% film. The XRD data indicate the film grown with 2% is a composite consisting of low levels of crystalline diamond and high levels of graphite-like sp^2 carbon. On the other hand, the 3% film is more graphitic, composed of all sp^2-bonded carbon. The data reveal the film crystallinity is strongly affected by the CH_4 concentration. The line widths for the film grown with 1% CH_4 are broader than those for the film grown with 0.5%. As stated above, this is due to the reduction in grain size from the micrometer to nanometer scale caused by the increased renucleation rate at 1%. The nominal crystallite size can be estimated from the line widths using the Scherrer

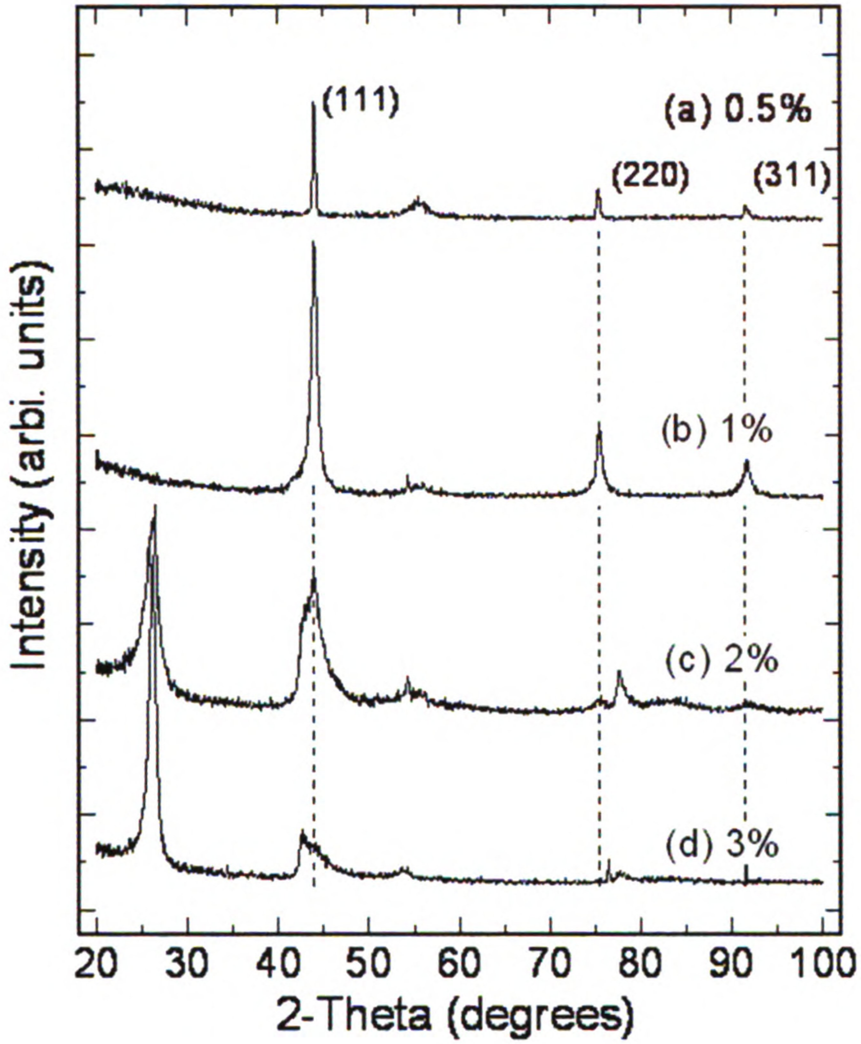

Figure 3.9. XRD patterns for carbon films deposited with various CH_4 concentrations in the Ar/H2 source gas mixture: (a) 0.5, (b) 1, (c) 2 and (d) 3%. The balance of the source gas was 5% H2 and 92–94.5% Ar. The growth time was 2 h for the 0.5, 1 and 2% films, and 0.25 h for the 3% film.

equation (3.2), in which t is the grain size, λ wavelength of the X-ray source, B the FWHM of the 2θ diffraction peak (in radians), and θ the diffraction peak

$$t = \frac{0.9\lambda}{B\cos\theta} \quad [3.2]$$

position.[65] The average grain size of the film grown with 1%was calculated to be 11 nm (diamond (111) line), consistent with the measured TEM value that ranged from 7–15 nm. The relative intensity ratios of the diffraction peaks are close to the expected values for cubic diamond.

3.3.3 Raman Spectroscopy of Films with Varying CH_4 Levels

Fig. 3.10a-d shows Raman spectra for the different films. The spectrum for each film is quite distinct, although there are some common peaks for the 0.5, 1 and 2% CH_4 films at 1333, 1150, 1470, 1550 and 1590 cm^{-1}. The most prominent peak for the 0.5% CH_4 film is the one-phonon diamond band at 1333 cm^{-1}.[34, 47, 66-72] This is consistent with the faceted morphology seen by SEM and the cubic diamond structure revealed by XRD. The line width of 12 cm^{-1} is considerably broader than the 2–4 cm^{-1} line width observed for single crystal diamond recorded with the same instrumental settings, but is typical for polycrystalline films. To a first approximation, the line width is inversely related to the phonon lifetime.[47, 70] Therefore, the higher the fraction of grain boundary or defect density, the shorter the phonon lifetime and the broader the line width will be. The next most intense peak is at 1470 cm^{-1}, with broader and less intense peaks at 1150, 1550, and 1590 cm^{-1}. The spectrum for the 1% CH_4 film is very characteristic of UNCD.[1, 16, 17, 61] The one-phonon diamond line at 1333 cm^{-1} is less intense relative to the peaks at 1150, 1470, 1550, and 1590 cm^{-1}, and is significantly broadened from 12 to 140 cm^{-1} as the film changed from a microcrystalline to an ultrananocrystalline morphology. The origin of the peaks at 1150, 1470 and 1550 cm^{-1} was previously discussed. The weak 1590 cm^{-1} peak is assigned to the G-band of crystalline graphite. The overall spectral intensity for

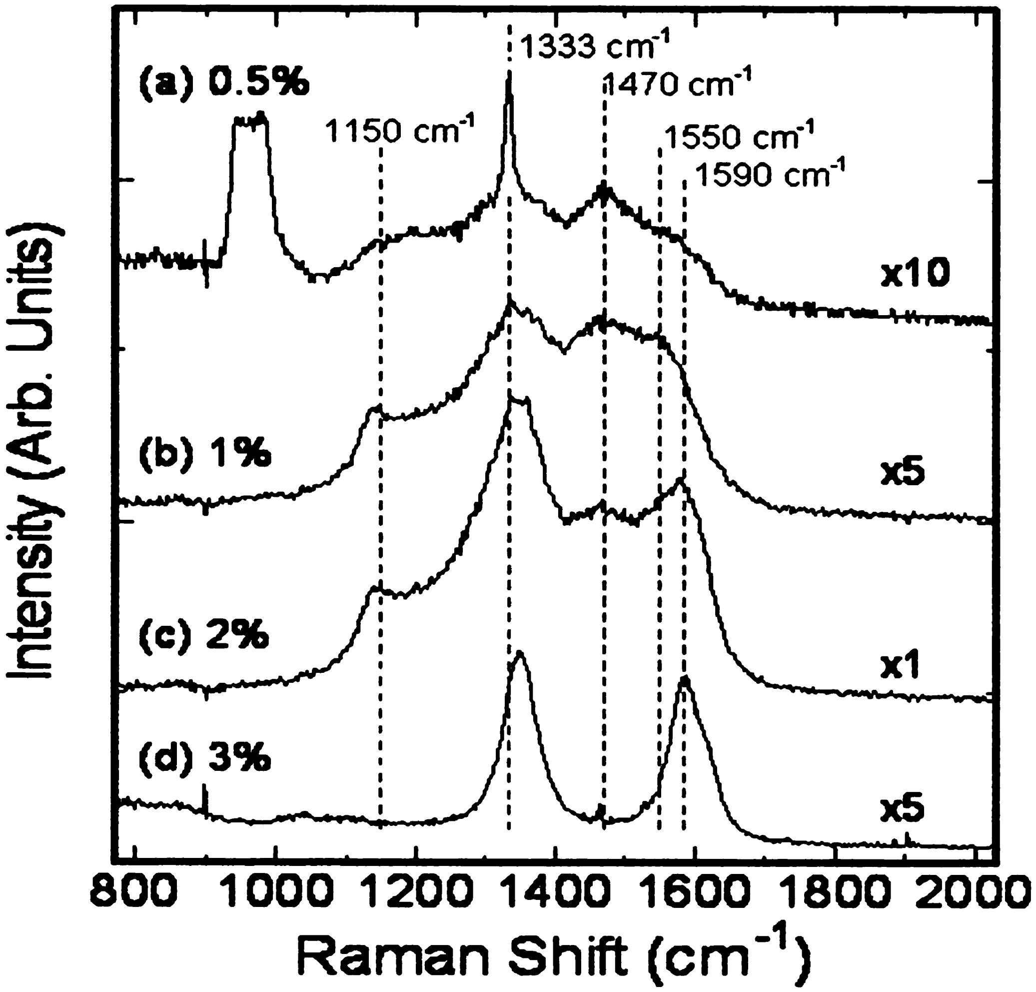

Figure 3.10. Raman spectra for carbon films deposited with various CH_4 concentrations in the Ar/H_2 source gas mixture: (a) 0.5, (b) 1, (c) 2 and (d) 3%. The broad band at 960 cm^{-1} is the second order phonon for the silicon substrate. The balance of the source gas was 5% H_2 and 92–94.5% Ar. The growth time was 2 h for the 0.5, 1 and 2% films, and 0.25 h for the 3% film.

the 1% film is twice that for the 0.5% film. This is because of a greater film thickness for the former and a higher relative fraction of grain-boundary sp^2-bonded carbon, which has a significantly higher cross-section with visible excitation compared with diamond.[34, 69] Since these same peaks are also in the spectrum for the 1% film, there must be small domains of ultrananocrystalline diamond in the 0.5% film, inter dispersed amongst the faceted microcrystallites. In addition to the decreased grain size for the 1% film, another reason for the line broadening at 1333 cm^{-1} is the scattering intensity that emerges at 1350 cm^{-1} (the so-called D-band for graphitic carbon).[63, 67, 73, 74]

For the 2% CH_4 film, the one-phonon diamond line at 1333 cm^{-1} is unresolvable due to the more intense scattering at 1350 cm^{-1}. The 1150 and 1470 cm^{-1} peaks are still present though. The intense scattering between 1330 and 1360 cm^{-1} (D-band) as well as a shift in the non-diamond sp^2 carbon scattering from a maximum at 1550 to 1590 cm^{-1} (G-band) is consistent with the transition of the C–C bonding from more sp^3 diamond to amorphous sp^2 carbon. Clearly, these spectral features are consistent with some aromatic clustering in the film. Moreover, the overall signal intensity increases by about a factor of 5 compared to the 1% CH_4 film due, in part, to the increased film thickness. The additional scattering intensity at 1360 cm^{-1} and the new maximum at 1590 cm^{-1} suggest a significant fraction of the carbon in the 2% CH_4 film is a disordered graphite-like sp^2carbon.[35, 36, 68, 74, 75] Single crystal graphite shows only a narrow G-line centered at *ca.* 1580 cm^{-1}. In microstructurally disordered graphitic materials, such as glassy carbon or microcrystalline graphite, the D-band at 1360 cm^{-1} is present along with a broadened G-band.[34, 62] The ratio of the 1360/1590 cm^{-1} bands tracks the microstructural disorder in the graphitic material. In other words, the D/G ratio increases as the carbon microstructural disorder and exposed graphitic edge plane increases. Tuinstra and Koenig used XRD in combination with Raman spectroscopy to show that the 1360/1580 cm^{-1} intensity ratio in graphitic materials is inversely proportional to the in-plane coherence length, L_a over a range of 2.5–1000 nm.[63]

For the 3% CH_4 film, there are no spectral features characteristic of UNCD as the 1333, 1150 and 1470 cm^{-1} peaks are absent. Rather, only the D- and G-bands are evident with peak widths (FWHM) of 50 and 60 cm^{-1}, respectively. The peak width of the G-line for the 3% CH_4sample is smaller than that for the 2% CH_4 sample consistent with a more microstructurally ordered graphitic phase and an increasing in-plane crystallite domain size, L_a. This result indicates the 3% film mainly consists of microcrystalline graphite, consistent with the XRD results as the spectrum is identical to that for glassy carbon.[66, 74]

3.3.4 C_2 Emission

Optical spectroscopy was used to measure the emission of C_2 dimer in the plasma as a function of the CH_4 concentration in the source gas. At CH_4 levels between 0.5 and 3%, the plasma emitted electromagnetic radiation with maxima at 516 and 656 nm. The emission at 516 nm is attributed to the $d^3\Pi \rightarrow a^3\Pi$ transition (Swanband) of the C_2 dimer.[76] On the other hand, the emission at 656 nm originates from atomic hydrogen H-α.[76] Figure 3.11a shows the emission intensity at 516 nm increased proportionally with the CH_4 concentration. The apparent growth rate also increased proportionally with the CH_4 concentration, as seen in Figure 3.11b. For example, the growth rate of the 1% CH_4 film is ~2 µm/h and the growth rate increased with increasing CH_4 concentration between 0.5 and 3%, in concert with the C_2 dimer emission intensity.

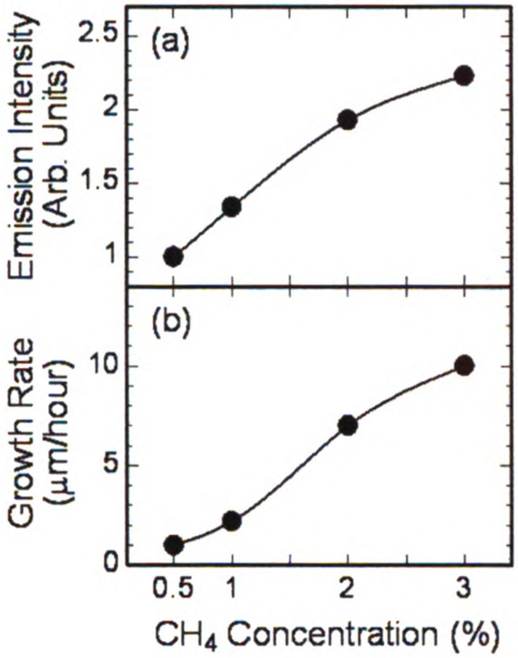

Figure 3.11. Dependence of the (a) optical emission intensity for the C_2 dimer (λ emiss=516 nm) and (b) growth rate on the CH_4 concentration in the source gas. The balance of the source gas was 5% H_2 and 92–94.5% Ar. The growth time was 2 h for the 0.5, 1 and 2% films, and 0.25 h for the 3% film.

3.3.5 Electrochemistry of Films with Varying CH_4 Levels

Electrochemical measurements can also be quite revealing about the type of carbon microstructure present in a film; particularly at the surface, which is in contact with an electrolyte solution.[75, 77] Fig. 3.12 shows background cyclic voltammetric *i–E* curves for the 1, 2 and 3% CH_4 films (10 ppm B_2H_6) in 0.1 M $HClO_4$. The 0.5% film was not studied; however, our group has previously reported on the electrochemical properties of this film, which are similar to those of the 1% film.[60, 78, 79] SEM, XRD and Raman spectroscopic data for these doped films were identical to the characterization data for the corresponding undoped films presented in Figs. 3.8 – 3.10. As can be seen, the area under the curve (i.e., charge) increases and the working potential window decreases with increasing CH_4 level. These trends are similar to those observed for carbon films deposited with varying CH_4 levels in H_2-rich source gas mixtures.[75, 77] The lowest background current and charge are seen for the UNCD film grown with 1% CH_4. The largest background currents are seen for the 2 and 3% films, which according to the XRD and Raman data contain a higher fraction of sp^2-bonded carbon. In other words, the decreasing potential window and increasing background current track the level of sp^2 carbon content in the film.[75, 77] A characteristic of high quality diamond, low in sp^2 carbon content, is a low voltammetric background current and wide potential window in acidic aqueous electrolyte solutions.[11, 60] In addition to the larger background current, peaks are present for the 2 and 3% films centered at 0.4 V. These peaks are likely due to electrochemically-active carbon–oxygen functional groups, specifically the quinone/hydroquinone couple that terminate the graphitic edge plane carbon.[80, 81] Such redox-active or ionizable (*e.g.*, carboxylic acid) functional groups do not exist on good quality,hydrogen-terminated diamond.

Cyclic voltammetric *i–E* curves for 1 mM $Ru(NH_3)_6^{+3/+2}$ +1 M KCl are shown in Fig. 3.13.[11, 60, 75, 77-79, 82-84] The curves are nearly identical in shape to each other, regardless of the film microstructure. Well-defined oxidation (*ca.* −0.13 V) and reduction (*ca.* −0.2 V) peaks of the same current magnitude are seen for all three electrodes with a peak potential separation, ΔE_p, of 65–80 mV.

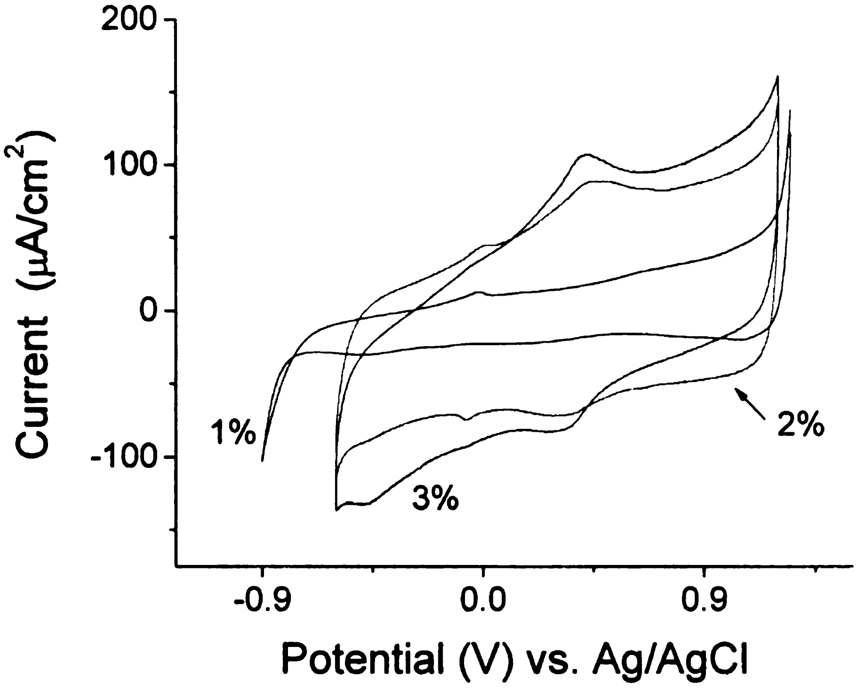

Figure 3.12. Background cyclic voltammetric i–E curves in 0.1 M $HClO_4$ for films deposited from 1, 2 and 3% CH_4. 2 ppm B_2H was added to the source gas for boron doping. The balance of the source gas was 5% H_2 and 92–94% Ar. The growth time was 2 h for the 1 and 2% films, and 0.25 h for the 3% film. The potential scan rate was 100 mV/s.

The reduction peak current (forward scan) is limited by semi-infinite linear diffusion of the redox analyte to the electrode surface, as evidenced by the fact that the peak current increased linearly with the scan rate$^{1/2}$ (r^2>0.99). All three films exhibited good electrochemical activity for this redox system regardless of the microstructure, as evidenced by ΔE_p values that are close to the theoretical value of 59 mV for a kinetically-reversible system. The heterogeneous electron-transfer rate constant for this redox system is most strongly influenced by the electronic properties of the electrode (*i.e.*, density of electronic states).[11, 60, 75, 77-79, 82-84]

The fact that all three films exhibited similar responses for this redox

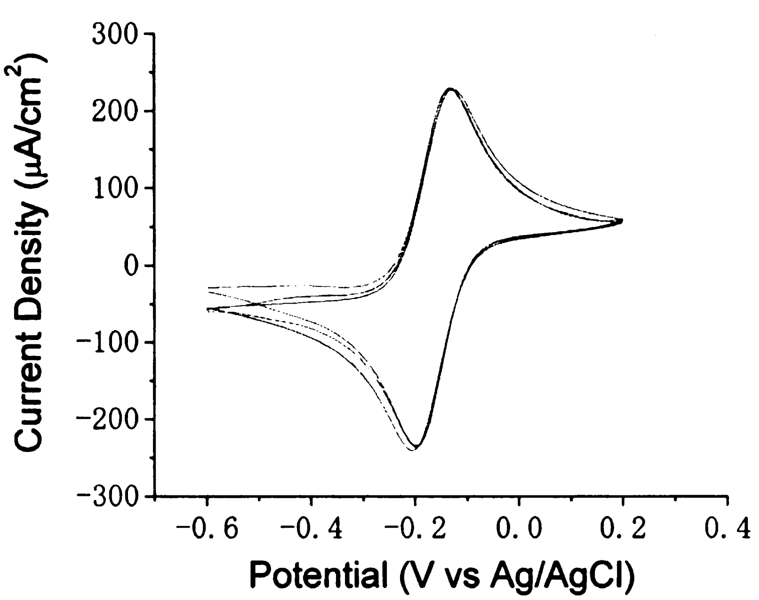

Figure 3.13. Cyclic voltammetric *i–E* curves for 1 mM $Ru(NH_3)_6^{+3/+2}$ in 1 M KCl at films deposited from 1, 2 and 3% CH_4. 2 ppm B_2H_6 was added to the source gas for boron doping. The balance of the source gas was 5% H_2 and 92–94% Ar. The growth time was 2 h for the 1 and 2% films, and 0.25 h for the 3% film. The potential scan rate was 100 mV/s.

system indicates that each possessed similar electronic properties even though the microstructures were considerably different. Fig. 3.14 shows cyclic voltammetric *i–E* curves for 10 μM 2,6-anthraquinone-disulfonate in 0.1 M $HClO_4$. This molecule strongly adsorbs on sp^2 carbon surfaces (*e.g.*, glassy carbon) with negligible adsorption on hydrogen-terminated diamond films and hydrogenate glassy carbon.[85] It can be used as a measure of the presence of sp^2-bonded graphitic carbon at the surface of the film as the coverage and strength of adsorption track the fraction of exposed edge plane (*i.e.,* degree of microstructural disorder).[86] The greater the fraction of graphitic edge plane, the greater the adsorbate coverage.[86]

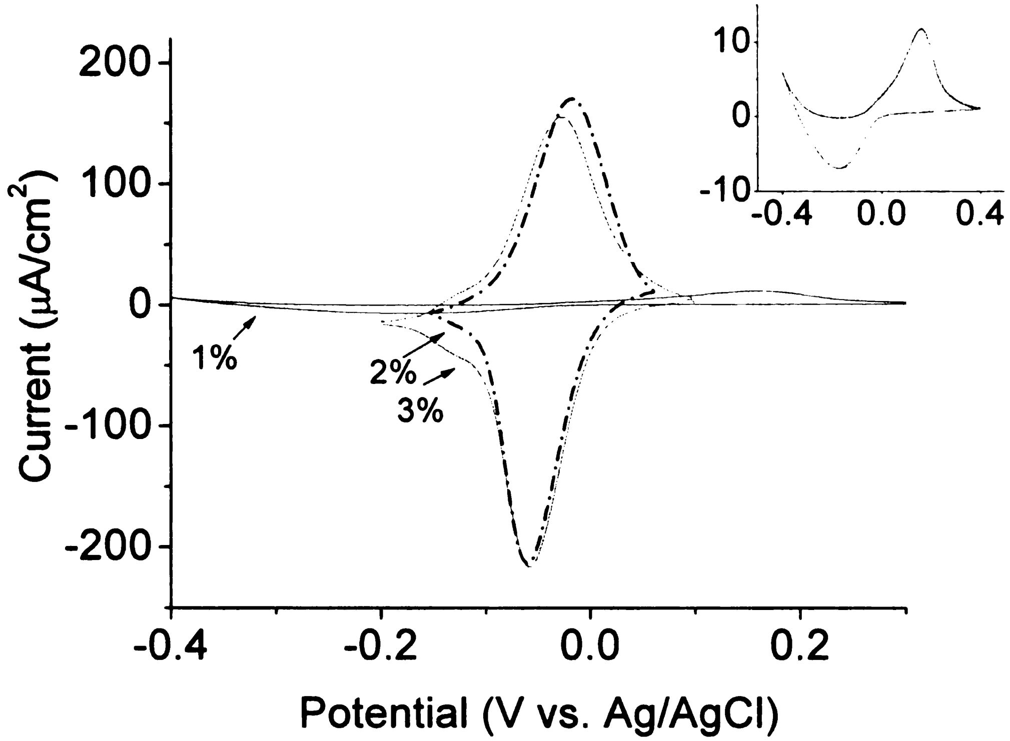

Figure 3.14. Cyclic voltammetric *i*–*E* curves for 10 μM 2,6-anthraquinone-disulfonate (2,6-AQDS) in 0.1 *M* $HClO_4$ at films deposited from 1, 2 and 3% CH_4. 2 ppm B_2H_6 was added to the source gas for boron doping. The balance of the source gas was 5% H_2 and 92–94% Ar. The growth time was 2 h for the 1 and 2% films, and 0.25 h for the 3% film. The potential scan rate was 100 mV/s. The voltammetric i–E curve for the 1% CH_4 film is presented as the inset. The positive-going current at −0.5 V is an artifact from the background correction.

The cyclic voltammetric *i*–*E* curves for the 2 and 3% films exhibit sharp oxidation and reduction peaks centered about −0.050 V. The peak currents and peak charge are similar in magnitude for these two films but are over 2 orders of magnitude greater than for the 1% film. Furthermore, ΔE_p is considerably less for the 2 and 3% films with values of 30–45 mV, compared with the 330 mV value seen for the 1% film. The smaller ΔE_p is indicative of more rapid electrode reaction kinetics at the films containing more sp^2-bonded carbon. While we did not perform detailed analysis of the curves, the peak shapes and current/charge magnitudes are consistent with the adsorption of AQDS on these two carbon surfaces. The peak currents and charge for this redox system at the 1% film are consistent with significantly less or no adsorption, as expected for good quality diamond.[85]

3.4 Conclusions

Phase-pure UNCD films were deposited on Si substrates by microwave-assisted chemical vapor deposition (CVD) using an Ar-rich source gas mixture. Adding B_2H_6, up to 50 ppm, to the source gas mixture for boron doping did not alter the film structure. The Raman, XRD, EELS, and NEXAFS data were all consistent with good quality UNCD at the film surface regardless of the B_2H_6 in the source gas. At a diborane source gas concentration of 50 ppm, there was an increase in signal for π-bonded carbon and a reduction in the absolute second band gap for diamond on the substrate side of film. The boron concentration in the films linearly tracked the diborane concentration in the source gas during growth, while electrical resistance varied inversely with the source gas concentration

Varying the CH_4 concentration in the source gas over a small range (0.5–3%) caused significant changes in the structure, hence the electrochemical properties of the resulting films. Phase-pure UNCD films, consisting of small particles with grain sizes of *ca.* 7–15 nm, were deposited only at the 1% CH_4 level. At 0.5% CH_4 , microcrystalline diamond films with grain sizes of *ca.*0.5 μm were formed. UNCD phases were inter dispersed amongst the faceted crystallites but the film was composed primarily of faceted crystallites. At 2% CH_4, a diamond-like carbon film was formed with UNCD phases interdispersed with graphite-like sp_2 carbon. The 3% CH_4 film was predominantly platelet nanocrystalline graphite. The electrochemical properties (voltammetric background current, potential window and AQDS adsorption) tracked the levels of sp^2-bonded carbon in the films. The results demonstrate that the morphology, microstructure, phase purity and electrochemical properties of the carbon films are strongly dependent on the CH_4 concentration over a relatively narrow range.

3.5 References

[1] J. E. Butler and A. V. Sumant, *Chemical Vapor Deposition* **14**:145 (2008).

[2] R. Arenal, O. Stephan, P. Bruno, and D. M. Gruen, *Applied Physics Letters* **94** (2009).

[3] S. Bhattacharyya, O. Auciello, J. Birrell, J. A. Carlisle, L. A. Curtiss, A. N. Goyette, D. M. Gruen, A. R. Krauss, J. Schlueter, A. Sumant, and P. Zapol, *Applied Physics Letters* **79**:1441 (2001).

[4] J. Birrell, J. A. Carlisle, O. Auciello, D. M. Gruen, and J. M. Gibson, *Applied Physics Letters* **81**:2235 (2002).

[5] J. Birrell, J. E. Gerbi, O. Auciello, J. M. Gibson, D. M. Gruen, and J. A. Carlisle, *Journal of Applied Physics* **93**:5606 (2003).

[6] D. M. Gruen, *MRS Bulletin* **23**:32 (1998).

[7] L. C. Qin, D. Zhou, A. R. Krauss, and D. M. Gruen, *Nanostructured Materials* **10**:649 (1998).

[8] J. Birrell, J. E. Gerbi, O. Auciello, and J. A. Carlisle, *Journal of Physics: Condensed Matter* **18**:S1771 (2006).

[9] J. A. N. Goncalves, G. M. Sandonato, and K. Iha, *Diamond and Related Materials* **11**:1578 (2002).

[10] M. Bernard, A. Deneuville, and P. Muret, *Diamond & Related Materials* **13**:282 (2004).

[11] S. Wang, V. M. Swope, J. E. Bulter, T. Feygelson, and G. M. Swain, *Diamond and Related Materials* **18**:669 (2009).

[12] T. Lin, G. Y. Yu, A. T. S. Wee, Z. X. Shen, and K. P. Loh, *Applied Physics Letters* **77**:2692 (2000).

[13] S. Jiao, A. Sumant, M. A. Kirk, D. M. Gruen, A. R. Krauss, and O. Auciello, *Journal of Applied Physics* **90**:118 (2001).

[14] T. D. Corrigan, D. M. Gruen, A. R. Krauss, P. Zapol, and R. P. H. Chang, *Diamond and Related Materials* **11**:43 (2002).

[15] A. F. Azevedo, S. C. Ramos, M. R. Baldan, and N. G. Ferreira, *Diamond and Related Materials* **17**:1137 (2008).

[16] O. A. Williams, M. Daenen, J. D'Haen, K. Haenen, J. Maes, V. V. Moshchalkov, M. Nesladek, and D. M. Gruen, *Diamond and Related Materials* **15**:654 (2006).

[17] D. Zhou, T. G. McCauley, L. C. Qin, A. R. Krauss, and D. M. Gruen, *Journal of Applied Physics* **83**:540 (1998).

[18] P. W. May and Y. A. Mankelevich, *Journal of Applied Physics* **100**:024301/1 (2006).

[19] P. W. May, M. N. R. Ashfold, and Y. A. Mankelevich, *Journal of Applied Physics* **101**:053115/1 (2007).

[20] P. W. May and Y. A. Mankelevich, *Journal of Applied Physics* **100**:024301 (2006).

[21] J. Birrell, J. E. Gerbi, O. Auciello, J. M. Gibson, J. Johnson, and J. A. Carlisle, *Diamond and Related Materials* **14**:86 (2005).

[22] O. A. Williams, M. Nesladek, M. Daenen, S. Michaelson, A. Hoffman, E. Osawa, K. Haenen, and R. B. Jackman, *Diamond & Related Materials* **17**:1080 (2008).

[23] R. Arenal, P. Bruno, D. J. Miller, M. Bleuel, J. Lal, and D. M. Gruen, *Physical Review B (Condensed Matter and Materials Physics)* **75**:195431 (2007).

[24] D. M. Gruen, *Annual Review of Materials Science* **29**:211 (1999).

[25] K. Okada, K. Kimoto, S. Komatsu, and S. Matsumoto, *Journal of Applied Physics* **93**:3120 (2003).

[26] J. Robertson, *Semiconductor Science and Technology* **18**:S12 (2003).

[27] S. Bhattacharyya, M. Lubbe, P. R. Bressler, D. R. T. Zahn, and F. Richter, *Diamond and Related Materials* **11**:8 (2002).

[28] L. Ponsonnet, C. Donnet, K. Varlot, J. M. Martin, A. Grill, and V. Patel, *Thin Solid Films* **319**:97 (1998).

[29] J. Bruley, D. B. Williams, J. J. Cuomo, and D. P. Pappas, *Journal of Microscopy-Oxford* **180** (1995).

[30] J. F. Morar, F. J. Himpsel, G. Hollinger, G. Hughes, and J. L. Jordan, *Physical Reveiw Letters* **54**:1960 (1985).

[31] J. C. Angus and C. C. Hayman, *Science (Washington, DC, United States)* **241**:913 (1988).

[32] A. Lafosse, A. Hoffman, M. Bertin, D. Teillet-Billy, and R. Azria, *Physical Review B* **73**:195308 (2006).

[33] W. Saslow, T. K. Bergstresser, and M. L. Cohen, *Physical Review Letters* **16**:354 (1966).

[34] D. S. Knight and W. B. White, *Journal of Materials Research* **4**:385 (1989).

[35] A. C. Ferrari and J. Robertson, *Physical Review B* **63** (2001).

[36] A. C. Ferrari and J. Robertson, *NATO Science Series, II: Mathematics, Physics and Chemistry* **24**:177 (2001).

[37] J. W. Ager, III, W. Walukiewicz, M. McCluskey, M. A. Plano, and M. I. Landstrass, *Applied Physics Letters* **66**:616 (1995).

[38] F. Pruvost, E. Bustarret, and A. Deneuville, *Diamond and Related Materials* **9**:295 (2000).

[39] R. G. Buckley, T. D. Moustakas, L. Ye, and J. Varon, *Diamond & Related Materials* **9** (1989).

[40] P. Gonon, E. Gheeraert, A. Deneuville, F. Fontaine, L. Abello, and G. Lucazeau, *Journal of Applied Physics* **78**:7059 (1995).

[41] R. Tubino, L. Piseri, and G. Zerbi, *Journal of Chemical Physics* **56** (1972).

[42] I. I. Vlasov, E. A. Ekimov, A. A. Basov, E. Goovaerts, and A. V. Zoteev, *Condensed Matter* (2008).

[43] K. Ushizawa, K. Watanabe, T. Ando, I. Sakaguchi, M. Nishitani-Gamo, Y. Sato, and H. Kanda, *Diamond and Related Materials* **7**:1719 (1998).

[44] A. Misra, P. K. Tyagi, B. S. Yadav, P. Rai, D. S. Misra, V. Pancholi, and I. D. Samajdar, *Applied Physics Letters* **89**:3 (2006).

[45] W. Fortunato, A. J. Chiquito, and J. C. Galzerani, *Journal of Material Science* **42** (2007).

[46] S. Osswald, V. N. Mochalin, M. Havel, G. Yushin, and Y. Gogotsi, *Physical Review B* **80**: (2009).

[47] J. W. Ager, III, D. K. Veirs, and G. M. Rosenblatt, *Phys. Rev. B Condens. Matter* **43**:6491 (1991).

[48] S. Prawer, K. W. Nugent, D. N. Jamieson, J. O. Orwa, L. A. Bursill, and J. L. Peng, *Chemical Physics Letters* **332**:93 (2000).

[49] M. C. Rossi, *Applied Physics Letters* **73**:1203 (1998).

[50] S. A. Stuart, S. Prawer, and P. S. Weiser, *Applied Physics Letters* **62**:1227 (1993).

[51] F. P. Bundy and J. S. Kasper, *Journal of Chemical Physics* **46** (1967).

[52] X. D. Zhu, Y. H. Xu, H. Naramoto, K. Karumi, A. Miyashita, and K. Miyashita, *Journal of Physics: Condensed Matter* **15** (2003).

[53] A. C. Ferrari and J. Robertson, *Philosophical Transactions of the Royal Society A: Mathematical, Physical and Engineering Sciences* **362**:2477 (2004).

[54] M. Yoshikawa, Y. Mori, H. Obata, M. Maegawa, G. Katagiri, H. Ishida, and A. Ishitani, *Applied Physics Letters* **67**:694 (1995).

[55] Y. Show, V. M. Swope, and G. M. Swain, *Diamond and Related Materials* **18**:1426 (2009).

[56] F. Brunet, A. Deneuville, P. Germi, M. Pernet, E. Gheeraert, and J. Mambou, *Diamond and Related Materials* **6**:774 (1997).

[57] F. Brunet, P. Germi, M. Pernet, A. Deneuville, E. Gheeraert, F. Laugier, M. Burdin, and G. Rolland, *Diamond and Related Materials* **7**:869 (1998).

[58] A. I. Shames, A. M. Panich, S. Porro, M. Rovere, S. Musso, A. Tagliaferro, M. V. Baidakova, V. Y. Osipov, A. Y. Vul, T. Enoki, M. Takahashi, E. Osawa, O. A. Williams, P. Bruno, and D. M. Gruen, *Diamond & Related Materials* **16** (2007).

[59] Y. Show, M. A. Witek, P. Sonthalia, and G. M. Swain, *Chemistry of Materials* **15**:879 (2003).

[60] Y. Show, M.-I. A. Witek, P. Sonthalia, and G. M. Swain, *Chemistry of Materials* **15**:879 (2003).

[61] D. Zhou, A. R. Krauss, L. C. Qin, T. G. McCauley, D. M. Gruen, T. D. Corrigan, R. P. H. Chang, and H. Gnaser, *Journal of Applied Physics* **82** (1997).

[62] J. Y. Huang, *Acta Materialia* **47**:1801 (1999).

[63] F. Tuinstra and J. L. Koenig, *Journal of Chemical Physics* **53**:1126 (1970).

[64] X. Wang, G. M. zhang, Y. L. Zhang, F. Y. Li, R. C. Yu, C. Q. Jin, and G. T. Zou, *Carbon* **41** (2003).

[65] L. G. Cancado, K. Takai, T. Enoki, M. Endo, Y. A. Kim, H. Mizusaki, A. Jorio, L. N. coelho, R. Paniago-Magalhaes, and M. A. Pimenta, *Applied Physics Letters* **88** (2006).

[66] Y. Wang, D. C. Alsmeyer, and R. L. McCreery, *Chemistry of Materials* **2**:557 (1990).

[67] W. A. Yarbrough and R. Messier, *Science (Washington, D. C., 1883-)* **247**:688 (1990).

[68] R. E. Shroder, R. J. Nemanich, and J. T. Glass, *Phys. Rev. B Condens. Matter* **41**:3738 (1990).

[69] J. Wagner, C. Wild, and P. Koidl, *Applied Physics Letters* **59**:779 (1991).

[70] M. Mermoux, L. Fayette, B. Marcus, N. Rosman, L. Abello, and G. Lucazeau, *Physical Status Solidi A* **154**:55 (1996).

[71] R. J. Nemanich, J. T. Glass, G. Lucovsky, and R. E. Shroder, *Journal of Vacuum Science & Technology, A: Vacuum, Surfaces, and Films* **6**:1783 (1988).

[72] K. W. R. Gilkes, H. S. Sands, D. N. Batchelder, J. Robertson, and W. I. Milne, *Applied Physics Letters* **70**:1980 (1997).

[73] Y. Wang, D. C. Alsmeyer, and R. L. Mccreery, *Chemistry of Materials* **2**:557 (1990).

[74] J. R. Dennison, M. Holtz, and G. Swain, *Spectroscopy (Eugene, Oregon)* **11**:38 (1996).

[75] J. A. Bennett, J. Wang, Y. Show, and G. M. Swain, *Journal of the Electrochemical Society* **151**:E306 (2004).

[76] D. Zhou, D. M. Gruen, L. C. Qin, T. G. McCauley, and A. R. Krauss, *Journal of Applied Physics* **84**:1981 (1998).

[77] M. C. Granger, J. Xu, J. W. Strojek, and G. M. Swain, *Analytica Chimica Acta* **397**:145 (1999).

[78] Q. Chen, D. M. Gruen, A. R. Krauss, T. D. Corrigan, M. Witek, and G. M. Swain, *Journal of the Electrochemical Society* **148**:E44 (2001).

[79] A. E. Fischer, Y. Show, and G. M. Swain, *Analytical Chemistry* **76**:2553 (2004).

[80] D. T. Fagan, I. F. Hu, and T. Kuwana, *Analytical Chemistry* **57**:2759 (1985).

[81] I. F. Hu, D. H. Karweik, and T. Kuwana, *Journal of Electroanalytical Chemistry and Interfacial Electrochemistry* **188**:59 (1985).

[82] K. R. Kneten and R. L. McCreery, *Analytical Chemistry* **64**:2518 (1992).

[83] P. Chen, M. A. Fryling, and R. L. McCreery, *Analytical Chemistry* **67**:3115 (1995).

[84] P. Chen and R. L. McCreery, *Analytical Chemistry* **68**:3958 (1996).

[85] J. Xu, Q. Chen, and G. M. Swain, *Analytical Chemistry* **70**:3146 (1998).

[86] M. T. McDermott, K. Kneten, and R. L. McCreery, *Journal of Physical Chemistry* **96**:3124 (1992).

Chapter 4

Microscopic Interpretation of Bare, Boron-doped Diamond Coated, and Pt-decorated Carbon Powders

Abstract

In this chapter, the core-shell coating methodology used to surface modify various carbon powders with boron-doped diamond is discussed, and the characterization of Pt-decorated diamond powders with microscopy and XPS is described. Sample morphology was evaluated with optical microscopy, scanning transmission microscopy, and transmission electron microscopy. The microstructure of the bulk sample was probed with Raman spectroscopy, XPS, and XRD. Localized elemental and microstructural analysis of the image area was performed with EDS, EELS, and energy filtered TEM. Samples examined include boron-doped ultrananocrystalline diamond (B-UNCD) on glassy carbon and Ketjen black powders, B-UNCD overgrown onto 500, 100, and 3-6 nm diamond powder, and Pt-decorated 100 nm diamond powder.

4.1 Introduction

This chapter presents electron microscopy results for BDD-coated powders and Pt-decorated diamond powder. The samples studied were: diamond powder (8 μm, 500 nm, 100 nm, 3-5 nm), glassy carbon powder, and

Ketjen black powder. Given the variability in sample temperature of the powder in our reactor (no independent substrate heating), and that the powder surface microstructure and chemistries are distinctly different, multiple carbon allotropes can be deposited during the coating process. Often the overcoatings are primarily B-UNCD with non-diamond sp^2 carbon phases interspersed. There is much literature containing microscopy of carbon including diamond, glassy carbon, carbon black, graphite, graphene, carbon nanotubes and diamond-like carbon (DLC). This work differs in that we have gained new insight into diamond formation on carbon powders, the nature of the Pt-diamond interaction, and observed formation of novel sp^3 bonded carbons.

Carbonaceous materials are commonly characterized by Raman spectroscopy, XRD, atomic force microscopy (AFM), and optical and electron microscopy. A major challenge to the characterization of boron-doped diamond grown on a carbon substrate is recognizing the deposited carbon from the pre-existing substrate. Since the majority of powders range from 3-150 nm, a technique providing spatial resolution <100 nm is needed. Raman spectroscopy and XRD have spatial resolutions of *ca.* 1 μm and are excellent bulk sample measurements. Only AFM and electron microscopy have a spatial resolution (<100 nm) necessary for the nano powders currently under study. AFM needs a relatively uniform (*e.g.* planar) surface, making powder sample preparation for AFM difficult. Electron microscopy has a theoretical resolution of 0.1 nm, and in the transmission electron microscope both the carbon morphology and microstructure can be determined, making electron microscopy the better method for this work.

As with most techniques, electron microscopy of carbon is not without challenges. Carbon can be difficult to image by electron microscopy due to its relatively low atomic mass, which leads to lower contrast and resolution.[1] Also, carbon sources from other than the sample may be present inside the microscope, such as from the hydrocarbon vacuum pump oil. This carbon impurity can affect the images, especially higher magnifications (*i.e.*, high e-beam power densities). Additionally, interpretation of micrographs can often be subjective. A common childhood game is to look at clouds and pick out everyday objects; trees, shrubs, and animals may all be imagined. The prudent microscopist must likewise be constantly vigilant against researcher bias. Instrumental conditions including sample preparation, magnification, depth-of-field, and aberrations can all lead to misinterpretation. To this extent, every attempt was made to minimize error in the interpretation of the micrographs contained herein. First, a large sample volume was used. This work is representative of nearly 150 samples, consisting of over 2,000 micrographs collected over four years. Secondly, the bulk sample characteristics were first examined with Raman spectroscopy to determine microstructure, and XRD to determine crystallinity. Thirdly, whenever possible, interpretation of the image area was confirmed with electron energy loss spectroscopy (EELS), selected area electron diffraction (SAD) and/or electron dispersive spectroscopy (EDS or EDAX). To further simplify interpretation, diamond substrates coated with B-

UNCD were primarily evaluated for their sp^2 composition after coating since significant amounts of sp^2 are not present beforehand. Likewise, carbon blacks coated with B-UNCD were primarily evaluated for the nucleation and growth of diamond and sp^3 content. Since carbon blacks have very little crystallinity before coating, the cubic structure of the deposited B-UNCD is easier to recognize on carbon black than B-UNCD grown onto an already existing diamond substrate. XPS analysis was conducted on the platinized powder in order to determine if there is strong metal-support interaction (SMSI) between the Pt and diamond.

4.2 Results

4.2.1 BDD coated Diamond Powders

The diamond powders were evaluated step-wise starting with the larger 8-12 µm diameter particles and progressing down to 3-6 nm powders. For the 8-12 µm powders only, microcrystalline BDD deposition conditions using a hydrogen-rich plasma were used. Studies for that powder size and BDD coating technique were previously reported.[2] For convenience, a micrograph of the as-received 8-12 µm diamond powder is shown in Figure 4.1. 500 and 100 nm diamond powders, as-received, are shown in Figures 4.2A, and 4.3A respectively. Other than size, both are morphologically similar, having an irregular shape with jagged features and several small secondary nucleation sites. The irregular shape and defects make it more difficult to recognize the BDD coating from the original substrate until the BDD layer is thick enough to smooth the jagged edges. After BDD deposition several large smooth cauliflower[3] like features are observed, as in Figure 4.1B and D. The cauliflower diamond is composed of individual ultrananocrystalline diamond crystals of 10-50 nm clumped together. Because the powder sample is static in the current reactor design, there is a high nucleation and growth rate at the surface. After approx. 1 h, B-UNCD overgrowth occurs on adjacent particles and a quasi B-UNCD film begins to form. This decreases surface area and blocks mass transport of the source gas through the interstitial spaces to powders at a lower depth. Engineering changes to the reactor design that would "stir" the particles in-situ and overcome this problem are being considered. At the edges of the sample, microcrystalline diamond is also observed. This may be due to a higher atomic hydrogen concentration near the edge of the plasma.[4] Crystallite size and surface roughness (*i.e.,* grain coarsening) are increased compared to those areas in the middle of the sample, as expected when the rate of crystal growth exceeds the rate of renucleation. Since 100 nm diamond powder was evaluated for both BDD overcoating and Pt-decoration, a more detailed characterization of this powder is provided. As mentioned, the 100 nm diamond powder is similar in morphology to the 500 nm except for size (Figure 4.3A). The jagged edges observed in the SEM are step layers. Each successive layer forms slightly behind the edge of the layer below homoepitaxially (Figure 4.3B-C). The powder appears to be mostly devoid of large areas of non-diamond

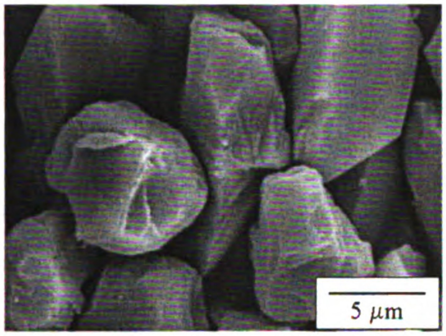

Figure 4.1. SEM image of 8-12 μm diamond powder as-received

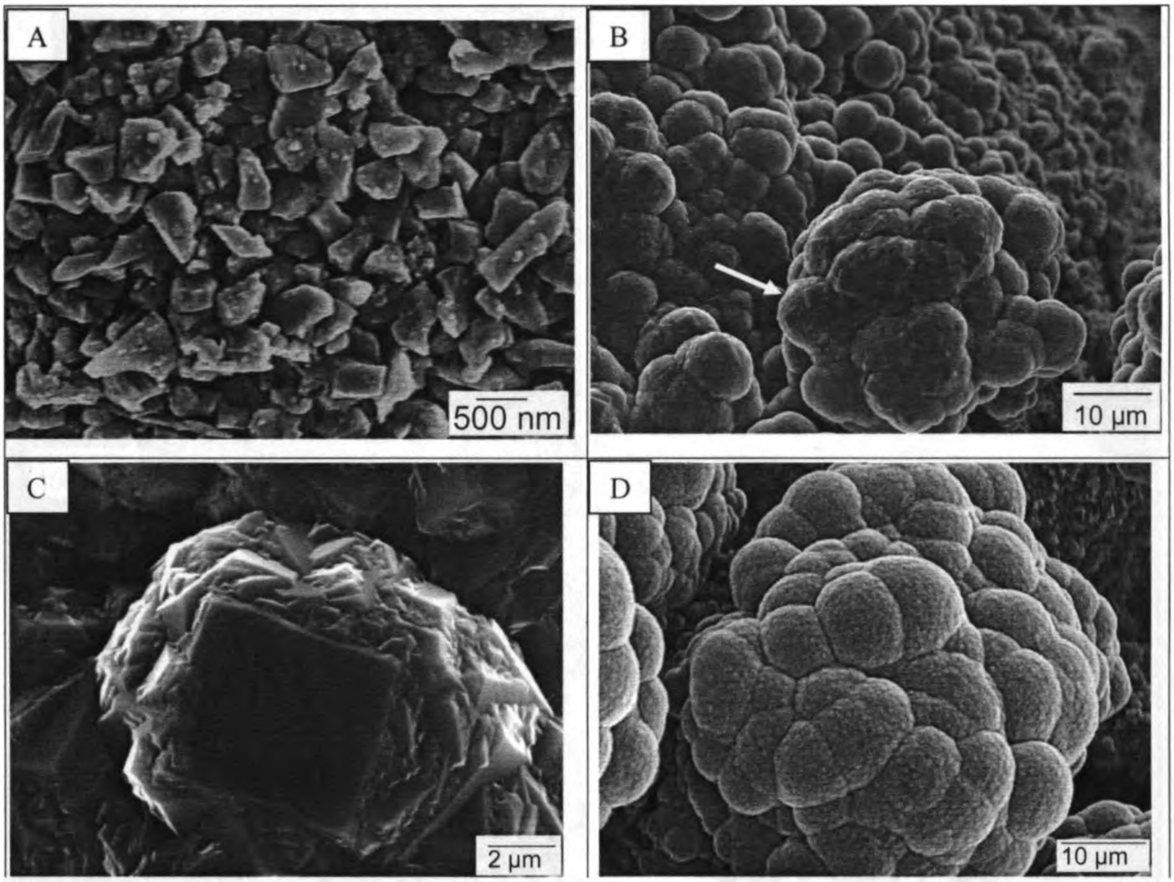

Figure 4.2. SEM images of 500 nm diam. diamond powder, (A) as-received, (B) coated with B-UNCD (the arrow denotes a region of microcrystalline growth), (C) close up of the microcrystalline diamond face, and (D) cauliflower or bolus B-UNCD diamond growth.

carbon, the crystal structure having long range order (Figure 4.3C). This agrees with the Raman and XRD spectra (not shown) for the powder, which is typical for phase-pure diamond (*i.e.*, no peaks for graphite). The lattice terminates with approx. 4-5 atomic layers (*ca.* 7 Å) of non-diamond at the edge, presumably of sp^2 carbon atoms (Figure 4.3D). The EELS signature is very similar to single crystal diamond (Figure 4.3E). In TEM of diamond, lattice lines from diffraction at the (111) planes are the most recognizable. Note the inter-planar distance for diamond (111) is at least 0.7 nm greater than the other diffracting planes so that

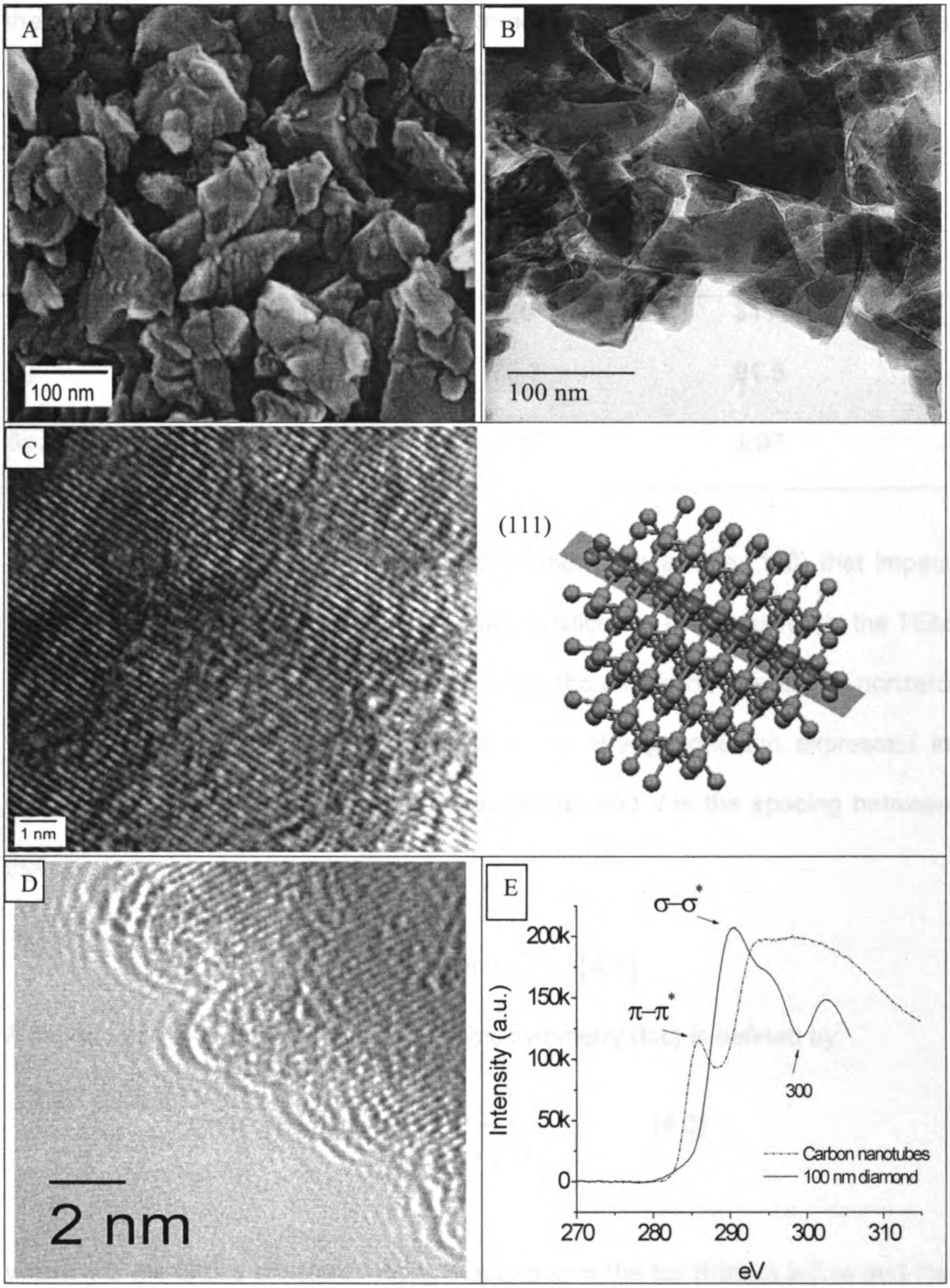

Figure 4.3. Morphology and microstructure of 100 nm diamond powder as-received. (A) SEM. (B) Low magnification TEM. (C) HRTEM and schematic showing the (111) lattice. (D) Edge site. (E) EELS of diamond powder overlaid with carbon nanotubes for comparison (intensities adjusted for comparison).

the (111) planes are generally better resolved by bright-field TEM than reflections arising from the (220) or (311) planes. XRD powder diffraction values are shown in Table 4.1.

Table 4.1. XRD diffraction of diamond.

hkl	**111**	**220**	**311**
2θ	43.9	75.3	91.5
Spacing (Å)	2.06	1.26	1.07

Diffraction from some planes of diamond, such as the (100) that impact surface bonding and electrochemical characteristics are not observed in the TEM or XRD. Lattice lines are only observed when the diffraction intensity is nonzero for a given Miller indices (*hkl)*, subject to the Bragg condition expressed in equation 4.1, where λ is the incident wavelength and d is the spacing between the planes in the atomic lattice.[5]

$$\lambda = 2d_{hkl}\sin\theta \qquad [4.1]$$

A diamond crystal with face centered cubic symmetry (fcc) is defined by:

$$d_{hkl} = \frac{a}{\left(h^2 + k^2 + l^2\right)^{1/2}} \qquad [4.2]$$

where a is the lattice constant, noting that $a=b=c$ in the fcc Bravais lattice and the constant is the distance between unit cells in a crystal lattice. The intensity of the diffracted beam is dependent upon the crystal structure factor. The structure factor describes the way in which an incident beam is scattered by the atoms of a crystal unit cell and is given by equation 4.3, where S is the structure factor, I is the intensity of the diffracted beam, and f is the atomic form factor or scattering amplitude of an atom.[5]

$$S_{hkl} = f\,e^{i(0)} = f \rightarrow I_{hkl} \propto \left|S_{hkl}\right|^2 = f^2 \qquad [4.3]$$

The structure factor for the fcc crystal is determined by equation 4.4

$$\begin{aligned} S_{hkl} &= \sum_i f_i e^{\,2\pi i(hx_i + ky_i + lz_i)} \qquad [4.4] \\ &= f\left\{1 + e^{\pi i(h+k)} + e^{\pi i(h+l)} + e^{\pi i(k+l)}\right\} \end{aligned}$$

with the result

$$S_{hkl} = \begin{cases} 4f, & h,k,l \quad \text{all even or all odd} \\ 0, & h,k,l \quad \text{mixed parity} \end{cases}$$

For example, the classically smooth (100) face of diamond, observable in the SEM of Figure 4.2C, has no diffraction intensity in TEM or XRD since reflections from a crystal with face centered cubic symmetry are forbidden when *hkl* is of mixed parity as with diamond (100).

To investigate the nucleation of B-UNCD onto the 100 nm diamond powder, a thin layer of powder was placed on a silicon wafer so that a high percentage was exposed to the source gas and plasma. The growth time was reduced to 20 minutes so that only a thin B-UNCD layer had time to form. Figure

4.4A-C are TEM micrographs of the B-UNCD-coated diamond powder after growth for only 20 min. Figure 4.4 is a lower magnification TEM image; an arrow indicates the powder of interest. The shape of the powder appears to have changed from the as-received particles, as it is now hexagonal (see Figure 4.3 for as-received powder images). Other diamond powders in the image, which appear to be similar to the as-received powder, may be used for comparison. They are probably from other areas on the substrate where no growth occurred and became mixed during casting onto the TEM grid.

Figure 4.4B is a higher magnification image of the B-UNCD-diamond powder. The circled region is the area investigated with HRTEM. There are also carbon nano fibers present in Figure 4.4B.[6] It appears the nano fibers may be connected to one side of the B-UNCD powder. The nano fibers are significant because they indicate these particles (both the nano fibers and B-UNCD powder) underwent carbon deposition. In other words, these particles were at the surface or near the plasma and experienced conditions conducive to carbon deposition, as compared to some buried particles where growth does not always occur. Figure 4.4C is an HRTEM of the circled region in Figure 4.4B. There are three areas of differing carbon microstructure in the image: diamond, amorphous carbon, and more ordered carbon planes. In the upper right hand corner of the image homoepitaxial diamond (111), very similar to the as-received diamond (Figure 4.3C), is observed. It is believed this is a nucleation site for carbon growth onto the original powder. Connected to this are regions of amorphous carbon and ultrananocrystalline diamond. Features like these were not observed

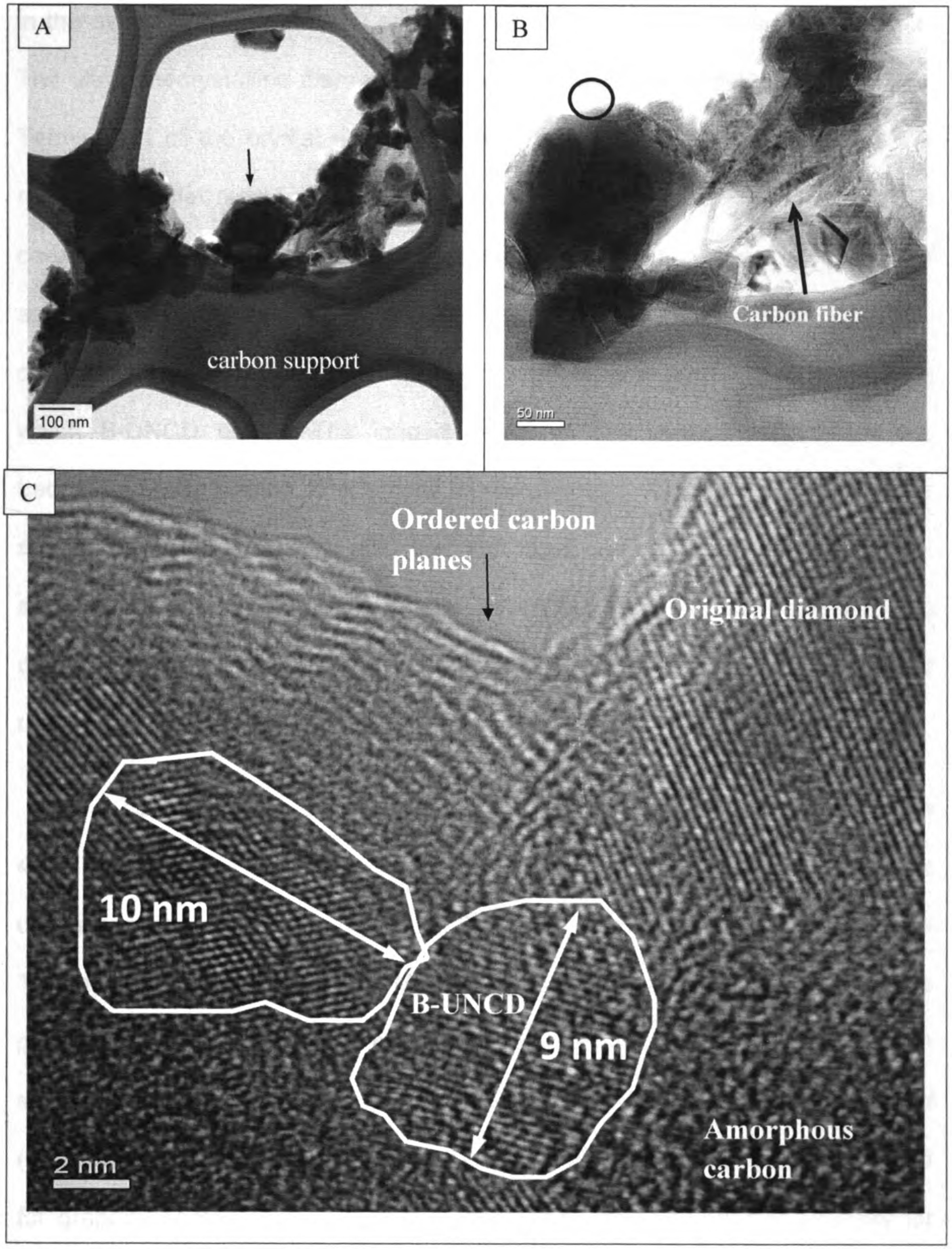

Figure 4.4. TEM images of B-UNCD coated 100 nm diam. diamond powder. (A) Overview , the arrow indicates the point of interest. (B) Closer view of 100 nm B-UNCD powder and carbon fiber. (C) HRTEM of region circled in image (B) of B-UNCD grains.

in the as-received powder and appear to be from the B-UNCD coating process. The ultrananocrystalline diamond grains are consistent in size with B-UNCD.[7-10] Termination of the crystal with non-diamond carbon was observed in the as-received powder (see Figure 4.3E), but here the 3-4 nm region of non-diamond carbon terminating the crystal is larger than 0.7 nm for the as-received powder. It appears from examining all the features in Figure 4.4A-C that carbon deposition occurs equally on all sides of the powder; there is no single nucleation site from which B-UNCD grows. The jagged edges of the as-received powder are becoming filled, leading to a smoother morphology. Because of the irregular surface, the growth conditions are not ideal and a mixture of B-UNCD, amorphous, and graphitic carbon are deposited. Rotating the powder in-situ during growth should expose the surface to more ideal growth conditions and reduce this non-diamond carbon.

A TEM image for 3-6 nm diamond powder as-received is shown in Figure 4.5A. This diamond powder was used sparingly for interrogation by TEM as it is difficult to distinguish it from deposited B-UNCD, since both have grain sizes of 5-10 nm. Figure 4.5B is an HRTEM showing the diamond core surrounded by a graphitic shell. The graphitic shell gives rise to the distinct features in the Raman spectrum in Figure 4.5C. The single phonon for nanocrystalline diamond (normally at 1326 cm^{-1}) is not resolved because it is hidden by the broad D-band for graphite centered at 1340 cm^{-1}.[11] Since the Raman scattering intensity for graphite is 50 times greater than for diamond, scattering from the graphitic shell masks the spectral response for diamond.[12, 13] The G-band for graphite is

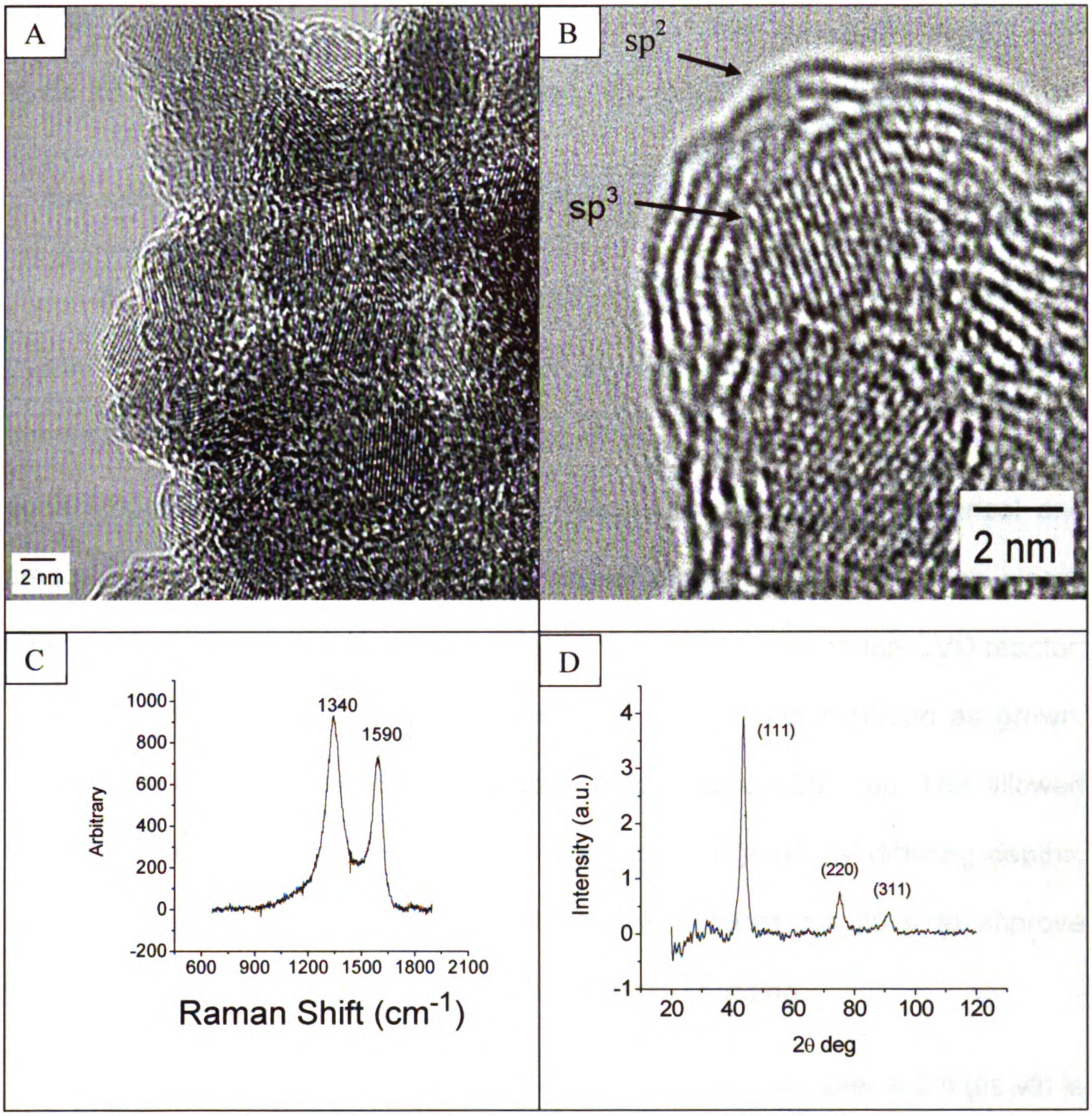

Figure 4.5. TEM images and spectroscopy of 3-6 nm diamond powder. (A) TEM image of as-received powder. (B) HRTEM demonstrating the cubic diamond core surrounded by a graphitic skin. (C) Raman spectrum of 3-6 diamond powder. (D) XRD spectrum of 3-6 nm diamond powder.

centered at 1590 cm^{-1}. The XRD for the 3-6 nm as-received powder is shown in Figure 4.5D. In contrast to the Raman spectrum, the XRD features arise from the diamond inner core with the expected peaks for diamond from the (111), (220), and (311) planes (see Table 4.1 for assignments). There is a small rise in signal at *ca.* 27 degrees that may be attributable to the (002) plane of graphite.

4.2.2 B-UNCD Coated Carbon Black

Scanning electron micrographs (SEM) of as-received and B-UNCD-GC powders are presented in Figure 4.6A-E. The as-received powder has a spherical shape and a nominal diameter of 4 μm. The surface morphology is quite smooth with little or no porosity. Since the particles are spherical and smooth, it is easy to distinguish the rougher diamond overlayer. The glassy carbon powder was placed on a Si wafer for B-UNCD growth in the CVD reactor. The entire wafer was then removed from the reactor and mounted as grown, without removing or disturbing the powder, onto a large SEM stub. This allowed for more accurate ex-situ evaluation for the B-UNCD growth at differing depths. The sample was then osmium (*ca.* 3 nm dia.) coated for 25 s to improve conductivity with the SEM stub and reduce sample charging.

The surface morphology of the B-UNCD-GC particles after a 2-h growth is rougher than that of the as-received powder, and is composed of nodular collections of diamond grains. The nodules are 50-100 nm in dimension. This surface morphology is characteristic of UNCD.[14-19] The images reveal that most of the GC powder surfaces at the top-side are well coated with UNCD. Figure 4.6B demonstrates the ideal result of this core-shell technique. There is a thin B-UNCD layer that has formed over the as-received GC powder. This provides the

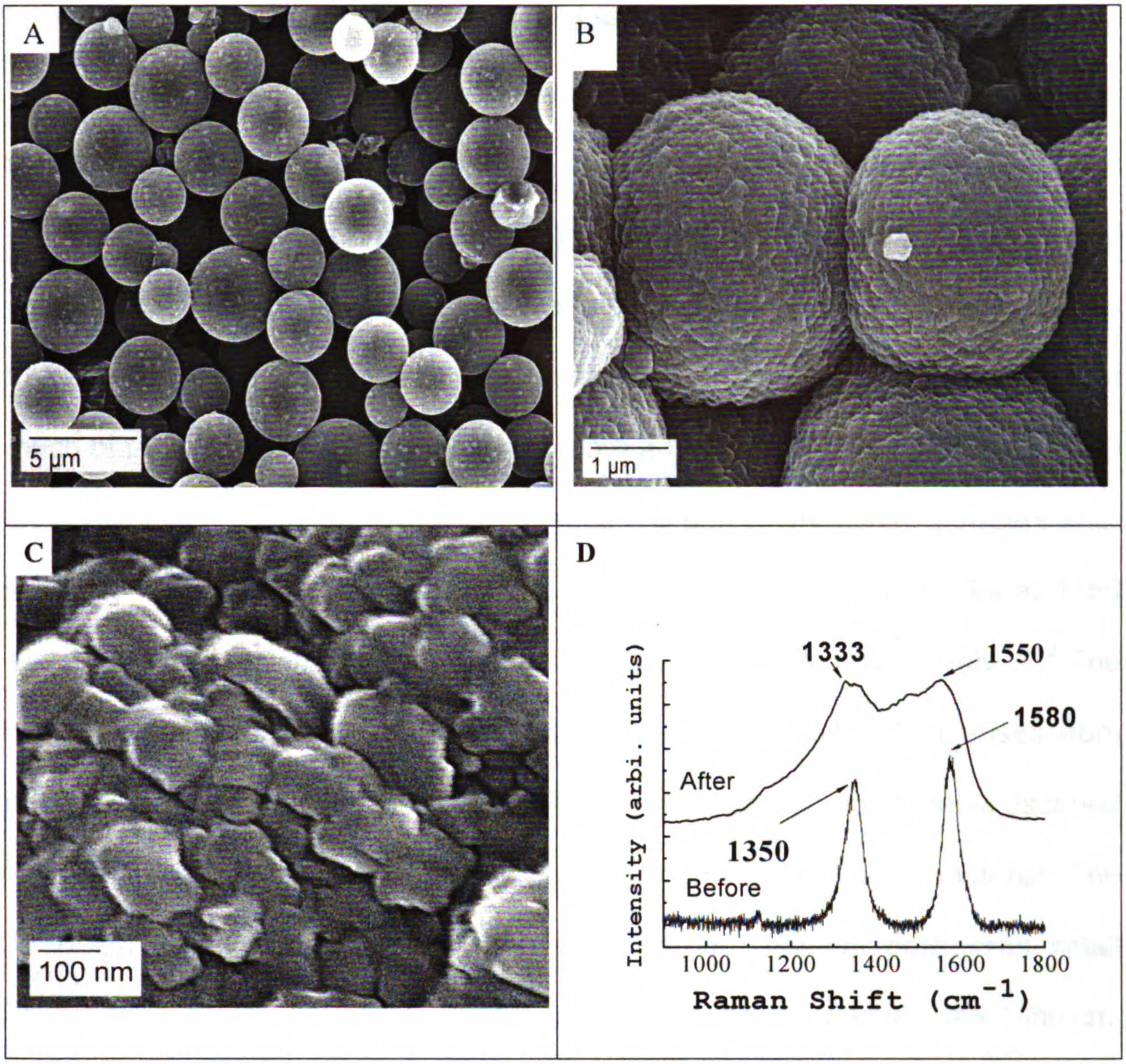

Figure 4.6. (A) Glassy carbon powder as-received. (B) Ideal example of the core-shell method, the B-UNCD coated GC powders still retain their original shape and surface area. (C) Close up of B-UNCD grains. (D) Raman spectroscopy of GC before and after B-UNCD coating.

desirable characteristics of the B-UNCD coating while retaining individual particle morphology and surface area. The higher magnification image (Fig. 4.6C) reveals that the nodular features of the UNCD actually consist of small faceted crystallites that are 50 nm, or so, in size. The B-UNCD grains are small enough to efficiently coat the entire sample without defects. A key reason for depositing the diamond from an Ar-rich rather than a more traditional H_2-rich source gas mixture is the reduced rate of carbon gasification in the Ar-rich environment. Coating sp^2-bonded carbon materials with diamond using traditional H_2-rich gas mixtures is complicated by the high rate of gasification that occurs in the presence of atomic hydrogen. Coating the glassy carbon powder with diamond grown from a traditional CH_4/H_2 gas mixture would certainly be challenging due to a significant mass loss via carbon gasification to CH_4 and C_2H_2. It is likely that much of the powder would be gasified before any deposition occurs. Figure 4.6D shows typical Raman spectra of the as-received and B-UNCD-GC powders after a 2-h deposition. The spectrum for the as-received powder has peaks at 1350 and 1580 cm^{-1}, which are the well-known D- and G-bands, respectively.[14-19] The broad peak at 1350 cm^{-1} represents a zone-edge A_{1g} mode that arises from disorder size and the peak centered at 1550 cm^{-1} is an E_{2g} mode that is ascribed to the in-plane lattice phonon of the graphitic domains within the material. The 1350 cm^{-1} mode becomes active when a carbon material possesses small crystallites or a high fraction of crystalline boundary. In other words, the 1350 cm^{-1} band tracks the fraction of edge plane or the degree of microstructural disorder. According to Tuinstra and Koenig, the D- and G-band intensity ratio (I_D/I_G) is inversely proportional to the effective crystallite size, L_a, in the direction of the graphite plane.[20-23] The ratio of 0.87 in the present spectrum is consistent with an L_a (*e.g.*, crystallite size) of 5.5 nm. This is reasonably consistent with the 2.9 nm value determined from x-ray diffraction linewidth analysis. The Raman spectrum for B-UNCD-GC was taken of the top surface of the sample. Although SEM images routinely revealed that most of the GC powder particles in a sample are fully covered by B-UNCD, incompletely coated particles were sometimes found. An example is shown in Figure 4.7A-B. The incomplete coverage is likely due to inhibited transport of reactive species to the surface, which slows the growth rate. Particles like these are somewhat buried in the powder sample. The images are useful because they provide an idea of the UNCD coating thickness, which appears to range from 100-500 nm. Closer inspection of the single particle

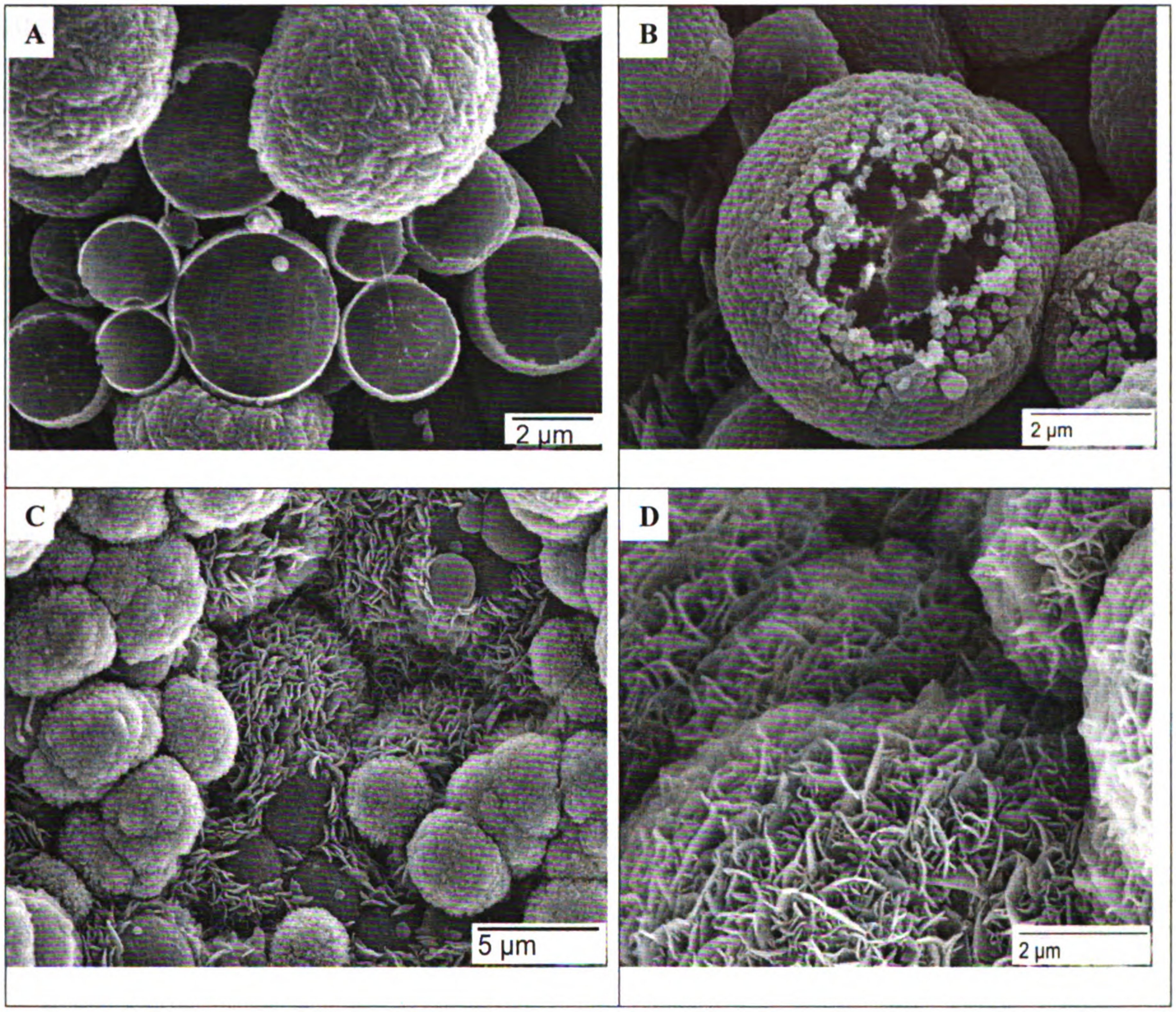

Figure 4.7. (A,B) SEM images of some partially coated B-UNCD-GC powders. (C) A mixed phase region of the sample with B-UNCD cauliflower type formation at the top, and thinly coated B-UNCD coated particles surrounded by graphite platelets at the bottom. (D) A close up of the graphite platelets.

shown in Figure 4.7B reveals some interesting surface morphological features. Ridge-like structures are seen on the underlying GC powder surface and it is on these ridges that the diamond nuclei appear to form. These ridge-like features are identical to those previously reported for GC plates treated in a hydrogen plasma (so-called hydrogenated glassy carbon).[23] In that work, a mechanism was proposed whereby atomic hydrogen chemisorbs at the graphitic edge plane sites progressively converting the aromatic C-C bonding to alicyclic hydrocarbons (*e.g.*, cyclohexane) followed by final ring opening hydrogen addition reactions to produce aliphatic moieties.[24-26] The hydrogenation reactions, prior to any gasification, convert the surface carbon atoms into a diamond-like structure. It is on this surface that diamond readily nucleates and grows. Mehandru et al. [25] and Lambrecht et al. [27] reported theoretical work showing the structure and energetics of the sequential addition of hydrogen atoms to the extended edge of a graphene sheet. The progressive hydrogenation transforms the aromatic rings to their saturated analogues. Their results showed that hydrogen atoms can chemisorb to a graphite sheet far from the edge causing distortion to a tetrahedral structure for the carbon atoms to which they are bound.

There were also regions in a sample where nanocrystalline graphite platelets were observed. SEM images showing this microstructure are presented in Figure 4.7C-D. Raman spectra were used to confirm that the platelet microstructure is indeed nanocrystalline graphite with a high fraction of exposed crystallite edges. A representative spectrum is presented in Figure 4.8, which shows a broad peak at 1360 cm^{-1} (D-band) that is associated with the high fraction of exposed crystallite boundaries and the 1580 cm^{-1} peak (G-band) assigned to the first-order phonon mode for graphite.[28] There is also a small peak at 1625 cm^{-1}, which is tentatively assigned to reduced symmetry of the nanocrystalline graphite impurity due to boron insertion during its formation.[20-23, 29] The platelets appear to be oriented predominantly with their graphene sheets normal to the GC powder surface. In other words, there is a high fraction of crystallite boundary or edge exposed. The platelets are on the order of 100-200 nm thick and 600-1000 nm wide. The I_D/I_G intensity ratio is 0.68. According to work by Tunistra and Koenig, this ratio corresponds to a crystallite size, L_a, of *ca.* 7 nm .[21] Based on this result, the platelets appear to consist of smaller, randomly-ordered graphitic crystallites. Morphologically and microstructurally similar diamond/carbon nanoflakes have been formed on silica spheres using variable gas phase CVD growth chemistries .[23]

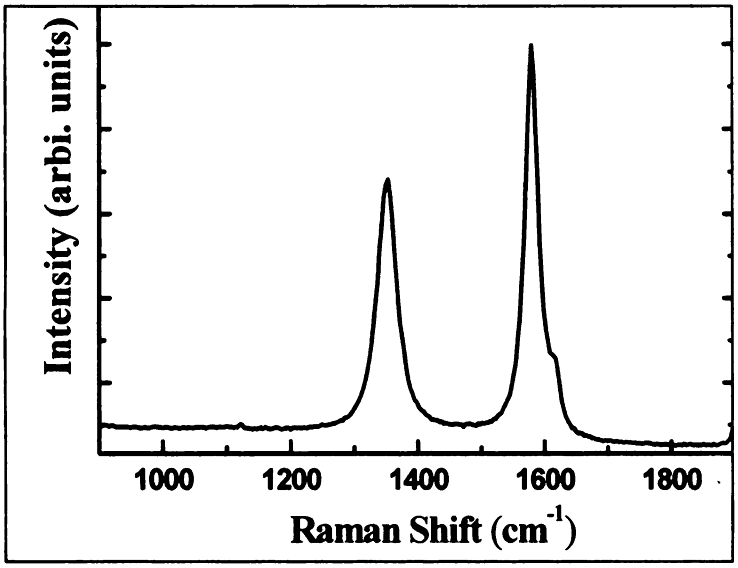

Figure 4.8. Raman spectrum of graphite

Ketjen black is a porous sp^2-bonded carbon black with a high specific surface area of 835 m^2/g. A TEM image of the as-received powder is shown in Figure 4.9A. Ketjen black appears to conform to the concentric crystallite model, with an outer layer of crystallites surrounding a center of more disorganized carbon with few layer planes.[30] The Raman spectrum and XRD pattern (not shown) were typical of carbon black. Compared to diamond and glassy carbon powders, the B-UNCD growth rate on Ketjen black is slower, needing approximately double the growth time before B-UNCD is confirmed with Raman spectroscopy or XRD. After diamond growth begins, the powder diameter decreases from approx. 40 to 10 nm. The arrow in Figure 4.9B indicates a

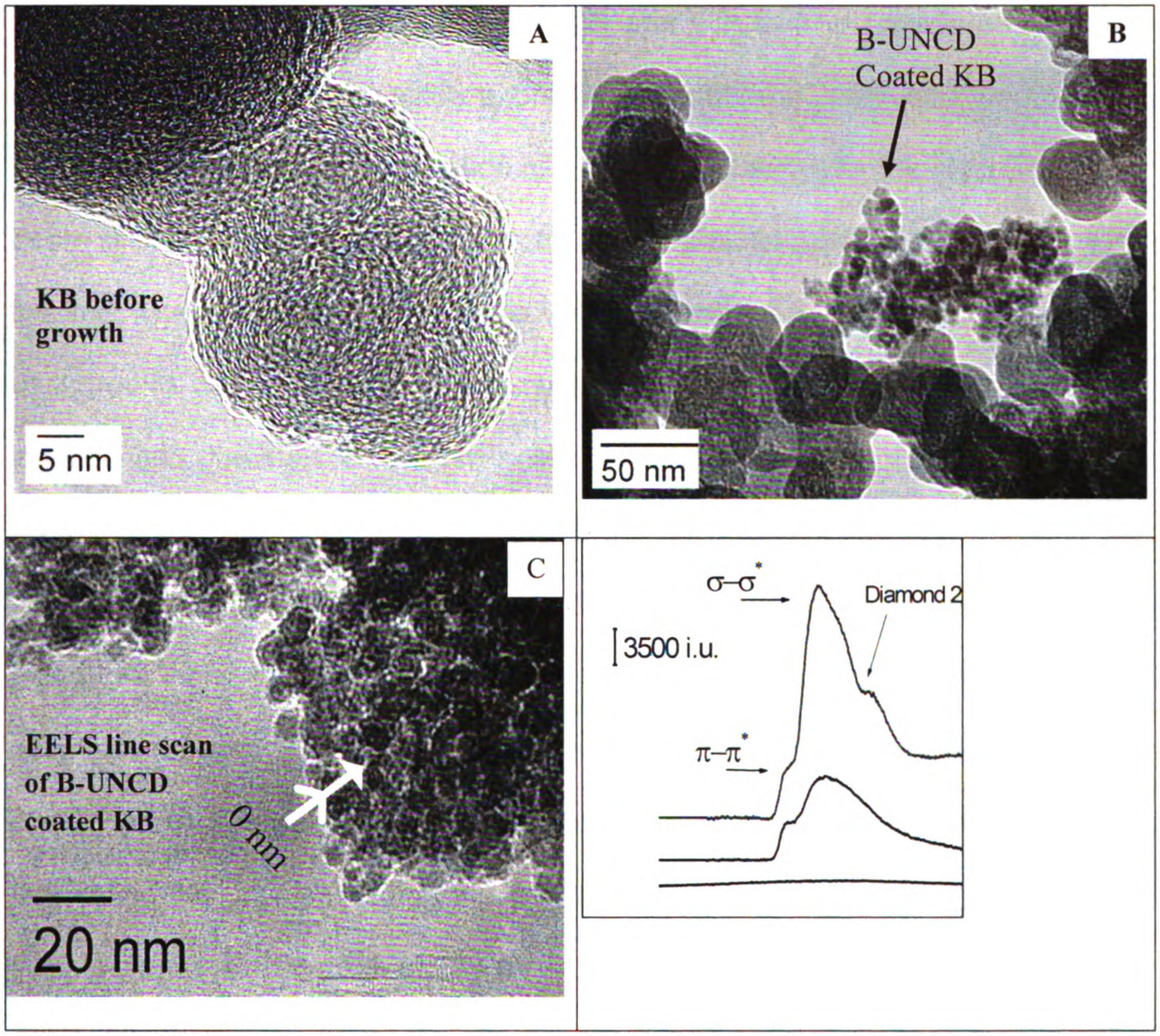

Figure 4.9. TEM images of (A) Ketjen black (KB) powder as-received, and (B) B-UNCD coated KB particles indicated by arrow. (C) Scanning transmission electron micrograph of the sample area used for the EELS line scan at right. The electron beam spot size was 0.7 nm.

congregation of B-UNCD coated Ketjen black powders after B-UNCD deposition; their size is notably different than the surrounding Ketjen black powders which were likely lower in the sample and did not undergo B-UNCD growth.

Figure 4.9C is a separate microstructure identified using scanning transmission electron microscopy (STEM) and EELS. The advantage of STEM over traditional TEM is the ability to precisely place the e-beam on a fixed point of the sample since the beam position can be manipulated with the scan coils. The beam spot size was 0.7 nm and spectra were collected approx. every 2 nm along the line. The scan was started in the void as a control measure to check for any background carbon signal. The arrows in Figure 4.9C are of the EELS scan location and direction, with 0 nm being the start of the scan in the void. Three representative traces from the resulting EELS spectra acquired at 0, 7 and 22 nm are shown in Figure 4.9D. At 0 nm (in the void), there is no appreciable carbon signal. At 7 nm, the spectrum is typical of carbon black as expected for the KB substrate powder. The spectrum obtained at 22 nm is the most interesting, as it displays EELS features of a mixed phase diamond and sp^2 microstructure, confirming the conclusion that the crystal structure observed in Figures 4.9 and 4.10 is diamond. The peak at 285 eV is associated with a $\pi \rightarrow \pi^*$ transitions. The rise for the sp^3 carbon σ-σ^* transition peak at 290 eV is sharper and the peak at 290 eV is narrower (*i.e.* more diamondlike) compared to the spectrum acquired at 7 nm (also refer to Figure 4.3). The most conclusive feature of the EELS spectrum at 22 nm being is the dip corresponding to the absolute second band gap for diamond, which is observed at 300 eV.[31]

TEM images of B-UNCD on KB are shown in Figures 4.10A-B. The Ketjen black powder still retains its original oval shape. Diamond grains are visible at the center nucleating on the original sp^2 core. The outer shell of the powder has been etched away, reducing the size from 30 to 15 nm in diameter. Figure 4.10B is an HRTEM of the B-UNCD grains. There are two grains identifiable in the image with their (111) indices offset by 57°. The grain boundary width in UNCD can be used as an indicator of diamond quality, as the grain boundary increases with the incorporation of non-diamond carbon and nitrogen.

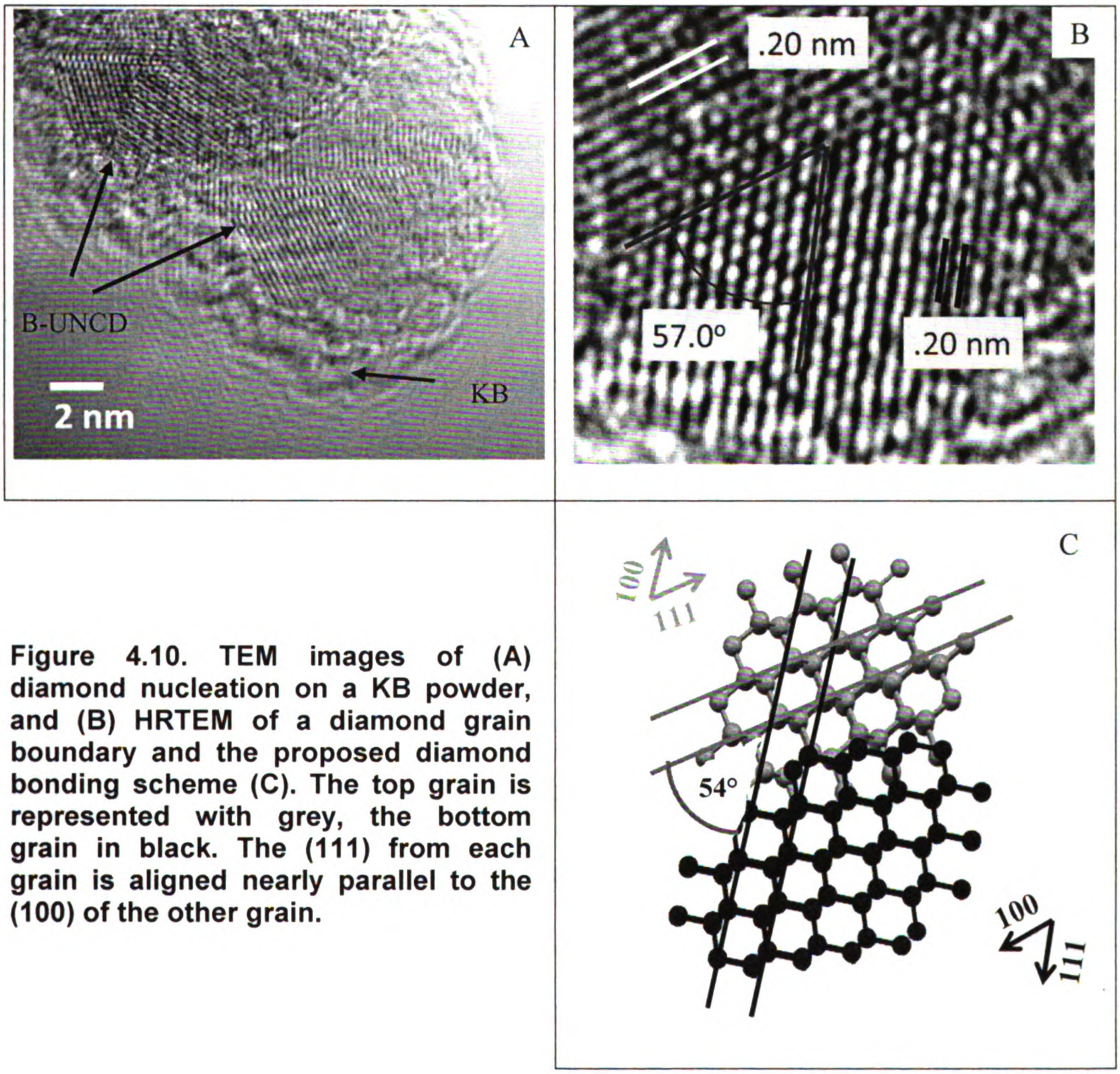

Figure 4.10. TEM images of (A) diamond nucleation on a KB powder, and (B) HRTEM of a diamond grain boundary and the proposed diamond bonding scheme (C). The top grain is represented with grey, the bottom grain in black. The (111) from each grain is aligned nearly parallel to the (100) of the other grain.

The grain boundary width in Figure 4.9B is small, approx. 0.2 nm, slightly larger than the C-C sigma bond length of 0.154 nm.[32-34] Close examination of the HRTEM reveals that at different regions along the grain boundary, the (111) orientation of the bottom grain extends into the top grain. This creates a dovetail type joint between the grains.

A proposed bonding scheme between the two grains is shown in Figure 4.10C. At a 57° offset between the (111) planes of the two grains, the (111) planes of the bottom grain intermittently extend and bond with the (100) planes of the top grain. Lattice lines from the (100) plane are not visible in the TEM image as diffraction from diamond (100) is not allowed in an fcc lattice according to equation 4.4. The (100) plane of diamond intersects the (111) plane at 54°, close to the 57° observed between the two grains here. Diamond crystal growth on the KB surface would therefore start along the $(01\bar{1})$ plane, which is orthogonal to the (111) plane. The large surface area of the ketjen black powder results in a higher hydrogen etching rate at the exposed edges, reducing the particle size to an area surrounding the diamond growth occurring at the center.

4.2.3 Non-Diamond Carbon

Non-diamond carbon is frequently observed in B-UNCD growth on powders due to the temperature gradient across the uneven surface and variations in mass transport of reaction gases through the interstitial spaces of the powder.[35] Our group and others have investigated the effect of the carbon concentration during growth, and its relationship to the formation of sp^2-bonded carbon in planar films.[3, 13, 36] Important conclusions are that localized high carbon concentrations lead to increased sp^2 formation. The majority of sp^2 carbon formed on B-UNCD coated powders can be removed by washing in concentrated H_2O_2 at 60° C. Most of the images in this section were acquired ex-situ, before the washing step. Though these structures represent a relatively small percentage of the overall carbon deposited, their recognition is useful to assess

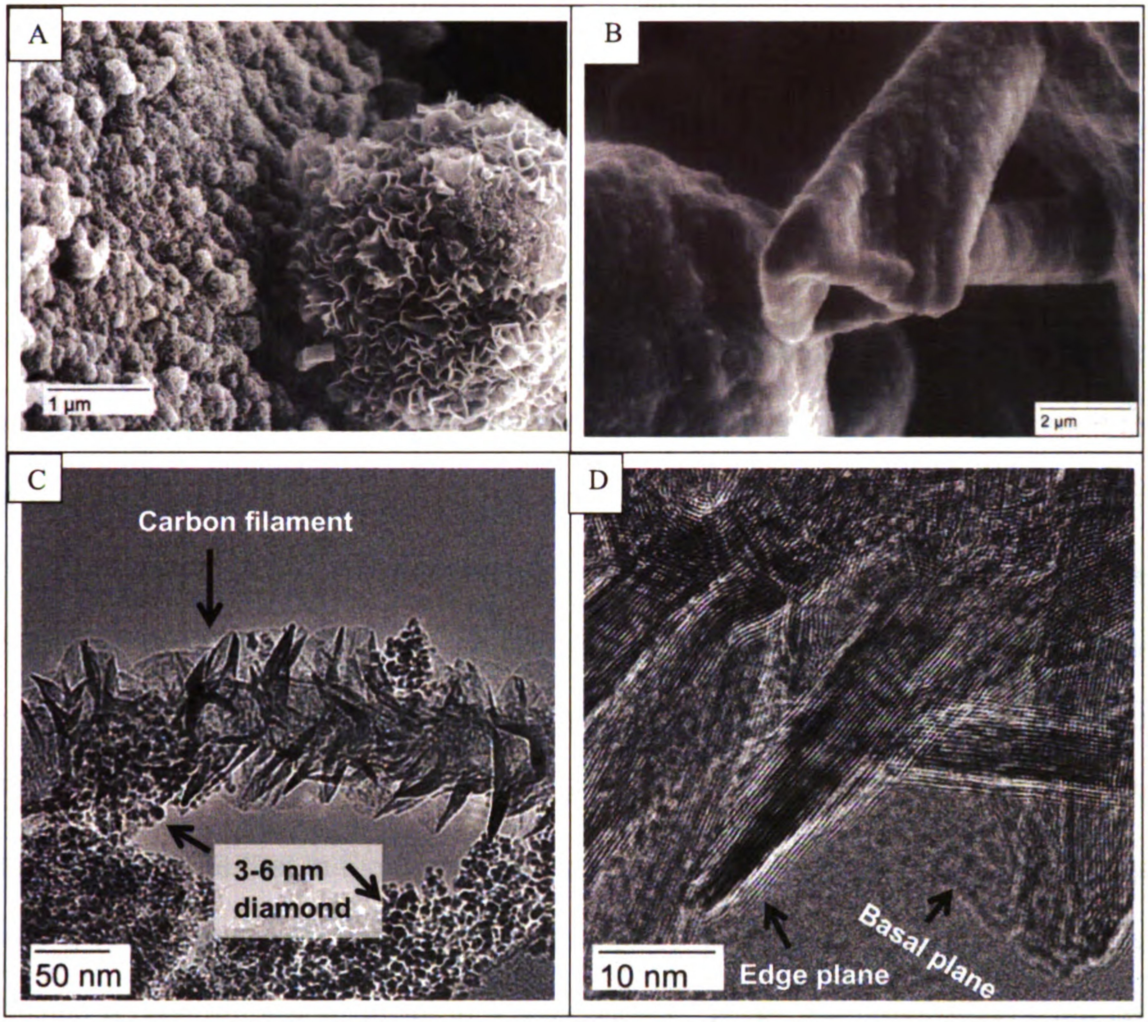

Figure 4.11. SEM and TEM images of graphitic structures co-deposited during B-UNCD growth onto varying sized diamond powders . (A) SEM image of macro scale graphite platelets. (B) SEM of carbon tubule formed at the sample top-side when the pressure was increased to 170 torr. (C) TEM image of a carbon filament, the 3-6 nm substrate diamond powder is also present in the image. (D) Close up of graphite edge plane and basal plane from the carbon filament in (C).

reactor growth conditions and carbon nucleation on a substrate. Formation of many of these structures is actually desirable for researchers investigating carbon nanotubes and graphene, which are also of great interest at the present time. Graphite is the most often observed sp^2-bonded carbon in the images. This is attributable to coherent diffraction from the (002) plane of graphite with a large 0.354 nm spacing, making it easier to resolve compared to amorphous sp^2 and tetrahedral amorphous sp^3 carbons which randomly scatter the electron beam. Also the disordered sp^2 cabon with a higher edge plane ratio is more hydrophilic, and likely disperses more in the isopropanol in which the powder is sonicated for drop casting on the TEM grid (*i.e.* it is washed away during sample preperation).

Figure 4.11A-D shows examples of graphitic carbon structures found after B-UNCD growth on diamond powders. Figure 4.11A is an SEM of a large conglomeration of graphitic platelets. This is similar to the structures observed in Figures 4.11C-D during B-UNCD grown on glassy carbon powder. Graphite tubules, such as that in Figure 4.11B, were found with less frequency. The tubule has a hollow core with graphite comprising the shell. This tubule formed while testing a different stage height in a new reactor. These new conditions were not well suited as the plasma became unstable, depositing a large (2 mm diam.) spot of carbon in approx. 1-2 min. The benefit was an easily recognizable portion of the sample for obtaining the electron micrograph and Raman spectrum. The Raman spectrum from an area where the tubule formed is shown in Figure 4.12. The D to G band intensity ratio I_D/I_G is .39 and a full width at half maximum of the G band at 1584 cm^{-1} is 47 cm^{-1}. These intensity and G band FWHM values are similar to those of graphite powder.[8, 37, 38] A carbon filament is shown in Figure 4.11C. The microstructure of the inner core is undetermined. Extending from the core are graphite moieties. HRTEM of the graphite in Figure 4.11D shows that the structures are predominately graphene sheets and carbon nanotubes. The graphene sheets are approx. 20 layers thick.

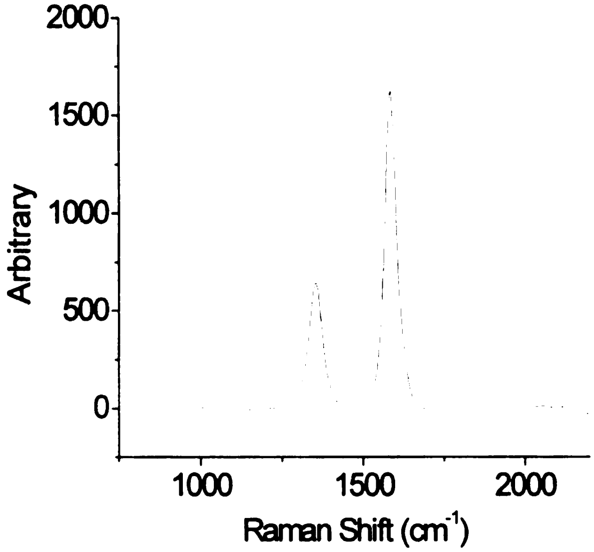

Figure 4.12. Raman spectrum acquired at the sample region containing the tubule in Figure 4.11B.

Diamond and graphite are the two crystalline forms of carbon. Diamond is more stable under high pressure and graphite is favored at atmospheric pressure. Transformation between these two phases is normally only seen under high temperature and pressure. Recently, R. K. Raman et al. and others reported on formation of an sp^3-like structure nonthermally in graphite under intense femtosecond laser excitation.[39, 40] The authors called this "Diaphite", having an interlayer spacing of 0.21 - 0.22 nm, without significant alteration to the graphite structure (slight shearing of the graphitic layers, followed by layer buckling). Figure 4.13 is TEM of “diaphite” observed after B-UNCD growth on 3-6 nm diamond powders. Acutance of the crystal structure was enhanced using the sharpen feature in Photoshop®. The

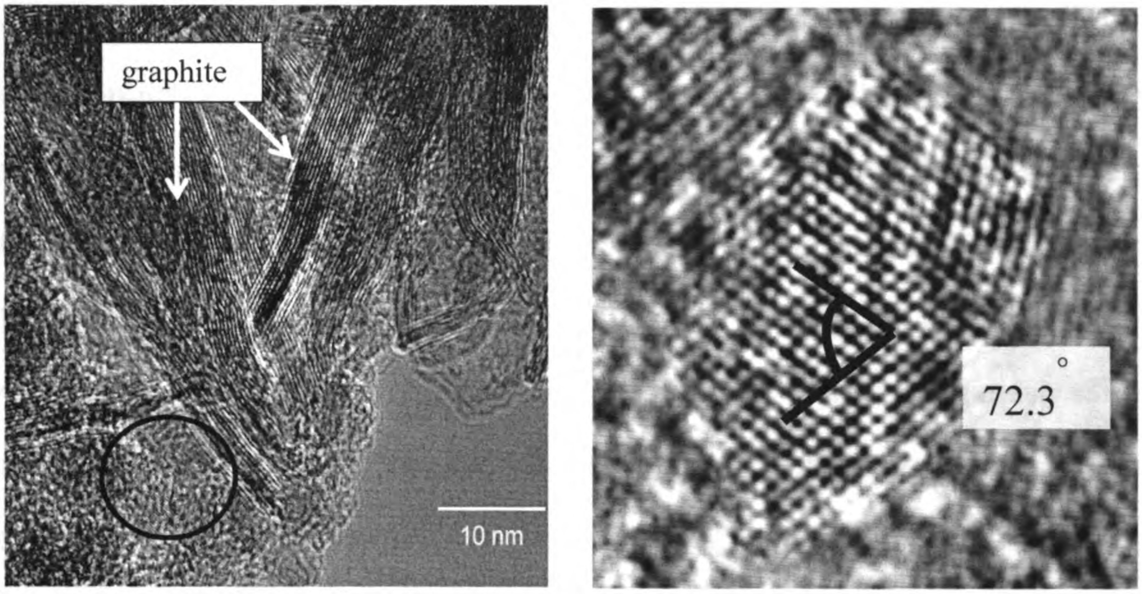

Figure 4.13 Diamond-like graphite or "diaphite" formed during B-UNCD deposition on 3-6 nm diamond powder. The circle indicates the region of the sample used for the close-up at right.

lattice lines intersect at an angle of 72.3° which corresponds to the intersection of the (002) and (101) planes of graphite.

The interlayer spacing of both planes is .21 nm. This is consistent with a reduction from 0.35 nm between the (002) planes and formation of sp^3 covalent bonding. This is the only example of "diaphite" discovered during this work.

4.3 Discussion

The HPHT diamond powders of sizes 100 nm, 500 nm and 8 µm as-received have a random shape with jagged edges (Figures 4.1 – 4.3). After B-UNCD growth the powders are smoother due to the overcoat. The carbon particle size increases with overgrowth over multiple nearby particles, and this causes a reduction in the specific surface area of approx. 50%.

As compared to BDD coated 8-12 µm diamond powders using a hydrogen-rich plasma, there is an expected increase in grain boundary fraction and non-diamond carbon incorporation in the B-UNCD coated powders (Figure 4.4). The grain boundary width at early stages (20 min) of B-UNCD growth on 100 nm diamond powder is larger (up to 7 nm) than for B-UNCD planar films (0.2 – 0.4 nm). Disordered carbon occupies these larger grain boundaries. SEM images, Raman spectroscopy, and electrochemistry (Chapter 6) all indicate that at slightly longer growth times (1 h) these areas of disordered carbon are mostly removed by hydrogen etching, or are covered with subsequent B-UNCD layers. The significance being that there is likely a minimum hydrogen concentration and/or growth time needed to minimize non-diamond carbon in the grain boundaries during early stages of B-UNCD growth. This may be a limiting factor in regards to the specific surface area achievable with this B-UNCD coating method (*i.e.*, short growth times are preferred to limit any increase in particle size).

The B-UNCD formed on carbon black powders has a well ordered diamond microstructure and small grain boundary width of 0.2 – 0.4 nm. The growth rate and B-UNCD varies with particle size, shape, and microstructure. The B-UNCD growth rate is glassy carbon > Ketjen black> graphite powder. Especially for glassy carbon powder, B-UNCD uniformly coats the entire surface with minimal changes to the original morphology (Figure 4.7). Lower in the GC powder sample graphite platelets form as a result of temperature gradients and reduced mass transport of reaction gases.[10, 19, 35, 36] During B-UNCD growth on

Ketjen black, the hydrogen etching rate of the outer ordered graphite sheets is higher than at the more turbostatic interior. Once the outer graphite sheets are removed, diamond nucleation > hydrogen etching and B-UNCD growth occurs. Hydrogen etching of the outermost carbon reduces the Ketjen black diameter from 30 to 10 nm. The reason for B-UNCD growth favoring the turbostatic interior portion is not entirely clear. A reasonable explanation is the more exposed edge planes offer more sites for hydrogen abstraction and carbon insertion to begin diamond lattice formation; whereas the outer more-ordered graphite sheets undergo hydrogen etching before carbon addition is possible.

Non-diamond carbon formed during B-UNCD deposition includes amorphous carbon, graphite, graphite fibers and graphene sheets (Figures 11, 12). Diamond like graphite or "diaphite" was also observed (Figure 13). The diamond like graphite has a reduced d_{002} lattice spacing from 0.35 to approx. 0.21 nm and a cubic structure. In addition to the diaphite reported by Raman et al., graphite-diamond transients have also been observed by Komninou et al.[39, 41] They reported fcc carbon structures formed by r.f. magnetron sputtering having a plane spacing of 0.32 nm and unit cell constant of ~0.5 nm.

Graphite tubules and fibers were regularly observed in nearly every B-UNCD coated sample. As mentioned at the beginning of this chapter, these micrographs must be considered along with Raman spectroscopy and XRD which measure the sample bulk. Under good growth conditions, the B-UNCD growth rate far exceeds the formation of sp^2-bonded carbons. Due to a greater rate of hydrogen etching and a slower B-UNCD growth rate, many sp^2 carbons are likely <100 nm and lend themselves to TEM imaging where they are more readily decipherable than in SEM. Therefor it is difficult to estimate the total sp^2 content from transmission electron microscopy alone. The XRD peak attributable to the (002) plane of graphite is either not observed or is very weak in these samples, suggesting a low graphite percentage. Also, there is almost no change to the electrical conductivity of B-UNCD diamond powders after H_2O_2 washing and re-hydrogenation which removes most sp^2. The sp^2 structures presented in this chapter undoubtedly contribute to the currents observed when these powders undergo anodic polarization in acid. [2, 42, 43] Due to time constraints, few images of post-anodically polarized powders were able to be acquired for B-UNCD powders. We did investigate 8-12 µm boron-doped microcrystalline diamond coated powders post anodic polarization with SEM and found the diamond powders to be "cleaner", with very few sp^2-bonded carbon formations found in the powder post polarization. Raman spectra of B-microcrystalline coated 8-12 µm diamond powders pre/post polarization in an EMLC column were devoid of any peaks for sp^2 carbons.

4.4 Formation and Structure of Platinum Electrocatalyst Particles on a Diamond Powder Support

This section discusses the structure of Pt deposits formed on 100 nm diam. oxygen and hydrogen-terminated diamond powder. Previous research on Pt decorated carbon blacks indicated that Pt dispersion and size vary with carbon support surface area (*inter alia,* as edge plane increases), and surface chemistry.[44] The purpose of this work was to learn (i) if the initial surface termination of the diamond powder has any significant influence on the formation of the nanoscale Pt particles in terms of the particle size and particle number, (ii) if any interfacial layer forms between the metal particles and the diamond, and (iii) if there is any registry between the atomic structure of the metal particles and the atomic structure of the substrate powder.

Studies of the electrochemical activity and stability of Pt adlayers on boron-doped diamond thin films and diamond-coated powders have been reported, although they contain little information regarding the physicochemical nature of the sites at which the electrocatalyst particles form.[44] For example, electrodeposited Pt particles on diamond thin films typically exhibit good activity and stability for the oxygen reduction[2] as well as the hydrogen and/or methanol electro-oxidation reactions.[45-47] High performance for catalyst activity requires good electronic communication between the Pt and diamond, and strong anchoring of the electrocatalyst particles on the diamond phase.

The 100 nm high pressure-high temperature (HPHT) diamond powder used here was <u>not</u> overcoated with a layer of boron-doped ultrananocrystalline diamond, as is typical. HPHT diamond is produced by mechanically pressing a carbon source, normally graphite, with enough pressure to produce diamond. Chemically, HPHT diamond is predominantly phase pure similar to natural diamond so that there are fewer sp^2 sites available for Pt attachment, meaning there is a greater likelihood for Pt-diamond interaction without convolution from competing sp^2 sites (see section 4.2.1). Also, the 100 nm diamond is easier to distinguish from the 2-10 nm diameter Pt particles by TEM.

Thermogravimetric analysis (TGA) was utilized to evaluate the gas phase oxidation resistance of the catalyst-loaded diamond powder.[45, 48] This technique explains gas phase oxidation, which we believe is a harsher, but reasonable mimic for the electrochemical oxidation that occurs in a fuel cell. With Pt present, a decrease in the onset temperature for gasification and a higher rate of carbon gasification are observed. The onset temperature is much lower for carbon black than for diamond. Therefore, diamond is significantly more resistant to thermal oxidation than carbon black in the presence of Pt.[49, 50] This work using Pt-decorated uncoated HPHT diamond was undertaken to create a standard with which the more complex chemical vapor deposition BDD coated materials (*vide supra*) may be compared .

X-ray diffraction patterns for the Pt-loaded hydrogen and oxygen terminated diamond powders are shown in Figure 4.14. The loading for both samples was experimentally determined to be 18 wt. % based upon thermogravimetric analysis. Peaks assigned to the Pt (111), (200), (220), (311) and (222), and the diamond (111), (220) and (311) crystalline planes are present. The broad background below 2θ of 30° arises from the grease used to mount powder on the glass stage. The relative intensity ratios for Pt (111) peak relative to the others is 1:3:7:7. This ratio is higher than the ratio for a standard Pt powder diffraction pattern of 1:2:4:4, so it appears that there is a preferential (111) orientation in the deposits on diamond. Importantly, the peak positions, line widths and peak intensity ratios are identical for both the hydrogen- and oxygen-terminated powders. This suggests that powder surface termination has little influence on the formation and structure of the chemically-impregnated Pt phase.

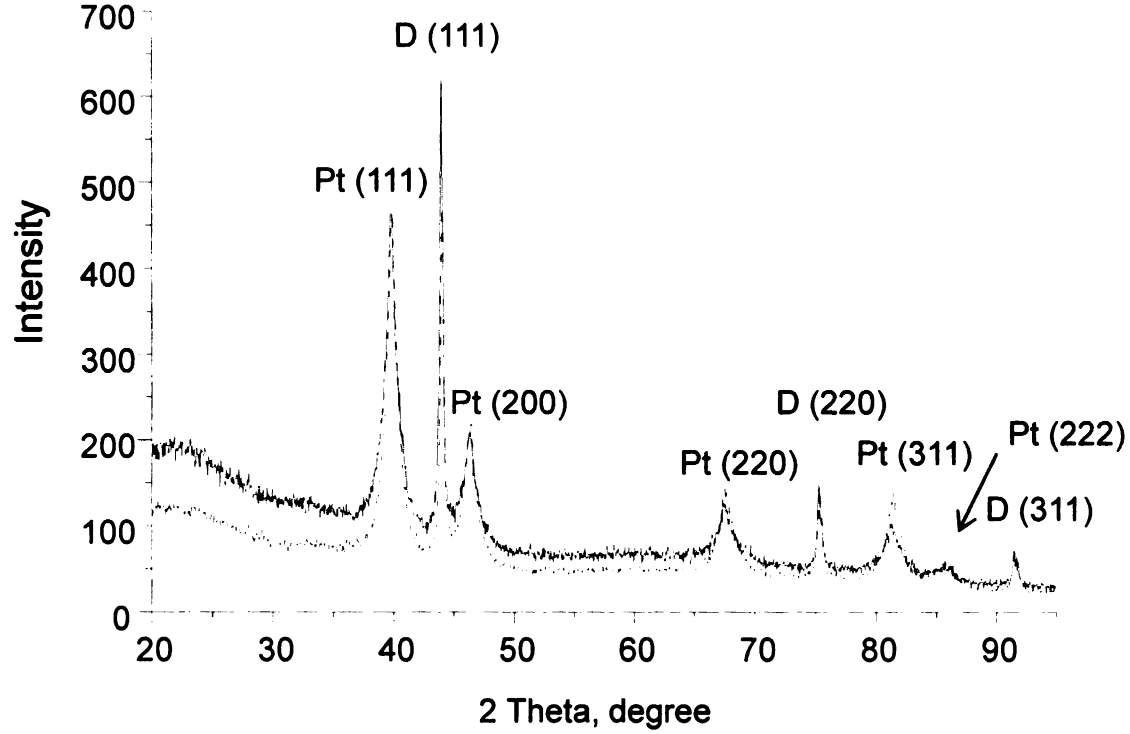

Figure 4.14. X-ray diffraction patterns for Pt-loaded (18% Pt/C) oxygen-terminated (solid line) and hydrogen-terminated (dash line) diamond powder (100 nm diam., 52 m^2/g).

It should be noted that diamond powder is microstructurally stable (*i.e*, no mass loss due to gasification) in the presence of Pt during the 400 °C annealing in air. Figure 4.15 shows a bright-field HRTEM image of the Pt-loaded diamond powder. The nanoscale Pt particles are easily distinguished from the relatively large diamond powder particles. Figure 4.15 is of the oxygen-terminated powder, although it should be noted that comparable images were obtained for the hydrogen-terminated powder. Pt particles are generally distributed over all areas of the powder. However, in a few locations, a higher Pt particle number can be seen at certain sites, particularly some of the crystallite edges. The particle size ranges from 1 to 10 nm with a nominal diameter of 5±2 nm (n=64). In this work, vigorous stirring was used during the impregnation in order to maintain a relatively constant Pt(II) concentration at the surface. The availability of Pt(II) near the surface becomes the rate-controlling step for nucleation. The supersaturation of Pt(II) near the surface is associated with adsorption, migration

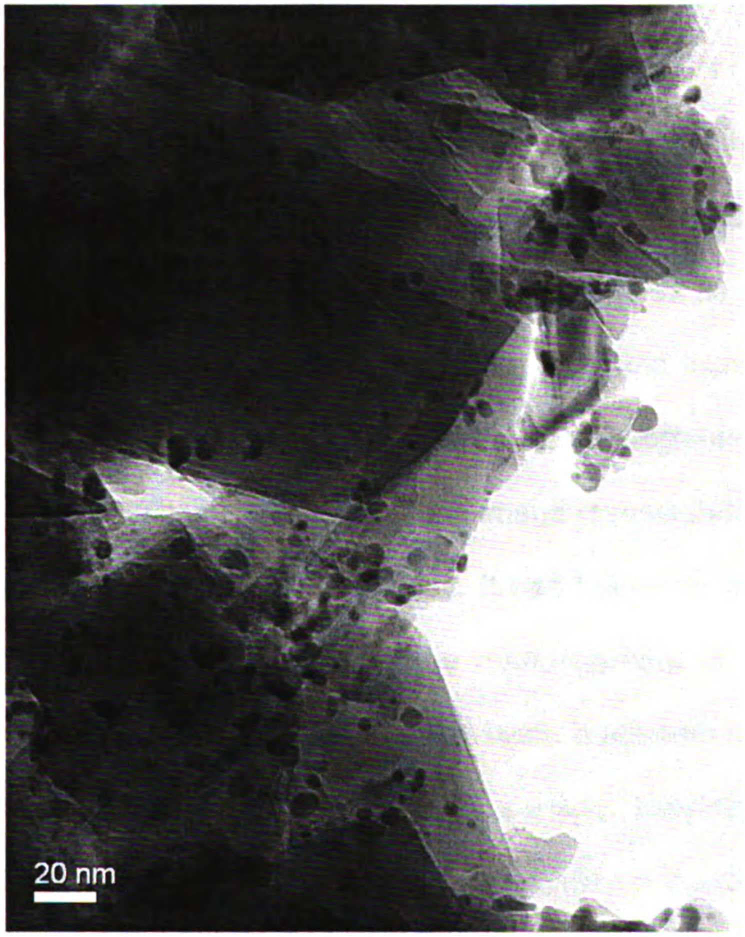

Figure 4.15. Bright field TEM image of Pt particles (dark spots) decorating the surface of oxygen-terminated diamond powder. The loading was 18 % Pt/C.

and capture of radicals on the surface.[51]

Figure 4.16A shows an HRTEM image of an individual Pt particle in contact with the diamond support. This particle is about 12 nm in diameter at the base. The Pt (111) planes are almost perfectly aligned (parallel) with the diamond (111) planes. This indicates that there is indeed some registry between the atomic arrangement of the Pt and the diamond substrate. An EDAX line profile was used to confirm that the particle is indeed Pt. Pt was additionally identified by measuring the lattice spacing in the image using the diamond (111) fringe spacing as an internal reference. The spacing was 2.26 Å, in agreement with the theoretical Pt (111) layer plane spacing. The Pt (111) and (200) planes also intersect at an angle of 54.9 °, which is close to the theoretical value of 54.8 °. Due to the *ca.* 10% lattice mismatch between Pt and diamond ($(a_{Pt}-a_D)/a_D$, where a_{Pt} and a_D are the lattice constants for Pt (3.92 Å) and diamond (3.57 Å), respectively), strain develops in the Pt deposits and increases with the particle size. Defects tend to form likely as a stress relief mechanism, like the one circled in Figure 4.16A. Close inspection of the image reveals there is no interfacial layer between diamond and the Pt deposit. It has been hypothesized that the post-deposition annealing might cause the rearrangement of the atoms of diamond near the Pt particles into a graphite-like layer. It appears that this does not occur and Pt forms directly on the diamond surface. Electron energy loss spectra (EELS) recorded in scanning transmission mode on the diamond, the Pt and the interfacial region between the metal and diamond further confirmed that no non-diamond interface exists. To limit any EELS background signal from the lacey

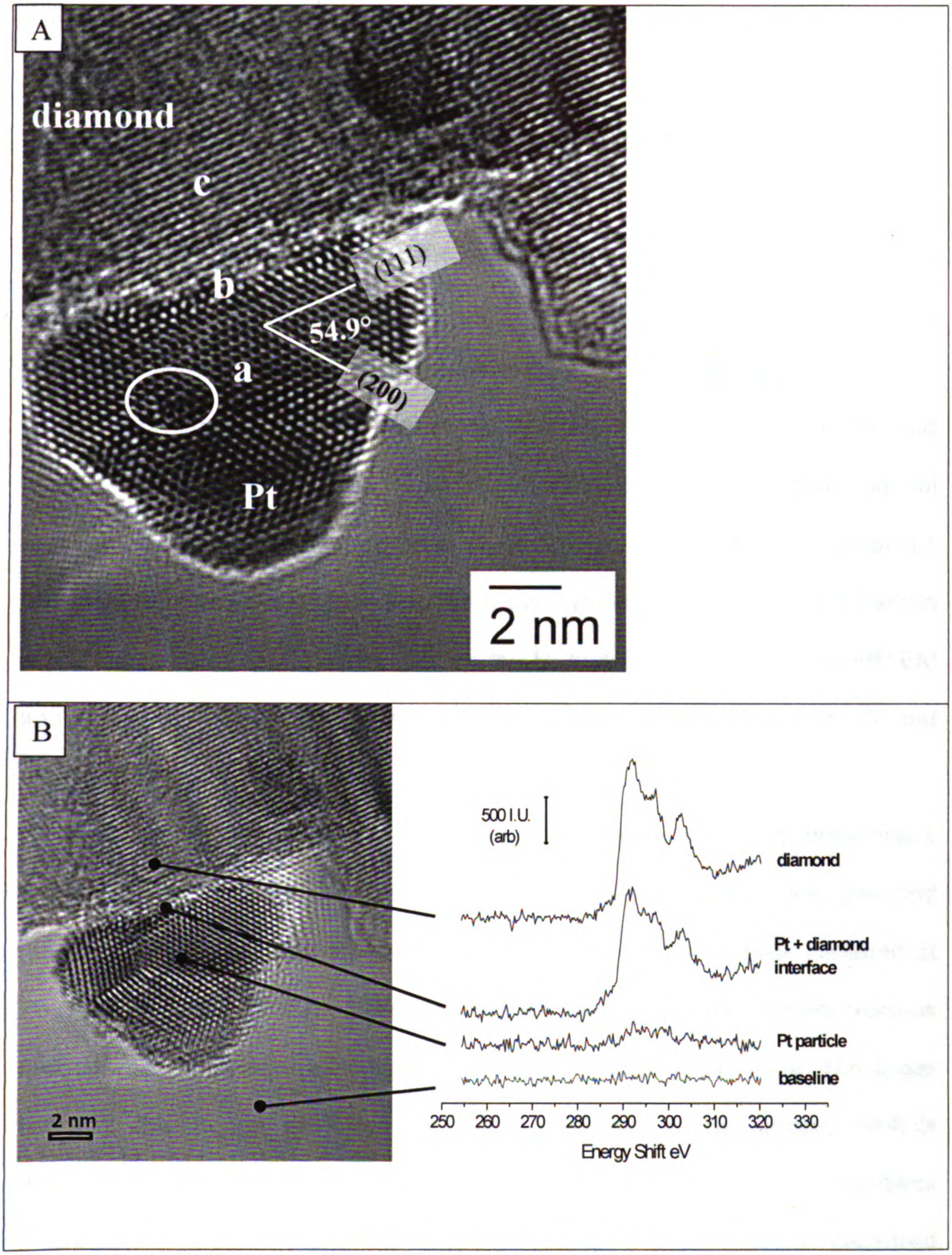

Figure 4.16 (A) High resolution HRTEM image of a Pt particle formed on an oxygen-terminated diamond powder particle, and (B) electron energy loss spectra for different spots (a-c) along the Pt/diamond solid. Scale bar is 2 nm in each.

carbon support on the TEM grid, EELS data were only collected from particles residing in the voids of the support so the electron beam was only interacting with the sample. Spectra were recorded using an electron beam size of *ca* 0.7 nm. Figure 4.16B shows the carbon K-shell ionization edge recorded at different spots, including on the Pt particle, the neighboring diamond crystal, the interface between the two phases, and in the void to serve as a control. At spot c, typical features of pure sp^3-bonded diamond are evident. The peak at 290 eV is the C1s core exciton (σ-σ^*), and the dip at *ca.* 300 eV corresponds to the second absolute bandgap of diamond.[52] At the interface (curve b), identical spectral features are seen. There is no peak at *ca.* 285 eV for the π-π^* transition as would be expected if a graphite-like interfacial layer existed. There is little carbon signal detected at spot a, since it is on the Pt metal particle. Both the HRTEM image and the EELS are consistent with direct interaction between Pt and diamond without any sp^2 carbon interfacial layer.

XPS analysis was conducted on the platinized powder in order to determine if there is strong metal-support interaction (SMSI) between the Pt and diamond (Figure 4.17). Pure metal Pt has binding energy for the $4f_{7/2}$ peak centered at 70.8 eV. When the Pt is interacting with a more electronegative element, such as carbon, the photoelectron binding energy will shift to a higher value. The larger the shift, the stronger the electronic coupling between the two phases. Shift of the metallic Pt doublet peaks in the Pt4f (7/2 and 5/2) XPS spectra indicates interaction between Pt and the support material. For commercial platinized Vulcan XC-72 carbon black, the Pt binding energies, $4f_{7/2}$ and $4f_{5/2}$, were 71.19

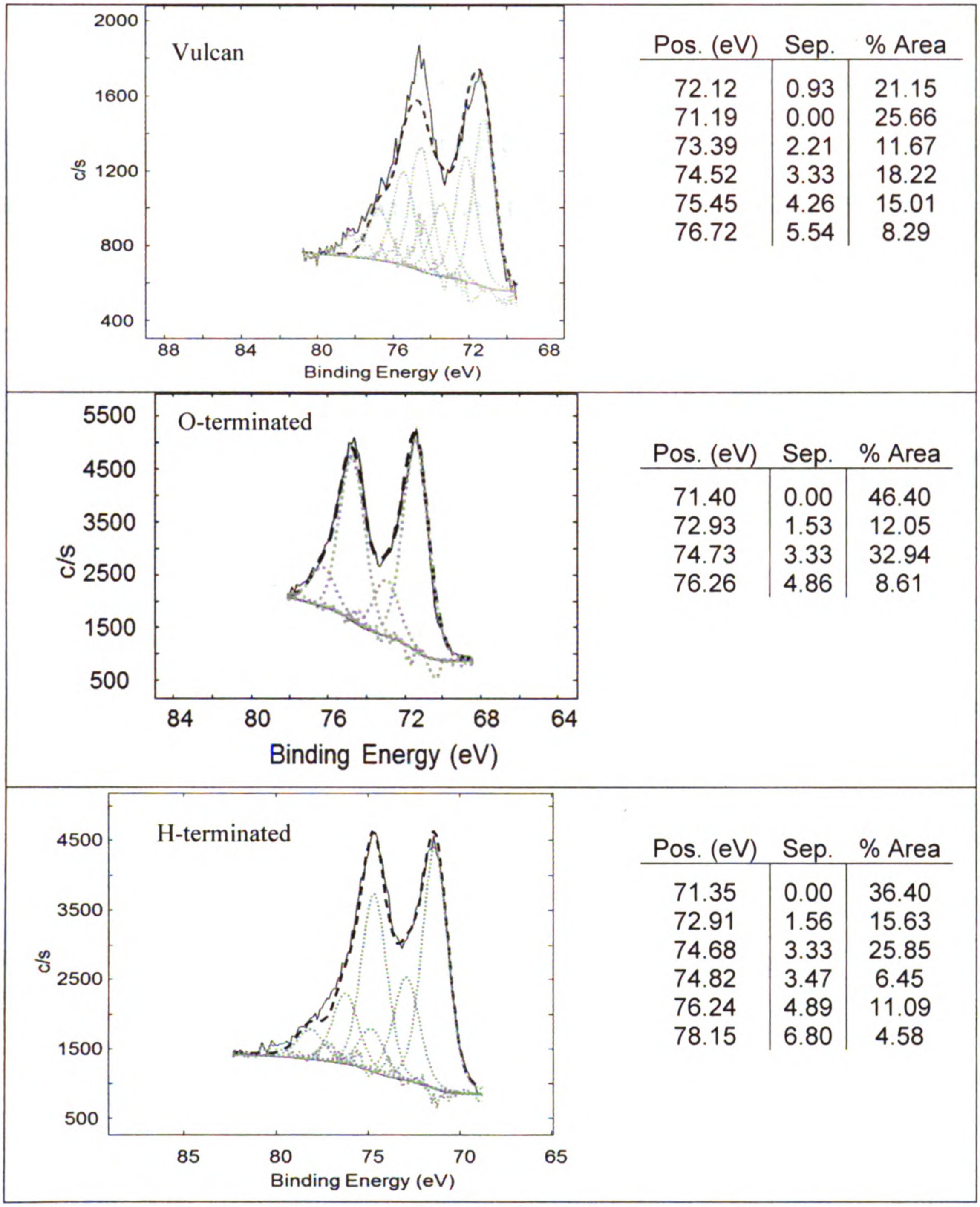

Pos. (eV)	Sep.	% Area
72.12	0.93	21.15
71.19	0.00	25.66
73.39	2.21	11.67
74.52	3.33	18.22
75.45	4.26	15.01
76.72	5.54	8.29

Pos. (eV)	Sep.	% Area
71.40	0.00	46.40
72.93	1.53	12.05
74.73	3.33	32.94
76.26	4.86	8.61

Pos. (eV)	Sep.	% Area
71.35	0.00	36.40
72.91	1.56	15.63
74.68	3.33	25.85
74.82	3.47	6.45
76.24	4.89	11.09
78.15	6.80	4.58

Figure 4.17. XPS spectra of Pt on (A) Vulcan XC-72, (B) O-terminated and (C) H-terminated diamond. Solid black line is the experimental data, dashed black line is simulated result, and dotted grey lines are deconvoluted peaks.

and 74.52 eV, respectively. Comparatively, a positive binding energy shift was also seen for Pt on diamond with binding energy of 71.40 and 75.73 eV. This indicates that a stronger electronic interaction exists between Pt-C for diamond than for carbon black. This could be one of the reasons for the higher stability of Pt on diamond substrate than on carbon black. Thermogravimetric analysis (TGA) was used as an accelerated degradation test method to assess the stability ofthe diamond powder toward oxidation/gasification. TGA curves for uncoated and platinized diamond powder are shown in Figure 4.18. For the bare diamond powder (solid line), full gasification occurred by 800 °C, which means all the diamond powder was gasified into CO and/or CO_2. For the platinized diamond (dash line), the normalized weight becomes constant once the temperature reached 700 °C. The residual weight is 13% of the initial weight, which is close to the Pt loading (0.2 (Pt)/(0.2 (Pt) + 1 (C)) = 17%). The platinized diamond powder is thermally stable at temperature up to 500 °C in air. Figure 4.18 demonstrates a

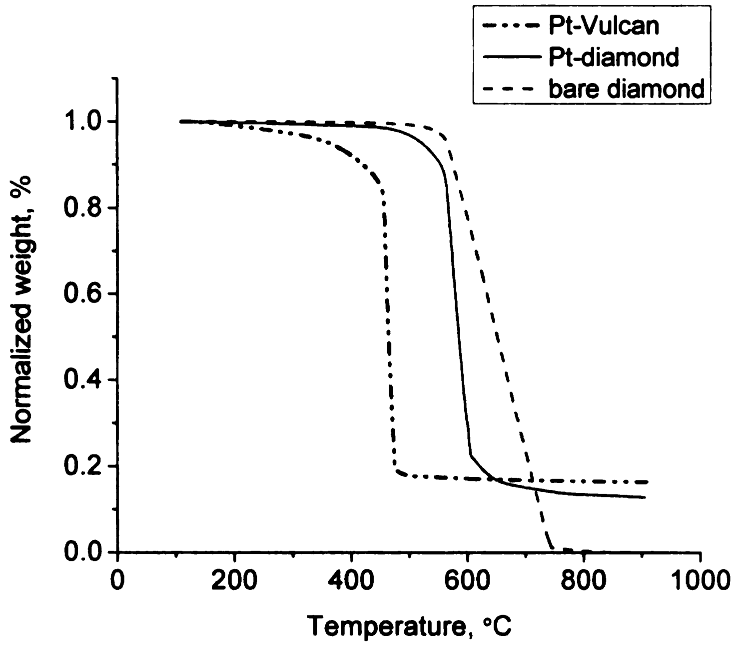

Figure 4.18. TGA curves for the air oxidation of oxygen-terminated diamond powder bare (solid line) and after Pt impregnation (dash line). The loading was 18% Pt/C.

shift of temperature for gasification of the platinized powder, compared with the bare powder. The temperature at which 50% of the initial weight was lost was 582 and 651 °C, respectively, for the platinized and bare diamond. Platinum is an electron donor when bonded with carbon, due to its lower electronegativity. At the carbon surface, Pt will possess a pseudo-positive charge causing a decrease in the energy barrier for oxygen chemisorption.[53] The mechanism of the catalytic gasification may proceed as follows: (i) oxygen atoms are formed on the catalyst surface from the dissociative chemisorption of air or water; (ii) at elevated temperature the chemisorbed oxygen atoms diffuse from the metal to nearby carbon sites; (iii) the oxygen atoms then react with the carbon to produce oxide functionalities; and (iv) the oxidation continues to produce CO and/or CO_2. A similar catalytic effect was observed for Pt-impregnated Vulcan XC-72. However, the temperature decreased from 721 to 428 °C after platinization.[53] The carbon microstructure is the primary factor determining the oxidation reaction rate. Sp^3-bonded carbon is more resistant to oxidation than sp^2-bonded carbon, particularly microstructurally disordered carbon, due to its dense 3-D bonding. The TGA data reveals the advantages of diamond: microstructural stability and oxidation resistance at high temperatures and in oxidizing environments.

The degree of electronic interaction between the Pt and the carbon support plays a critical role in the stability and activity of the catalyst. Electron transfer from Pt to the carbon contributes to the coupling between the two phases. The Pt/carbon electronic interaction can be enhanced on carbon surfaces by pretreatment in strong oxidants, acids, H_2O_2 and O_2. Research on the effect of such surface pretreatment of sp^2 carbons is of great interest. Yu and Ye reviewed the results published by different research groups.[54] For sp^2 carbon supports, such as carbon black, nanofibers and nanotubes, the benefits of oxidative pretreatment are still somewhat unclear with regard to the effect of surface functional groups on the Pt particle distribution and anchoring.[54] Here the effect of surface chemistry (H- vs. O-termination) on metal phase formation was compared. The O-terminated powder was re-hydrogenated in hydrogen plasma for 30 min. After re-hydrogenation, the O/C ratio on the surface significantly decreased from 11 to 4 atomic %, as determined by XPS shown in Table 4.2. Surface oxygen decreases *ca.* 10% after H_2 plasma treatment on diamond surfaces, including ultrananocrystalline, and microcrystalline diamond planar films that were similarly treated. XRD line positions and line widths were identical for both surface terminations suggesting that the surface chemistry has little effect on the catalyst formation. Figure 4.19 shows TEM images of Pt on hydrogenated diamond powder. Refer to Figures 4.15 and 4.16 for similar images of oxygen-terminated diamond. The Pt particles are highly dispersed on

Table 4.2. XPS data for hydrogen and oxygen terminated diamond.

	H-Terminated (%)		O-Terminated (%)	
	C1s	O1s	C1s	O1s
100 nm diamond powder	95.5	4.5	88.3	11.3
Ultrananocrystalline planar film	97.56	2.09	80.32	13.58
Microcrystalline planar film	98.07	1.93	87.52	10.79

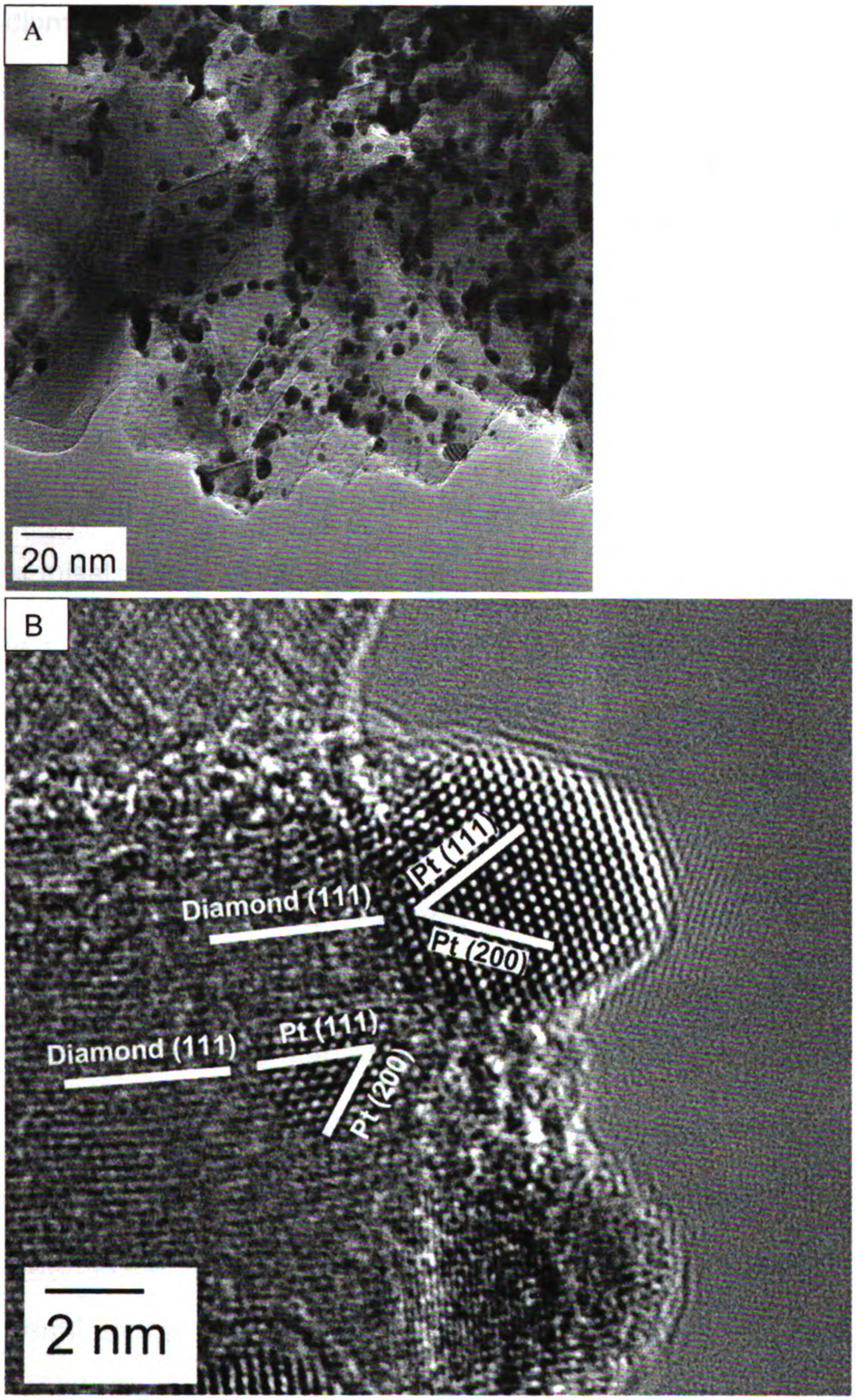

Figure 4.19 (A) Bright field TEM image of Pt deposited on hydrogen-terminated diamond powder, and (B) an HRTEM image of a Pt particle formed on a diamond powder particle. Image A reveals a uniform distribution of Pt particles over the entire powder sample. Image B shows the Pt(111) growth nearly co-planar with diamond (111) planes.

diamond powder, as seen in Figure 4.19A. Clearly, the surface termination has little influence on the formation of Pt particles by this impregnation method. The nominal particle size is 5±2 nm, which is identical to that found for the O-terminated sample. Figure 4.19B is the HRTEM image of Pt anchored to the diamond. Two Pt particles are present in the image. It can be seen that the middle particle is epitaxially oriented with the diamond (111) plane. The Pt (111) planes are almost perfectly aligned with diamond (111) planes. Furthermore, the Pt particle is in full contact with the diamond surface. The upper right Pt particle is misaligned with respect to the diamond (111) surface. There are 2-3 atomic layers of Pt atoms at the interface that are in good registry with the diamond (111) surface, as demarked by the rectangle in Figure 4.19B. However, there is a change in orientation further out into the particle, which helps to relieve the internal strain.

The SMSI between the Pt and H-terminated diamond was studied by XPS (Figure 4.17). The binding energies of the Pt4f doublets were 71.35 and 74.68 eV which are slightly (0.05eV) lower than binding energies on O-terminated diamond powder. The metal-semiconductor-junction analogy in inductive models for metal-support interactions indicated Fermi levels of metal and support are the key parameters.[44, 55] Electrons flow from the metal into the support due to the higher Fermi energy of the metal. This causes a corresponding increase in the Fermi energy of the support until the two become equal. Hydrogen-terminated diamond possesses higher Fermi energy than does oxygen-terminated diamond. The electron affinity of oxygen-terminated diamond is about 1eV more positive than that for the hydrogenated-terminated surface.[56] The Fermi level shift after hydrogenation decreases electron exchange from Pt to diamond. This is consistent with the lower binding energy of metal Pt doublets on hydrogen than on oxygen-terminated diamond.

4.5 Conclusions

Diamond and sp^2 carbon powders were microscopically evaluated before and after B-UNCD coating. The HPHT diamond powders of sizes 100 nm, 500 nm and 8 µm as-received have a random shape with jagged edges. After B-UNCD growth the powders appear smoother due to the overcoat. The carbon particle size increases and the specific area decreases by approximately 50% after B-UNCD growth. Raman spectroscopy and XRD confirmed the bulk of the coating is B-UNCD. Formation of B-UNCD was verified on glassy carbon and Ketjen black powders, two microstructurally and morphologically different carbon black powders. Good quality B-UNCD formed on both carbon black powders. Hydrogen etching was more pronounced for the higher surface area Ketjen black. Small amounts of adventitious carbon co-deposit during B-UNCD growth in the interstitial spaces, due to temperature and concentration gradients near the cooler substrate-side of the sample.

The formation and structure of Pt electrocatalyst particles on both hydrogen and oxygen terminated diamond powder was investigated. A uniform distribution of Pt particles was observed after chemical impregnation over the entire powder surface regardless of the surface termination. Surface chemistry

has little effect on the nominal particle size and distribution on the powder (Figures 4.15 and 4.19). Pt particles form epitaxially with the diamond (111) planes. A line/screw defect forms in the Pt crystal bulk during growth and 2-3 atomic layer from the Pt-diamond interlayer. The Pt changed growth direction, which helps to release internal strain of Pt coming from the lattice misfit with diamond substrate. Both high resolution TEM and EELS reveal direct bonding between Pt and diamond without any detectable sp^2 carbon interfacial layer. XPS measurements determined the Pt binding energy for the 4f doublets shifted positively to 71.4 eV and 75.73 eV, indicating that a stronger electronic interaction exists between Pt-C for diamond than for carbon black.

4.6 References

[1] S. L. Flegler, J. W. Heckman, and K. L. Klomparens, Scanning and Transmission Electron Microscopy: An Introduction, Oxford University Press, 1993.

[2] A. E. Fischer and G. M. Swain, *Journal of the Electrochemical Society* **152**:B369 (2005).

[3] Y. Show, V. M. Swope, and G. M. Swain, *Diamond and Related Materials* **18**:1426 (2009).

[4] J. Birrell, J. E. Gerbi, O. Auciello, and J. A. Carlisle, *Journal of Physics: Condensed Matter* **18**:S1771 (2006).

[5] D. B. Williams and C. B. Carter, Transmission Electron Microscopy A Textbook for Materials Science, Springer, New York, 2004.

[6] M. H. Al-Saleh and U. Sundararaj, *Carbon* **47**:2 (2009).

[7] R. Arenal, O. Stephan, P. Bruno, and D. M. Gruen, *Applied Physics Letters* **94** (2009).

[8] J. Birrell, J. A. Carlisle, O. Auciello, D. M. Gruen, and J. M. Gibson, *Applied Physics Letters* **81**:2235 (2002).

[9] T. D. Corrigan, D. M. Gruen, A. R. Krauss, P. Zapol, and R. P. H. Chang, *Diamond and Related Materials* **11**:43 (2002).

[10] S. Jiao, A. Sumant, M. A. Kirk, D. M. Gruen, A. R. Krauss, and O. Auciello, *Journal of Applied Physics* **90**:118 (2001).

[11] S. Prawer, K. W. Nugent, D. N. Jamieson, J. O. Orwa, L. A. Bursill, and J. L. Peng, *Chemical Physics Letters* **332**:93 (2000).

[12] D. S. Knight and W. B. White, *Journal of Materials Research* **4**:385 (1989).

[13] J. A. Bennett, J. Wang, Y. Show, and G. M. Swain, *Journal of the Electrochemical Society* **151**:E306 (2004).

[14] A. E. Fischer, M. A. Lowe, and G. M. Swain, *Journal of the Electrochemical Society* **154**:K61 (2007).

[15] Y. Show, M.-I. A. Witek, P. Sonthalia, and G. M. Swain, *Chemistry of Materials* **15**:879 (2003).

[16] D. M. Gruen, *Annual Review of Materials Science* **29**:211 (1999).

[17] D. M. Gruen, *MRS Bulletin* **23**:32 (1998).

[18] J. Birrell, J. E. Gerbi, O. Auciello, J. M. Gibson, D. M. Gruen, and J. A. Carlisle, *Journal of Applied Physics* **93**:5606 (2003).

[19] J. E. Butler and A. V. Sumant, *Chemical Vapor Deposition* **14**:145 (2008).

[20] R. J. Nemanich and S. A. Solin, *Physical Review B: Condensed Matter* **20**:392 (1979).

[21] Y. Wang, D. C. Alsmeyer, and R. L. McCreery, *Chemistry of Materials* **2**:557 (1990).

[22] J. R. Dennison, M. Holtz, and G. Swain, *Spectroscopy (Eugene, Oregon)* **11**:38 (1996).

[23] F. Tunistra and J. L. Koenig, *Journal of Chemical Physics* **53**:1126 (1970).

[24] R. DeClements, G. M. Swain, T. Dallas, M. W. Holtz, R. D. Herrick, II, and J. L. Stickney, *Langmuir* **12**:6578 (1996).

[25] Q. Chen and G. M. Swain, *Langmuir* **14**:7017 (1998).

[26] T.-C. Kuo and R. L. McCreery, *Analytical Chemistry* **71**:1553 (1999).

[27] S. P. Mehandru, A. B. Anderson, and J. C. Angus, *Journal of Physical Chemistry* **96**:10978 (1992).

[28] W. R. L. Lambrecht, C. H. Lee, B. Segall, J. C. Angus, Z. Li, and M. Sunkara, *Nature (London)* **364**:607 (1993).

[29] M. Mermoux, B. Marcus, G. M. Swain, and J. E. Butler, *Journal of Physical Chemistry B* **106**:10816 (2002).

[30] K. Kinoshita, Carbon : Electrochemical and Physicochemical Properties, Wiley, New York, 1988.

[31] J. K. Lee, P. John, S. C. Kim, W. S. Lee, and J. I. B. Wilson, *Diamond and Related Materials* **17**:1216 (2008).

[32] J. F. Morar, F. J. Himpsel, G. Hollinger, G. Hughes, and J. L. Jordan, *Physical Reveiw Letters* **54**:1960 (1985).

[33] M. Petravic, A. Hoffman, G. Comtet, L. Hellner, and G. Dujardin, *Fizika A* **8**:275 (1999).

[34] S. Bhattacharyya, M. Lubbe, P. R. Bressler, D. R. T. Zahn, and F. Richter, *Diamond and Related Materials* **11**:8 (2002).

[35] Y. Einaga, G. S. Kim, S. G. Park, and A. Fujishima, *Diamond and Related Materials* **10**:306 (2001).

[36] P. W. May and Y. A. Mankelevich, *Journal of Applied Physics* **100**:024301/1 (2006).

[37] K. Okada, K. Kimoto, S. Komatsu, and S. Matsumoto, *Journal of Applied Physics* **93**:3120 (2003).

[38] R. Arenal, P. Bruno, D. J. Miller, M. Bleuel, J. Lal, and D. M. Gruen, *Physical Review B (Condensed Matter and Materials Physics)* **75**:195431 (2007).

[39] R. K. Raman, Y. Murooka, Chong-Yi, Ruan, T. Yang, S. Berber, and D. Tomanek, *Physical Reveiw Letters* **101**:077401

(2008).

[40] J. Kanasaki, E. Inami, K. Tanimura, H. Ohnishi, and K. Nasu, *Physical Reveiw Letters* **102** (2009).

[41] P. Komninou, G. Nouet, T. Kehagias, S. Logothetidis, M. Gioti, and T. Karakostas, *Diamond and Related Materials* **8**:688 (1999).

[42] A. Ay, V. M. Swope, and G. M. Swain, *Journal of the Electrochemical Society* **155**:B1013 (2008).

[43] D. Y. Kim, B. Merzougui, and G. M. Swain, *Chemistry of Materials* **21**:2705 (2009).

[44] M. A. Fraga, E. Jordao, M. J. Mendes, M. M. A. Freitas, J. L. Faria, and J. L. Figueiredo, *Journal of Catalysis* **209**:355 (2002).

[45] G. Siné, I. Duo, B. Roustom, G. Fóti, and C. Comninellis, *Journal of Applied Electrochemistry* **36**:847 (2006).

[46] L. Guo, V. M. Swope, B. Merzougui, L. Protsailo, M. Shao, Q. Yuan, and G. M. Swain, *Journal of the Electrochemical Society* **157**:A19 (2010).

[47] J. A. Bennett, Y. Show, S. Wang, and G. M. Swain, *Journal of the Electrochemical Society* **152**:E184 (2005).

[48] N. Spataru, X. Zhang, T. Spataru, D. A. Tryk, and A. Fujishima, *Journal of the Electrochemical Society* **155**:B264 (2008).

[49] D. A. Stevens, M. T. Hicks, G. M. Haugen, and J. R. Dahn, *Journal of the Electrochemical Society* **152**:A2309 (2005).

[50] D. A. Stevens and J. R. Dahn, *Carbon* **43**:179 (2004).

[51] L. Calvillo, M. Gangeri, S. Perathoner, G. Centi, R. Moliner, and M. J. Lazaro, *Journal of Power Sources* **192**:144 (2009).

[52] B. R. Pamplin, Crystal growth, Pergamon Press, Oxford, New York,, 1975.

[53] P. L. Walker and P. A. Thrower, *Chemistry and Physics of Carbon* **16**:R3 (1981).

[54] X. Yu and S. Ye, *Journal of Power Sources* **172**:133 (2007).

[55] M. C. Roman-Martinez, D. Cazorla-Amoros, A. Linares-Solano, C. S.-M. De Lecea, H. Yamashita, and M. Anpo, *Carbon* **33**:3 (1995).

[56] S. A. Stevenson, Metal-support interactions in catalysis, sintering, and redispersion, Van Nostrand Reinhold Co., New York, 1987.

Chapter 5

Microstructural Stability of Boron-Doped Diamond-Coated Diamond Powders During Potentiostatic Polarization in Aqueous Acid As Probed using Electrochemical Methods and In-situ Raman Spectroscopy: Comparison with sp^2 Carbon Powders

Abstract

Electrochemical and in-situ Raman spectroscopic measurements were made with boron-doped diamond (BDD) powder (8-12 µm diam., 0.6 m^2/g, 2 S/cm) before, during and after potentiostatic polarization in aqueous acid. Electrodes were prepared by casting a powder slurry on a glass slide with Nafion serving as the binder. The potentiostatic polarization was performed in either 0.1 M $HClO_4$ or 0.1 M H_2SO_4 at 1.0, 1.2 and 1.4 V vs. Ag/AgCl. The polarizations were conducted at two temperatures: room temperature and 80 °C. Comparison studies were also performed on Vulcan XC-72 (220 m^2/g, 1 S/cm) and several microstructurally-varied sp^2 carbon powders; graphite (3 m^2/g, 6 S/cm), glassy carbon (2 m^2/g, 2 S/cm) and acetylene black (68 m^2/g, 2 S/cm). The goal was to learn more about how the BDD powder microstructure might be altered during anodic polarization. In addition to the electrochemical and Raman spectroscopic measurements, scanning electron microscopy (SEM), x-ray diffraction (XRD), electrical conductivity and BET surface area measurements were used to evaluate the powder properties. The rate and extent of oxidation increased in the order of BDD < graphite < glassy carbon << acetylene black << Vulcan. The

oxidation charge for each carbon powder increased with the polarization potential and the temperature, tracking the degree of microstructural disorder and the specific surface area of the carbon. A key finding was that no microstructural damage, alteration of the electrical conductivity, or corrosion of the BDD powder occurred during a 1-h polarization under the severest test conditions (1.4 V vs. Ag/AgCl in 0.1 M H_2SO_4 at 80 °C). For the graphite and glassy carbon powders, surface oxides formed initially during the polarization at the native edge plane sites. This oxidation stressed the lattice, causing the layer planes to fracture, thus exposing new edge plane sites at which additional surface oxides formed. Importantly, there was no alteration of the electrical conductivity or corrosion of these powders under the most severe conditions. Significant changes were, however, seen for the acetylene black and Vulcan powders. Major microstructural changes were seen for both during the polarization. Polarization under the severest conditions produced increases in the surface area of the acetylene black, possibly by increasing the porosity, but there was no evidence for any alteration in the electrical conductivity of the powder electrode or corrosion. The Vulcan powder corroded severely, which caused large increases in the electrical resistance of the powder electrode.

5.1 Introduction

This study was conducted to probe what microstructural changes might occur to boron-doped microcrystalline diamond (BDD) coated diamond powder. Electrochemical and in-situ Raman spectroscopic investigations of the microstructural stability of BDD were conducted during anodic polarization in acidic media as a function of potential (1.4 V vs. Ag/AgCl) and temperature (room temperature and 80 °C). Comparison studies were performed with a commonly used fuel cell carbon, Vulcan XC-72R, and with microstructurally well-characterized sp^2 carbon powders (graphite, glassy carbon and acetylene black) at stepwise anodic potentials (1.0, 1.2, and 1.4 V vs. Ag/AgCl). The purpose was to learn more about how the carbon microstructure is altered during the early stages of electrochemical polarization. The present work complements other published work, like that by Kangasniemi and co-workers ,[1] who focused on the surface oxidation of carbon black, whereas this work focuses on the microstructural changes. In addition to the electrochemical and Raman measurements, SEM, XRD, BET surface area and electrical conductivity measurements were made to characterize the powders before, during and after polarization.

5.2 Results

Some of the physical properties of the sp^3 and sp^2 carbon powders are summarized in Table 1. The electrical conductivity, specific surface area and

Table 5.1. Physical Properties of the sp^3 and sp^2 carbon powders and the powder films with a Nafion binder.

		Powder conductance [S/cm]§	BET surface area [m^2/g]*	d_{002} [A]**	Nafion [wt %]	Film coverage [mg/cm^2]
sp^2	Graphite	6	3.0	3.37	10	3.75
	Glassy carbon	2	2.3	3.44	10	1.5
	Acetylene black	2	68	3.49	15	0.75
	Vulcan XC-72	1	220	3.62	20	0.375
sp^3	8-12 mm Boron doped diamond	2	0.63	N/A	5	64

§ 30 mg of powder was placed in a glass tube (0.114 cm^2) with a 240 g weight.
* N_2 adsorption at -196 °C.
** obtained from powder XRD.

XRD d_{002} interplanar spacing values are presented. It can be seen that the electrical conductivity of the BDD sp^3 and sp^2 carbon powders range from 1-10 S/cm. The specific surface areas range from *ca.* 1-250 m^2/g with the acetylene black and Vulcan powders possessing the largest values. As the sp^2 carbon powder becomes more microstructurally-disordered, reflected by an increasing d_{002} spacing, the specific surface area increases. The particle size of graphite crystallites within the two carbon blacks was calculated from the line width (FWHM) of the (002) reflection using the Scherrer equation. Values of 2.5 and 1.2 nm were determined for acetylene black and Vulcan, respectively.[2-4] The electrically-conducting diamond powder has a relatively low specific surface area, 0.6 m^2/g, because of the large particle size (8-12 μm) and lack of any porosity.

Figure 5.1 shows oxidation charge vs. time (*Q-t*) curves for different sp^2 carbon powder films recorded during potentiostatic polarization in 0.1 M $HClO_4$ at room temperature. The charge has been normalized to the mass of the carbon

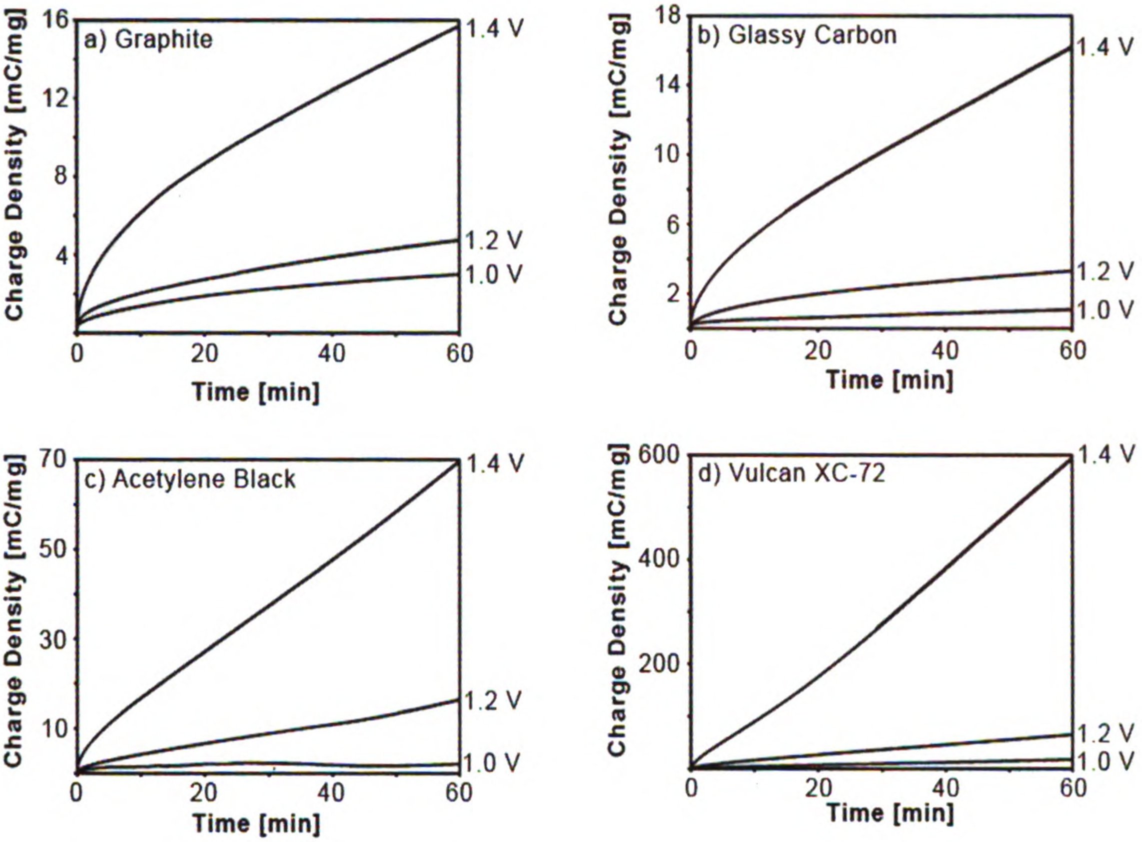

Figure 5.1. Chronocoulometric *Q-t* curves for a) graphite, b) glassy carbon, c) acetylene black and d) Vulcan XC-72 carbon powders a during 1-h potentiostatic polarization in 0.1 M $HClO_4$ at room temperature. The polarization potentials were 1.0, 1.2 and 1.4 V vs Ag/AgCl. The charge data are normalized to the mass of the carbon powder exposed to the solution.

powder exposed to the electrolyte (~1 cm^2 times the loading (see Table 5.1)). The total charge passed during the 1-h polarization increased with the applied potential in the following order: graphite < glassy carbon < acetylene black < Vulcan. For example at 1.4 V, the charge passed for these four carbons was 16, 16, 70 and 600 mC/mg of carbon, respectively. This trend correlates with the degree of microstructural disorder (see Raman data below), the specific surface area and the d_{002}-layer plane spacing (see Table 1). The more microstructurally-disordered the carbon is, the less resistant to oxidation it is; therefore, the greater the oxidation charge passed. This is because there is a greater fraction of reactive edge plane and defect sites exposed in the more disordered materials; sites at which the oxidation reaction rate is most rapid.[5]

Potentiodynamic *i-E* curves were recorded for the powders in the same electrolyte before and after each potentiostatic polarization period to probe for changes in the surface oxide content, surface area and/or electrode resistance caused by microstructural damage and carbon corrosion. Representative examples are presented in Figure 5.2. The magnitude of the overall background current increased with the polarization potential for all the carbons, except for graphite (Fig. 5.2a). This trend is consistent with a high degree of oxidation resistance (*i.e.*, microstructural stability and corrosion resistance). The most notable change was the increased redox current and charge centered at *ca.* 0.45 V (Fig. 5.2a). This current is associated with electroactive surface carbon-oxygen functionalities that populate the exposed edge plane and defect sites.[1, 6-8] There are multiple carbon-oxygen functional groups that can form but only the quinone/hydroquinone couple is redox-active in this potential range. [1, 6-8] These electrochemical data indicate that oxidation of the graphite powder under these conditions primarily involves formation of surface oxides at the native edge plane and defect sites with little associated alteration of the microstructure. For the glassy carbon powder, both the current and charge for the redox-active functional groups, as well as the background current over the entire potential range, increased with polarization potential. This is consistent with an increase in the

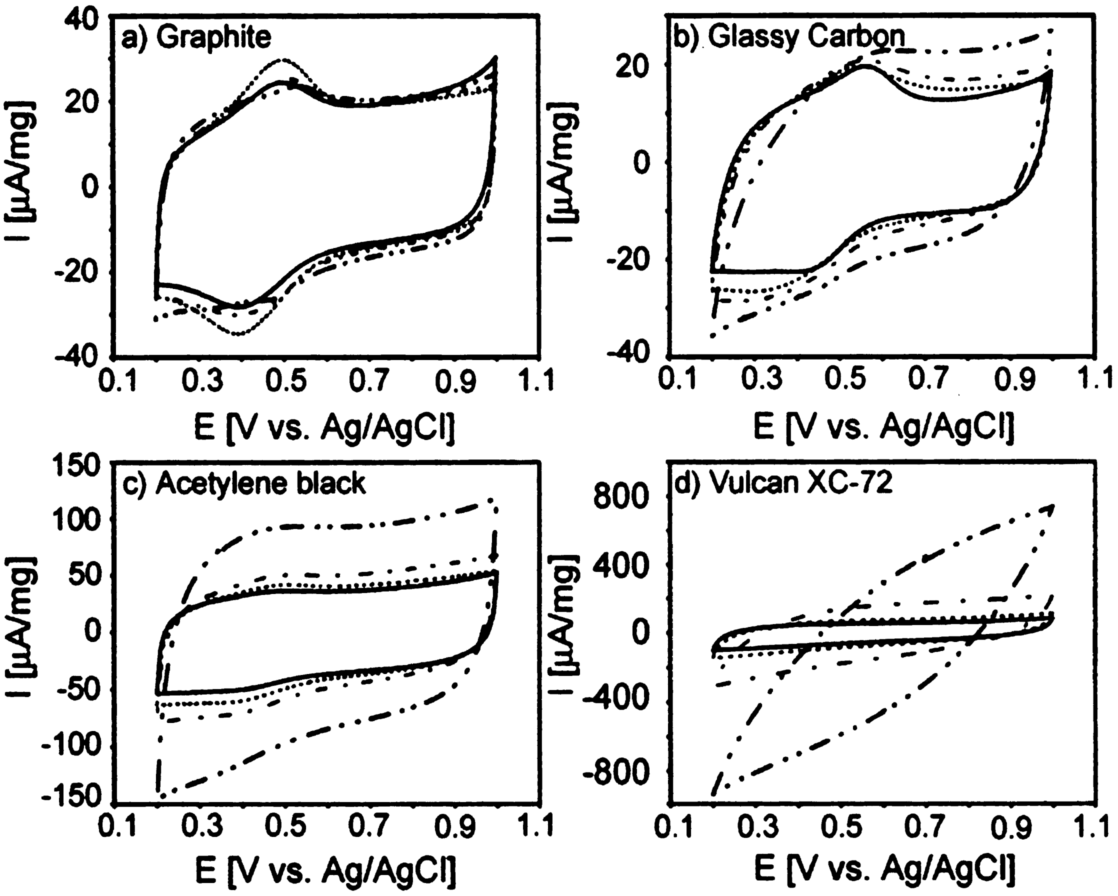

Figure 5.2. Potentiodynamic *i–E* curves for a) graphite, b) glassy carbon, c) acetylene black, and d) Vulcan XC-72 carbon powders before and after a 1-h polarization in 0.1 M $HClO_4$ at room temperature. Curves are shown for the as cast film (———) and the same film after polarization at 1.0 V (............), 1.2 V (— • —), and 1.4 V (— •• —). Scan rate = 50 mV/s. The currents are normalized to the mass of powder exposed to the solution.

powder surface area as well as an increase in electroactive carbon-oxygen functional group coverage at newly exposed edge plane and defect sites.

Much more significant increases in the background current were found for both the acetylene black and Vulcan powders. Due to the large specific surface areas of these materials, the current and charge associated with the redox-active functional groups is not resolved from the sizable background current. These potentiostatic polarization conditions produce surface oxidation that not only increases the oxide coverage but also increases the overall surface area contacting the electrolyte solution. For the most part, the damage was not severe enough to increase the ohmic resistance within the powder electrode as a consequence of carbon corrosion. The exception to this is the Vulcan powder after the 1.4 V polarization. The background cyclic voltammogram adopts a significant slope relative to the zero-current line that is caused by a major increase in the electrode resistance. Likely, localized carbon corrosion occurs, which leads to reduced particle-to-particle contact.

Q-t curves recorded during the potentiostatic polarization of the sp^3 and sp^2 carbons at 80 °C in 0.1 M H_2SO_4 are shown in Figure 5.3. Stability testing under these conditions is the benchmark for PEMFC carbon support evaluation. Again, the charge data have been normalized to the mass of the carbon powder exposed to the electrolyte (~1 cm^2). As was the case at room temperature, the total charge passed during the 0.5 h polarization increased with the applied potential in the following order: graphite < glassy carbon << acetylene black << Vulcan. Importantly, the specific charge passed for the sp^2 carbons was orders of magnitude larger than for the BDD powder (Fig. 5.3e). For example at 1.4 V, the charge passed for the four sp^2-bonded carbons was 35, 50, 300 and 900 mC/mg, respectively. As was the case for the room temperature polarizations, the oxidation charge passed increased with the potential for each of the powders with the largest charge seen for the powders with the more disordered microstructure. The oxidation was more extensive at the higher temperature as the charge passed at 80 ^{o}C was 2, 4, 4 and 1.5 times larger for graphite, glassy

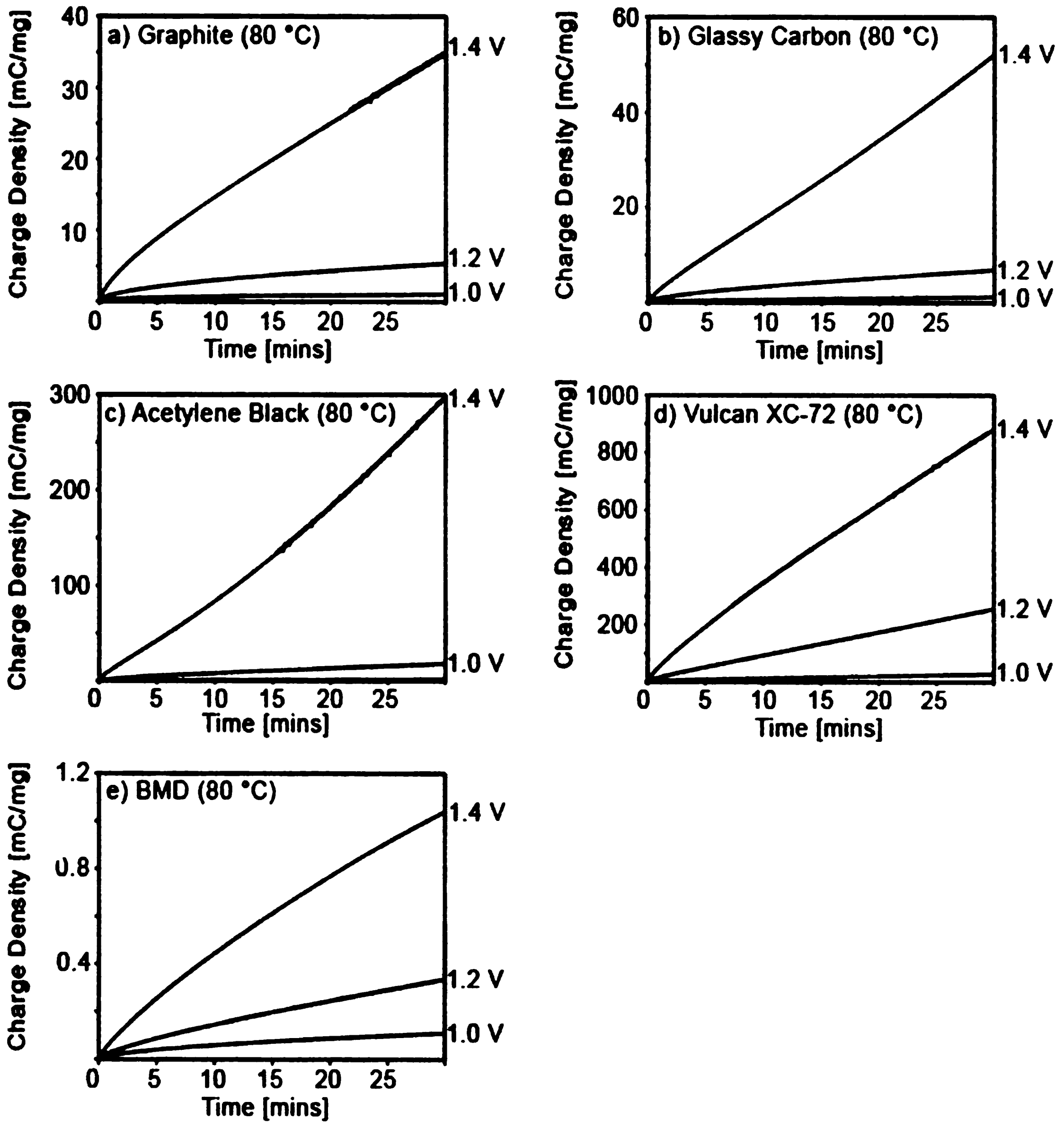

Figure 5.3. Chronocoulometric *Q-t* curves for a) graphite, b) glassy carbon, c) acetylene black, d) Vulcan XC-72, and e) boron-doped diamond powder during a 1-h potentiostatic polarization in 0.1 M H_2SO_4 at 80 °C. The polarization potentials were 1.0, 1.2 and 1.4 V vs. Ag/AgCl. The charge data are normalized to the mass of powder exposed to the solution.

carbon, acetylene black and Vulcan, respectively, than the charge passed at room temperature in $HClO_4$. Again, this correlates with the degree of microstructural disorder, the specific surface area and the d_{002} interlayer spacing (see Table 1).

Potentiodyamic *i-E* curves recorded before and after polarization at 80 °C are presented in Figure 5.4. The curves for the BDD powder were largely unchanged after polarization at any of the potentials, with a current magnitude 1-3 orders of magnitude lower than that for the sp^2 carbon powders. This demonstrates the BDD powder is microstructurally stable and relatively void of ionizable surface carbon-oxygen functionalities both before and after polarization.[5, 9-16] Clearly, the graphite powder is the most stable toward oxidation of all the sp^2 carbons as the magnitude of the overall background current remained relatively unchanged. The current and charge for the redox-active surface carbon-oxygen functionalities increased slightly with the potential indicative of minor exposure of some additional edge plane where these groups can form. Overall, polarization under these conditions primarily involves increased surface oxide formation with little apparent microstructural alteration. For the glassy carbon, acetylene black and Vulcan powders, the background current magnitude at all potentials increased, particularly after polarization at 1.4 V. The increased current reflects the increased exposed surface area due to microstructural degradation, as well as surface oxide formation. As was the case at room temperature, the potentiodynamic *i-E* curves for Vulcan not only increased in magnitude with polarization potential but they adopted a sloped shape due to increased electrode resistance presumably due to carbon corrosion. Reduced particle-particle contact results from the carbon support loss, and this leads to the increased ohmic resistance.

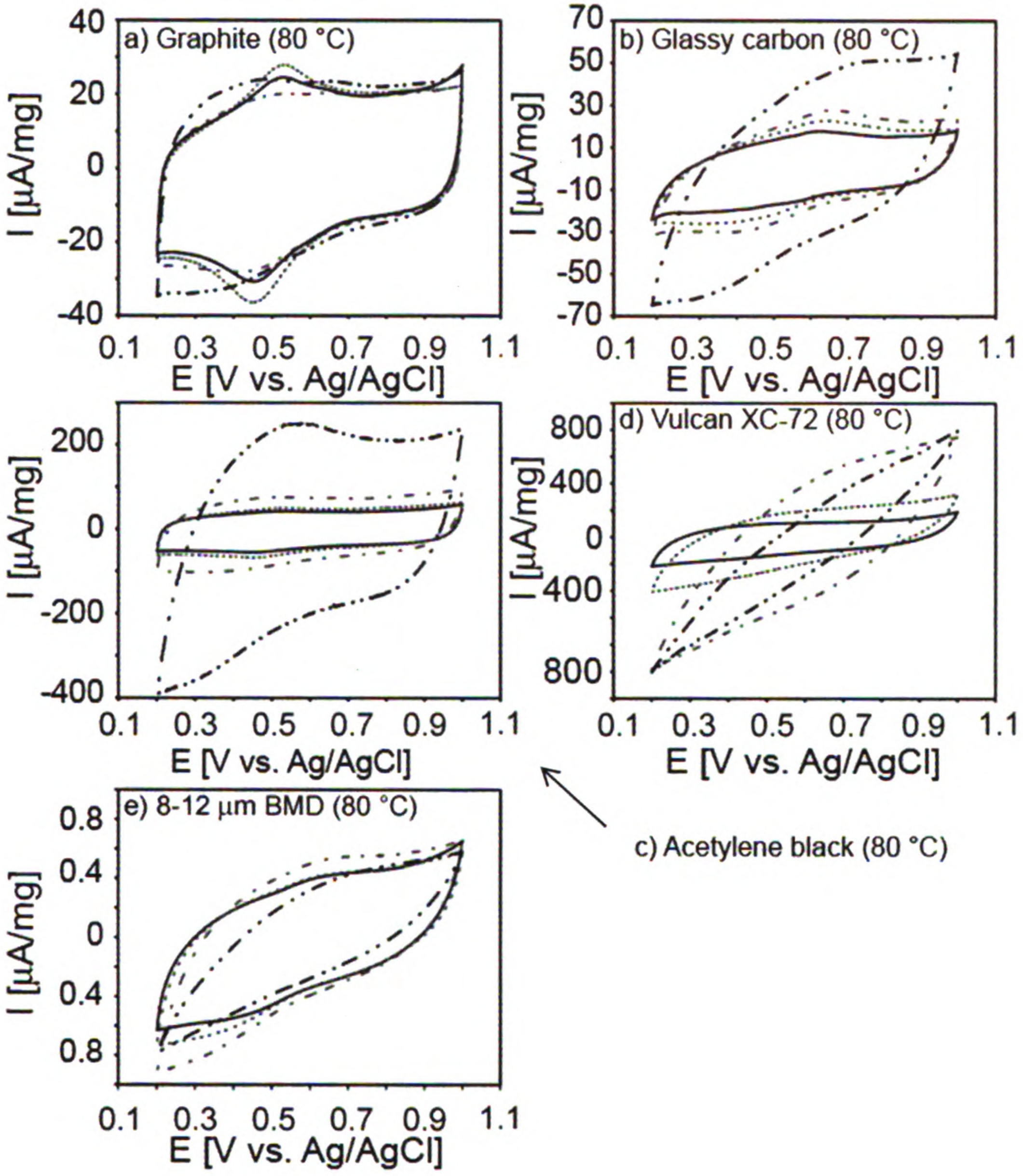

Figure 5.4. Potentiodynamic *i–E* curves for a) graphite, b) glassy carbon, c) acetylene black, d) Vulcan XC-72, and e) boron-doped diamond powders before and after a 1-h polarization in 0.1 M H_2SO_4 at 80 °C. Curves are shown for the as cast film (———) and the same film after polarization at 1.0 V (…………), 1.2 V (— • —), and 1.4 V (— •• —). Scan rate = 50 mV/s. The currents are normalized to the mass of powder exposed to the solution.

Plots of the oxidation charge passed at 1.4 V versus the specific surface area of the carbon are presented in Figure 5.5. Curves for both the room temperature and 80 °C data are presented. There is a clear correlation between the charge magnitude and the specific surface area. SEM images of the powders were also obtained to confirm the absence or presence of structural degradation

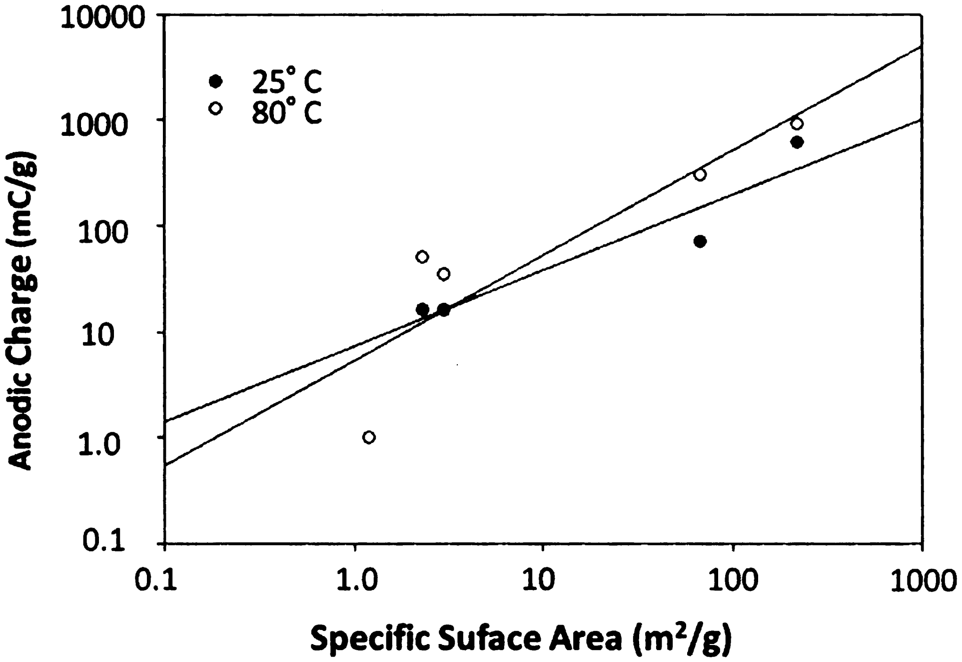

Figure 5.5. Plot of the anodic charge passed for each of the sp^2 and sp^3 carbon powders versus the specific surface area of the material. The charges were recorded at 1.4 V in 0.1 M $HClO_4$ at 25 °C and in 0.1 M H_2SO_4 at 80 °C.

and corrosion after polarization. Images for the graphite and glassy carbon powders before and after the 1.4 V polarization at 80 °C are presented in Figure 5.6a-d. No detectable changes in the morphology or microstructure of the graphite powder were found, as is apparent when comparing these images. The flat graphite flakes that range in size from *ca.* 5-75 μm were unchanged in shape after polarization. The microstructural stability of the graphite powder was further confirmed by an unchanged XRD d_{002} ($2\theta = 26.7^{\circ}$) linewidth after polarization. In contrast, some of the glassy carbon powder particles were structurally degraded during the polarization, as shown in Figures 5.6c and d.[11, 17] The images reveal that some of the spherical particles were fractured and reduced in size consistent with both microstructural degradation and corrosion (mass loss).

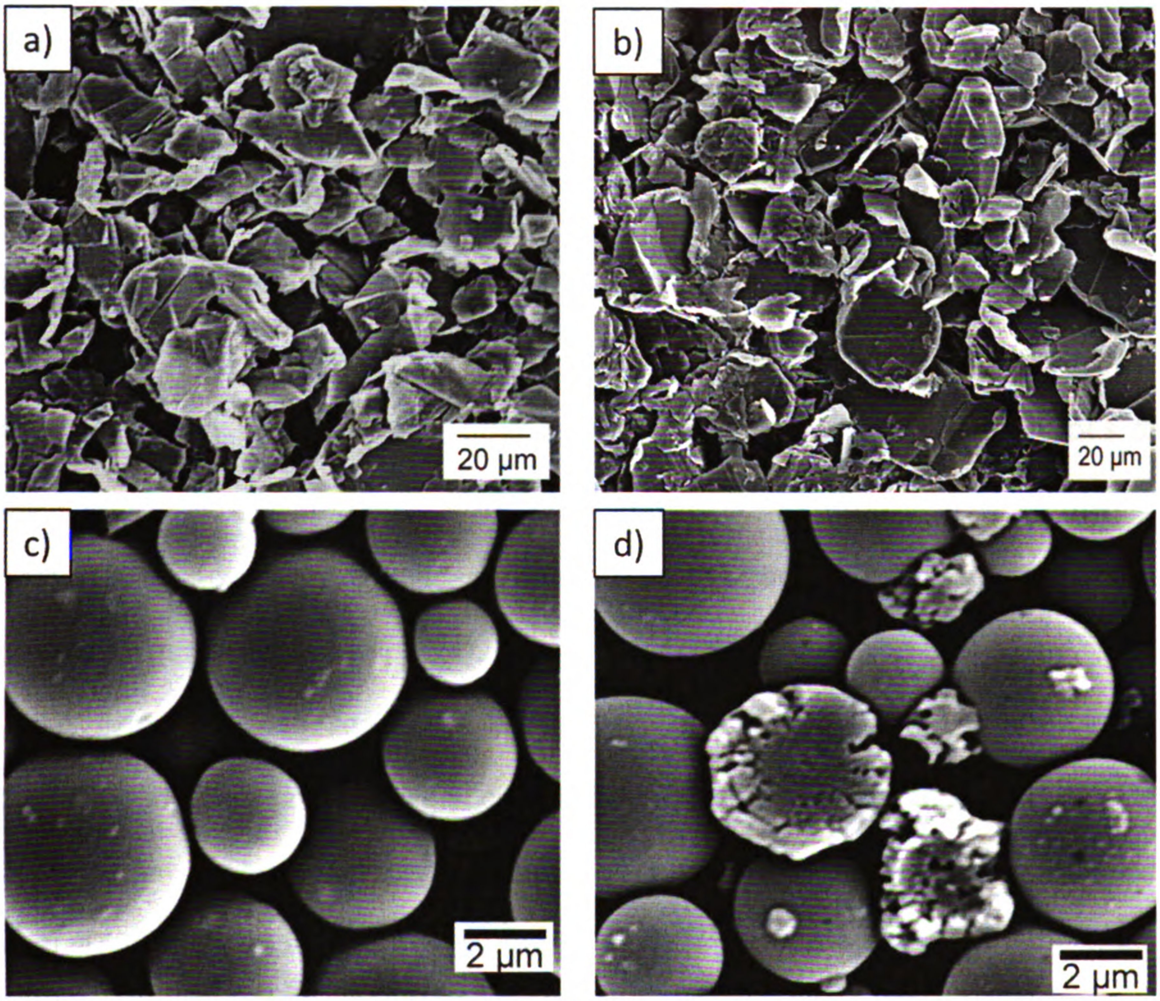

Figure 5.6. SEM micrographs of graphite powder: a) as cast and b) after 30 min of anodic polarization at 1.4 V and 80 °C in 0.1 M H_2SO_4, and glassy carbon powder: c) as cast and d) after 30 min of the same anodic polarization. µm

Figure 5.7a-f shows SEM images of BDD, acetylene black, and Vulcan powders before and after the 1.4 V polarization at 80 °C. The diamond particle morphology and size were unaffected by the polarization (Fig. 5.7a and b).[9, 11, 18] The small size of the acetylene black and Vulcan powders (< 10 nm) makes them difficult to individually resolve by SEM. Recall that particle sizes of 1-3 nm were calculated from the XRD d_{002} linewidths. For this reason, there are no obvious morphological or microstructural changes visible for the acetylene black (Fig. 5.7a and b) even though the coulometric and voltammetric data indicate an increased surface area after polarization. There is also no obvious morphological or microstructural change in the Vulcan powder (Fig. 5.7c and d) even though the electrochemical results are consistent with microstructural degradation and corrosion. Close inspection of the images, however, reveals more voids in the powder network after the 1.4 V polarization. The voids are the darker regions of the image and their presence may result from loss of carbon due to corrosion. This would explain the significant increase in electrode resistance seen in the potentiodynamic curves (Fig. 5.4).

Additional investigation of the sp^3 and sp^2 carbon powder microstructure during anodic polarization was accomplished by in-situ Raman spectroscopy.[19-22] The Raman spectrum for sp^2 carbon materials consists of a G-band centered near 1580 cm^{-1} and a D-band at ~1350 cm^{-1}.[19-22] The more microstructurally ordered the material is, the less intense the D-band is and the narrower the G-band tends to be. Therefore, the D-to-G band intensity ratio (D/G) reflects the degree of microstructural disorder (*i.e.*, fraction of exposed edge plane) of the sp^2

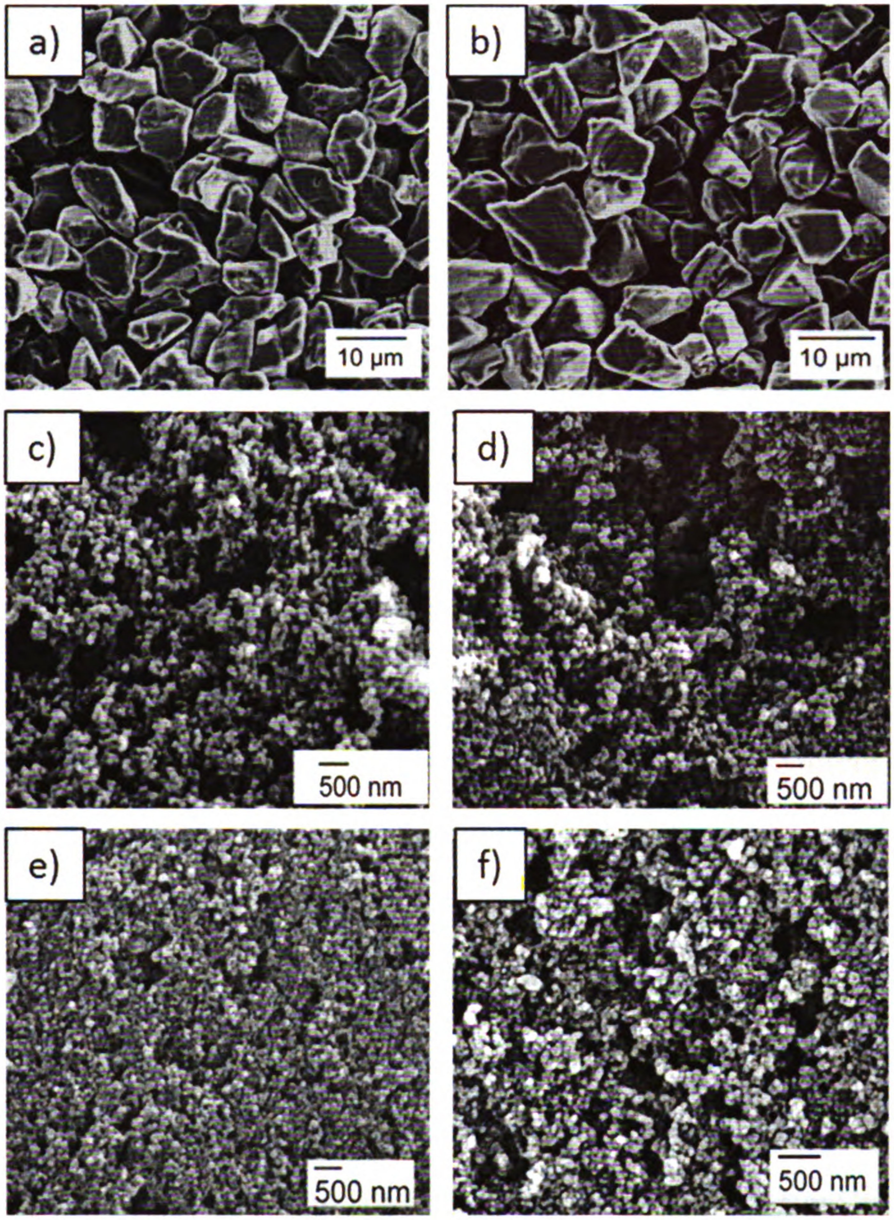

Figure 5.7. SEM micrographs of 8-12 μm diameter boron-doped diamond powder: a) as cast and b) after 30 min of anodic polarization at 1.4 V and 80 °C in 0.1 M H_2SO_4, and acetylene black: c) as cast and d) after 30 min under the same anodic polarization conditions. Images for: Vulcan XC-72 e) as cast and f) after 30 min under the same anodic polarization conditions.

carbon. The G-band has been assigned to the in-plane lattice vibrational mode of graphite while the 1625 cm^{-1} band corresponds to a peak in the density of vibrational states for graphite, [19-22] but has also been reported for intercalation compounds and oxidized sp^2 carbon.[21] The D-band has been the subject of much study. Wang et al. reported detailed Raman investigations of carbon materials and concluded that this band is an inherent mode of the graphite lattice, which becomes observable when the lattice symmetry is broken by a crystallite edge.[21] The chemical composition of the edge or the size of the associated crystallite does not influence the frequency of the D band, but the presence of the edge permits scattering by D-band phonons.[21]

For all the powders, the Raman measurements were made at room temperature and 1.4 V in 0.1 M $HClO_4$ for 120 min, except for the Vulcan, which was only polarized to 1.2 V. Not only was the polarization potential less for this material, but the incident laser intensity was also reduced by 75% in order to minimize damage of the powder. Raman spectra for the different sp^3 and sp^2 carbons are shown in Figure 5.8. Each spectrum for the BDD powder (Fig. 5.8e) is characterized by a sharp first-order phonon peak at 1330 cm^{-1} (FWHM = 10 cm^{-1}) with negligible scattering between 1500-1600 cm^{-1} that is due to sp^2 carbon impurity. The line position, intensity and linewidth were unchanged during the polarization consistent with a high level microstructural stability. The first-order phonon peak position and the linewidth remained nearly constant over 2 h at 1.4 V (Table 3).[22-24] This is consistent with there being little structural change in the BDD powder. The powder structural stability was further confirmed by XRD analysis. The diamond (111) and (220) diffraction peaks were unchanged in position ($2\theta = 43.76^o$) and linewidth (FWHM = 0.10^o) after a 30 min, 1.4 V polarization in 0.5 M H_2SO_4 at 80 °C. The background in the Raman spectrum did change with polarization time. Below 1300 cm^{-1}, the background decreased with

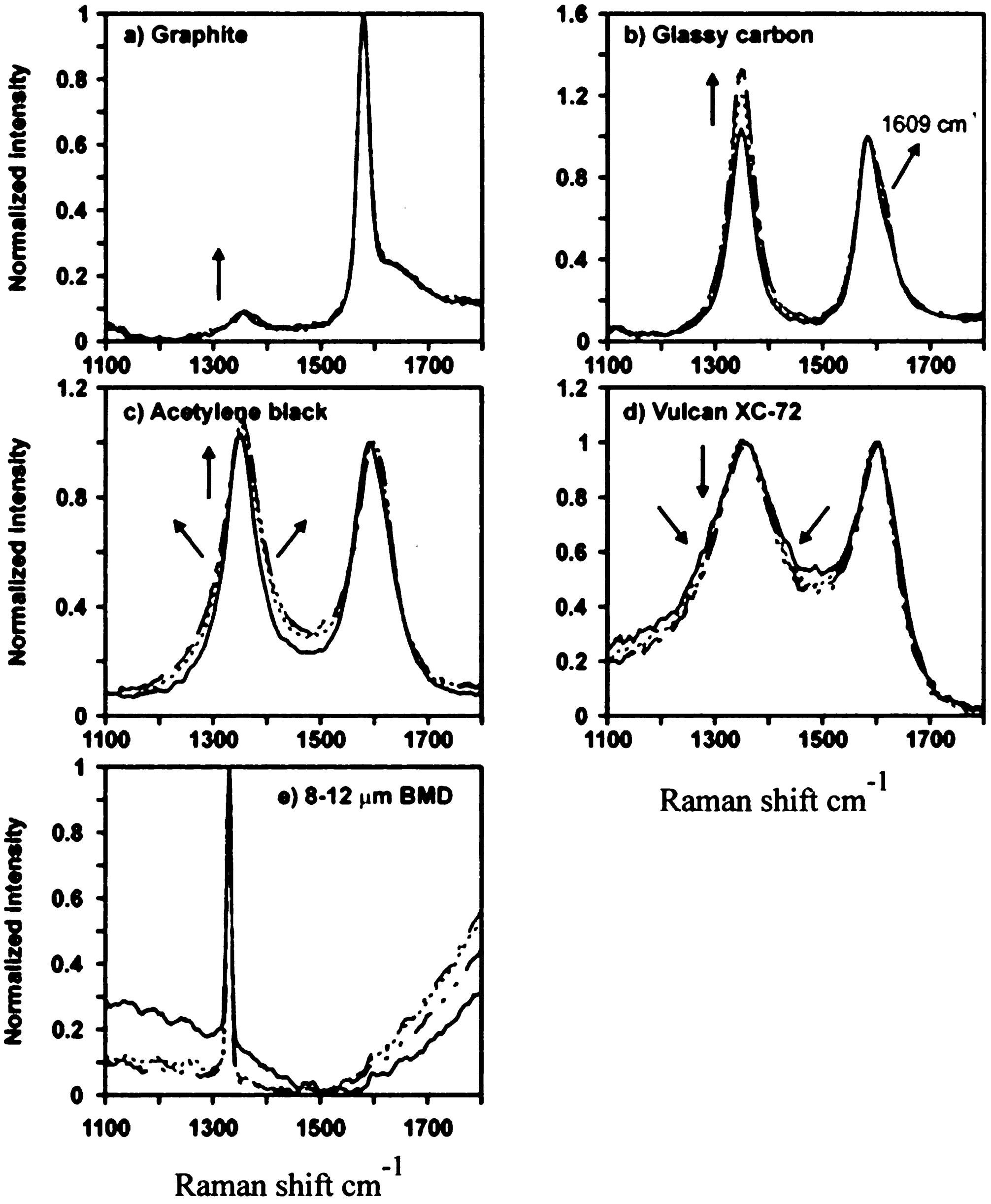

Figure 5.8. ***In-situ*** **Raman spectroelectrochemical measurements of a) graphite, b) glassy carbon, c) acetylene black, d) Vulcan XC-72, and e) boron-doped diamond powder in 0.1 M $HClO_4$ at room temperature. Spectra are shown for the open circuit potential (———) and after 30 min (............), 60 min (— • —) and 120 min (— •• —) of anodic polarization at 1.4 V vs. Ag/AgCl. The exception is Vulcan XC-72, which was polarized at 1.2 V. The polarizations were performed at room temperature. The arrows show the direction of peak intensity increase with polarization time.**

time while the background above 1600 cm^{-1} increased. The cause(s) for this are unclear at present but may be related to changes in structure or chemical composition of the Nafion® binder.

The spectrum for the graphite powder has a weakly intense D-band at 1353 cm^{-1} as well as an intense and narrow G-band at 1580 cm^{-1} (Fig. 5.8a). There is also a shoulder present at *ca.* 1625 cm^{-1}. Even though oxidation of the surface occurred (see Fig. 5.2), there was no change in the peak position and only a slight increase in the D/G band intensity ratio with the change in surface chemistry. Figure 5.9a shows that the D/G band intensity ratio increased from 0.91 to 0.98 during the 2-h polarization. This ratio increase is consistent with minor microstructural changes that lead to the exposure of additional edge plane density. It is at these edge plane sites where the surface oxides form.

Figure 5.8b shows Raman spectra for glassy carbon powder as a function of time during the polarization. The D-band intensity increased with polarization time but did not change in position or width (FWHM). The G-band intensity was unchanged, but a shoulder at *ca.* 1610 cm^{-1} developed over time. Figure 5.9b shows that the D/G band intensity increased from *ca.* 1.05 to 1.32 during the first 70 min of the polarization, but remained unchanged afterward. The increased ratio is consistent with a greater fraction of edge plane exposure during the early stages of polarization. This is followed by a period where the microstructure remains relatively unchanged. The initial microstructural alterations may be caused by limited anion intercalation, as evidenced by the emergence of the 1610 cm^{-1} shoulder. Some limited intercalation is expected because of the turbostratic microstructure and the small size of the ordered domains. This intercalation strains the graphene sheets of the ordered domains, which ultimately results in layer-plane fracturing. This is a likely reason for the increased D/G ratio. After the initial microstructural damage, the oxidation reaction mechanism likely involves direct gasification to CO_2. At this point, a constant D/G is reached. For this reason, glassy carbon as well as acetylene black and Vulcan powders are more susceptible to corrosion than is the graphite powder.

Figure 5.8c shows spectra for acetylene black that are similar to those for glassy carbon. The D-band intensity and width (FWHM) increased with polarization time, but the position remained unchanged. The G-band intensity remained unchanged with no shoulder at *ca.* 1610 cm^{-1}. Figure 5.9c shows that the D/G band intensity increased from 1.03 to 1.08 during the first 1h of polarization but remained unchanged afterward. The increase in the D/G band intensity ratio is consistent with a slight increase in the fraction of edge exposed during the early stages of polarization. There is a surface area increase associated with this microstructural change, as evidenced in the cyclic voltammograms shown in Fig. 5.2. During the early stages of polarization, slight changes in the microstructure caused by the electrochemical generation of graphite oxide on the surface likely produces strain, which causes the lattice damage.[6, 21, 25] At these times, the oxidation charge passed is likely for this process. However, at later times, the oxidation charge passed is mainly for corrosion.

The trends for Vulcan are quite different. Polarization of this carbon at 1.4 V resulted in severe mass loss due to corrosion so the tests could be performed

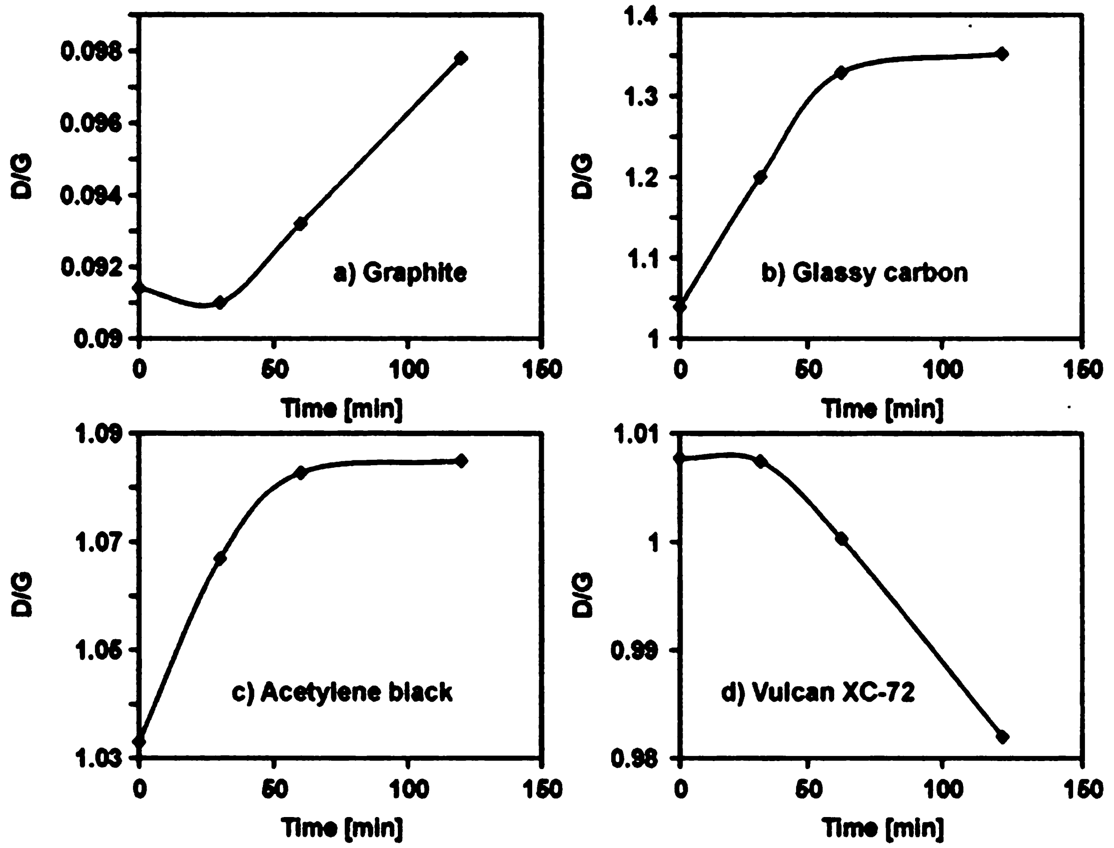

Figure 5.9. Raman spectroscopic D (~1350 cm^{-1})- to G (~1580 cm^{-1})- band intensity ratios for a) graphite, b) glassy carbon, c) acetylene black, and d) Vulcan XC-72 carbon powders as a function of the polarization time at 1.4 V vs. Ag/AgCl in 0.1 M $HClO_4$ at room temperature. The anodic polarization potential for the Vulcan XC-72 powder was only 1.2 V.

only at a less positive potential (1.2 V). The D-band intensity and linewidth decreased with increasing polarization time at 1.2 V. Figure 5.8d shows spectra for Vulcan after polarization at the different potentials. Clearly, the spectral features for this powder are similar to the spectra for acetylene black and glassy carbon. The G-band intensity and line position remained relatively constant with polarization time. Figure 5.9d shows that for the first 30 min of the polarization the D/G intensity ratio was constant but after this period, the ratio decreased continuously from about 1.01 to 0.98. This is consistent with the loss of some edge plane density with time, most likely due to corrosion. This trend is consistent with the apparent powder loss (void formation) in the SEM image in Figure 5.7 and the highly resistive potentiodynamic *i-E* curve in Figure 5.2.

5.3 Discussion

The electrochemical oxidation of carbon powders involves multiple steps, with the overall reaction mechanism depending on the native carbon microstructure as well as the applied potential, solution pH and ionic composition, and temperature. In the severest case, the carbon is fully oxidized or corroded to CO/CO_2 and this causes catastrophic electrode failure in terms of lost electrocatalyst activity and increased ohmic resistance. If the carbon is only partially oxidized to form surface carbon-oxygen functionalities and oxide phases, electrocatalyst may be lost (agglomeration or detachment) due to the microstructural alterations associated with the surface oxidation.[6, 21, 25-28] Finally, oxidation of the carbon support can reduce the hydrophobicity necessary for proper water management during PEMFC operation (4,8,12).[1, 29, 30] In summary, carbon support oxidation can deleteriously affect the lifetime and performance of PEMFCs.

Taken together, the results reported herein provide insight on how the microstructurally-different carbon powders undergo electrochemical oxidation under conditions that would be experienced during PEMFC start-stop cycling under H_2-starvation. The extent of oxidation and associated microstructural degradation increases in the following order: BDD << graphite < glassy carbon << acetylene black << Vulcan. With the exception of BDD, the specific oxidation charge passed increased with potential for each material and was greatest for the more microstructurally-disordered carbons. Clearly, conducting BDD powder is the most oxidation-resistant of all the carbons tested and is quite dimensionally stable. Most relevant for this discussion is what happens during potentiostatic polarization at 1.4 V and 80 °C in 0.1 M H_2SO_4. This polarization produced a specific charge for BDD that is an order of magnitude less than for graphite and glassy carbon powder, and over 2 orders of magnitude less than that for acetylene black and Vulcan powders. The potentiodynamic *i-E* curves recorded for BDD pre- and post-polarization were unchanged indicative of an unaltered particle microstructure and maintenance of good particle-particle contact within the powder/binder network. In other words, under these test conditions, the integrity of the diamond/binder interface appears to remain intact. The surface atoms of the diamond powder are terminated with hydrogen after growth. This surface chemistry is, however, readily converted to an oxygenated one (*e.g.*, OH functional groups) during the early stages of polarization, even at the lowest potential of 1.0 V. The major difference between diamond and the sp^2 carbon powders is the strong three-dimensional lattice bonding that exists within the former. This strong bonding imparts a high degree of structural stability. The in situ Raman spectroscopic data confirm this as the line position and linewidth of the diamond phonon mode (1333 cm^{-1}) were unchanged during the polarization.[22-24] In summary, the electrochemical oxidation of BDD under these conditions simply involves a transformation of the surface chemistry without any microstructural alteration. Most of the oxidation charge passed under these conditions is associated with oxygen evolution (*i.e.*, water oxidation) with only a small fraction, mainly at the early times, due to surface oxidation.

The electrochemical oxidation of the sp^2 carbon powders is more complex and involves a combination of surface oxide formation at native edge plane and defect sites, potential-dependent intercalation of anions and solvent molecules that cause layer plane exfoliation, oxidation of the intercalation compound or solvent molecules leading to subsurface gas evolution which produces blistering and layer plane fracturing, surface oxide formation at the newly formed edge plane and defect sites, and gasification or corrosion. The electrochemical oxidation mechanism of graphite has been discussed in the literature.[25, 26, 31] Of the sp^2 carbons evaluated, graphite powder is most resistant to surface oxidation and microstructural degradation. The potentiodynamic *i-E* curves recorded pre- and post-polarization revealed that coverage of electroactive surface carbon-oxygen functional groups increases with the polarization potential. Largely though, the exposed surface area and microstructure remained unaltered based on the relatively constant voltammetric charge pre- and post-polarization (Figs. 3,5). The electrochemical oxidation produces surface oxides at the native edge plane and defect sites.[1, 6, 25-27, 31] The oxide formation and or some minor anion and solvent intercalation strains the lattice, producing minor microstructural damage. This damage, indicated by the minor Raman D/G peak ratio increase

(Fig. 5.9), creates new edge plane sites at which the surface oxides can form. Besenhard and Fritz reported that the graphitic layer plane spacing increased from 335 to 650 pm following graphite oxide formation.[27] Alsmeyer and McCreery studied the lattice damage to HOPG brought about by potential-dependent anion intercalation and subsequent oxidation in acidic media.[31] They found the relative order of the damage-inducing acids was $HNO_3 > HClO_4 > H_2SO_4$. They also found that intercalation always accompanied surface oxidation. Goss et al. reported subsurface gas evolution occurs at sites of anion and/or solvent intercalation. The gas evolution produces lattice strain and eventual layer plane fracturing.[25] Any intercalation must occur at solution-accessible edges. Since the SEM images of the graphite powder post-polarization revealed no evidence of any structural damage, and the electrochemical measurements indicated no change in electrode resistance, we conclude that oxidation under these conditions simply involves surface oxide formation with minimal lattice damage or carbon corrosion. The results are consistent with the mechanism proposed by Gewirth and Bard based on ECSTM studies.[26] The authors suggested that formation of graphite oxide occurs according to a nucleation and growth mechanism. Irreversible breaking of C-C bonds and the formation of the graphite oxide phase occurred initially at the step and defect sites. The oxide phase formation occurred most rapidly along the step edges and defects, and at a slower rate on the basal plane. The basal plane was unaffected by the anodic polarization until the oxide grows in from the edge plane and defect sites. The graphite oxide phase is amorphous, porous and chemically stable in acid.[28, 32]

The oxidation mechanism of glassy carbon is somewhat different. This powder is microstructurally disordered with a significant fraction of exposed edge plane.[7, 8, 21, 28, 32] For this reason, the specific oxidation charge passed at each of the polarization potentials is greater than for graphite. The microstructural disorder is reflected in a Raman D/G peak intensity ratio of 1.05 prior to oxidation. Glassy carbon is a turbostratic material and the ordered domains of graphitic carbon are quite small in lateral dimension.[4, 33] This means there is little internal volume for anion and solvent intercalation. The potentiodynamic *i-E* curves recorded pre- and post-polarization revealed the coverage of electroactive surface carbon-oxygen functional groups increases with the polarization potential as does the charge under the curve (Figs. 5.2, 5.4). This is consistent with an increase in the thickness of the surface oxide phase, as shown using ellipsometry in the work by Kepley and Bard.[32] There is a high fraction of exposed edge plane where the graphite oxide phase can nucleate and grow. The amorphous oxide is an extension of the electrode, and this increases the electrode area in contact with the solution. Eventually, the oxide growth causes some structural damage, which further increases the specific surface area of the electrode. The structural damage is likely caused by some minor anion and solvent intercalation associated with oxide formation that strains the lattice. This damage creates new edge plane sites for additional oxide growth. The increasing Raman D/G peak intensity ratio during the first 60 min of polarization at 1.4 V is consistent with such microstructural damage. After 60 min, the D/G intensity ratio reached a constant value indicative of an unchanging microstructure. It is supposed that this is the point at which the GC lattice can be damaged no further by graphite oxide formation. Therefore, at this point, most of the charge is likely associated with carbon corrosion. Evidence for corrosion can be seen in the SEM images presented in Figure 5.6.

The trends for the acetylene black were similar to those for glassy carbon. Acetylene black is as microstructurally-disordered as glassy carbon based on the initial D/G ratio of 1.04. Therefore, this material has a significant fraction of exposed edge plane. The cyclic voltammetric background current increased with the polarization potential, and the oxidation charge passed at each potential was significantly greater than for graphite or glassy carbon. This is due to the greater specific surface area. The increase in background current is consistent with an increase in the exposed electrode area due to the formation of surface oxides. There is some evidence for the redox-active surface carbon-oxygen functional groups after polarization at all of the potentials, but the peak currents are not as well resolved as they are for glassy carbon or graphite. Interesting though, the slope of the curves did not change, so there was no apparent increase in the electrode resistance. During polarization at 1.4 V, the D/G ratio increased from 1.04 to 1.35 during the first 50 min of the polarization indicative of a greater fraction of exposed edge plane. However, after this period, the ratio remained unchanged for the remainder of the polarization period. We suppose this is the point at which the acetylene black lattice can be damaged no further by graphite oxide formation. Therefore, at this point, most of the charge is likely associated with carbon corrosion.

The most reactive material is Vulcan XC-72. The reason for this is the microstructural disorder and the high specific surface area. The cyclic voltammetric background current increased progressively with the polarization potential consistent with an increased exposed surface area. During the 1.2 V polarization, the voltammetric curves adopted a sloped shape indicative of an increase in the ohmic resistance. Unlike the other powders, the background current after the 1.4 V polarization is smaller than for the powder after the 1.2 V polarization. This is consistent with mass loss due to carbon corrosion. As mentioned above, polarization at 1.4 V caused severe corrosion, so the in situ Raman measurements had to be made at 1.2 V. Corrosion of Vulcan under these conditions is well established.[1, 34] During the first 30 min of the 1.2 V polarization, the D/G remained constant at approximately 1.01. Surface oxide growth likely occurs at the existing edge plane sites during this period as well as at the newly created edge plane and defect sites caused by the oxide formation. However, after the 50 min mark, the D/G ratio progressively decreased. This is consistent with a reduction in the fraction of edge plane exposed. Clearly, the edge plane density is reduced due to carbon corrosion. The corrosion likely occurs preferentially at the more microstructurally-disordered regions of the powder leaving a more microstructurally-ordered phase. Consistent with this mechanism is the major increase in electrode resistance seen in the background cyclic voltammograms and the apparent voids seen in the SEM image (Fig. 5.7).

5.4 Conclusions

The microstructural stability of BDD coated diamond powder was investigated and compared to sp^2 carbon powders. The oxidation charge passed at potentials between 1.0 and 1.4 V vs. Ag/AgCl at room temperature and 80 °C increases in the following order: BDD < graphite < glassy carbon << acetylene black << Vulcan. This charge tracks the degree of microstructural disorder as determined by Raman spectroscopy as well as the specific surface area of the material. The least reactive material is the BDD powder followed by graphite and glassy carbon. On BDD, there is no significant microstructural degradation or corrosion under any of the polarization conditions. There is simply a change in surface chemistry from a hydrogen to an oxygen termination. Of the sp^2 carbon powders, graphite is the least susceptible to oxidation. The polarization produces a surface oxide phase and some minor microstructural damage; however, there is no evidence of any corrosion. Polarization of the glassy carbon causes surface oxide formation, microstructural damage and carbon corrosion.

The most reactive carbons were acetylene black and Vulcan. The polarization causes surface oxide formation and microstructural damage to acetylene black. After the formation of a complete oxide phase, corrosion commences. Corrosion of the Vulcan powder is the most severe and commences at a lower potential that for the other carbons. The corrosion removes the more microstructurally-disordered regions of the powder, leaving behind more microstructurally-ordered phases.

5.5 References

[1] K. H. Kangasniemi, D. A. Condit, and T. D. Jarvi, *Journal of the Electrochemical Society* **151**:E125 (2004).

[2] J. Biscoe and B. E. Warren, *Journal of Applied Physics* **13**:364 (1942).

[3] T. Ungar, J. Gubicza, G. Ribarik, C. Pantea, and T. W. Zerda, *Carbon* **40**:929 (2002).

[4] K. Kinoshita, Carbon : Electrochemical and Physicochemical Properties, Wiley, New York, 1988.

[5] R. L. McCreery, *Chem. Rev. (Washington, DC, U. S.)* **108**:2646 (2008).

[6] K. Kinoshita and J. Bett, *Carbon* **11**:237 (1973).

[7] I. F. Hu, D. H. Karweik, and T. Kuwana, *Journal of Electroanalytical Chemistry and Interfacial Electrochemistry* **188**:59 (1985).

[8] D. T. Fagan, I. F. Hu, and T. Kuwana, *Analytical Chemistry* **57**:2759 (1985).

[9] A. Ay, V. M. Swope, and G. M. Swain, *Journal of the Electrochemical Society* **155**:B1013 (2008).

[10] Q. Chen, M. C. Granger, T. E. Lister, and G. M. Swain, *Journal of the Electrochemical Society* **144**:3806 (1997).

[11] A. E. Fischer and G. M. Swain, *Journal of the Electrochemical Society* **152**:B369 (2005).

[12] M. C. Granger, M. Witek, J. Xu, J. Wang, M. Hupert, A. Hanks, M. D. Koppang, J. E. Butler, G. Lucazeau, M. Mermoux, J. W. Strojek, and G. M. Swain, *Analytical Chemistry* **72**:3793 (2000).

[13] G. M. Swain, *Journal of the Electrochemical Society* **141**:3382 (1994).

[14] J. Xu, Q. Chen, and G. M. Swain, *Analytical Chemistry* **70**:3146 (1998).

[15] R. Bowling, R. T. Packard, and R. L. McCreery, *Langmuir* **5**:683 (1989).

[16] P. Chen, M. A. Fryling, and R. L. McCreery, *Analytical Chemistry* **67**:3115 (1995).

[17] D. Y. Kim, B. Merzougui, and G. M. Swain, *Chemistry of Materials* **21**:2705 (2009).

[18] A. E. Fischer, M. A. Lowe, and G. M. Swain, *Journal of the Electrochemical Society* **154**:K61 (2007).

[19] F. Tuinstra and J. L. Koenig, *Journal of Chemical Physics* **53**:1126 (1970).

[20] R. J. Nemanich and S. A. Solin, *Physical Review B: Condensed Matter* **20**:392 (1979).

[21] Y. Wang, D. C. Alsmeyer, and R. L. McCreery, *Chemistry of Materials* **2**:557 (1990).

[22] J. R. Dennison, M. Holtz, and G. Swain, *Spectroscopy (Eugene, Oregon)* **11**:38 (1996).

[23] R. J. Nemanich, J. T. Glass, G. Lucovsky, and R. E. Shroder, *Journal of Vacuum Science & Technology, A: Vacuum, Surfaces, and Films* **6**:1783 (1988).

[24] M. Mermoux, B. Marcus, G. M. Swain, and J. E. Butler, *Journal of Physical Chemistry B* **106**:10816 (2002).

[25] C. A. Goss, J. C. Brumfield, E. A. Irene, and R. W. Murray, *Analytical Chemistry* **65**:1378 (1993).

[26] A. A. Gewirth and A. J. Bard, *Journal of Physical Chemistry* **92** (1988).

[27] J. O. Besenhard and H. P. Fritz, *Chem. Int. Ed. Engl* **22** (1983).

[28] G. K. Kiema, G. Gitzpatrick, and M. T. McDermott, *Analytical Chemistry* **71**:1378 (1999).

[29] B. C. H. Steele, *Journal of Materials Science* **36**:1053 (2001).

[30] M. F. Mathias, R. Makharia, H. A. Gasteiger, J. J. Conley, T. J. Fuller, C. I. Gittleman, S. S. Kocha, D. P. Miller, C. K. Mittelsteadt, T. Xie, S. G. Yan, and P. T. Yu, *Electrochemical Society Interface* **14**:24 (2005).

[31] D. C. Alsmayer and R. L. McCreery, *Analytical Chemistry* **64** (1992).

[32] L. J. Kepley and A. J. Bard, *Analytical Chemistry* **60** (1988).

[33] P. Harris, *Critical Reviews in Solid State and Materials Sciences* **30**:235 (2005).

[34] C. H. Paik, T. D. Jarvi, and W. E. O'Grady, *Electrochemical and Solid-State Letters* **7**:A82 (2003).

Chapter 6

The Physicochemical and Electrochemical Properties of Diamond Powders Coated with Boron Doped Ultrananocrystalline Diamond (B-UNCD)

6.1 Introduction

In this Chapter, the preparation of moderately high specific surface area (~50 m^2/g) and electrically conducting (~0.6 S/cm) diamond powder is described. The powders were prepared by coating 500 and 100 nm diam. particles with a layer of boron-doped ultrananocrystalline diamond (B-UNCD diamond). The B-UNCD was deposited from an Ar-rich source gas mixture consisting of 1% CH_4, 5% H_2, and 94% Ar with 10 ppm B_2H_6 used for boron doping. Smooth, nanograined diamond is formed in these Ar-rich mixtures because of a high rate of renucleation that is achieved by virtue of the gas-phase composition and growth conditions. Because of the high renucleation rate, ultrananocrystalline diamond is a more practical coating for substrate powders than diamond deposited from H_2-rich CH_4/H_2 source gas mixtures. The powders were characterized before and after UNCD overcoating by scanning electron microscopy (SEM), high resolution transmission electron microscopy (HRTEM), Raman spectroscopy, and Brunauer–Emmett–Teller (BET) surface area and electrical conductivity measurements. Additionally, the electrochemical properties of the powders were evaluated using $Fe(CN)_6^{-3/-4}$, $IrCl_6^{-2/-3}$, and $Fe^{+3/+2}$ as redox probes by mounting the powders in a pipette electrode.[1] Finally, the microstructural stability and corrosion resistance of the conductive diamond powder was evaluated during anodic polarization at 1.4 V vs. Ag/AgCl in 0.5 M H_2SO_4 for 1.5 h at 80 °C. This is an accepted accelerated degradation test for carbon electrocatylst support materials intended for use in PEMFCS. This potential was selected because such values can periodically be experienced in fuel cell stacks during start-up under H_2-starved conditions.[2-5] Carbon corrosion (gasification) can occur under this condition that is significant enough to produce lost catalyst activity and increased ohmic resistance. For comparison, 3–4 μm diam. glassy carbon (GC) powder was also tested. The powders were evaluated by cyclic voltammetry and SEM before and after anodic polarization.

6.2 Results

6.2.1 Diamond Powder Morphology and Microstructure

The morphology of the powder before and after B-UNCD deposition was investigated by SEM. Figure 6.1A shows an SEM image of 500 nm diam. powder prior to deposition. The uncoated powder particles are irregularly shaped with sharp jagged edges. The facet surfaces, however, are relatively smooth. After deposition, the seed particles were covered by a diamond overlayer possessing a nodular morphology, as seen in Fig. 6.1B. The jagged edges are no longer present because of this overlayer. The nodular morphology is characteristic of diamond grown from Ar-rich source gas mixtures and results from the high rate of renucleation during growth.[6-8] In other words, new nucleation events frequently happen that limit any one of the nuclei from growing into a large crystal. It appears in the image that much of the diamond powder surface has been covered with the doped UNCD overlayer. Particle–particle fusion, an inevitable occurrence with this approach, is evident in the three coalesced particles in the upper part of the image. This coalescence reduces the specific surface area but likely improves the electrical conductivity through increases in the carrier mobility. It is more difficult to resolve morphological changes of the smaller 100 nm diam UNCD coated powders. Images of the powder before and after coating are presented in Fig. 6.1C and 6.1D. After coating, there is a considerable increase in the size of most of the seed particles with significant size variability. Based on the variable particle size, there are undoubtedly some regions where the rate of diamond growth is higher than others. Additionally, the larger particles also result

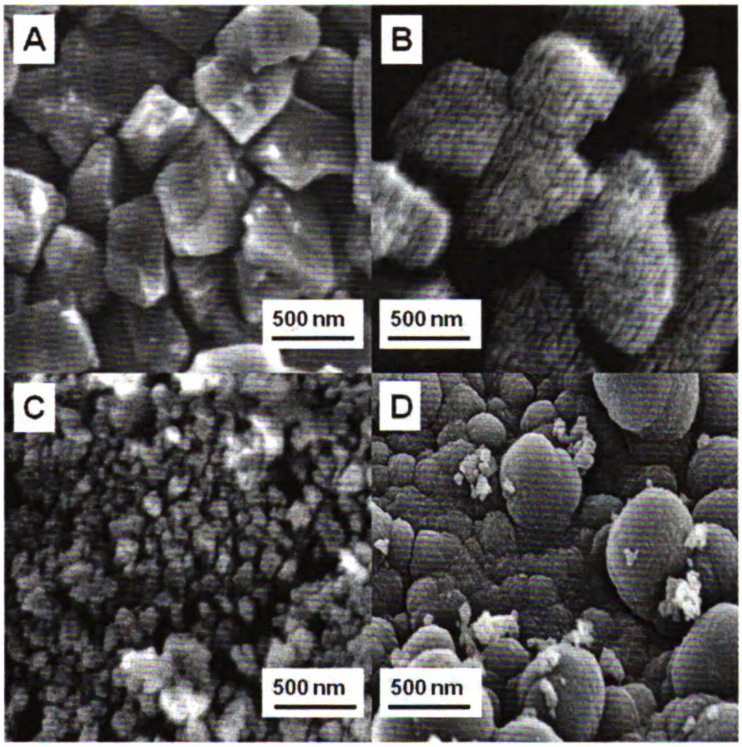

Figure 6.1. SEM images of 500 and 100 nm diam. diamond powder (A) and (C) before, and (B) and (D) after deposition of a boron-doped UNCD for 2 h.

from extensive particle–particle fusion. In fact, particle coalescence appeared more prominent for the 100 nm than for the 500 nm diam. powder. This caused a reduction in the specific surface area from 53 to 26 m^2/g (Table 6.1). A challenge with preparing conducting diamond powder via this core-shell approach is the balance between the growth time and conditions needed to achieve a near complete coating of individual particles with the avoidance of significant particle fusion.

Raman spectroscopy was used to evaluate the microstructure of the uncoated and coated powders. Figure 6.2 shows typical Raman spectra for a 100 nm diam diamond powder sample before and after B-UNCD deposition. The spectrum for the coated 500 nm diam. diamond powder had similar spectral features. The spectrum for the uncoated diamond powder consists of a single peak at 1332 cm^{-1} with a full width at half maximum (fwhm) of 8 cm^{-1}.[9, 10] This is the first-order phonon mode for cubic diamond. There is little photoluminescence background and little scattering in the 1500–1600 cm^{-1} region that is characteristic of sp^2 and mixed sp^2/sp^3-bonded carbon impurity. The fwhm is inversely related to the phonon lifetime.[10] The relatively narrow linewidth for the powder compares favorably with that seen for a diamond standard and indicates that the powder particles are relatively defect-free.

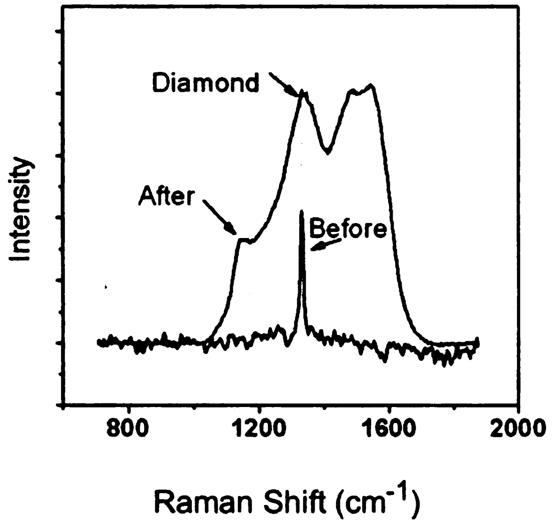

Figure 6.2. Visible Raman spectra of 100 nm diam. diamond powder before and after coating with a layer of boron-doped ultrananocrystalline diamond.

The spectrum for the coated powder is identical to that for UNCD films deposited from Ar-rich source gas mixtures.[11, 12] In addition to the diamond peak at 1332 cm^{-1}, which is largely buried within more intense scattering in this region, the spectrum has 4 additional peaks at 1150, 1350, 1450, and 1550 cm^{-1}. All these peaks are associated with non-diamond carbon phases, being comprised of both sp^2 and sp^3 hybridizations at the grain boundaries. The peaks at 1150 and 1450 cm^{-1} are associated with trans-polyactylene-like carbon in the grain boundaries and the peaks at 1150 and 1550 are attributable to the D and G bands of graphite, respectively.[13-15] Spectrum for B-UNCD is dominated by the sp^2 grain boundary carbon due to the large scattering cross section.[13-15]

6.2.2 *Specific surface area and electrical conductivity measurements*

The specific surface area of the powders was determined by the BET method before and after coating with boron-doped diamond. As shown in Table 6.1, the specific surface area of the 100 nm doped diamond powder was 27 m^2/g after coating. The specific surface area of the powder decreased by *ca.* 50% after diamond coating due mainly to particle–particle fusion and multiple particle overgrowth. This is consistent with the SEM image shown in Fig. 6.1, which revealed extensive particle–particle fusion and a corresponding increase in the particle size. Specific surface areas of other powders are also shown for comparison.

In order to verify that a conductive layer formed over the diamond particles, electrical resistance measurements were made on the dry powder and the calculated conductivities are presented in Table 6.1. The uncoated diamond powder had no measurable conductivity after it had been cleaned by acid washing. This is an important point to mention. As-received detonation nanodiamond powder often possesses some electrical conductivity, but this conductivity arises because of sp^2 carbon impurity phases; onion-skin graphene structure at the particle surface.

Table 6.1 Electrical conductivity and specific surface area of the uncoated, B-UNCD coated diamond, and sp^2-bonded carbon powders before and after acid washing. Values shown are means +/- standard deviations

Powder Sample	Conductivity	BET (m^2g)
100 nm powder uncoated-acid	< 1 µS	53
100 nm powder coated	0.47±0.14	26
100 nm powder coated-acid	0.41±0.02	26
500 nm powder uncoated	0.59±0.05	8
500 nm powder coated	0.45±0.04	N/A
Glassy Carbon	1.41±0.24	1-2
Vulcan XC-72	1.87±0.19	250

Anything chemically or electrochemically that alters the structure of this impurity phase (*e.g.*, acid washing) will necessarily decrease the electrical conductivity.

In contrast, the electrical conductivity of the diamond-coated powder arises from a distinctly different mechanism; the carrier concentration and carrier mobility within the doped diamond overlayer. After a 2-h B-UNCD overcoating, the conductivity of the 500 and 100 nm diam. powders increased to nominal values of 0.59 and 0.41 S/cm, respectively. Importantly, the conductivity was not significantly altered after acid washing, consistent with a chemically stable, doped diamond overlayer. Furthermore, this result proved that adventitious non-diamond sp^2 carbon impurity that might form on the diamond surface during deposition does not contribute to the electrical properties; as such an impurity phase would be expected to be removed by the acid treatment.

The electrical conductivity measurements are the most definitive data for the existence of a doped diamond overlayer. For comparison, the nominal conductivities of the GC and Vulcan XC-72 powders were slightly higher at 1.4 and 1.9 S/cm, respectively.

6.2.3 Background cyclic voltammetric current density–potential curves

Background cyclic voltammetric *i-E* curves provide insight on the physicochemical properties of conductive diamond powders. The potential limits, voltammetric features, and the magnitude of the background current are all sensitive to the microstructure of the carbon phase on the surface, the surface chemistry and the electronic properties. Figure 6.3 shows typical curves in 1 M KCl for the 500 and 100 nm diam. doped diamond powder. The currents are normalized to the electrode area. To ensure maximum wetting of the powder, the potential was cycled extensively between −0.5 and 1.2 V. During the cycling, the diamond powder surface becomes more hydrophilic due to the incorporation of surface carbon–oxygen functionalities. As a consequence, more of the powder surface slowly wets with the supporting electrolyte solution. Measurements with the powders were not begun until the background voltammetric current reached a constant level. These stabilized curves were obtained after a few cycles and

Table 6.2. Cyclic voltammetric peak potential separation (ΔE_p) and peak current ratio ($i_p^{forward}/i_p^{reverse}$) for various redox analysis at 500 nm and 100 nm doped diamond powder, and glassy carbon powder electrodes

Analyte	Electrode	ΔE_p	$i_p^{forward}/i_p^{reverse}$
$Fe(CN)_6^{-3/-4}$	500 nm	76 ± 6	0.99
	100 nm	120 ±14	0.95
	GC	76 ± 4	1.00
$IrCl_6^{-2/-3}$	500 nm	81 ± 4	0.99
	100 nm	98 ± 8	1.00
	GC	67 ± 2	1.00
$Fe^{+3/+2}$	500 nm acid washed	221 ± 30	0.97
	500 nm	560 ± 28	0.92
	rehydrogenated	121 ± 89	0.98
	GC		

remained unchanged with additional cycling. This is consistent with a constant wetted area during the measurements. Due to its electrically insulating nature, the curve for the uncoated diamond powder exhibited zero current at all potentials (dotted line). The background current for the 500 nm powder is lower than that for the 100 nm diamond powder due to a reduced surface area exposed to the solution. This results because of the lower specific surface area of the 500 nm diam. powder and the greater mass of the 100 nm diam. powder. The background current for the 500 nm powder electrode is small and featureless

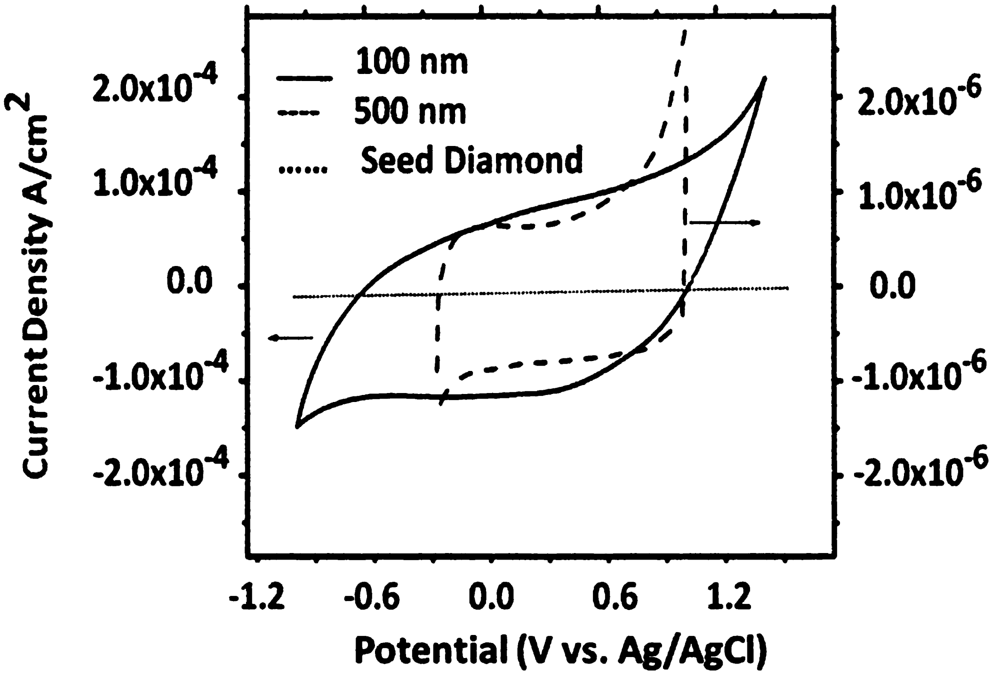

Figure 6.3. Background cyclic voltammetric *i-E* curves for acid-washed 500 and 100 nm diam. B-UNCD-coated powders recorded using the pipette electrode. A comparison curve for the insulating diamond powder (prior to nanocrystalline diamond deposition) is also shown. The curves were recorded in 1 M KCl at 50 mV/s. The currents are normalized to the area of the electrode contacting the supporting electrolyte solution.

between −300 and 800 mV. At the anodic limit, chlorine is presumably generated from the oxidation of chloride. The origin of the cathodic current, which begins to flow at −0.3 V, is unknown. This current does not appear to be associated with the reduction of dissolved O_2, as it is still present in the voltammograms after solution purging with N_2. The apparent potential window for the 100 nm powder is wider than that for the 500 nm powder electrode, particularly at negative potentials, as some cathodic current begins to flow at −0.6 V that is due to an unknown reaction. The wider potential window is due, at least to some extent, to ohmic resistance within the powder network. This is discussed further below. Evidence for this is the shifted slope of the *i-E* curve relative to the zero current line.

6.2.4 Cyclic voltammetric response for different redox systems

Figure 6.5 shows a series of cyclic voltammetric *i-E* curves for $Fe(CN)_6^{-3/-4}$ and $IrCl_6^{-2/-3}$ at pipette electrodes prepared with coated diamond and GC powders. The currents are normalized to the geometric area of the electrode (0.002 cm^2). The $Fe(CN)_6^{3-/4-}$ redox couple does not undergo simple electron transfer at carbon electrodes as is commonly thought [45-50].[16-21] The heterogeneous electron-transfer rate constant for this redox systems at carbon electrodes is strongly influenced by the electrode surface cleanliness, electrolyte type, and concentration, as well as the electrode's density of electronic states near the formal potential of the couple. The rate constant is relatively insensitive to the surface oxygen functionalities on sp^2 carbon electrodes as long as a thick oxide film is not present [46-48]; however, it is quite sensitive to the presence of surface oxygen on diamond electrodes [49, 50].[20, 21] The heterogeneous electron-transfer rate constant for $IrCl_6^{2-/3-}$ is relatively insensitive to the surface microstructure, surface oxides, and adsorbed monolayers on sp^2 carbon

electrodes. It is primarily influenced by the electrode's (both sp^2 and sp^3 carbon) density of electronic states near the formal potential.[6-8, 17-19] This redox system was chosen to probe the electronic structure of the powder electrode, which is related to the density of charge carriers and their mobility. The boron-doping level and homogeneity are very important determinants of fast charge transfer kinetics. In Figure 6.4A and B, curves are shown for these two redox systems at 500 nm doped diamond powder electrodes. Well defined, peak-shape voltammograms

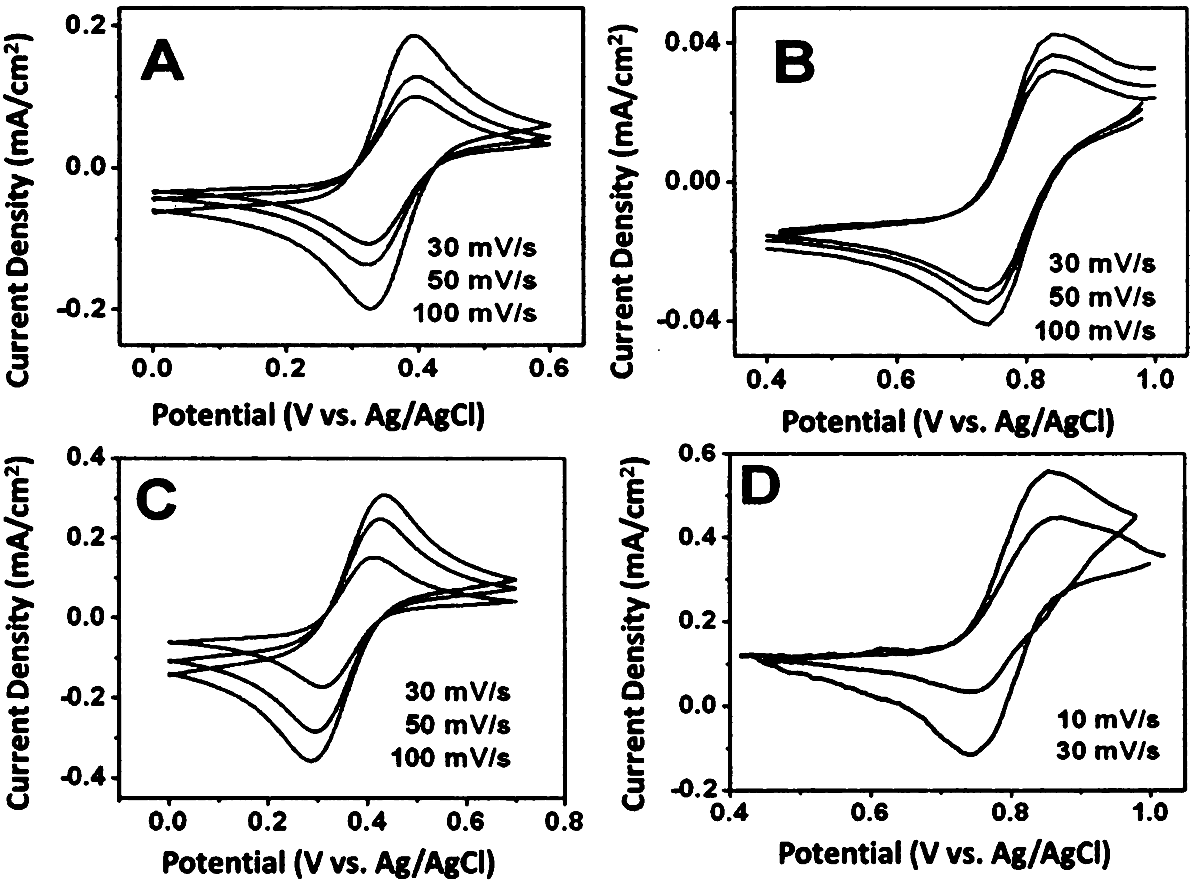

Figure 6.4 Cyclic voltammetric *i-E* curves for 1 mM $Fe(CN)_6^{3-/4-}$ in 1 M KCl at (A) 500 nm and (C) 100 nm diam. B-UNCD-coated diamond powder electrodes. Cyclic voltammetric *i-E* curves for 1 mM $IrCl_6^{2-/3-}$ in 1 M KCl at (B) 500 nm diam. B-UNCD-coated diamond powder and (D) 100 nm B-UNCD-coated diamond powder electrodes. The curves were recorded using the pipette electrode, and the currents are normalized to the geometric area of the electrode, 0.002 cm^2.

are seen for both redox systems at all the scan rates. At the lowest scan rate, 30 mV/s, the nominal ΔE_p values were 76 and 81 mV, respectively (see ΔE_p Table 6.2). The oxidation peak current for $Fe(CN)_6^{-4}$ and the reduction peak current for $IrCl_6^{-2}$ varied linearly with (scan rate)$^{1/2}$ from 10 to 300 mV/s ($r^2 > 0.98$), indicative of a reaction rate limited by semiinfinite linear diffusion of the reactant.

In Fig. 6.4 C and D, curves are shown for the two redox systems at the 100 nm doped diamond powder. Well-defined, peak-shaped voltammograms are also seen for both at the different scan rates. At the lowest scan rate, 30 mV/s, the nominal ΔE_p values were 120 and 98 mV, respectively, for $Fe(CN)_6^{-3/-4}$ and $IrCl_6^{-2/-3}$. These same redox systems were tested at a GC powder electrode (Figure 6.5). Nominal ΔE_p values of 76 and 67 mV were observed at 30 mV/s. Clearly, the 500 nm powder exhibits electrochemical activity similar to that of the GC powder. Furthermore, the electrochemical activity for these two redox systems is similar to that seen for thin films of B-UNCD.[22, 23] Larger peak splitting is seen for the 100 nm powder, even though the electrical conductivity of the powder is similar to that for the 500 nm powder. This apparently arises because of ohmic resistance within the powder network in the pipette electrode. In fact, measurements as a function of the concentration revealed an increasing ΔE_p with increasing concentration for both redox systems (30 mV/s) indicative of ohmic resistance affecting the peak splitting. Additional evidence for the ohmic resistance is the sloping background voltammetric i-E curve seen in Fig. 6.3. The resistance arises from the incomplete overcoating of the powder particles and their irregular shape, which reduces the particle-particle contact.

The electrode response for $Fe^{+3/+2}$ was also tested using as-received and

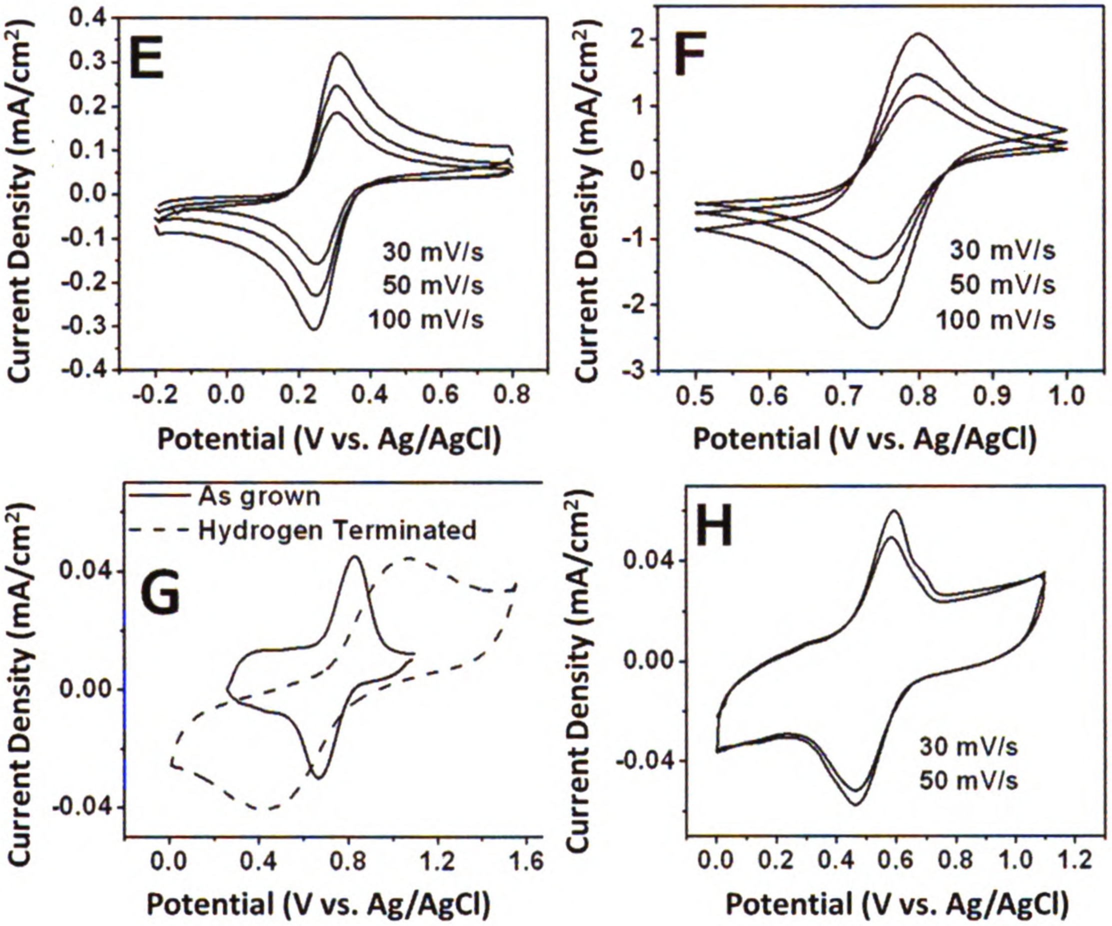

Figure 6.5. Cyclic voltammetric *i-E* curves at GC powder electrodes for (E) for 1 mM $Fe(CN)_6^{3-/4-}$ in 1 M KCl and (F) for 1 mM $IrCl_6^{2-/3-}$ in 1 M KCl. Cyclic voltammetric *i-E* curves for 1 mM $Fe^{3+/2+}$ in 1 M $HClO_4$ at (G) 500 nm diam. B-UNCD-coated diamond powder and (H) GC powder electrodes. The curves were recorded using the pipette electrode, and the currents are normalized to the geometric area of the electrode, 0.002 cm^2.

acid washed/rehydrogenated 500 nm B-UNCD coated diamond powder to study the effect of surface chemistry on the response. The McCreery group has shown that the $Fe^{+3/+2}$ redox system is catalyzed at carbon electrodes by a specific chemical interaction with surface carbonyl functionalities.[24] Therefore, the heterogeneous electron-transfer rate constant is highly sensitive to the presence of oxides on sp^2 and sp^3 carbon electrodes.[20, 21, 24] The ΔE_p for the as-grown powder was nominally 221 mV. This powder consists of both sp^3 and sp^2 carbon impurity due to the variation in temperature during deposition. It is supposed that some carbon–oxygen functionalities exist at sites within the impurity phase. After acid washing and rehydrogenation, ΔE_p increased considerably to 560 mV (50 mV/s). It was the same powder that was used to obtain the voltammograms for $Fe(CN)_6^{-3/-4}$ and $IrCl_6^{-2/-3}$ in Fig.6.4A and B. Therefore, the large increase in ΔE_p for $Fe^{+3/+2}$ is not due to ohmic resistance effects but rather to a loss in surface carbon–oxygen functionalities. The large ΔE_p for this redox system is consistent with the sluggish kinetics typically seen for this redox system at hydrogen-terminated ultrananocrystalline diamond thin-film electrodes.[20, 21, 24]

6.2.5 Morphological and microstructural stability testing

One motivation for investigating boron-doped diamond powders is their potential use as a dimensionally-stable electrocatalyst support material. Figure 6.6 shows continuous amperometric current density–time (i-t) curves recorded for 100 and 500 nm doped diamond powders during a constant potential polarization at 1.4 V vs Ag/AgCl in 0.5 M H_2SO_4. The polarization was performed for 1 h at 80 °C. A curve for GC powder is also shown, for comparison. The current is

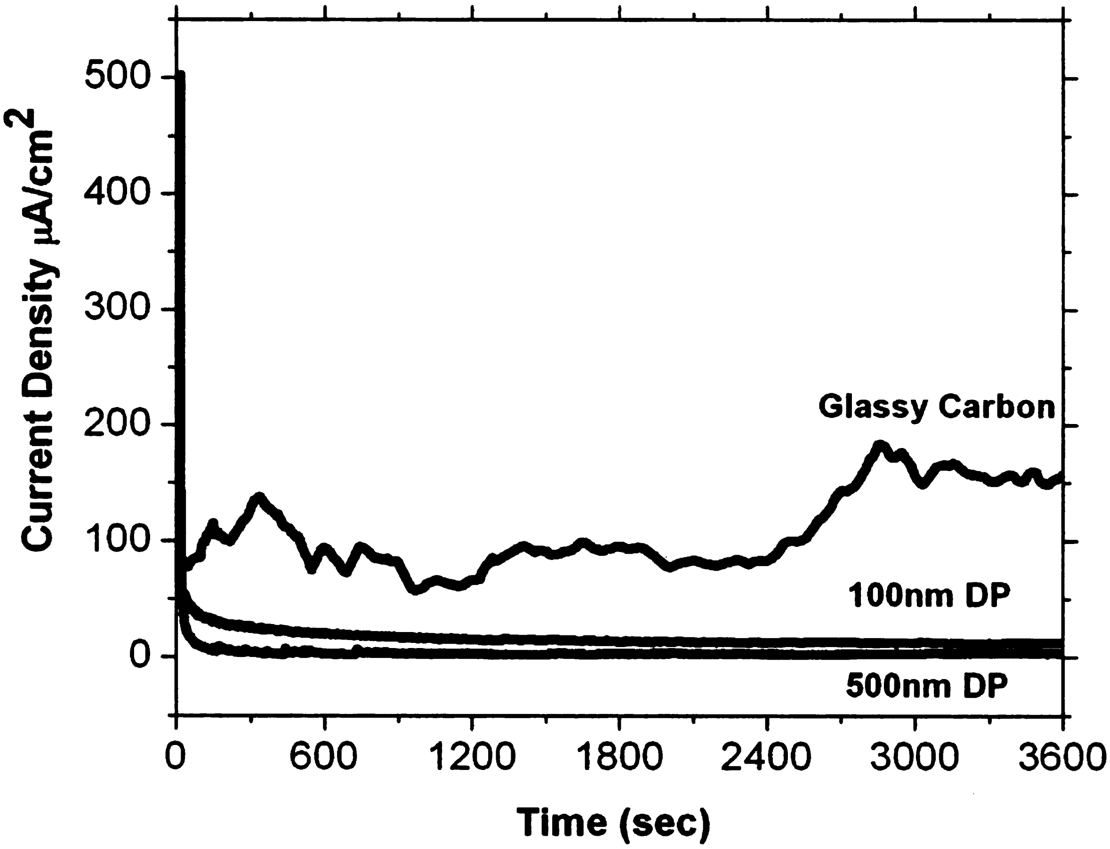

Figure 6.6. Continuous amperometric *i-t* curves for 500 and 100 nm diam. B-UNCD-coated diamond powders recorded at 1.4 V vs. Ag/AgCl in 0.5 M H_2SO_4 for 1 h at 80 °C. A comparison curve for GC powder is also shown. The curves were recorded using the pipette electrode. The currents are normalized to the area of the electrode contacting the supporting electrolyte solution.

normalized to the area contacted by the supporting electrolyte solution. The curves reveal that significantly less current density passes through the diamond powders as compared to the GC powder. The *i-t* profiles for the two diamond powders are relatively smooth and devoid of temporal fluctuations. The current for the GC powder, on the other hand, is significantly greater and there are sizable temporal fluctuations seen. These fluctuations are due to dynamic increases in the surface area of the powder as the particles morphologically degrade and corrode. There is also a general increase in the current starting at about the 2400 s mark. This is consistent with an increase in the electrode area

due to microstructural degradation and corrosion. Integration of the *i-t* curves yields the oxidation charge passed. This charge results from oxidation of the powder, which involves a combination of surface carbon–oxygen functionality formation, microstructural degredation, and corrosion (i.e., gasification of the carbon). The total charge passed was greater for the GC powder (0.4 C/cm^2) than for the diamond powders (0.06 C/cm^2). This is consistent with the diamond powders being less active than the GC powder toward oxidation. Several processes could contribute to the oxidation current for sp^2 carbon powders: intercalation and subsequent oxidation of the intercalation compound, and surface oxide formation at existing edge plane sites and at edge sites formed as a result of the lattice strain caused by the oxide formation, gas evolution, and corrosion or gasification.

From these electrochemical data alone, one cannot determine if any morphological or microstructural degradation of the carbon occurred. Additional electrochemical tests and SEM imaging were performed to gain more insight regarding possible degradation. For example, cyclic voltammetric i-E curves were recorded for the 500 and 100 nm B-UNCD coated diamond and GC powders in 0.5 M H_2SO_4 before and after polarization at 1.4 V. Representative curves for all three electrodes are presented in Fig. 6.7 A-C. For the 500 nm doped diamond powder, the cyclic voltammograms are largely unchanged after the polarization (Fig. 6.7A). The currents are normalized to the electrochemically active area. If

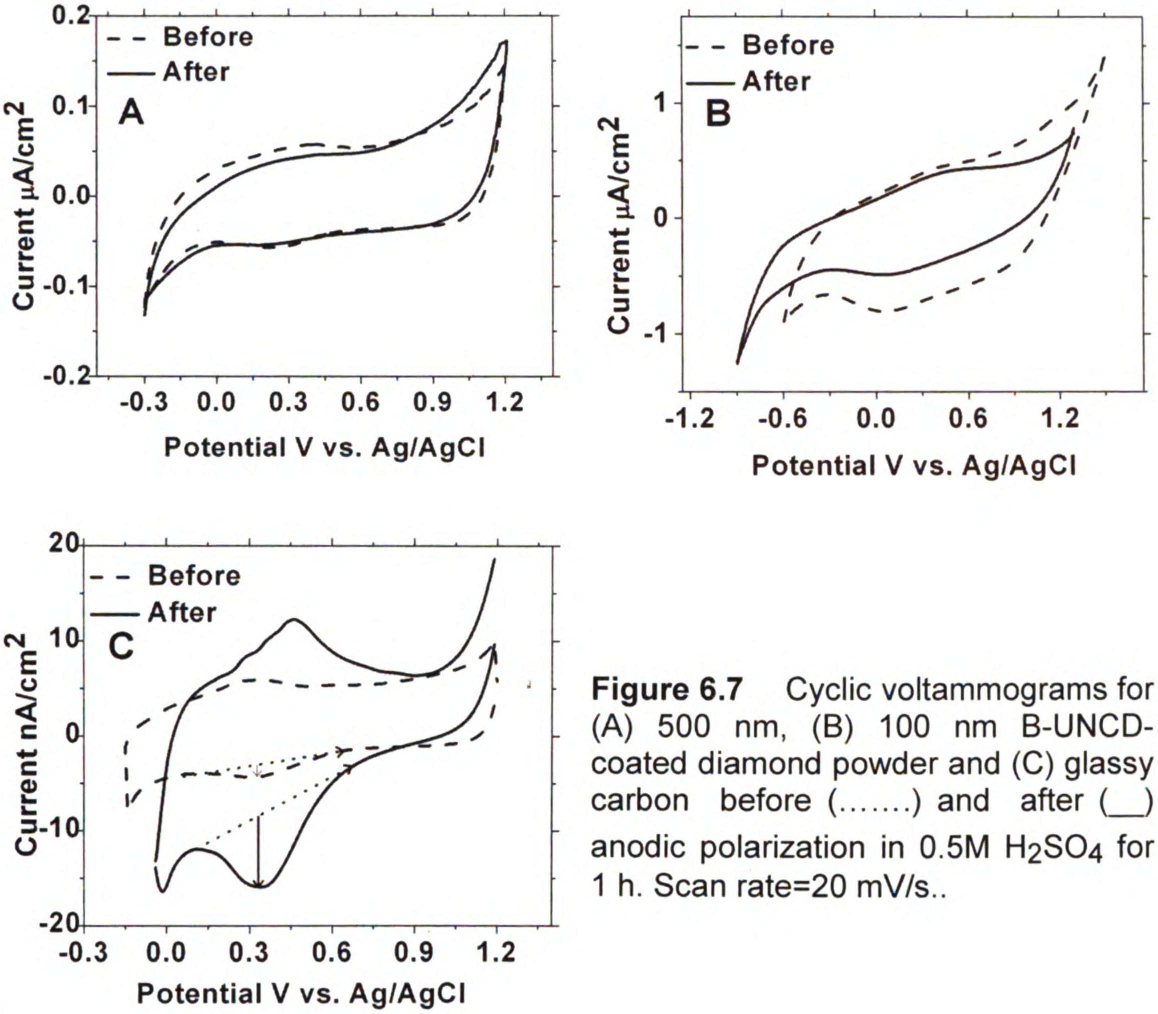

Figure 6.7 Cyclic voltammograms for (A) 500 nm, (B) 100 nm B-UNCD-coated diamond powder and (C) glassy carbon before (…….) and after (__) anodic polarization in 0.5M H_2SO_4 for 1 h. Scan rate=20 mV/s..

the surface had been damaged by degradation and corrosion, then an increased background current would be expected due to an increase in the surface area of the powder exposed to the solution. It is also possible that if the degradation were severe enough, then the powder particle–particle contact would be significantly compromised, leading to an increase in the electrode ohmic resistance. This would be evidenced by a sloping voltammetric *i-E* curve rather than one that is symmetric around the zero current line. The fact that the curves are largely unchanged is good evidence for the absence of significant structural degradation or corrosion. The diamond surface gets converted from an H-terminated one to an O-terminated one. There is, however, no microstructural change associated with oxidation of diamond, simply a change in surface chemistry. This is consistent with previous studies of the dimensional stability of diamond powders and thin films supported on Si.[25, 26] The fact that the curves are unchanged indicates that there is no significant increase in the wetted area of the electrode after polarization.

There is minor change in the curve for the 100 nm B-UNCD-coated diamond powder. First, the curve prior to polarization is sloped due to some ohmic resistance within the powder network. It is supposed that this is due to limited contact between the hard, irregularly shaped particles as well as incomplete doped diamond coverage around the particles. Achieving a uniform coverage of doped diamond around the seed particles is more arduous the smaller the particle size. The upward slope of the curve actually increases some after polarization, consistent with an increase in the ohmic resistance of the powder network. Furthermore, unlike the curve for the 500 nm diamond powder, the curve for the 100 nm powder prior to polarization is characterized by small oxidation and reduction peaks between 0 and 0.2 V. These peaks are often seen on disordered sp^2 carbon materials (see the GC powder data in Fig. 6.7 C) and result from redox-active carbon–oxygen functional groups (*e.g.*, hydroquinone/quinone couple) formed at the edge plane sites.[27-31] Such redox-active functional groups are not expected for diamond and are normally not observed. Their presence here may mean these small powder particles have some sp^2 carbon impurity exposed with reactive sites where these functional groups can readily form. The background current and charge slightly decrease after the polarization, and the redox peaks are still present with amplitude that is about the same as before the polarization. It is possible that the reduced background current seen is caused by the loss of some of the nondiamond carbon impurity from the diamond powder surface in the forms of CO and or CO_2.[32] The cyclic voltammetric *i-E* curve for the GC powder was significantly altered after the anodic polarization (Fig. 6.7C). Specifically, the peak current and charge for the redox-active functional groups increased.[31] The peak positions are largely unchanged. The increased peak amplitude results from the formation of greater functional group coverage because of microstructural degradation and corrosion, processes that produce new active sites for the functional group formation. The overall background current and charge also increased after polarization, consistent with an increase in the exposed surface area due to microstructural damage.

SEM was used to confirm the presence or absence of morphological and microstructural damage to the powders. Characteristic images of the GC and 500 nm doped diamond powders, before and after polarization, are presented in Fig. 6.8 A-D. These powders were taken from the portion of the sample exposed to the electrolyte solution during the 1.4 V polarization. Prior to polarization, spherically smooth, GC particles are seen with diameters of 3–4 µm (Fig. 6.8A). After polarization, morphological and microstructural degradation is seen (Fig. 6.8B). Some particles were fractured and broken apart during the polarization, which produced a greater surface area and led to the formation of a greater

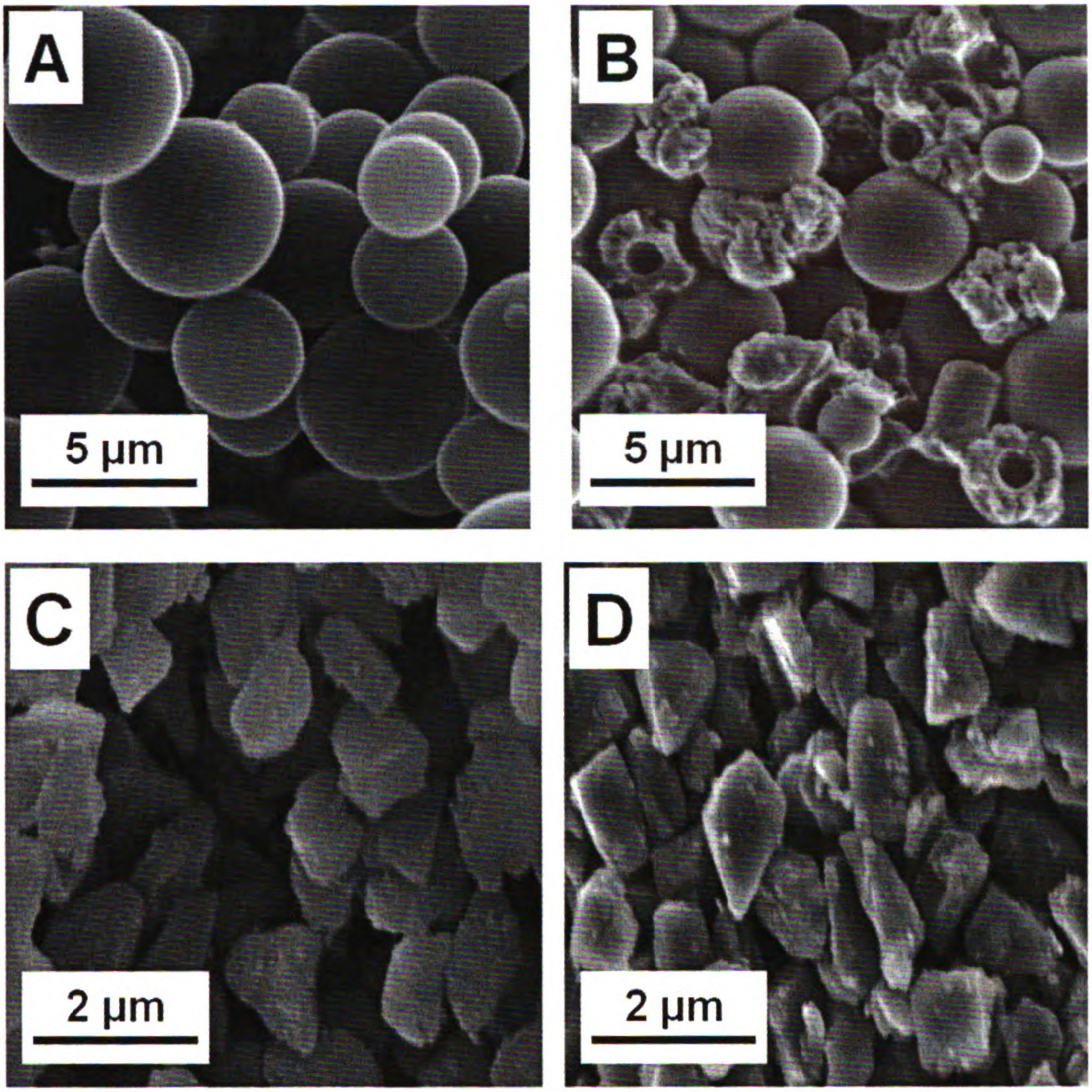

Figure 6.8. SEM images of GC powder (A) before and (B) after 1-h polarization at 1.4 V vs. Ag/AgCl in 0.5 M H_2SO_4 for at 80 °C. Images are also shown of 500 nm B-UNCD-coated diamond powder (C) before and (D) after the same anodic polarization. The polarization was performed using the pipette electrode.

number of redox-active carbon–oxygen functional groups. Not only does the polarization degrade the powder morphology and microstructure, but if allowed to proceed long enough, would result in significantly increased ohmic resistance through the powder network due to reduced particle connectivity. In contrast, there was no apparent change in the structure of the 500 nm doped diamond powder after polarization. Sharp, irregularly shaped crystals are apparent before and after polarization. The nominal diameters are the same, and there is no evidence for any particle roughening or pitting.

6.3 Discussion

The results demonstrate that high surface area (~170 m^2/g) and electrically conducting (~1 S/cm) diamond powder can be formed by overcoating inexpensive diamond abrasive with a layer of boron-doped ultrananocrystalline diamond. In this core-shell approach, one must empirically determine the growth conditions needed to achieve maximum homogeneity in the overlayer while avoiding significant particle–particle fusion, which reduces the specific surface area. Our procedure for producing the electrically conducting diamond powder is not optimal but does enable materials to be produced for proof-of-concept investigations. New reactor designs are required for more rapid, efficient, and homogeneous diamond coatings over individual substrate particles. For instance, designs where the powders are suspended in or repeatedly get transported through the plasma would be ideal for achieving a more homogeneous coating.

The physicochemical properties of the carbon coating depend on powder position in the plasma. In our approach, the powders were spread across a Si wafer with most but not all of the particles immersed in the plasma. The height of the particles differed so the temperature and plasma density were variable across the powder sample. Independent substrate temperature control, rather than collisional heating in the plasma, would be ideal for achieving a more uniform sample temperature and hence, a more phase-pure diamond coating.

Furthermore, particles buried in the center of the sample interact less with the reactive plasma species than particles at the surface. This leads to heterogeneity in the coverage and type of carbon formed. Even with these current technological limitations, the results clearly demonstrate that electrically conducting diamond particles can be produced by the core-shell approach and that these particles are more resistant to microstructural degradation and corrosion during anodic polarization than are GC powders.

The pipette electrode allows one to test the electrochemical properties of the powders conveniently without the need for a binder. The electrical conductivity data presented in Table 6.1 indicate that the packed powders are highly conducting, on par with GC and Vulcan XC-72 sp^2 carbon powders. A difficulty, however, with making a low-resistance electrode out of diamond is not the electrical conductivity of the individual powder particles but rather the resistance that results from poor particle–particle contact when packed. The diamond particles are hard and irregularly shaped. Therefore, they do not pack efficiently to yield high particle–particle contact areas and cannot be compressed to increase the conductivity. The contact resistance, R_C, between particles is given by Eq. 6.1, and this limits the electrical conductivity of packed powders. It is larger for smaller diameter powders because the contact radius, b (cm), becomes smaller between two spherical particles

$$R_c = \frac{\rho}{2b} \qquad [6.1]$$

where ρ is the specific resistivity (Ω cm) and b is the contact radius (cm).[31] Innovative strategies will be needed to achieve lower resistance powder electrodes with small diameter diamond powders, like preparing electrodes with mixed diameter powders.

Reasonably good electrochemical behavior was exhibited by both the 500 and 100 nm doped diamond powders toward several aqueous redox systems. The data, particularly that for the 500 nm doped diamond powder, were very comparable to data obtained for high-quality, boron-doped nanocrystalline diamond thin-film electrodes. The voltammetric data for the 100 nm doped diamond powder were more influenced by ohmic resistance than were the data for the 500 nm powder.

6.4 Conclusion

The deposition of B-UNCD layer on the insulating 500 and 100 nm diamond powder via CVD and its electrochemical, microstructural, and morphological characterization was reported. On the basis of these results, we can conclude that, 100 and 500 nm diam. diamond powders are coated with a thin layer of boron-doped diamond. According to BET surface area measurements, the uncoated powders have higher surface area than the coated diamond powder. Overcoating makes the particles larger due to particle–particle fusion, which reduces the specific surface area. The relatively high electrical conductivity after acid washing proved that the electronic properties of the diamond powder result from the doped diamond overlayer and not from any adventitious nondiamond carbon impurity phase. SEM images and Raman spectroscopy yielded further evidence in support of a B-UNCD overlayer. Both powders exhibited electrochemical responses for $Fe(CN)_6^{3-/4-}$, $Ir(Cl)_6^{-2/-3}$, and $Fe^{+2/+3}$ that were comparable to typical responses seen for high-quality, B-UNCD thin-film electrodes. The electrochemical behavior of the powders was assessed using a pipette electrode that housed the packed powder with no binder. The 100 nm doped diamond powder electrodes were more plagued by ohmic resistance effects than were the 500 nm powder electrodes because of reduced particle contact. Importantly, it was found that the doped diamond powder electrodes are dimensionally stable and corrosion-resistant during anodic polarization at 1.4 V vs Ag/AgCl (1 h) in 0.5 M H_2SO_4 at 80 °C. In contrast, GC powder polarized under identical conditions underwent significant microstructural degradation and corrosion.

6.5 References

[1] R.-I. Stefan and S. G. Bairu, *Analytical Chemistry* **75**:5394 (2003).

[2] C. He, S. Desai, G. Brown, and S. Bollepalli, *Electrochemical Society Interface* **14**:41 (2005).

[3] H. A. Gasteiger, S. S. Kocha, B. Sompalli, and F. T. Wagner, *Applied Catalysis B* **56**:9 (2005).

[4] M. F. Mathias, R. Makharia, H. A. Gasteiger, J. J. Conley, T. J. Fuller, C. I. Gittleman, S. S. Kocha, D. P. Miller, C. K. Mittelsteadt, T. Xie, S. G. Yan, and P. T. Yu, *Electrochemical Society Interface* **14**:24 (2005).

[5] L. M. Roen, C. H. Paik, and T. D. Jarvi, *Electrochemical and Solid-State Letters* **7**:A19 (2004).

[6] G. M. Swain, in Electroanal. Chem., Vol. 22 (A. J. Bard and I. Rubinstein, eds.), Marcel Dekker, 2003, p. 181.

[7] S. Alehashem, F. Chambers, J. W. Strojek, G. M. Swain, and R. Ramesham, *Analytical Chemistry* **67**:2812 (1995).

[8] Y. Show, M. A. Witek, P. Sonthalia, and G. M. Swain, *Chemistry of Materials* **15**:879 (2003).

[9] D. S. Knight and W. B. White, *Journal of Materials Research* **4**:385 (1989).

[10] M. Mermoux, B. Marcus, G. M. Swain, and J. E. Butler, *Journal of Physical Chemistry B* **106**:10816 (2002).

[11] D. Zhou, T. G. McCauley, L. C. Qin, A. R. Krauss, and D. M. Gruen, *Journal of Applied Physics* **83**:540 (1998).

[12] J. Birrell, J. E. Gerbi, O. Auciello, J. M. Gibson, D. M. Gruen, and J. A. Carlisle, *Journal of Applied Physics* **93**:5606 (2003).

[13] A. C. Ferrari and J. Robertson, *Physical Review B* **63** (2001).

[14] A. C. Ferrari and J. Robertson, *NATO Science Series, II: Mathematics, Physics and Chemistry* **24**:177 (2001).

[15] J. Birrell, J. E. Gerbi, O. Auciello, J. M. Gibson, J. Johnson, and J. A. Carlisle, *Diamond and Related Materials* **14**:86 (2005).

[16] M. C. Granger, M. Witek, J. Xu, J. Wang, M. Hupert, A. Hanks, M. D. Koppang, J. E. Butler, G. Lucazeau, M. Mermoux, J. W. Strojek, and G. M. Swain, *Analytical Chemistry* **72**:3793 (2000).

[17] P. Chen, M. A. Fryling, and R. L. McCreery, *Analytical Chemistry* **67**:3115 (1995).

[18] Q. Chen and G. M. Swain, *Langmuir* **14**:7017 (1998).

[19] K. R. Kneten and R. L. McCreery, *Analytical Chemistry* **64**:2518 (1992).

[20] M. C. Granger and G. M. Swain, *Journal of the Electrochemical Society* **146**:4551 (1999).

[21] I. Yagi, H. Notsu, T. Kondo, D. A. Tryk, and A. Fujishima, *Journal of Electroanalytical Chemistry* **473**:173 (1999).

[22] G. M. Swain, *Journal of the Electrochemical Society* **141**:3382 (1994).

[23] J. Wang, G. M. Swain, T. Tachibana, and K. Kobashi, *Journal of New Materials for Electrochemical Systems* **3**:75 (2000).

[24] C. A. McDermott, K. R. Kneten, and R. L. McCreery, *Journal of the Electrochemical Society* **140**:2593 (1993).

[25] A. E. Fischer and G. M. Swain, *Journal of the Electrochemical Society* **152**:B369 (2005).

[26] V. M. Swope, I. Sasaki, A. Ay, and G. M. Swain, *ECS Trans.* **3**:27 (2007).

[27] J. F. Evans and T. Kuwana, *Analytical Chemistry* **49**:1632 (1977).

[28] J. F. Evans and T. Kuwana, *Analytical Chemistry* **51**:358 (1979).

[29] C. W. Miller, D. H. Karweik, and T. Kuwana, *Analytical Chemistry* **53**:2319 (1981).

[30] D. T. Fagan, I. F. Hu, and T. Kuwana, *Analytical Chemistry* **57**:2759 (1985).

[31] K. Kinoshita, Carbon : Electrochemical and Physicochemical Properties, Wiley, New York, 1988.

[32] M. Cai, M. S. Ruthkosky, B. Merzougui, S. Swathirajan, M. P. Balogh, and S. H. Oh, *Journal of Power Sources* **160**:977 (2006).

Chapter 7

Electrochemically Modulated Liquid Chromatography Using a Boron-Doped Diamond Powder Stationary Phase

Abstract

The performance of boron-doped diamond powder (BDDP) as a stationary phase in electrochemically-modulated liquid chromatography (EMLC) is reported on. EMLC manipulates retention through changes in the potential applied (E_{appl}) to a conductive packing. Porous graphitic carbon (PGC) has routinely been utilized as a material in EMLC separations. The performance of BDDP as a stationary phase in EMLC was investigated and its stability, both compositionally and microstructurally, as a packing relative to PGC was compared. The results show that BDDP is stable over a wide range of E_{appl} values (i.e. -1.2 to +1.2 V vs. Ag/AgCl, sat'd NaCl). The data also reveal that electrostatics play a key role in the adsorption of the aromatic sulfonates on the BDDP stationary phase, and that these analytes are more weakly retained in comparison to the PGC support. This methodology provides a means to better understand molecular adsorption and retention mechanisms on carbonaceous support materials.

7.1 Introduction

Carbonaceous packings (*e.g.*, porous graphitic carbon (PGC)) have been used in a wide variety of liquid chromatography separations.[1-9] Carbon-based materials differ microstructurally and chemically from commonly used reversed-phases. From a retention perspective, carbonaceous packings have a π-electron selectivity that is superimposed on classical reversed-phase characteristics.[1-9]

Electrochemically modulated liquid chromatography (EMLC) is a separation technique that manipulates retention by changes in the potential applied (E_{appl}) to a conductive stationary phase. In other words, the packing functions as both a stationary phase and a working electrode in a chromatographic column designed to function as a three-electrode electrochemical cell. [8, 10-23] Past work has shown that carbon materials, like PGC and glassy carbon (GC),[13] are viable stationary phases for EMLC and there are several intriguing examples in which these packings have been coated with conductive polymers, like polyvinylferrocene and polypyrrole.[24-26] Recent work has also demonstrated that, by monitoring the influence of E_{appl} on the capacity factor (k') for analyte retention, a chromatographic tool for the examination of electrosorption phenomenon can be devised.[10, 11, 21]

Stationary phases in EMLC must possess several properties: high surface area, compositional and microstructural stability, and high electrical conductivity. Note that stability must also include the inertness of the packing material over a wide range of E_{appl}. To date, the greatest degree of success in EMLC has been achieved using PGC. This material has a high surface area (120 m^2/g)[9, 10] and a high inherent electrical conductivity (≥ 0.01 Ω-cm)[22], which is requisite for functioning as a working electrode. PGC is also available as micron-sized particles with a narrow dispersity. However, the tendency of this material to slowly oxidize at high anodic potentials (> +0.5 V) over a few days of continuous use can prove problematic with respect to compositional stability and, therefore, retention reproducibility.[27, 28] This oxidation not only alters the surface chemistry but also can change the microstructure and the local electronic properties (*i.e.*, density of states); both of which can have a significant influence on retention.

This chapter describes initial tests of an alternative carbonaceous packing for EMLC: boron-doped diamond powder (BDDP). The conducting powder was formed by overcoating insulating diamond powder in a hydrogen-rich plasma with a layer of boron-doped diamond on 8-12 μm diamond powder.[29, 30] As compared to glassy carbon materials, BDDP is more hydrophobic, is much more compositionally and morphologically stable, exhibits electrolysis in conventional aqueous media, and is less prone to surface fouling. [27-35]

Reports over the past decade have established the superior morphological and microstructural stability of diamond thin films with respect to several sp^2 carbon materials, including GC and highly-oriented pyrolytic graphite.[36-41] Recent work has also investigated the electrochemical stability of BDDP.[29, 30, 42] In those reports, BDDP of various diameters were anodically polarized ≥ +1.2 V vs. SHE at both room temperature and at 85° C in aqua acids. It was found that the doped diamond powder electrodes are dimensionally stable and corrosion-resistant during anodic polarization, while glassy carbon powder polarized under identical conditions underwent significant microstructural degradation and corrosion.

The goal of this preliminary work was to prepare columns packed with BDDP and to examine the possibility of probing molecular interactions at this material via retention changes with respect to E_{appl}. Experiments with BDDP were carried out to: (1) characterize its microstructure and electrical conductivity; (2) assess its utility in the reproducible manipulation of separations by using a mixture of aromatic sulfonates (ASFs) via changes in E_{appl}; and (3) to compare its retention properties with respect to that of PGC. This chapter discusses these initial findings.

7.2 Results and Discussion

7.2.1 Material Characterization

Figure 7.1 presents an SEM image of BDDP. Though clearly not ideal from a separation perspective, the image reveals that the particles are irregularly shaped, with sizes ranging between *ca.* 8 and 12 μm. The particles possess sharp jagged edges, which hinder efficient packing. The small spots observed on some particles are probably due to the secondary nucleation of diamond on the much larger particles. The crystal structure of the BDDP was investigated by XRD. Figure 7.2 shows an XRD spectrum for the powder sample. Three reflections are observed at 2θ values of 43.9°, 75.5°, and 91.5°, and are assigned to the (111), (222), and (311) crystallographic planes of cubic diamond, respectively. This conclusion is based on a comparison with a reference diamond

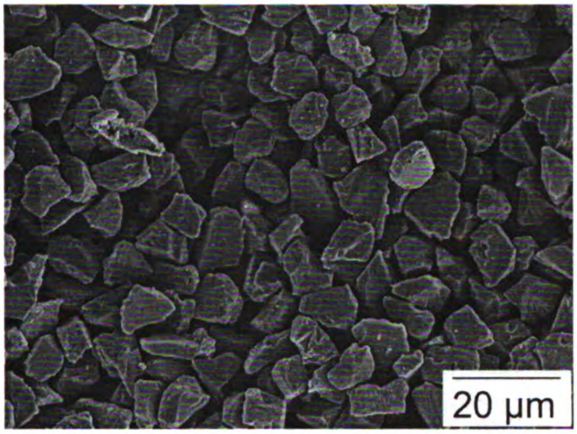

Figure 7.1 SEM image of BDDP.

material: ASTM 6-0675. The diffraction data reveal that the bulk of the conductive overcoating is sp^3-bonded carbon.

Raman spectroscopy was used to examine this material because of its sensitivity to the microstructure (sp^2 and sp^3 carbon bonding), boron-doping level, and residual stress (intrinsic and thermal).[43-46] Figure 7.3 presents a Raman spectrum for the BDDP. The spectrum shows the distinctive first-order diamond phonon peak at 1330 cm^{-1}. The diamond particles are free of detectable sp^2 non-diamond carbon impurities, as indicated by the absence of scattering between 1350 and 1580 cm^{-1}. The basis of this conclusion can be qualified by

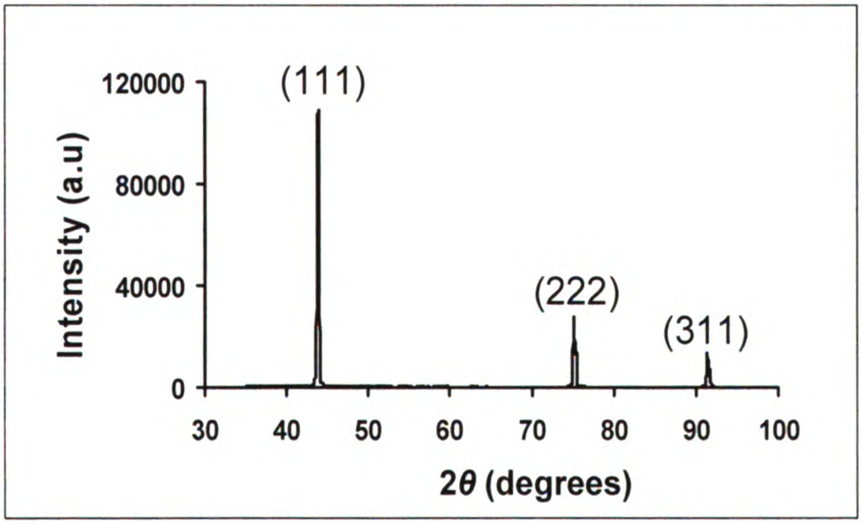

Figure 7.2 XRD pattern of BDDP.

recognizing that the scattering cross-section for graphite is *ca.* 50 times larger than that for diamond at visible excitation wavelengths.[43, 44]

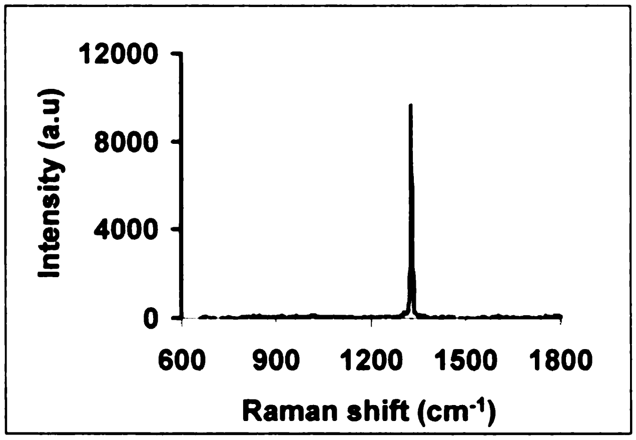

Figure 7.3 Raman spectrum of BDDP.

7.2.2 Retention as a function of E_{appl}

The influence of E_{appl} on the retention of ASFs has previously been examined on both GC and PGC.[10-14] The change in retention generally follows predictions based on electrostatic forces but varies slightly between solutes. These differences reflect a complex mixing of donor-acceptor, dispersive, and solvophobic interactions between the solute and the solid phase.[47] Past work has also found that, if present, the small amounts of oxygen containing surface groups (*e.g.*, carboxylic acids, quinones, and phenols) can contribute to retention through dipole and hydrogen bonding interactions.[48-53]

The importance of the above interactions is likely to differ at BDDP, which is devoid of an extended π-bonding system, and has a hydrogen-terminated surface. Termination renders the surface nonpolar and, therefore, highly hydrophobic.[54-57] In other words, chemisorbed hydrogen replaces carbon-oxygen functionalities on the surface during hydrogenation.[58, 59] Oxygen-containing groups can form at surface sites (both diamond and non-diamond carbon), and are usually present at low levels in high-quality hydrogen-terminated diamond thin films.[29]

The effect of E_{appl} on the separation of a four-component ASF mixture

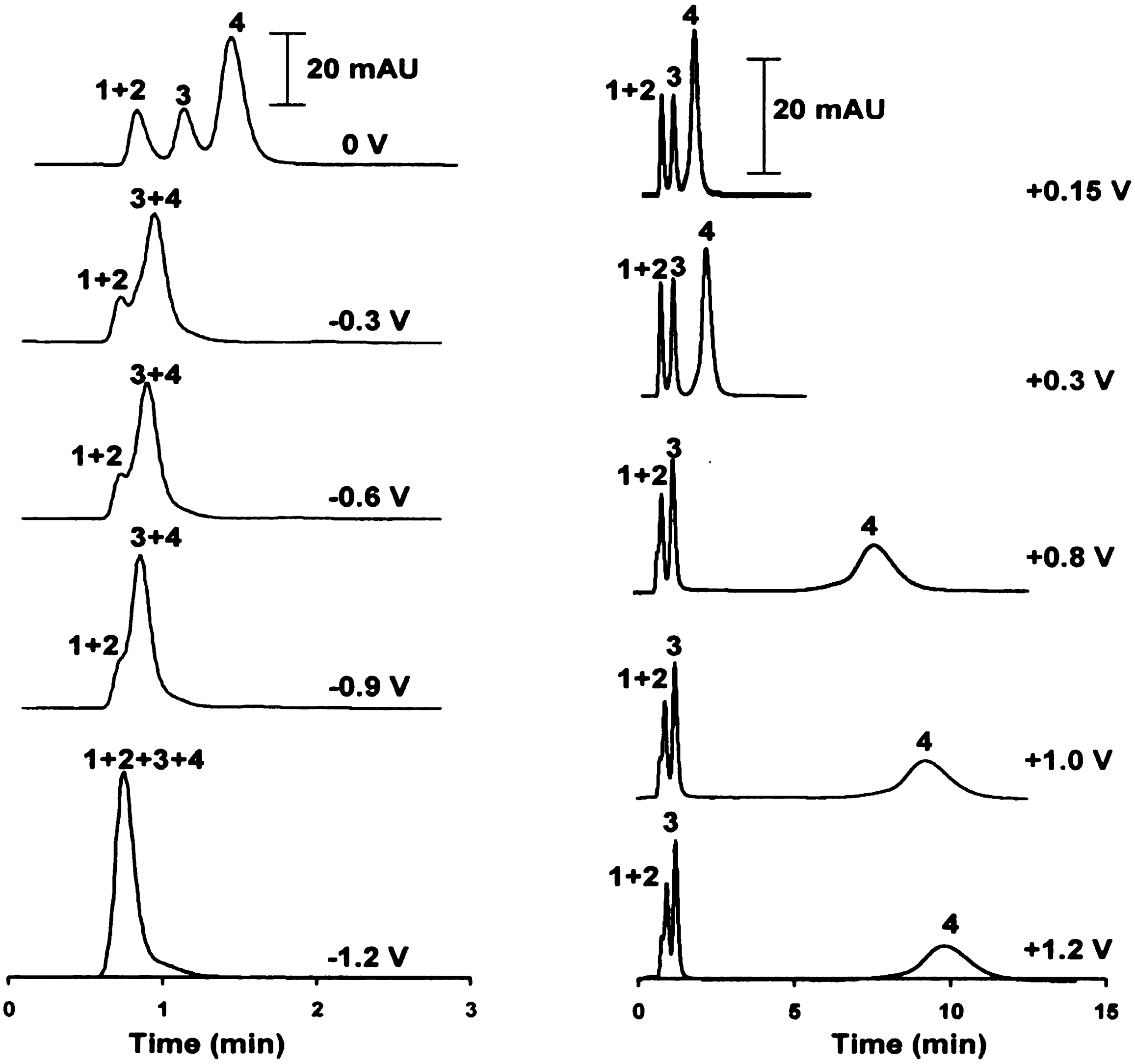

Figure 7.4 Chromatograms illustrating the effect of E_{appl} (V vs. Ag/AgCl sat'd NaCl) on the retention of a mixture of BDS (1, 5 µM), BS (2, 5 µM), TS (3, 10 µM) and NDS (4, 2 µM) on a BDDP-packed EMLC column. The mobile consisted of 0.10 M $LiClO_4$ (aq). The flow rate is 0.4 mL/min.

(BDS, BS, TS, and NDS) is presented in Figure 7.4 for values ranging from -1.2 to +1.2 V (vs. Ag/AgCl, sat'd NaCl) on a BDDP-packed EMLC column. This span in E_{appl} is much larger than the usable range for PGC, which is roughly from -1.0 to +0.5 V. Above +0.5 V, the PGC surface can slowly oxidize over a few days of continuous use at edge planes and defects sites to form carbon-oxygen surface groups that may be redox–active and or ionizable.[58, 59] These changes lower the reproducibility of retention and the overall effectiveness of the separation.

As is evident, the retention of all four analytes is strongly dependent on E_{appl}. At -1.2 V, the ASFs co-elute with the void volume. However, as E_{appl} becomes more positive, the retention of some of the analytes begins to extend beyond that of the void volume. At -0.9 V, the k' values for TS (k' = 0.34) and NDS (k' = 0.32) are smaller than those at -0.15 V by factors of 1.7 and 3.6, respectively. The application of more positive values of E_{appl} results in further increases in retention. At +0.45 V, the k' values for BDS/BS (BDS and BS were not resolved at any value of E_{appl}, which we ascribe to the low surface area for the BDDP packing), TS, and NDS are 0.28, 0.84, and 4.57, respectively. These values represent an increase by a factor of 1.3 or more over those at 0 V. The modulation of ASF retention is summarized in Figure 7.5 through ln k'-E_{appl} curves. The error bars in ln k' are roughly the size of the data points and represent the results of four replicate separations. The plots of TS and NDS extend from +1.2 to -0.9 V. The curves for BDS/BS covers +1.2 V to 0 V because BS and BDS eluted with the void volume ($k' \approx 0$) at more negative values of E_{appl}. Each compound follows a linear dependence, which is consistent with past

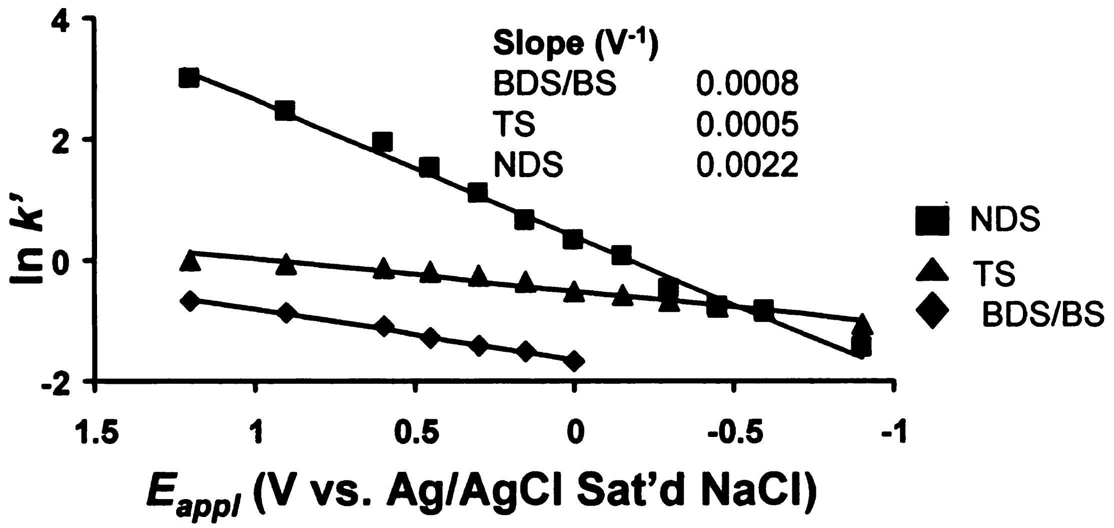

Figure 7.5 Plots of ln *k'* vs. E_{appl} for BDS (5 μM), BS (5 μM), TS (10 μM) and NDS (2 μM). Four replicate injections were made at each E_{appl}, and the data points are roughly the size of the error bars.

findings, and reflects the role of electrostatics on the EMLC-based manipulation of adsorption.[10]

Though not yet understood, the slope of the plots in Figure 7.5 do not all follow the observed dependence found when using PGC as a packing in EMLC.[11] In particular, the slopes for BDS and BS are indistinguishable from each other despite the difference in ionic charge. This observation, which suggests a possible mechanistic difference in electrosorption phenomenon at the two materials, merits further investigation. Together, these data demonstrate the ability of EMLC to alter molecular adsorption over a wide potential range when using BDDP as a stationary phase. This ability is highlighted by the retention of NDS, which undergoes an increase in *k'* by a factor of ~53 between -1.2 and +1.2 V. The next subsection briefly details the findings from a study of retention reproducibility and packing stability.

7.2.3 BDDP Stability

The stability of BDDP was examined by checking the day-to-day reproducibility of retention times of the four ASFs at several values of E_{appl}, especially above +0.5 V. This was accomplished by calculating the relative standard deviation (%RSD) of eight runs obtained in two days (four consecutive injections of the mixture on each day) at different E_{appl} values. Retention times typically exhibited less than a 5% RSD for ASFs from day-to-day comparison. For example, the RSD of TS and NDS at +0.8 V for two consecutive days were 3.6 and 1.6%, respectively. This finding demonstrates that BDDP microstructure remains comparatively stable over a wide range of E_{appl} values. The basis for this conclusion arises from earlier experiments using PGC. Excursions to values of E_{appl} in access of +0.5 V often led to decreases in retention. This situation proved particularly problematic when carrying out EMLC separations at elevated temperatures in order to measure thermodynamic parameters (*e.g.,* enthalpy and entropy) of adsorption. In these cases, the retention times ASFs decreased as much as 20%.[60]

Characterization by X-ray photoelectron spectroscopy revealed that these decreases (both in room and elevated temperature studies) corresponded to an increase in the amount of oxygen containing surface functional groups, which, at least quantitatively render the carbon surface less hydrophobic. Thus, the morphological and microstructural stability of BDDP point to its potential use as a model material to study the thermodynamics of electrosorption phenomenon (*e.g.* enthalpy and entropy of adsorption) by examining the dependence of retention with respect to temperature and pressure.

7.2.4 Comparison of BDDP to PGC

To develop a very brief comparison of the molecular adsorption characteristics of BDDP, a separation of a mixture of BDS, BS, TS, and NDS using 0.10 M $LiClO_4$ (aq) was carried out at different values of E_{appl} (+0.3, +0.1, and 0 V) using a PGC-packed column. As reported previously,[10,14] the time for all compounds to elute increased with E_{appl}. Figure 7.6 shows a chromatogram of the ASFs using the PGC-packed column at +0.3 V. The analysis took *ca.* 65 min for BDS, BS, and TS to elute from the PGC-packed column, but only *ca.* 3 min from the BDDP-packed column (Figure 4). NDS did not detectably elute from the PGC-packed column after *ca.* 80 min at any value of E_{appl}; longer times were not tested. The long elution times in the aqueous mobile phase are consistent with stronger interactions of the π-system of the analytes with PGC, which in nearly

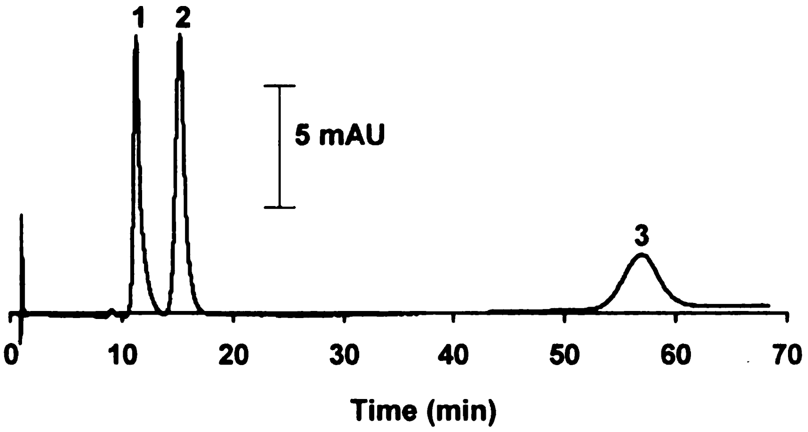

Figure 7.6 Chromatogram showing the retention of a 20 µM mixture of BDS (1), BS (2), and TS (3) on a PGC-packed EMLC column. The E_{appl} was +0.3 V (vs. Ag/AgCl sat'd NaCl). The mobile phase consisted of 0.10 M $LiClO_4$ (aq). The flow rate is 0.4 mL/min.

all cases dictates the use of a mixed (*e.g.*, acetonitrile/water) mobile phases in order to decrease retention.[1]

Table 7.1 Comparison of retention of 4-toluenesulfonate at BDDP and PGC-packed columns. E_{appl} vs. Ag/AgCl

E_{appl} (V)[b]	k'_P	k'_B	K_{ratio}
+0.30	54.83	0.79	5.6
+0.15	46.66	0.70	5.4
0	37.49	0.60	5.1

Table 7.1 compares the electrosorption of TS on BDDP- and PGC-packed columns at the three values of E_{appl} after accounting for the difference in the absolute surface area of the packings and void volume of the two different columns. This approach develops via eqn. 7.1, which defines the partition coefficient, *K*, for chromatographic column as

$$K = k' \frac{V_{mp}}{A_{sp}} \qquad (7.1)$$

where V_{mp} is the volume of the mobile phase and A_{sp} is the surface area of the column packing. Thus, by dividing K_P by K_B, the impact of V_P, V_B, A_P, and A_B can be taken into consideration to give K_{ratio}

$$K_{ratio} = \frac{K_P}{K_B} \qquad (7.2)$$

where the subscripts *B* and *P* assign the appropriate variables to either BDDP or PGC, respectively. Based on this treatment, the data in Table 7.1 show that TS is retained more strongly on a PGC-packed column by at least a factor of five when compared to BDDP. This is consistent with electrostatics controlling interactions with BDDP stationary phase. PGC possesses a higher percentage of edge plane and XPS measurements after use show % oxygen increases with use. Oxygen functional groups at the PGC surface along the higher edge plane density allows greater adsorption through either pi-pi, ion-dipole, or dipole-dipole interactions.[59, 61, 62] While much more in-depth investigation is needed, the differences in capacity factor are presently attributed, at least in part, to the importance of these interactions in the retention at PGC.

7.3 Conclusions

This chapter presents initial findings on BDDP as the stationary phase in EMLC separations. The work herein demonstrates the utility of EMLC for fine-tuning separations with BDDP. Due to the inert nature and a wide potential window of conductive diamond, EMLC separations were carried out at high positive and negative potentials without observable limitations due to surface oxidation and the microstructural changes associated with it, or solvent electrolysis common with other carbon-based materials.

Acknowledgements

This work was a collaborative effort with Dr. Grace Muna and Prof. Marc Porter at the University of Utah and supported by the University of Utah USTAR Initiative, the Biodesign Institute of Arizona State University, the Ames Laboratory-USDOE at Iowa State University (contract DE-AC 02-0ZH11358), and the Fraunhofer Center for Coatings and Laser Applications at MSU.

7.4 References

[1] J. H. Knox and Q. H. Wan, *Chromatographia* **42**:83 (1996).

[2] D. Maxime, B. Maiete, D. Jerome, G. Nicole, and P. Martine, *Journal of Chromatography A* **1114** (2006).

[3] S. Mazan, G. Cretier, N. Gilon, J. M. Mermet, and J. L. Rocca, *Analytical Chemistry* **74**:1281 (2002).

[4] M. Shibukawa, H. Terashima, H. Nakajima, and K. Saitoh, *Analyst (Cambridge, United Kingdom)* **129**:623 (2004).

[5] M. Shibukawa, A. Unno, T. Miura, A. Nagoya, and K. Oguma, *Analytical Chemistry* **75**:2775 (2003).

[6] K. Anders, B. Mattias, and C. J. Christine, *Journal of Chromatography A* **797**:75 (1998).

[7] B. kaur, *LC-GC* **8** (1990).

[8] J. L. Hern and J. H. Strohl, *Analytical Chemistry* **50**:1954 (1978).

[9] P. T. Jackson, M. R. Schure, T. P. Weber, and P. W. Carr, *Analytical Chemistry* **69**:416 (1997).

[10] D. W. Keller and M. D. Porter, *Analytical Chemistry* **77**:7399 (2005).

[11] D. W. Keller, L. M. Ponton, and M. D. Porter, *Journal of Chromatography, A* **1089**:72 (2005).

[12] E.-Y. Ting and M. D. Porter, *Analytical Chemistry* **70**:94 (1998).

[13] R. S. Deinhammer, E.-Y. Ting, and M. D. Porter, *Journal of Electroanalytical Chemistry* **362**:295 (1993).

[14] R. S. Deinhammer, E.-Y. Ting, and M. D. Porter, *Analytical Chemistry* **67**:237 (1995).

[15] R. S. Deinhammer, M. D. Porter, and K. Shimazu, *Journal of Electroanalytical Chemistry* **387** (1995).

[16] H. Deng, G. J. Van Berkel, H. Takano, D. Gazda, and M. D. Porter, *Analytical Chemistry* **72**:2641 (2000).

[17] E.-Y. Ting and M. D. Porter, *Journal of Chromatography, A* **793**:204 (1998).

[18] E.-Y. Ting and M. D. Porter, *Analytical Chemistry* **69**:675 (1997).

[19] S. Wang and M. D. Porter, *Journal of Chromatography, A* **828**:157 (1998).

[20] M. Ho, S. Wang, and M. D. Porter, *Analytical Chemistry* **70**:4314 (1998).

[21] L. M. Ponton and M. D. Porter, *Analytical Chemistry* **76**:5823 (2004).

[22] J. A. Harnisch and M. D. Porter, *Analyst (Cambridge, United Kingdom)* **126**:1841 (2001).

[23] J. A. Harnisch, D. Gazda, J. Anderegg, and M. D. Porter, *Analytical Chemistry* **73** (2001).

[24] R. F. Antrim, R. A. Scherrer, and A. M. Yacynych, *Analytica Chimica Acta* **164**:283 (1984).

[25] A. R. Ghatak-Roy and C. R. Martin, *Analytical Chemistry* **58**:1574 (1986).

[26] T. Nagaoka, M. Fujimoto, H. Nakao, K. Kakuno, J. Yano, and K. Ogura, *Journal of Electroanalytical Chemistry* **364**:179 (1994).

[27] R. C. Engstrom, *Analytical Chemistry* **54**:2310 (1982).

[28] R. L. McCreery, in Electroanalytical Chemistry, Vol. 17 (A. J. Bard, ed.), New York, 1991.

[29] A. E. Fischer and G. M. Swain, *Journal of the Electrochemical Society* **152**:B369 (2005).

[30] A. Ay, V. M. Swope, and G. M. Swain, *Journal of the Electrochemical Society* **155**:B1013 (2008).

[31] K. Nishimura, K. Das, and J. T. Glass, *Journal of Applied Physics* **69**:3142 (1991).

[32] M. C. Granger, M. Witek, J. Xu, J. Wang, M. Hupert, A. Hanks, M. D. Koppang, J. E. Butler, G. Lucazeau, M. Mermoux, J. W. Strojek, and G. M. Swain, *Analytical Chemistry* **72**:3793 (2000).

[33] A. E. Fischer, Y. Show, and G. M. Swain, *Analytical Chemistry* **76**:2553 (2004).

[34] Y. Show, M.-I. A. Witek, P. Sonthalia, and G. M. Swain, *Chemistry of Materials* **15**:879 (2003).

[35] M. A. Lowe, A. E. Fischer, and G. M. Swain, *Journal of the Electrochemical Society* **153**:B506 (2006).

[36] A. E. Fischer, M. A. Lowe, and G. M. Swain, *Journal of the Electrochemical Society* **154**:K61 (2007).

[37] G. M. Swain, *Journal of the Electrochemical Society* **141**:3382 (1994).

[38] B. J. Cruickshank, A. A. Gewirth, R. M. Rynders, and R. C. Alkire, *Journal of the Electrochemical Society* **139**:2829 (1992).

[39] R. Bowling, R. T. Packard, and R. L. McCreery, *Langmuir* **5**:683 (1989).

[40] C. A. Goss, J. C. Brumfield, E. A. Irene, and R. W. Murray, *Analytical Chemistry* **65**:1378 (1993).

[41] Q. Chen, M. C. Granger, T. E. Lister, and G. M. Swain, *Journal of the Electrochemical Society* **144**:3806 (1997).

[42] D. Y. Kim, B. Merzougui, and G. M. Swain, *Chemistry of Materials* **21**:2705 (2009).

[43] D. S. Knight and W. B. White, *Journal of Materials Research* **4**:385 (1989).

[44] J. R. Dennison, M. Holtz, and G. Swain, *Spectroscopy (Eugene, Oregon)* **11**:38 (1996).

[45] R. J. Nemanich, J. T. Glass, G. Lucovsky, and R. E. Shroder, *Journal of Vacuum Science & Technology, A: Vacuum, Surfaces, and Films* **6**:1783 (1988).

[46] Y. Wang, D. C. Alsmeyer, and R. L. McCreery, *Chemistry of Materials* **2**:557 (1990).

[47] P. Nikitas, *Journal of Electroanalytical Chemistry* **484**:137 (2000).

[48] B. J. Bassler and R. A. Hartwick, *Journal of Chromatographic Science* **27**:162 (1989).

[49] B. J. Bassler, R. Kaliszan, and R. A. Hartwick, *Journal of Chromatography* **461**:139 (1989).

[50] N. Tanaka, T. Tanigawa, K. Kimata, K. Hosoya, and T. Araki, *Journal of Chromatography* **549**:29 (1991).

[51] O. Chiantore, I. Novak, and D. Berek, *Analytical Chemistry* **60**:638 (1988).

[52] N. L. Weinberg and T. B. Reddy, *Journal of Applied Electrochemistry* **3**:73 (1973).

[53] T. L. Hafkenscheid and E. Tomlinson, *Advances in Chromatography (New York, NY, United States)* **25**:1 (1986).

[54] G. M. Swain, A. B. Anderson, and J. C. Angus, *MRS Bulletin* **23**:56 (1998).

[55] W. Haenni, P. Rychen, M. Fryda, and C. Comninellis, *Semiconductors and Semimetals* **77**:149 (2004).

[56] H. B. Martin, A. Argoitia, J. C. Angus, and U. Landau, *Journal of the Electrochemical Society* **146**:2959 (1999).

[57] H. B. Martin, A. Argoitia, U. Landau, A. B. Anderson, and J. C. Angus, *Journal of the Electrochemical Society* **143**:L133 (1996).

[58] R. DeClements, G. M. Swain, T. Dallas, M. W. Holtz, R. D. Herrick, II, and J. L. Stickney, *Langmuir* **12**:6578 (1996).

[59] J. Xu, Q. Chen, and G. M. Swain, *Analytical Chemistry* **70**:3146 (1998).

[60] L. M. Ponton, *In dissertation, Iowa State University* (2004).

[61] R. L. McCreery, *Chem. Rev. (Washington, DC, U. S.)* **108**:2646 (2008).

[62] P. Harris, *Critical Reviews in Solid State and Materials Sciences* **30**:235 (2005).

Chapter 8

Conclusions and Future Research Directions

Potential-dependent carbon degradation is an important problem with both the electrocatalyst support in polymer electrolyte membrane fuel cells, and the stationary phase in electrochemically-modulated liquid chromatography.[1-3] While there have been significant advancements in fuel cell materials during the past decade, degradation of the carbon electrocatalyst support remains a key issue. Long-term microstructural stability and strong electrosorption of certain analytes are limiting factors for sp^2 carbons use as the stationary phase in EMLC.

The research presented in this dissertation focused on the development and characterization of an alternative to sp^2 carbon powders that has superior corrosion resistance and morphological stability in electrochemical environments, namely boron-doped diamond coated powders. The boron-doped diamond overlayer was grown using plasma-assisted CVD. Two types of diamond overlayers were coated: microcrystalline and ultrananocrystalline (B-UNCD). The growth conditions for the B-UNCD coated powders were determined by investigating the effects for varying concentrations of both the carbon source (1-3% methane) and the dopant (0-50 ppm B_2H_6) concentrations in the source gas phase. The dopant concentration within 0-50 ppm B_2H_6 had little effect on the film microstructure, while at CH_4 concentrations above 1% diamond-like carbon and nanoplatelet graphite were incorporated into the B-UNCD phase. The optimum CH_4 level was found to be 1%.

The BDD overlayer was formed on several different substrates including: 8-12 µm, 500, 100, and 3-6 nm diameter diamond powders, glassy carbon powder, and Ketjen black. For the BDD coated diamond powders, the specific surface area after growth ranged from 1-170 m^2/g and the conductivity varied 0.1 – 2 S/cm. The electrical conductivity increases orders of magnitude after coating from < 1×10^{-6} S/cm to ~0.1 S/cm. The electrical conductivity was extremely stable after coating, and is attributable to the doped diamond overlayer. Pt particle formation on 100 nm diamond powders was investigated. Chemical impregnation produced an adlayer with a nominal diameter of *ca.* 5 nm regardless of hydrogen or oxygen surface termination. Pt particles were found to form epitaxially with the diamond (111) planes. The metal particles form directly on the diamond with no interfacial layer. Strong surface to metal interactions were found.

The morphology and microstructure of the B-UNCD coated powders before and after growth were probed with Raman spectroscopy, electron microscopy, XRD, and EELS. B-UNCD is the predominant microstructural phase found during deposition, with lesser amounts of non-diamond sp^2 carbon phases interspersed. Electrochemical and in situ Raman spectroscopic measurements were made using BDD coated powders before, during and after potentiostatic polarization in acid at 1.0, 1.2 and 1.4V vs. Ag/AgCl at room temperature and 80 °C. Comparison studies were also performed with several varied sp^2 carbon powders. It was found that the BDD coated powders are dimensionally stable and corrosion resistant, while the carbon black powders underwent more severe microstructural degradation during these test conditions.

Boron-doped diamond coated diamond powders were also tested as a stationary phase for EMLC. An EMLC column was constructed using the coated powder as the stationary phase, and the performance of this column was compared with that of a column packed with porous graphite powder. The BDD coated powder can be operated at a broader range of potentials, (-1.2 to +1.2V vs. Ag/Cl compared to -1.0 to +0.5 for PGC) and the reproducibility of the column performance after 2 days use ≥ +0.5 V was 3.6% or lower RSD while up to 20% RSD is observed for PGC packed columns.

Suggestions for future research are discussed in the following sections.

Chapter 3: ***Physical, Electrical and Electrochemical Characterization of Boron-Doped Ultrananocrystalline Diamond thin-Films Deposited from $CH_4/H_2/Ar/B_2H_6$ Source Gas Mixtures***

B-UNCD thin films on Si were prepared with varying B_2H_6 (0-50 ppm) and CH_4 concentration (0.5 to 3% v/v) to investigate the dependence of the B-UNCD morphology, microstructure and phase purity on the source gas concentration. There were no significant microstructural changes among the films with up to 50 ppm B_2H_6. There were minor differences in the NEXAFS (backside) and Raman spectra for the 50 ppm film.

1) Future work might involve studying if and how elevated B_2H_6 concentration in the source gas alters the diamond-like microstructure.

Chapter 4: ***Microscopic Interpretation of Bare, Boron-doped diamond Coated, and Pt-decorated Carbon Powders***

B-UNCD formation on diamond powders (500, 100, and 3-6 nm diam.) and carbon black powders (glassy carbon and Ketjen black) was evaluated using electron microscopy, Raman spectroscopy, EELS, and XRD. The B-UNCD coating formed on the powder is the predominant microstructural phase deposited, with non-diamond sp^2 carbon phases interspersed. Successful B-UNCD formation over a broad range of powders in terms of size and microstructure was demonstrated.

The formation and structure of Pt electrocatalyst particles on both hydrogen and oxygen terminated diamond powder was investigated. A uniform distribution of Pt particles was observed after chemical impregnation over the entire powder surface regardless of the surface termination. Surface chemistry has little effect on the nominal particle size and distribution on the powder

1) The microscopic evaluation of these powders was as-received, or as-grown. The microscopic and spectroscopic work presented in this dissertation can be used as a reference to compare these same powders after electrochemical testing. Future work should focus on:
    a. Evaluating the microstructure and morphology of the B-UNCD coated powders after anodic polarization.
    b. As mentioned in Chapter 4, 3-6 nm diamond powder was used sparingly for microscopic evaluation as it has an sp^3 diamond core surrounded by a graphitic skin. This convolutes interpretation. More samples need to be examined to determine

the coating efficiency of these <10 nm diamond powders with B-UNCD.

c. More images need to be acquired for Pt-decorated B-UNCD coated powder. The diamond powder used in this study was <u>not</u> B-UNCD coated.

d. Pt particles are ca. 5-7 nm before anodic polarization. We evaluated a limited number of samples after anodic polarization with mixed findings. In some samples the particle size and dispersion was maintained, while in other samples there was significant Pt migration. Microscopic studies of anodically polarized powder is difficult due the presence of a binder needed to form the powder electrode.

Chapter 5: Microstructural Stability of Boron-Doped Diamond-Coated Diamond Powders During Potentiostatic Polarization in Aqueous Acid as Probed Using Electrochemical Methods and In-situ Raman Spectroscopy: Comparison with sp^2 Powders

Electrochemical and *in situ* Raman spectroscopic measurements were made with BDD powder (8-12 µm diam.) before, during and after potentiostatic polarization in aqueous acid. Electrodes were prepared by casting a powder slurry on a glass slide with Nafion serving as the binder. The potentiostatic polarization was performed in either 0.1 M $HClO_4$ or 0.1 M H_2SO_4 at 1.0, 1.2 and 1.4 V vs. Ag/AgCl. Comparison studies were performed with several carbon black powders. It was found that the boron-doped diamond powders are dimensionally stable and corrosion resistant, while the carbon black powders underwent more severe microstructural degradation.

1) The standard for testing PEMFC fuel cell electrocatalyst support materials is now the pellet method. The electrocatalyst support to be tested (*e.g.* B-UNCD powder) is formed into a pellet by first mixing with a binder and then mechanically pressing into a pellet. Fellow researchers in our laboratory are currently conducting experiments with higher surface area B-UNCD diamond (170 m^2/g) using this method. These pellets can be mounted in the homemade cell just as the cast films, and similar in-situ Raman measurements performed.

Chapter 6: The Physiochemical and Electrochemical Properties of Diamond Powders Coated with Boron-Doped Ultrananocrystalline Diamond

Both powders exhibited electrochemical responses for $Fe(CN)_6^{3-/4-}$, $Ir(Cl)_6^{-2/-3}$, and $Fe^{+2/+3}$ that were comparable to typical responses seen for high-quality, boron-doped ultrananocrystalline diamond thin-film electrodes. The electrochemical behavior of the powders was assessed using a pipette electrode that housed the packed powder with no binder. The 100 nm doped diamond powder electrodes were more plagued by ohmic resistance effects than were the 500 nm powder electrodes because of reduced particle contact. Importantly, it was found that the doped diamond powder electrodes are dimensionally stable and corrosion-resistant during anodic polarization at 1.4 V vs Ag/AgCl (1 h) in 0.5 M H_2SO_4 at 80 °C.

Chapter 7: Electrochemically Modulated Liquid Chromatography Using a Boron-Doped Diamond Powder Stationary Phase

Due to the inert nature and a wide potential window of conductive diamond, EMLC separations were carried out at high positive and negative potentials without observable limitations due to surface oxidation and the microstructural changes associated with it, or solvent electrolysis common with other carbon-based materials.

1) Future EMLC experiments should use conductive diamond-coated particles with higher surface areas. Although, much higher surface areas may not be possible to back pressures. As a practical note, we were unable to find a frit less than 1 µm to contain smaller stationary phase particles in the column during the course of this work.

8.1 References

[1] E. Antolini, *Journal of Materials Science* **38**:2995 (2003).

[2] A. J. Appleby, *Corrosion (Houston, TX, United States)* **43**:398 (1987).

[3] H. A. Gasteiger, S. S. Kocha, B. Sompalli, and F. T. Wagner, *Applied Catalysis B* **56**:9 (2005).